THESE

Présentée à

L'U.F.R. DES SCIENCES ET TECHNIQUES
DE L'UNIVERSITÉ DE FRANCHE-COMTÉ

pour obtenir le

GRADE DE DOCTEUR DE L'UNIVERSITÉ DE FRANCHE-COMTÉ
spécialité : Sciences pour l'Ingénieur

Etude de la tenue à long terme de matériaux composites immergés pour structures de récupération d'énergies marines

Long term durability of composites for ocean energy conversion systems

Par
Amélie BOISSEAU

Soutenue le 17 Janvier 2011 au centre IFREMER de Brest devant la Commission d'Examen :

Présidente	M.C.	LAFARIE-FRENOT	Professeur – ENSMA, Poitiers
Rapporteurs	F.	JACQUEMIN	Professeur – Université de Nantes
	P.	OLIVIER	Professeur – Université de Toulouse
Directeurs de thèse	P.	DAVIES	Ingénieur de recherche HDR – IFREMER
	F.	THIEBAUD	Professeur – Université de Franche Comté
Invités	L.	PETERS	Application development leader – 3B
	R.	NICKEL	Sales engineer – Hexion™
	C.	RENAUD	Research associate – OCV™
	D.	PERREUX	Professeur – Université de Franche Comté
	D.	CHOQUEUSE	Ingénieur – IFREMER

REMERCIEMENTS

REMERCIEMENT n.m. Action de remercier, d'exprimer sa gratitude ; phrase, paroles par lesquelles on remercie.

Les remerciements constituent un exercice délicat mais auquel on se plie volontiers afin de montrer sa gratitude à toutes les personnes qui ont contribué de près ou de loin à la progression du travail de thèse. Travail qui peut, quelque fois, s'apparenter à de la monomanie…

En premier lieu, je tiens à remercier mes directeurs de thèse Peter Davies et Frédéric Thiébaud ainsi que Dominique Choqueuse et Dominique Perreux de m'avoir accordé leur confiance durant mes travaux de recherche et de m'avoir guidé dans mes choix tout en me laissant une grande autonomie. Ils ont chacun, dans leur domaine et à leur manière, su poser un œil neuf sur mes travaux et apporter des solutions lorsque les données expérimentales et les modèles numériques me donnaient du fil à retordre. Je tiens également à remercier Yvon Le Guen de m'avoir accueillie dans son service Matériaux & Structures au sein de l'Ifremer.

Je remercie vivement les rapporteurs du Jury de thèse, Messieurs F. Jacquemin et P. Olivier, qui ont relevé le défi d'évaluer un manuscrit de près de trois cents pages tout en anglais. Je remercie également Madame la présidente du Jury, M.C. Lafarie-Frenot, de m'avoir accordé de son temps afin de juger de mon travail.

De plus, ma gratitude va aux représentants des partenaires industriels co-financeurs de la thèse, Messieurs C. Renaud et G. Adolphs (OCV™), P. Nellissen et L. Peters (3B) et R. Nickel (Hexion™) qui ont suivi l'évolution de mon travail et apporté toute leur expertise.

Durant ces trois années de travail de thèse, j'ai eu l'opportunité de croiser un grand nombre de personnes dans les bureaux, les couloirs, les halls d'essais, les labos ou ailleurs. Toutes ces personnes ont participé directement ou indirectement à me faire avancer sur la « voie du thésard » semée d'embuches et d'écueils mais également de bons moments et de rencontres.

Je tiens donc à remercier l'ensemble du service Matériaux & Structures qui a su me faire une place au sein de son équipe. Je remercie tout d'abord les habitants du Donjon, Denise, ma collègue de bureau pendant un an pour nos discussions professionnelles (ou pas), Pierre-Yves pour son avis sur la chimie des matériaux (et le football) et enfin Benoit pour ses conseils de sage sur la modélisation numérique, les algorithmes génétiques, les statistiques ou le mode de consommation optimal des *Granola*. Je remercie également Nico pour son aide lors des manips les pieds dans l'eau ainsi que Dédé qui m'a laissé envahir son atelier. Je n'oublie pas non plus Albert et Philippe pour leurs conseils d'ainés durant les essais, Bertrand qui a toujours pris le temps de se pencher sur mes problèmes informatiques ainsi que Luc pour son génie bricoleur. Je remercie également Florence qui a pris le temps de m'expliquer avec brio toutes les subtilités administratives.

Je remercie également l'équipe du service mitoyen, Interfaces & Capteurs pour tous les bons moments passés autour d'un café, d'un thé et/ou d'une part de gâteau à refaire le monde : les Florences, Caro, Manu, Florent, Manue, Marie-Pierre, Catherine, Romain, Géraldine et tous les autres …

Je remercie également Philippe Crassous pour sa gentillesse, son humour, sa patience et son accueil au MEB, souvent au pied levé.

Enfin, je ne saurai oublier tous les amis qui m'ont soutenu pendant ces trois ans, qui ont supporté (presque) sans rien dire mes complaintes et mes coups de gueule, mes moments d'euphorie et de découragement, mes phases d'activité intense et de procrastination. Je remercie donc Mélanie pour ses conseils avisés « d'ancienne » et nos fous rires dans le bureau, les habitants du p'tit manoir (au grand complet) pour toutes les soirées en leur compagnie, Clex-infos-services-coatching-de-fin-de-thèse et Aurélie pour toutes leurs attentions et tous les moments passés ensemble, plus particulièrement lors de nos fréquentes escapades en ville pour effectuer des contrôles qualité ou autour d'une bonne table. Je remercie également toutes les personnes qui m'ont permis de ne pas penser qu'à la thèse, les sportifs du club, les artificiers d'Auguste ou les pirates du Fort de Berthaume.

Je n'oublie pas non plus de remercier Jacques Vabres et Sir Lipton pour leur soutien au quotidien.

Enfin je remercie ma moitié qui m'a encouragée et poussée quand l'envie n'était plus là, qui m'a calmée quand l'angoisse se dessinait et qui m'a soutenue lorsque la fatigue se faisait sentir.

Merci à mes parents, à ma sœur et à ma famille qui m'ont toujours soutenue.

TABLE OF CONTENTS

INTRODUCTION

There is considerable interest in ocean energy at present, as a renewable alternative to fossil fuels. Major wave energy and tidal turbine projects are underway and the first commercial projects are appearing. The development of ocean energy conversion systems places more severe requirements on materials than similar land-based structures such as wind turbines. Intervention and maintenance at sea are more costly, so long term durability must be guaranteed if ocean energy supply is to be economically viable.

Composite materials offer many advantages over metallic structures, with respect to ease of fabrication of complex profiles, light weight for installation, and many composites marines structures have shown remarkable longevity.

Nevertheless, material selection is critical. In the case of a composite material reinforced with glass fibre, the choice of glass is important if stress corrosion is to be avoided, while resin chemistry must be optimised to limit matrix damage. Fibre/matrix interface properties are also critical when composites are immersed for long periods and the know-how of both fibre and resin producers is essential to develop these.

The main objectives of this study are first to identify and quantify the influence of the specific environmental marine conditions on the composite material behaviour. Secondly to quantify the influence of the glass fibre type (E-glass, Advantex® or HiPer-tex™ fibres) as a function of the environment, air or natural circulating sea water. Then to develop a numerical model to understand the coupling phenomena between the mechanical damage and the water absorption. Last, to evaluate the long term durability of composite structures for ocean energy conversion systems.

This collaborative study has been performed jointly with the University of Franche-Comté, two glass fibre manufacturers, OCV™ and 3B, a resin formulator, Hexion™ and a research institute, IFREMER.

This thesis is divided in five parts as described below :

Current state of art	• Composite structures • Fatigue of wind turbines & ocean energy experience • Fatigue testing and characterization • Sea water ageing	***Chapter I***
Test procedures	• Material & fabrication • Quality control • Natural sea water ageing • Mechanical tests • Numerical analysis	***Chapter II***
Composite characterization	• Material characterization • Kinetics of diffusion • Mechanical characterization	***Chapter III***
Numerical modelling based on test results	• Mechanical analysis of static behaviour • Water diffusion • Coupling mechanical damage & ageing • Evolution of damage analysis	***Chapter IV***
Discussion	• Material parameters • Test parameters • Integration in a turbine blade model	***Chapter V***

CHAPTER I
SCOPE OF THE STUDY

I- SCOPE OF THE STUDY

This first chapter presents the industrial context of the PhD work and a bibliographic review of the concepts included in the study. This is followed by a summary of the tests used in previous studies and a review of the different approaches for modelling fatigue damage and to explain sea water ageing.

1- Industrial context

Recent increases in oil prices have focussed attention on alternative sources of energy. Ocean energy is one of the most promising, and the resource can be broadly split into five groups [1-3] : tides, waves, tidal currents, temperature gradients and salinity gradients.

Several recent evaluations of these resources suggest that their potential is of the same order as that of the present capacity of electricity generation worldwide [3]. Interest in ocean energy is not new, tidal barrage plants have been operating for many years including the barrage on the Rance estuary, in Brittany, which has been producing electricity since *1966* [4]. What is new is the level of current development and investment, several demonstration projects in the *0.5* to *1.5 MW* range are either being evaluated or will shortly be deployed, particularly wave and tidal current systems.

Many devices have been proposed for wave and tidal energy conversion [1-3] but one feature of all the systems is that long term durability is essential. Maintenance free operation is a pre-requisite if these systems are to be economically viable. This, together with light weight, is one of the main reasons for considering composites rather than metallic structures for these applications. Fortunately there is extensive experience of composites in marine structures and in the next section a brief overview of this experience will be presented. Many studies of composites in water are also available and these will be briefly reviewed. Another source of information concerning composites in large structures is wind turbine blades where cyclic loading has been examined in some detail, and this will be briefly described too. Some short term information has also been gained from prototype ocean energy devices, and this will be summarized.

1.1- Composite marine structures

Glass fibre reinforced polymers have been the preferred material choice for small boat-builders for over *50* years [5, 6]. Other applications include high speed ferries and a recent overview [7] provides data for the composites used in marine vessels. Military naval applications have used large quantities of glass reinforced composites since the MCMV (Mine Counter-Measure Vessel) programmes started in the *1960*'s. *Smith* has given a detailed overview of the different concepts developed by different navies [8] and some information on large composite submarine structures is also available [9].

The offshore industry has become interested in composite materials in recent years and several large projects have generated both material data (e.g. the Marinetech programme [10]) and prototype experience on structures such as risers [11].

Underwater applications also include oceanographic systems, glass/epoxy has been used in instrumentation housings (*Figure 1a*), and benthic landers (*Figure 1b*), two applications developed at IFREMER. The former are generally filament wound cylinders [12] while the latter is a *2* meter high structure designed to remain in deep sea for months or years.

Developed in *1997* this is still in service and has been used in campaigns down to more than *4 000 m* depth.

Finally, an application very similar to wave energy converters is that of navigation buoys, moored at sea and exposed to the environment in very severe conditions. There are over *4 000* buoys around the French coast, a recent conference summarized experience in this area where polymer and composite floating buoys are increasingly being used to replace steel [13, 14].

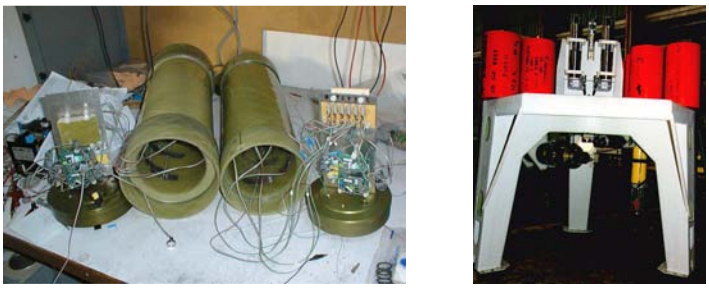

(a) *(b)*

Figure 1. *a) Instrumentation housings, b) MAP benthic lander*

1.2- Composites in water

In parallel with applications in service there have been many laboratory studies of the influence of moisture on composite properties. Early studies focussed on relative humidity and large amounts of data were published, e.g. [15].

As part of a development of the use of composites for cooling water tubes a large number of durability studies were performed by EDF in collaboration with IFREMER and the University of Franche-Comté [16, 17]. These studies generated data on composite properties after immersion in water for periods over *10* years. Mechanical properties of aged samples were evaluated periodically and a loss in properties was noted after *2.5* years in water at *60°C*. This was attributed to hydrolysis of the epoxy resin, and underlines the importance of resin selection; the anhydride hardener initially selected is not stable over long periods at *60°C*. Selection of an alternative hardener solved the problem, though it should be noted that even after *10* years' immersion at *20°C* the mechanical properties of the original (anhydride) material were still intact.

1.3- Fatigue loading experience (Wind turbine structures)

There have been many studies of fatigue in composites and a recent book gives a good overview [18]. A major source of data on cyclic loading of composites, both from laboratory tests and in service, is the wind energy industry. Composites are the preferred material for wind turbine blades. Glass reinforced composites have been the first choice since the *1970*'s, though recently carbon has found some applications as blade lengths extend over *50 m*. *Echtermeyer et al.* presented results from the EU Joule project [19] in *1996*, and more recently the European projects FACT and OPTIMAT have generated large amounts of fatigue data [20].

There is still some discussion over how to model cumulative damage in composites, in particular how to take into account the loading history effects related to the chronology of high and low loads [21]. Nevertheless, typical loading spectra have been defined such as the eight proposed in the WISPER (WInd SPEctrum Reference) sequence [22]. These spectra can be used for the evaluation of new designs by simulation and to define appropriate test

procedures. In parallel with this approach there has also been considerable interest in reliability based predictions [23].

1.4- Use of composites in prototype ocean energy structures

First it should be noted that the amount of information available in the open literature from prototype tests is quite limited, as these are generally commercial developments.

Concerning tidal turbines, the Seaflow project, a *300 kW* prototype two-blade tidal turbine immersed off the Devon coast in June *2003* [24], used 11 meter diameter composite rotor blades instrumented with strain gauges. The construction involved a central *65 mm* thick carbon composite spar covered by stiffened glass/epoxy fairings [25]. Also in *2003* a Norwegian tidal power station was installed near Hammerfest, using *10 m* long glass fibre composite blades. In *2008* within the Seagen project a *1.2 MW* twin turbine was immersed [26], using a similar design to Seaflow again from Marine Current Turbine. The blades were longer than those tested in the Seaflow project, each *7.5 m* long. One of the turbines shed two blades following a computer incident [27] but the project continued after repair, and by February *2010* had delivered over *350 MWh* of power into the grid. Another large scale prototype (*500 kW*) with *6 m* long composite (glass and carbon) blades was immersed by Tidal Generation Limited in *2009*. In the USA, in the RITE project, following development trials with a *3 m* diameter turbine, six turbines were installed in *2007* in New York. These used *4.9 m* diameter turbines each with three composite blades, similar to existing wind turbine designs. Some blade failures were noted and the blades had to be redesigned.

The first French tidal turbine prototype to be tested at sea was developed within the Sabella project [28]. This is a six-blade turbine made of glass fibre composite fairings on steel spars, which was immersed off the Brittany coast in April *2008*. *Figure 2a* shows the system in service. The blades are composites sandwich structures, including a central metallic spar with glass reinforced composite facings on a foam core as shown on *Figure 2b*.

(a) *(b)*

Figure 2. *a) Sabella tidal turbine during assembly, b) Detail of blades during manufacture*

Other composite tidal turbine blades have been used in the OpenHydro project [29], and a recent paper described work conducted on composite blades as part of a study for an *11 m* diameter blade for a demonstration plant in Japan [30]. In addition to turbine blades, composites are also of interest for shrouds, mounting frames and other components of these systems.

Composites are also of interest for wave energy devices. For example, Wave Dragon is considering a composite structure for a full-scale, multi-megawatt device (their *20 kW* prototype is made of steel), the Pelamis prototype used composites and within FO3, the Norwegian wave power project, a generator is integrated in a floating platform construction which is built in composite.

All these examples show that composites will be a critical part of ocean energy devices, and a thorough understanding of their long term behaviour in sea water is essential.

2- Bibliographic study

This bibliographic study is divided into three main parts. The first one focusses on the mechanical characterisation of the composite materials and the test techniques used. The second part is related to the understanding and the prediction of the fatigue behaviour of fibre-reinforced composites. The last part refers to sea water ageing and its effects on a composite material.

Composite materials range from filled elastomers to ceramic composites, produced by many different manufacturing techniques with a wide range of reinforcement variations. The characterization of composite materials can involve mechanical, physico-chemical or chemical analyses.

In this background literature study, we have focussed on the test techniques used in previous studies of the mechanical characterization of glass/epoxy materials under quasi-static and fatigue loads. The majority of the tests described were applied to unidirectionally reinforced materials; this is of interest here as our initial aim in the present study is to evaluate the influence of different types of glass fibre, not to perform tests which stress the matrix. The objective of this bibliography is to highlight relevant test methods, not to compile test data.

During this part of the bibliographic study, we have found various specific mechanical test methods, and this underlines the limitations of standard tests, particularly for cyclic loading in water. A short section on standard test methods is given first, then the different methods for quasi-static loading will be described, followed by those used for fatigue tests.

In addition, the dimensioning of composite structures requires a material behaviour model. Fatigue of fibre-reinforced composite materials is a complex phenomenon. There is therefore a vast literature available, so it is necessary to limit the frame of work.

The fatigue life and the mechanical properties of composite materials depend on many factors including the matrix behaviour, the fibre behaviour, volume fractions, fibre orientation, moisture content, porosity, applied stress, strain rate and stress amplitude, as well as the coupling between these parameters. Most research studies on fatigue behaviour of composite materials rely on performing a lot of fatigue experiments on small scale material specimens, sometimes followed by limited tests on larger scale structural components.

Various ways to understand or predict the fatigue behaviour of composite materials have been found during this bibliographic study. After a short introduction, we have first focussed on the criterion used as a indicator of damage or failure, and then on the methods and tools used to describe and predict the lifetime of composite material subjected to cyclic loading.

In addition to the mechanical stresses, the environment causes degradation of the physical and chemical structure of these materials. The influence of ageing on mechanical characteristics is widely recognised.

In the final part of the bibliographic study, a overview of the water diffusion mechanisms is proposed and the main analytical formulations are summarized. Then the effects of water diffusion on mechanical behaviour are presented.

2.1- Standard test methods

Various bodies propose standard test methods for unidirectional composites. The most frequently used are ISO (International Standards Organization), when available, and ASTM (American Society for Testing Materials). The latter provide compilations of test methods [31]. In certain cases French (AFNOR) or German (DIN) documents are used. It should also be noted that certain industries (Aerospace and Automotive in particular) have developed their own composite test methods.

Tensile testing is usually performed according to ISO 527. Compression is far more controversial, there are many different fixtures (ASTM proposes at least four) and without any consensus (except to agree that any published compression test values for unidirectional specimens should be treated with extreme caution). In-plane shear characterization is also difficult, and again several standards exist. A tensile test on a *+/-45°* specimen is often used. For flexure ISO 178 and ASTM D790 are popular.

Sims has compared various standards and been instrumental in trying to harmonise standard methods for mechanical testing of composites [32].

There is little guidance in the standards on how to measure through-thickness properties of composites and there are far fewer standard test methods for fatigue testing. ASTM proposed a tension fatigue method (D3479) but this is a very general document.

2.1.1. Quasi-static tests

Quasi-static tests are performed on unidirectional specimens in order to obtain the intrinsic properties of the material, such as elastic constants (moduli E_1, E_2, E_3, G_{12}, G_{23}, G_{13}, and Poisson's ratios ν_{12}, ν_{23}, ν_{13}) and strengths.

These initial properties can be determined either directly, from tests involving simple loading such as tensile or compression, or indirectly from more complex tests such as three-point bending, four-point bending and other less well-known configurations.

a) Tensile tests

The characteristics of composite materials are most easily defined using tensile tests, on impregnated yarns, on rectangular [33-36] or profiled composite specimens. The dimensions of tensile specimens are standardized but for particular applications thinner or thicker samples may be used if they are more representative of the final application.

Tensile tests can be performed on dry fibres, but are very difficult to perform correctly as it is hard to uniformly tension a bundle of dry fibres. *Pauchard* [37] performed tensile tests with acoustic emission on dry fibres of *100 mm* length (*Figure 3*) to examine their damage behaviour.

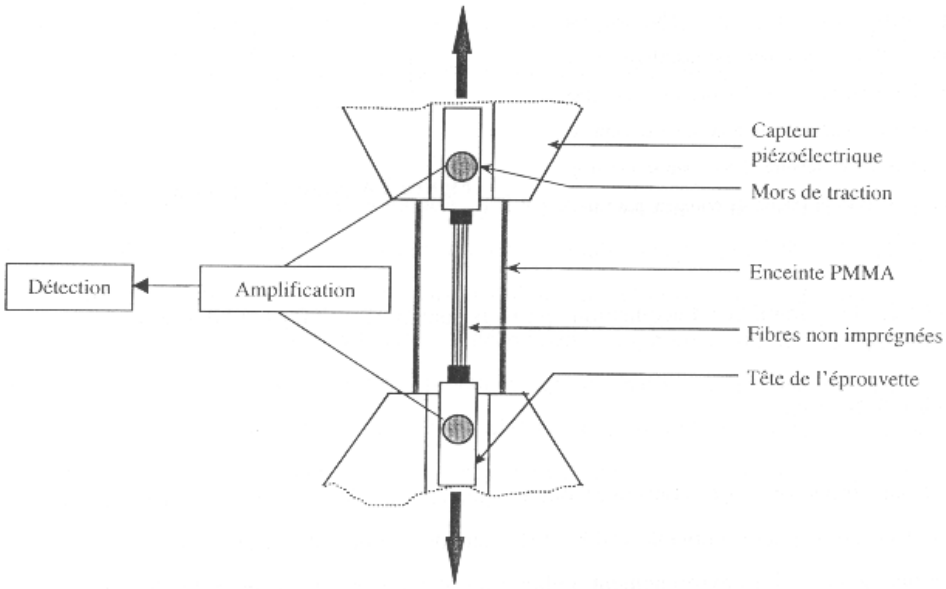

Figure 3. *Tensile device to study damage in dry glass fibres in tension [38]*

Examples of standard tests with rectangular specimens are described by *Perrot* [33], *Ellyin & Kujawski* [34], *Philippidis & Vassilopoulos* [35] and *Kujawski* [36]. Their dimensions are similar (*200 x 20 x 10 mm* [33], *200 x 12.7 x 5 mm* [34] or *250 x 25 x 2.6 mm* [35]), specimen widths vary between standards, and they have been tested with or without aluminium or composite end tabs (*Figure 4*).

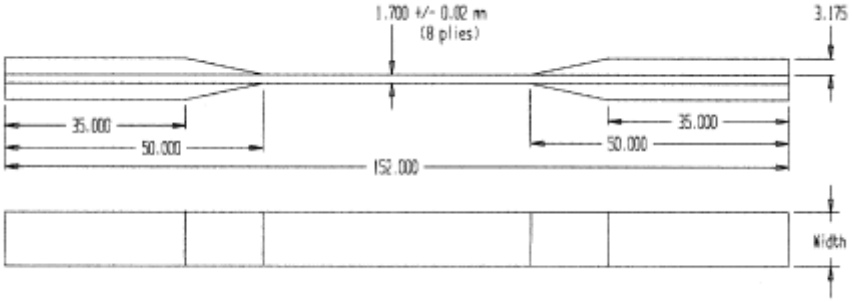

Figure 4. *Typical specimen dimensions [36]*

Such specimens can also be used for cyclic loading as it will be shown below.

b) Compression tests

Several authors have used compression tests to measure modulus and strength of unidirectional glass/epoxy composites, but the most serious problems in the compression testing of composite laminates is premature failure caused by global buckling. *Schultheisz & Wass* [39] have reviewed compression tests methods and micromechanical failure theories. So, test methods are based on special fixtures to restrict buckling, such as the Illinois Institute of Technology Research Institute (IITRI) and Celanese fixtures. However, they create other problems, including debonding between end tabs/specimens interfaces and mid-plane delamination due to high interlaminar stresses. *Tan & Knight* [40] have presented an extrapolation method for the evaluation of compression strength of unidirectional composites and shown that the strength is correlated with the end taper angles.

c) Three-point bending

Three-point bending is widely used for glass/epoxy composite characterization. It is a simple test requiring a minimum of instrumentation and no special specimen preparation.

The test standards for three-point bending such as ASTM 790 [31], define the dimensions of the samples, the support span, the load span and the radius of the loading points based upon the ratio L/d.

One example can be found in the PhD work of *Pauchard* [38], who used image analysis to detect the superficial monofilament failure. The load was applied at room temperature at a constant speed of *5 mm/min*. The support span measured *130 mm* which is 26 times specimen depth, in order to limit shear effects.

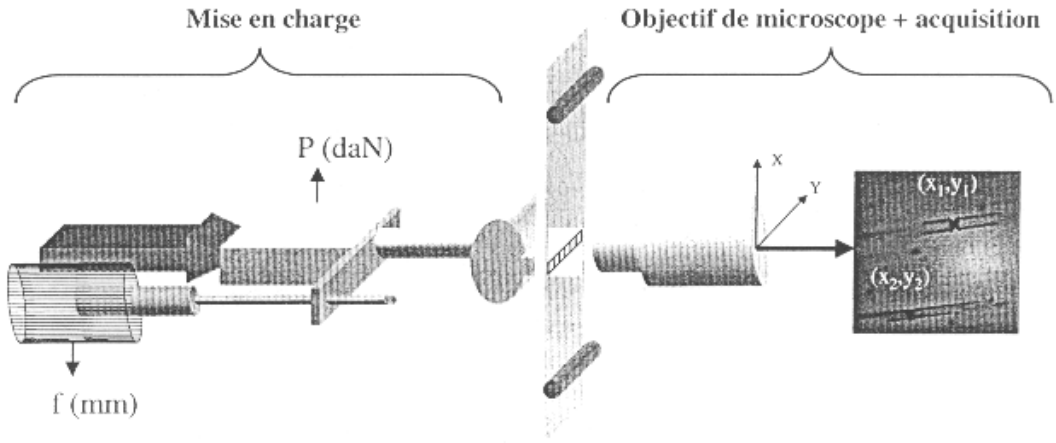

Figure 5. *Schematic diagram of the three-point bending test with image analysis system [38]*

d) Four-point bending

ASTM 790 [31], also describes four-point bending, and again defines the dimensions of the samples, the support span, the load span and the radius of the loading points based upon the ration L/d. Various examples can be found for glass/epoxy materials [41-46]. However, nominally similar tests performed using this method can still involve differences such as the shape of the sample or the set-up.

For example, during the tests carried out by *Caprino et al*. [41, 42] in order to validate his fatigue model, the specimens used were rectangular (*80 x 12 x 3.9 mm* [41] or *80 x 20 x 4 mm* [42]). All the tests were carried out at room temperature, adopting an outer span *66 mm* and an inner span *22 mm*. The specimens were loaded up to failure in stroke control.

For *Kim et al.* [43], the specimens were even smaller (*50 x 10 x 1 mm*) and the outer span and inner span were respectively *25 mm* and *12.5 mm* (*Figure 6*).

Such small specimens may be strongly affected by the stress field around load points.

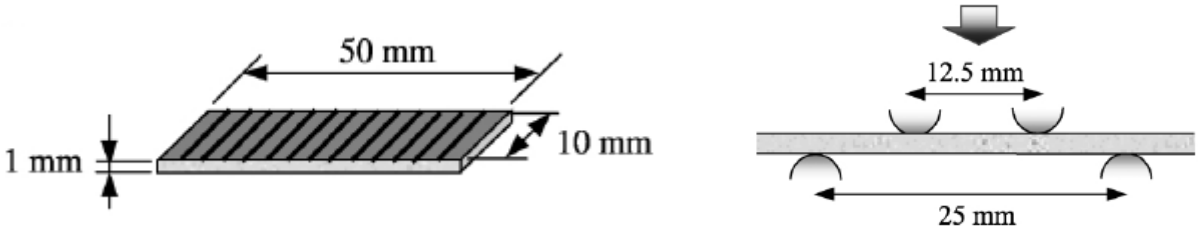

Figure 6. *Example showing dimensions of flexural specimens and basic conditions of the four-point bending test [43]*

In the literature, we can also find four-point flexure tests carried out on structural elements such as I-beams (*Figure 7)* [44]. For example, I-beams, of length *1 200 mm*, web depth *125 mm*, flange width *75 mm* and thickness *3 mm*, were tested using a constant displacement mode of control.

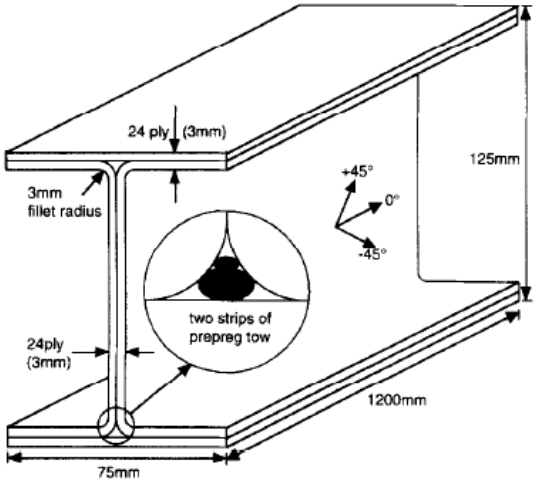

Figure 7. *Dimensions of the I-beam [44]*

The basic conditions of the four-point bending system can be modified in order to focus on pure bending with large displacements and rotations [45], or to apply both bending and shear loads [46].

Zineb et al. [45] proposed an original device making pure bending loading possible in large transformations. Their sample was embedded at each end using a sleeve with a rigid body movement (*Figure 8*).

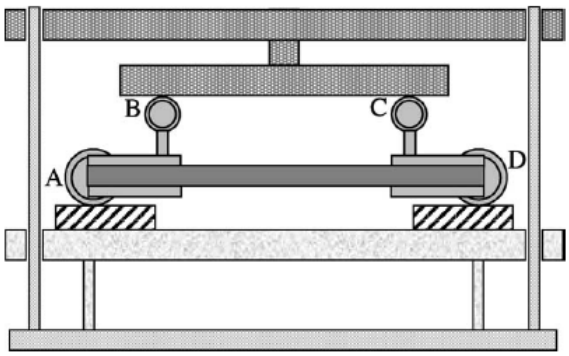

Figure 8. *Kinematic diagram of a four-point bending bench allowing large transformations [45]*

Another device, developed by *Ferry et al.* [46] (*Figure 9*) generates multiaxial stress states involving both four-point bending and torsion components. But it can also generate pure bending and pure torsion loads. However, this clearly requires a much more complex test fixture and is not suited to tests in sea water.

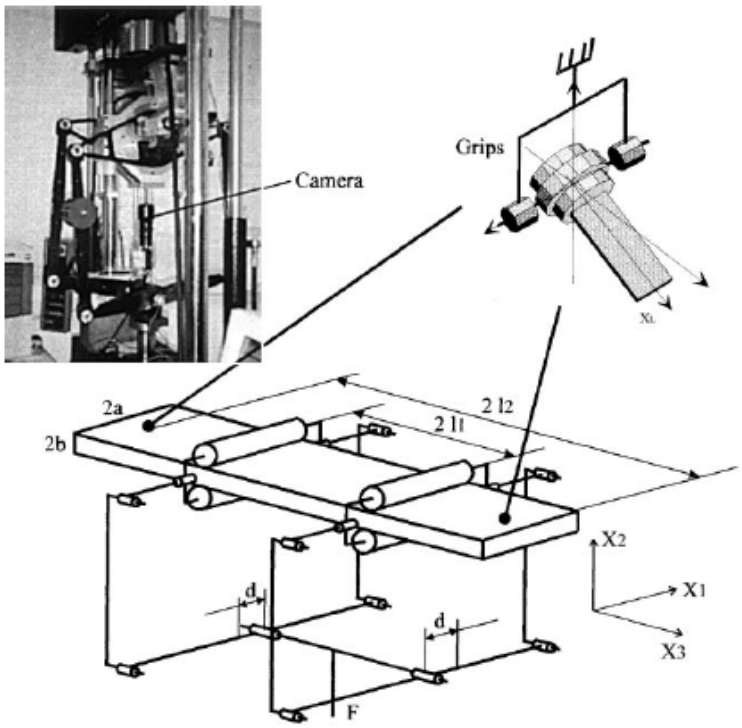

Figure 9. *Experimental device [46]*

All the tests described above were carried out with un-notched specimens. Flexural tests can also be used to test samples with implanted defects, under either three-point (End Notched Flexure ENF) or four-point (4ENF) loads, *Figure 10* [33], and these enable the resistance to shear delamination to be measured using a critical strain energy release rate (G_{IIc}) [47]. These tests can also be performed under cyclic loads [48].

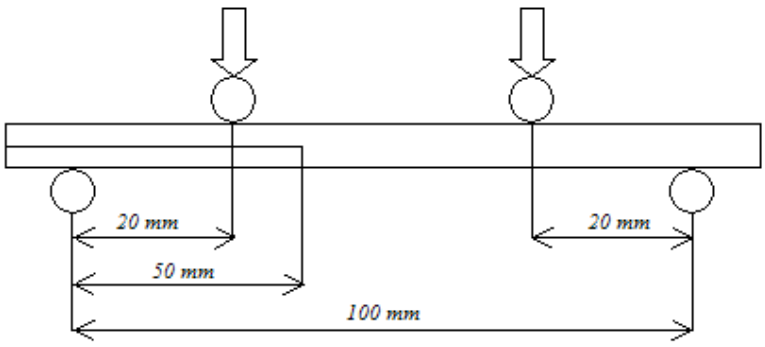

Figure 10. *Four-point End Notched Flexure Test [33]*

e) Other experimental set ups for quasi-static tests

In addition to the bending and tensile tests, some other combined loading devices have been proposed, e.g. [49]. In that work, solid cylindrical specimens were loaded in torsion and tension or compression in a proportional manner. The specimens were subjected to pure compression, pure torsion and combined compression-torsion under displacement control loading, rotation control loading and combined displacement-rotational control loading, respectively (*Figure 11*).

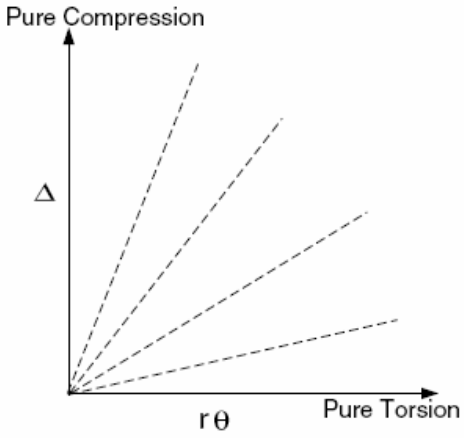

Figure 11. *Different loading paths in a displacement/rotation control test [49]*

Various other devices have been proposed for biaxial tensile testing, in particular cruciform specimens which can be loaded in special machines, but there is no standard test method to measure properties under biaxial loading. The complexity of these specimens makes interpretation of results difficult.

Once the quasi-static behaviour has been characterized, cyclic loads can be applied to determine the fatigue behaviour.

2.1.2. Fatigue tests

Fatigue is the progressive and localized structural damage that occurs when a material is subjected to cyclic loading. In order to predict life time of a composite material, fatigue test programmes are used to establish the resistance of the material to repeated loading. As for quasi-static tests the data are often normalized and there is a range of geometries and configurations.

Sims [18] has reviewed the basics of fatigue test methods, difficulties that need to be avoided and the degree of standardization achieved.

a) Tensile tests

Tension-tension fatigue tests are performed with either rectangular specimens [35, 50-53] or with "dog-bone" specimens [54, 55]. Such tests are usually performed at room temperature but a few tests have been carried out in a humid environment [56]. A load ratio *R* (minimum stress/ maximum stress) of *0.1* is often used.

The dimensions of the rectangular specimens can vary greatly (from *150 x 25 x 6 mm* [50] to *250 x 25 x 2*.6 *mm* [35]), they can have aluminium or composite tabs glued to the ends

[35, 52] or again they can be notched [51]. Nevertheless, the test method is always the same, the specimens are cyclically tested in tension with constant amplitude.

Example of tests with "dog-bone" specimens are given by *Ferreira et al.* [54] (*Figure 12*) and *Dyer & Isaac* [55] (*Figure 13*). This geometry is used to ensure a failure in the central part of the specimen. As previously, specimens are usually loaded in constant amplitude load or displacement mode.

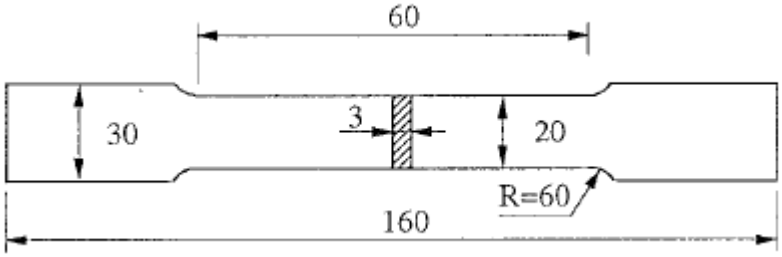

Figure 12. *Fatigue test specimens (dimension in mm) [54]*

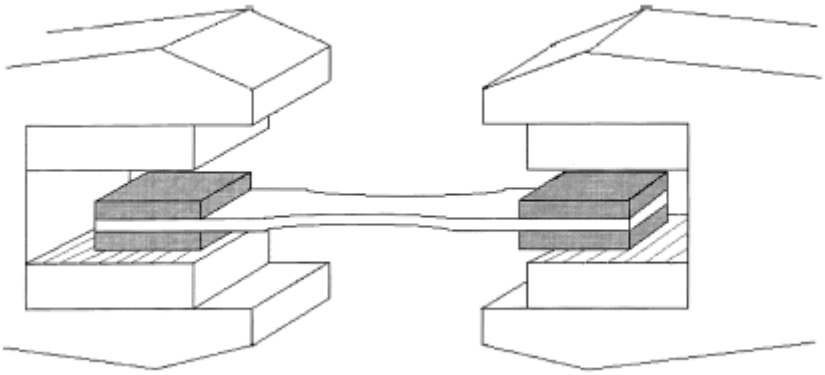

Figure 13. *Schematic diagram showing the gripping arrangement used for fatigue test [55]*

Shan & Liao [56] have described tension-tension fatigue tests in air and in distilled water at *25°C* (*Figure 14*) in order to quantify the environmental fatigue.

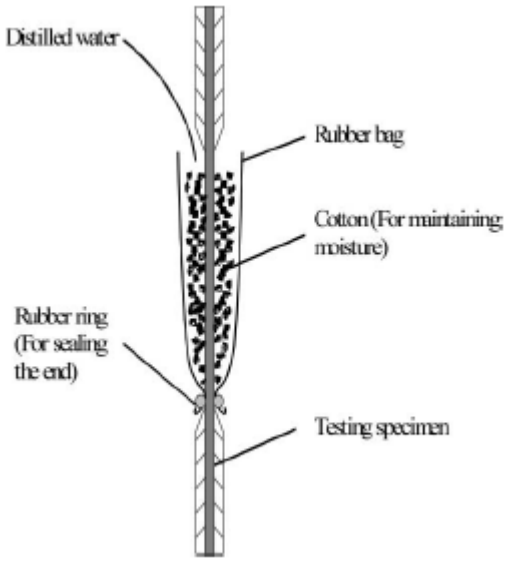

Figure 14. *Environmental fatigue specimen set-up [56]*

b) Tension-compression tests

When data for other loading ratios such as *R=-1* are required the experimental set-up becomes more complicated. The standard specimen geometries for tension and compression are quite different, the former tend to be long to obtain good strain data from extensometers, while the latter are short to avoid buckling. Anti-buckling guides may then be a solution, though these can introduce parasite loads. An extensive programme of fatigue testing was performed for wind turbine applications within the OPTIMAT European project. The data are available on the OPTIMAT website [57] and specimen geometries are described there. For those tests parallel sided tension/compression samples were used with a short (*35 mm*) free length.

c) Three-point bending

In the literature, three-point bending is often used for fatigue tests. However, there is no standard for this type of tests. The dimensions of the specimens, the support span and the support noses radii can all vary. *Salvia et al.* [58, 59] used a specimen *100 mm* long, *10 mm* width and *3 mm* thick and a load span of *60 mm* in order to avoid shear effects. *O'Brien et al.* [60] chose smaller specimens (*57.2 x 6.35 x 5.56 mm*) and a span length of *50.8 mm* (*Figure 15*).

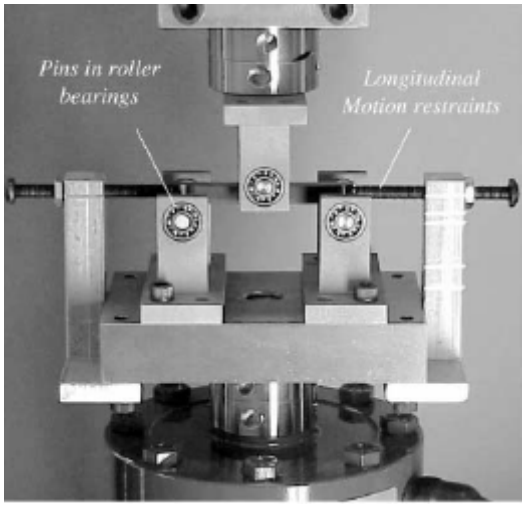

Figure 15. *Three-point flexure fatigue test fixture [60]*

An alternative fatigue test method uses undulating bending, developed by *Fiore* & *Vincent* [61]. The test device is composed of a moving support span with an eccentric displaceable crank mechanism. The maximal specimen thickness for their fixtures was *5 mm* and the maximal deflection was *40 mm*.

In all the flexural test methods described previously, the goal was to minimise the shear in the specimens. *Roudet et al.* [62] have developed a three-point bending test with predominant shear. The length of the specimen was chosen equal to *100 mm* and the thickness was *5.6 mm*. The distance between fixed rollers was *4 mm* and the moving roller was centred (*Figure 16*).

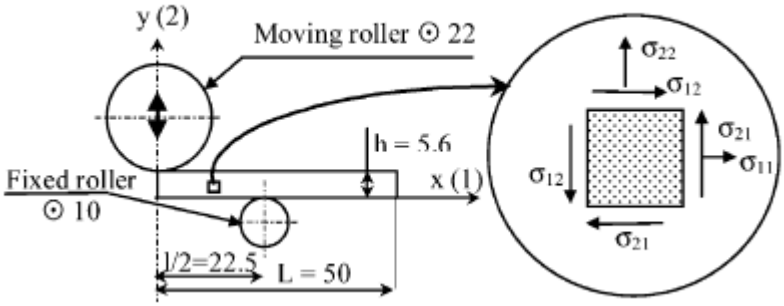

Figure 16. *Device and specimen geometries – Stress definition [62]*

Three-point bending fatigue tests can be performed in water as shown in *Pauchard*'s PhD thesis [38]. An hydraulic cylinder and a cross bar were used to impose a displacement to four specimens tested simultaneously, placed in water at *40°C* (*Figure 17*).

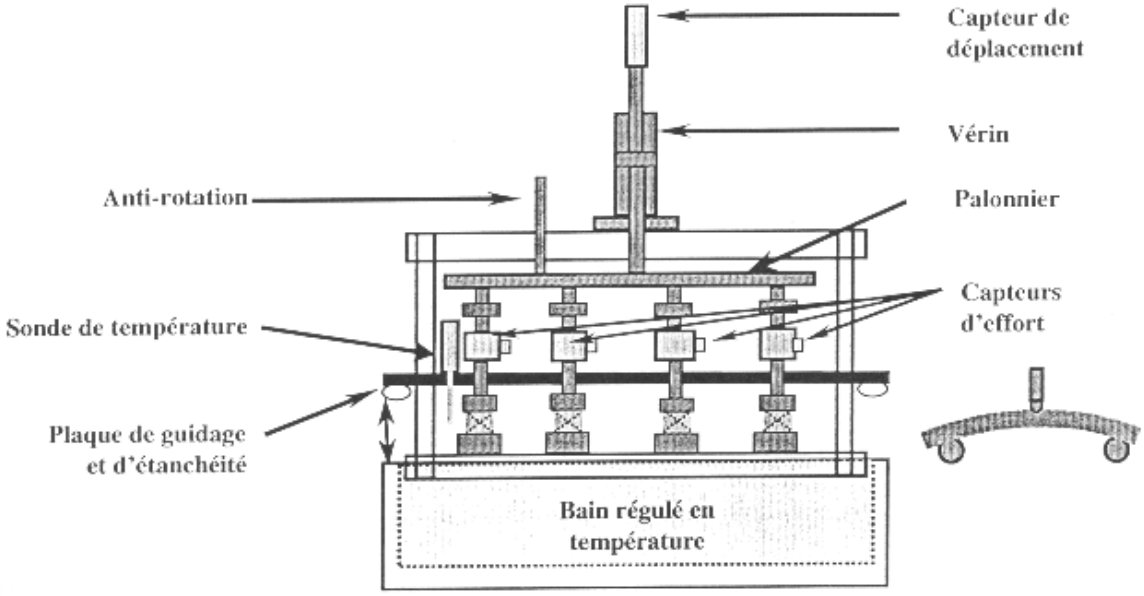

Figure 17. *Fatigue device in water [38]*

d) Four-point bending

The four-point bending devices used for fatigue tests are generally the same as those for three-point bending with a modified upper span [60, 61].

During the tests performed by *O'Brien et al*. [60], the bottom span length was *50.8 mm* and the top span length was *25.4 mm* (*Figure 18*).

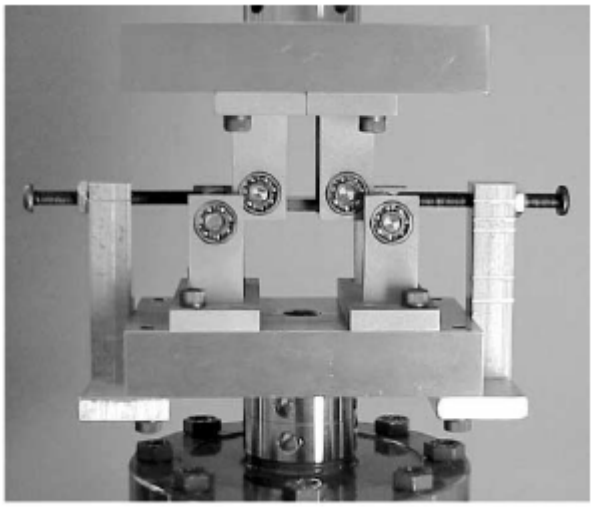

Figure 18. *Four-point flexure fatigue tests fixture [60]*

e) Other experimental set ups for fatigue tests

In addition to the "traditional" bending and tensile fatigue tests, there are a number of variants. These include compression bending tests [58] on samples *100 mm* long, *10 mm* width and *3 mm* thick. In this test an axial compression is applied to the sample. The specimen is gripped in loading devices allowing free rotation at each end (*Figure 19*).

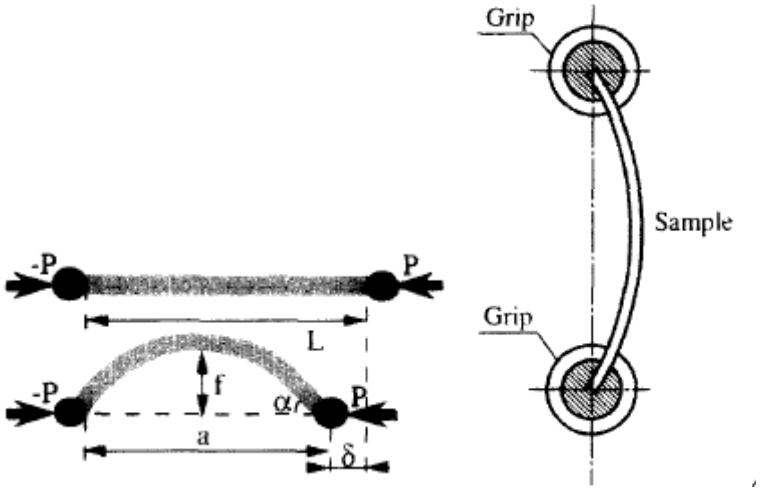

Figure 19. *Principle of compression bending test method [58]*

Bellenger et al. [63] carried out fatigue tests with an "alternative bending device" (*Figure 20*). One end of the sample was in contact with the grip of the input testing shaft, while the other end was maintained between two fixed rollers fixed to a load cell.

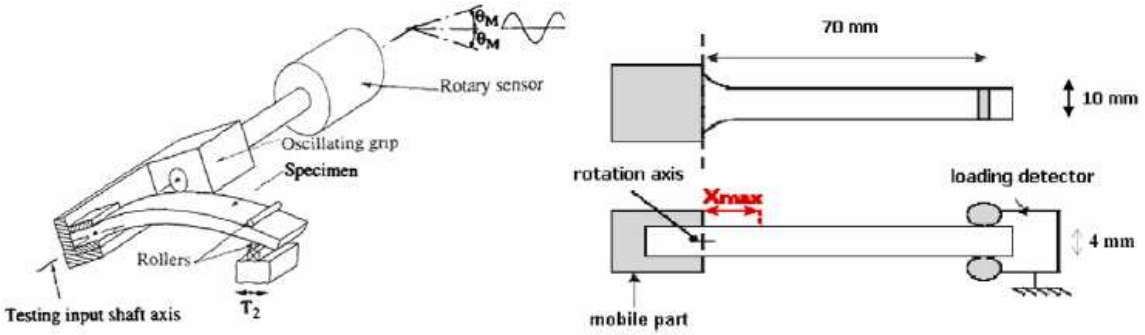

Figure 20. *Alternative bending device used for fatigue tests by Bellenger et al. [63]*

The experimental set up developed by *Van Paepegem & Degrieck* [64, 65] is specially designed for flexural fatigue tests on cantilever beams. The fatigue tests are performed with a displacement controlled bending device.

Their device, shown below (*Figure 21 and Figure 22*), imposes an alternating displacement to one end of the specimen while the other end is clamped. The amplitude of the imposed displacement is a controllable parameter and is constant throughout the whole fatigue test.

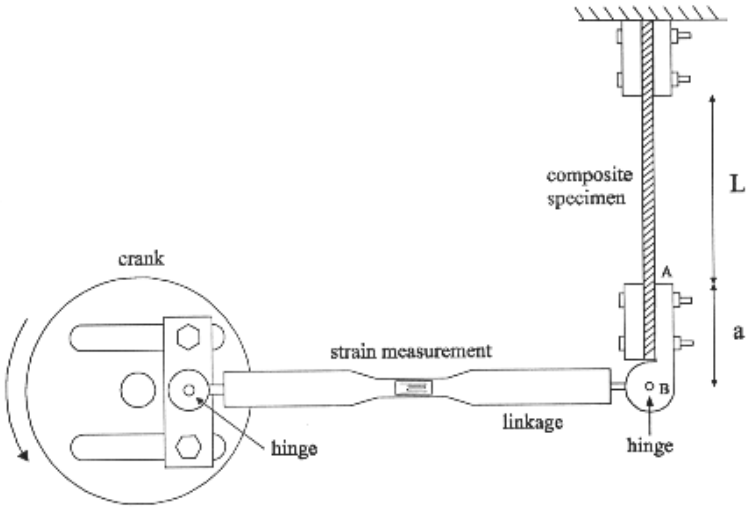

Figure 21. *Schematic drawing of the crank-linkage mechanism [64]*

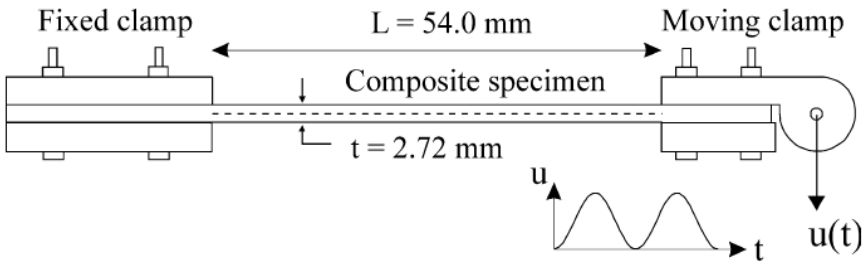

Figure 22. *Schematic representation of the experimental bending fatigue set up [65]*

El Assal & Khashaba [66] carried out combined torsion/bending and pure torsion fatigue tests on composite rods of *7.9 mm* diameter (*Figure 23*). The load was imposed at one end of the specimen by an oscillating spindle driven by means of a connecting rod, crank and double eccentric pulleys. The test specimen was fixed in the testing machine using special grips that provide combined torsion/ bending loads (*Figure 24*).

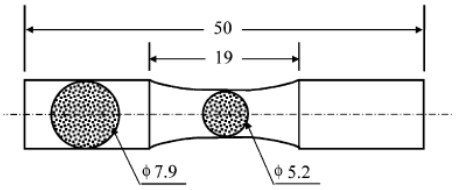

Figure 23. *Dimensions of the specimen [66]*

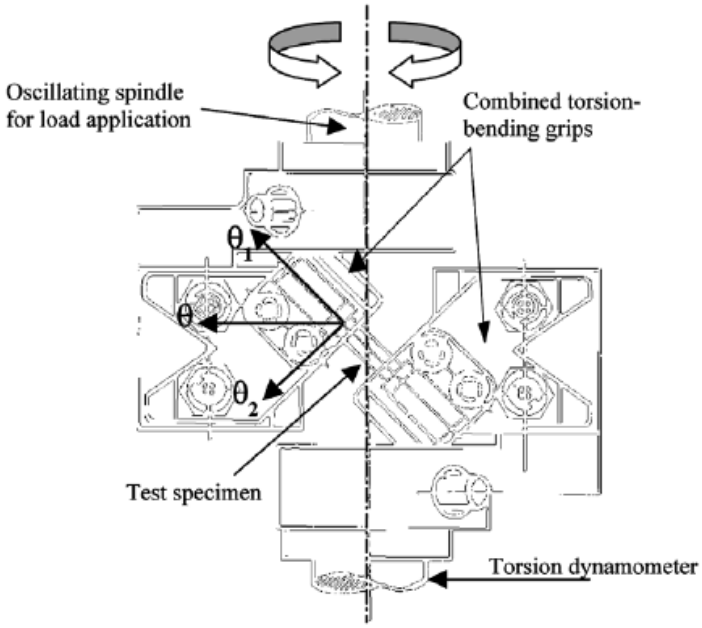

Figure 24. *Gripping of specimen for combined loading (torsion/bending).*

The controlled test displacement θ is resolved into two components, θ_1 (bending) and θ_2 (torsion).

Fatigue tests can also be performed on these unidirectional rods using a constant deflection fatigue testing machine [64].

The final fatigue test method presented here is used to characterise the shear behaviour under cyclic loads [67]. Different requirements have led to the design and manufacture of a testing device, termed the “Cube Test” (*Figure 25*). The particular case of cubic specimens enables the shearing behaviour of the material to be studied in relation to the chosen orientation of the specimen in the device, so the 1-2, 2-3 and 1-3 planes can be loaded. The specimens are instrumented with 3-element strain gage rosettes bonded on both the front and the back. Precise specimen preparation is critical for such tests.

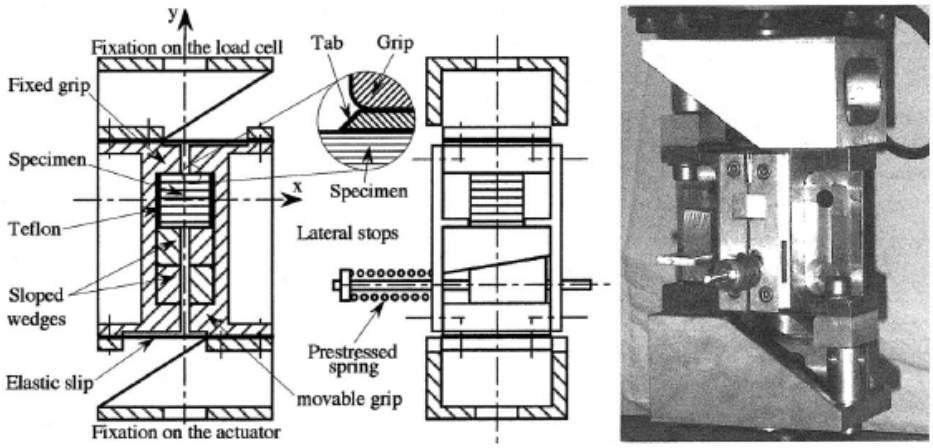

Figure 25. *Schematic drawing and view of the shear testing machine [67]*

2.2- Fatigue behaviour of fibre-reinforced composite materials

The "fatigue effect", in general terms, is the reduction of remaining strength or stiffness, and possible failure, after a finite number of load cycles has been applied. These load cycles are lower in magnitude than the load required to cause failure in a single cycle. Damage mechanisms due to fatigue loading are not uniform, and consist of discrete events which cause non-uniform and inhomogeneous material response. In addition, these damage mechanisms can take different forms depending on various parameters.

2.2.1. The different types of damage in fibre-reinforced composite materials

Understanding fatigue failure is difficult and complex because a large number of parameters may influence the response. These include microstructure and material properties, dimensions and geometry, production techniques, loading conditions and environmental factors. The damage mechanisms caused by fatigue loading are different in a unidirectionally reinforced composite to those in a composite formed by a combination of several plies in various directions.

For loads applied parallel to the fibres of a unidirectional composite, the damage mechanisms can be divided into three types as shown on *Figure 26*. The first mechanism of damage is fibre breakage, which causes local shear stress concentrations (*Figure 26a*). It occurs when the stress applied is higher than the strength of the fibre. In contrast with this mechanism, the second and the third types are due to matrix damage which grows until it finds an interface. At low strains, cracks are limited to the matrix itself (*Figure 26b*). When a crack is long enough, the stress concentration at its end can cause a fibre/matrix interface failure (*Figure 26c*).

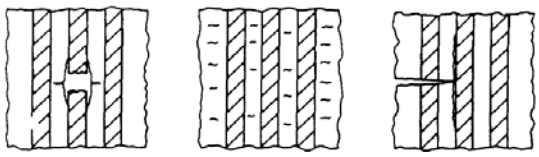

Figure 26. *Fatigue damage in unidirectional composites loaded in the direction of fibres.[68]*

a) Fibre breakage, interfacial debonding ; b) Matrix cracking ; c) Interfacial shear failure

However, the more useful composite materials are composed of a combination of different plies in different directions, with a stacking sequence based on the design load requirements. In this type of composite under fatigue loading, the initial damage consists of matrix cracking transverse to the fibre direction in the off-axis plies. The cyclic stress level controls which plies will form cracks while the number of loading cycles influences the number of cracks formed. Damage development continues until each off-axis ply has attained an equilibrium or saturation crack spacing. This regular crack spacing is characteristic of the material and the laminate stacking sequence, but independent of the load.

In E-glass chopped strand mat, *Owen & Dukes* [69] observed a series of damage events similar to those of continuous fibre laminates. It was shown that damage could be initiated at any point along a strand and did not seem to be associated with fibre ends.

In fabric-reinforced laminates the earliest signs of damage take the form of transverse fibre debonding among the weft fibre strands. Continued cycling leads to the development of intensive damage in the form of delaminations located at the undulations.

Schultz et al. [70] have performed tensile fatigue tests on fabric-reinforced laminates in the weft fibre direction and showed that, in woven fabric composites, cracks initiated early during fatigue, and developed along the transverse threads. These cracks were considered to initiate at the centre of the fibre undulations. In addition, loss of stiffness causes a local softening and a maximum strain appears at the centre of the undulation.

When a comparison of the fatigue performance of woven and non-woven laminates is made (*Figure 27*), we can see that the non-woven laminates have higher fatigue strength, in flexural and in axial fatigue. This is due to the better alignment of their reinforcing fibres.

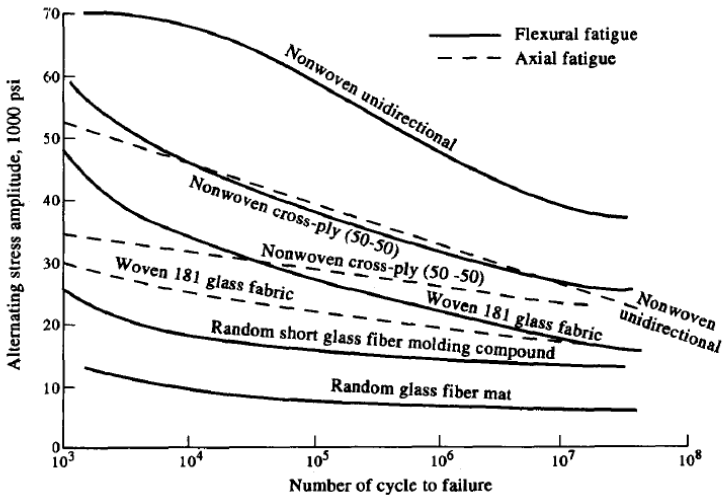

Figure 27. *Comparison of fatigue performance of various glass reinforced plastic laminates [68] (1000 Psi=6.89MPa)*

2.2.2. Characterization of S-N curves

In high-cycle fatigue, material performance is commonly characterized by an S-N curve, also know as a Wöhler curve. This curve, derived from single stress level fatigue tests, is the representation of the magnitude of the maximum stress (*S*) against the logarithmic scale of cycles to failure (*N*).

These S-N curves can be used with a fatigue failure criterion to estimate multi-stress level fatigue lives for design applications. However, variability of testing, material characteristics and specimen preparation can result in a large degree of scatter in the data. It is

therefore crucial to choose a method to characterise the S-N curve of a material which will give a good fit to experimental data [68]. As specimens will manifest variation in their number of cycles to failure, the S-N curve should ideally be a S-N-P curve including the probability of failure after a given number of cycles of a certain stress. It has been found that the scatter in fatigue life can be statistically explained by a log-normal distribution or a Weibull distribution [42].

2.3- Damage and failure criteria

An important step in fatigue studies is the analysis of the generated or available information to assess the life characteristics of the material. In the literature, various authors propose damage prediction models for composite materials based on different damage and failure criteria. These models include, residual strength degradation, stiffness degradation and damage mechanisms based theories.

2.3.1. Residual strength degradation

Most of the currently used life prediction methods for resin-matrix composite materials are based on using the residual strength as a damage parameter. The first residual strength degradation fatigue theories were proposed by *Halpin et al*. [71] and *Wolff* [72],who used life-prediction methods for metals for guidance.

A general fatigue theory for composite materials based on residual strength degradation can be developed by making the following three assumptions [73] :

i. the static strength distribution is two-parameter Weibull;
ii. the residual strength after *n* cycles of constant amplitude loading is related to the initial static strength by a deterministic equation;
iii. fatigue failure occurs when the residual strength decreases to the maximum applied cyclic stress.

In order to understand the environmental fatigue behaviour of unidirectional glass-carbon/epoxy hybrid composites, *Shan & Liao* [56] used the residual strength as a damage criteria. Fatigue and environmental fatigue were carried out at stress levels of *30*, *45*, *65* and *85 %* of average ultimate tensile strength (UTS) until failure. Specimens that had survived to 10^7 cycles were loaded to failure under tension to determine their residual strength. This study allowed them to highlight the effect of stress corrosion in environmental fatigue behaviour. It was shown that at *30 %* UTS all dry specimens and most of the wet specimens survived 10^7 cycles, though a small difference in residual strength was observed (*Figure 28*).

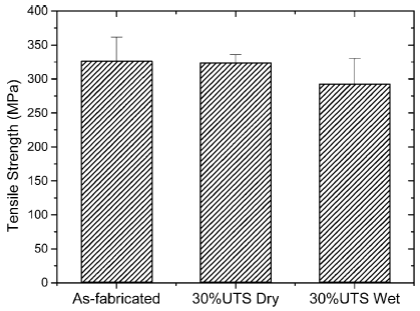

Figure 28. *Difference in residual strength for all-glass specimens subjected to 10^7 cycles under 30% UTS [56]*

Post et al. [50] have studied an E-glass/vinyl ester composite laminate subjected to variable amplitude fatigue loading. They have carried out residual strength at five points during the lifetime for each stress level studied. The tests were performed by loading a specimen under constant amplitude fatigue for a specific number of cycles, then stopping the test and breaking the specimen using the same method as for an ultimate tensile test. This work provided a better understanding of load order impacts in design of composite structures based on constant amplitude fatigue tests. In addition, the simple residual strength model proposed was accurate for constant amplitude loading and worked very well in the case of ordered block spectrum loading where the blocks were relatively large.

Epaarachchi & Clausen [74] proposed a model which describes the strength degradation of an ideal glass fibre-reinforced plastic composite subject to constant amplitude, constant frequency loading. This model can be used to predict the fatigue behaviour of a composite material using a well-defined number of tests. It shows excellent agreement between predictions and experimental data found in the literature for a wide range of glass fibre reinforced composites.

The fatigue theories based on residual strength degradation require an extensive experimental fatigue data base for each specimen under consideration and, furthermore, these theories suffer from another major weakness. The residual strength degradation is not uniquely related to the state of damage and it is not a sensitive measure of damage accumulation when loading in the fibre direction. It changes very slowly with damage accumulation until close to failure and then drops rapidly [73].

2.3.2. Stiffness degradation

Various attempts have been made to overcome the weaknesses of the fatigue theories based on the residual strength degradation. These involve the formulation of fatigue theories based on damage parameters that show greater changes throughout the fatigue life. One such parameter is stiffness variation. Therefore stiffness is a potential non-destructive parameter which can be used to monitor the in-service fatigue damage in the composite specimen.

Results from a large research effort on the fatigue of fibre-reinforced composite materials enables us to conclude that for a vast majority of fibre-reinforced composite materials, the modulus evolution can be divided into three stages : initial decrease (stage I) , approximately linear reduction (stage II) and final failure (stage III) as shown on *Figure 29*. Moreover, the loss of stiffness due to the gradual deterioration of a fibre-reinforced composite leads to a redistribution of the stress and a reduction of stress concentration in a structural component.

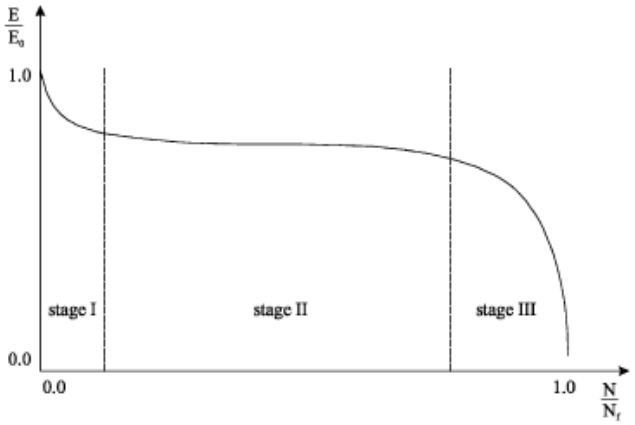

Figure 29. *Typical stiffness degradation curve for a wide range of fibre-reinforced composite materials [75]*

A large number of authors have chosen the stiffness degradation as a damage criterion. For example *Van Paepegem & Degrieck* [64, 65, 75, 76] used this for all their studies and *Sedrakian et al*. [77] also chose this approach to develop their damage model.

To understand the effect of the fibre volume fraction on the fatigue of a GFR pultruded rod composite, *Abd Allah et al*. [78] used the residual stiffness ratio as a failure criterion. The relationship between the residual stiffness ratio and the normalized fatigue life was independent of stress amplitude S_a and the fibre volume fraction V_f (*Figure 30*). This result suggests that the specific stiffness ratio is an appropriate design criteria.

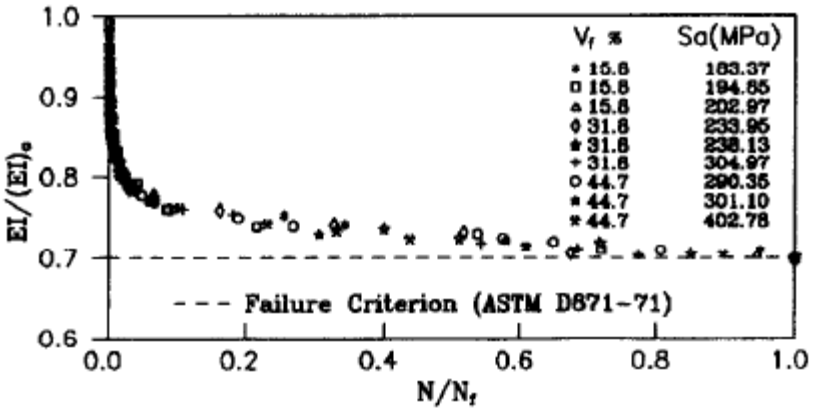

Figure 30. *Variation of residual stiffness ratio versus normalized fatigue life for various values o Sa and Vf [78]*

During their studies on flexural fatigue behaviour of a unidirectional glass fibre reinforced polymer, *Salvia et al*. [79] have recording the evolution of the stiffness of the sample as a measure of the damage. In the case of three-point bending three types of stiffness loss curves have been plotted, according to the properties of the matrix and the test conditions (*Figure 31*). The general results of this study show, however, that beyond the properties of the elementary components, i.e. type of matrix, reinforcement and sizing, the capacity of an UDGFRP to withstand dynamic loading depends strongly on the processing route and processing defects.

Ferreira et al. [54] also used the loss of stiffness as a damage parameter and proposed that this damage parameter has a nearly linear relationship with the rise of temperature of specimens during tensile fatigue tests, as shown on *Figure 32*, though there is considerable scatter in their data.

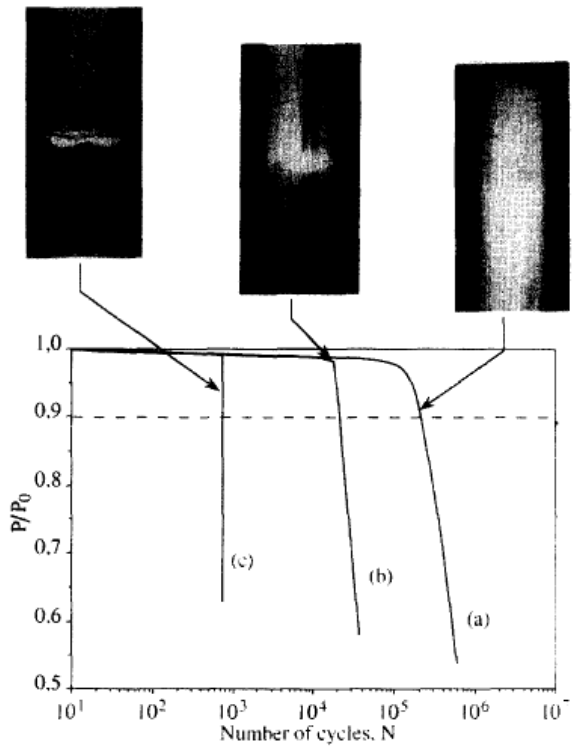

Figure 31. *Stiffness loss curves and associated failure features (three- point bending) [79]*

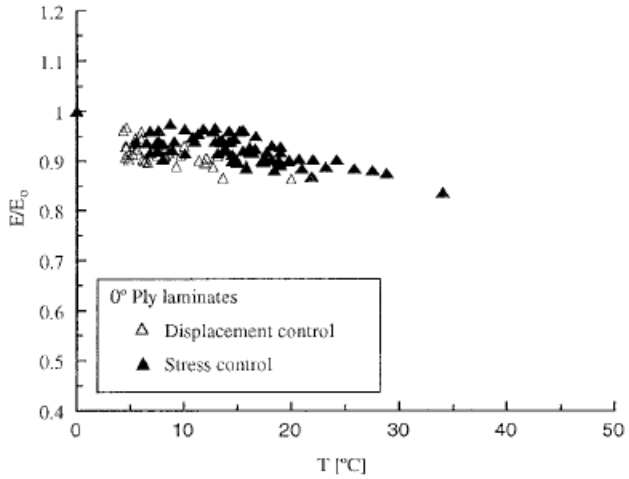

Figure 32. *Stiffness loss plotted against the rise of temperature for 0° Ply laminate [54]*

To characterize the fatigue behaviour of glass fibre reinforced polyester and polyurethane-vinyl-ester, *Dyer & Isaac* [55] have used both S-N tests and damage accumulation mechanism studies. To evaluate the micro-mechanisms that occurred during fatigue and how damage accumulated throughout the sample lifetime, they have measured the stiffness change during fatigue cycling. Three different types of glass fibre fabric were used, combined into various lay-ups, in order to consider the effects of matrix, cloths and lay-up on the fatigue behaviour. By comparing the curves of stiffness variation versus normalized cycles obtained for all these various combinations (*Figure 33*), the authors suggested that matrix material, fibre type and lay-up determine the extent of each stage, the degree to which each form of damage occurs and the site of the damage in the laminate.

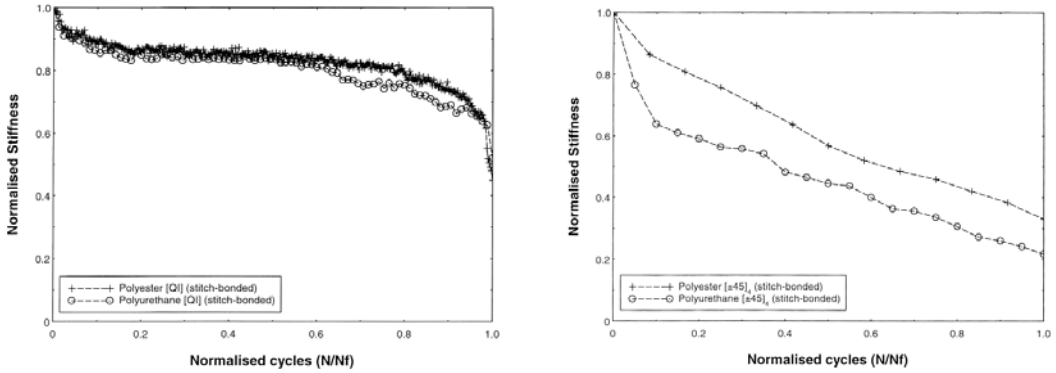

(a) *(b)*

Figure 33. *Stiffness variation versus normalized cycles for two different materials combinations : a) Quasi-isotropic stitch-bonded lay-up in polyester(+) and polyurethane-vinyl-ester (o) resins, b)* $[\pm 45]_4$ *stitch-bonded lay-up in polyester(+) and polyurethane-vinyl-ester (o) resins [55]*

Vauthier et al. [80], and *Pauchard* [38], have used the stiffness loss as a criterion of fatigue damage to analyse the effects of hygrothermal ageing of a unidirectional glass/epoxy composite under dynamic fatigue in three-point bending. They have recorded the stiffness loss curves continuously [80] or periodically [38]. *Vauthier et al.* [80] have chosen a *10 %* decrease in the stiffness as a conventional lifetime criterion.

In order to understand the stress corrosion cracking effect in unidirectional glass/epoxy composites, *Pauchard et al*. [81] and *Chateauminois & Pauchard* [82, 83] have continuously monitored the relative stiffness loss during three-point bending tests. Their study was restricted to the initial stages of damage development, i.e. when the damage consists mainly of the accumulation of broken glass fibres at the microscopic level and before the appearance of macroscopic damage in terms of matrix cracks.

Even for non-conventional test methods consisting of fatigue shear tests on unidirectional glass/epoxy composite cubic specimens [67], a damage factor representative of stiffness loss has been chosen. The same fatigue damage indicator has been chosen by *Roudet et al.* [62] to study a new three-point bending system with predominant shearing. For fatigue analysis under combined bending and torsional loads, *El-Assal & Khashaba* [66] have used a *30 %* reduction from the initial applied moment as a failure criterion which also corresponds to a stiffness loss.

Nevertheless, as pointed out in the previous sections, both the residual strength degradation and stiffness degradation fatigue theories have the major weakness that they do not accurately model the physics of the damage accumulation process.

2.3.3. Damage mechanisms

In addition to the residual strength degradation and stiffness degradation, another well-known approach is to take into account one or more damage variables directly related to measurable manifestations of damage, such as the number of transverse matrix cracks, the delamination size or the delamination depth.

For example, *Salvia & Vincent* [59] have chosen to focus on the size of the damaged zone as a function of the number of cycles during a three-point bending fatigue test. They have noted that the different stages of damage growth, observed *in situ* by optical microscopy,

can be related to the stiffness change of the sample. Two main stages have been noted ; stage I, for which the microscopic damage grew in the form of a superficial diffuse crack in the central zone of the sample ; and stage II, during which the damage zone spread towards the neutral plane.

To identify the type and the rate of damage development in I-beams (see *Figure 7*), *Attia et al*. [84] and *Gilchrist et al.* [85] have examined the beams after cyclic loading using ultrasonic inspection, dye-penetrant enhanced X-ray radiography, edge replication and optical microscopy methods.

The long term characteristics of glass/epoxy bars loaded under bending and torsion have been studied by *Ferry et al*. [46] using a visual acquisition system to follow the evolution of the damage in terms of number of cycles. These measurements provided the evolution of the delamination depth as a function of the number of cycles *(Figure 34).*

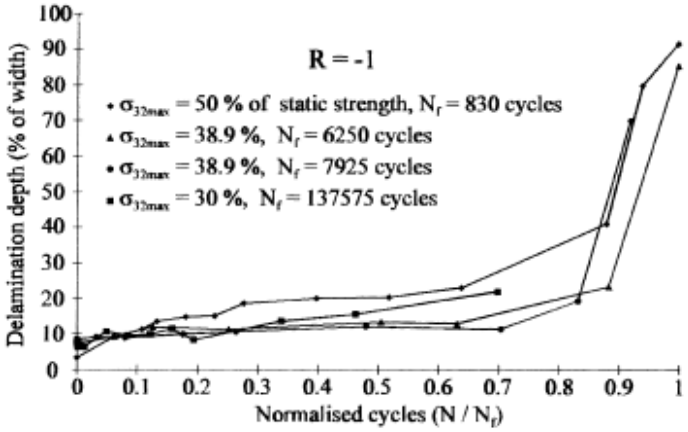

Figure 34. *Change in delamination depth versus the normalized cycles [46]*

To study the flexural behaviour of sandwich structures, the visual monitoring of failure modes [86] and the evolution of the crack length [87] have been used to define damage and failure criteria.

When an accurate measurement of damage is not possible, the complete failure of the specimen is taken to determine the fatigue life [35, 41, 42, 51, 60, 88], and the S-N curves can be used (*Figure 35*). After fatigue failure has occurred, the specimens are examined with a microscope to identify the details of the failure location.

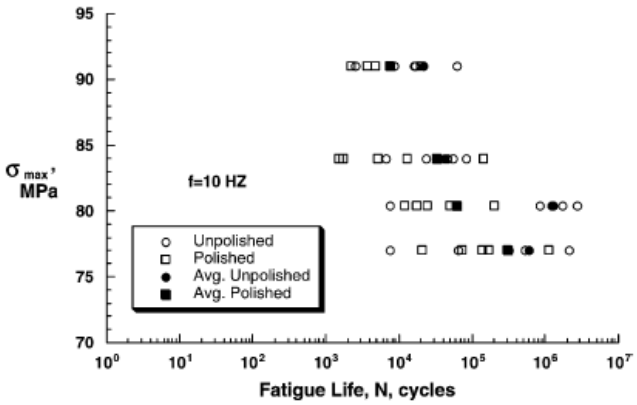

Figure 35. *Maximum cyclic tension versus fatigue life for glass/epoxy specimens tested in three-point bending both polished and unpolished [60]*

2.3.4. Other failure and damage criteria used

In order to have a better understanding of the fatigue behaviour of the material, some authors [34, 63] have used a combination of various criteria. For example, *Bellenger et al.* [63] have studied the thermal and mechanical fatigue of glass fibre composites by observing the crack initiation, measuring the surface temperature and the rigidity loss of the specimen.

Ellyin & Kujawski [34] have shown that the effect of the rate and the frequency is significant in fatigue loading of angle-ply $\pm 45°$ glass/epoxy laminates by using both cyclic creep accumulation and stiffness degradation as damage criteria. Definition of an appropriate test frequency is thus important to avoid unrealistic damage mechanisms.

2.4- Damage models and prediction of the lifetime

Being able to predict the fatigue response and the residual life of a composite material is crucial when designing such materials for optimised performance and avoiding failure. Even if the damage model identification strongly depends on the modelling scale, it is possible to classify these models in four main groups. The most widespread type of predictive model in the literature is the analytical one, which uses empirical laws. The other models are the statistical approach, generally based on a Weibull distribution, damage accumulation combined with stress redistribution, and finally the stress corrosion cracking models.

Of course, these four types of models are not the only ones, we can also find models based on the Tsai-Hill failure criterion [51] or on a FTPF (failure tensor polynomial in fatigue) criterion [88]. A review of life-prediction methods for constant and variable stress can be found in literature [18]. In addition, several studies have been performed on other types of composites, especially reinforced with carbon fibres [89, 90] but this aspect is not developed in this study.

2.4.1. Simple analytical models

Several empirical relations have been established for predicting fatigue life such as Basquin's relation, the conventional straight line in an S-N curve and Coffin and Manson's relation. Various authors [17, 50, 56, 62, 67, 74, 78, 91, 92] have used these analytical models to describe or predict the behaviour of a composite material.

A large number of these analytical models are based on S-N curves, which are the conventional representations of the fatigue life of the materials. For example, *Abd Allah et al.* [78] have used a power function to fit the S-N relationships of GRP rods at various values of fibre volume fraction. *Kensche* [91] has used a prediction method based on the linear Palmgren-Miner damage accumulation rule, the wind energy specific load sequence WISPER and a constant amplitude life diagram derived from the S-N curves. The Palmgren-Miner rule is a linear damage model which has been widely used in metal fatigue applications and has carried over to composite fatigue. This rule states that where there are k different stress magnitudes in a spectrum Si (with $1 \leq i \leq k$), each contributing $ni(Si)$ cycles, then if $Ni(Si)$ is the number of cycles to failure of a constant stress reversal Si, failure occurs when :

$$\sum_{i=1}^{k} \frac{n_i}{N_i} = C \qquad \textbf{(Eqn. 1)}$$

C is experimentally found to be between 0.7 and 2.2.

Roudet et al. [62] have described the fatigue behaviour with a pseudo-Wöhler curve defined in terms of deflection amplitude or of maximum strain (*Figure 36*).

Talreja [93] has presented an approach to the characterization of damage in composite materials based on the concept of internal state variables. These variables represent damage in composite material as internal structural rearrangements. The applicability and the accuracy of his approach has been illustrated by a wide range of examples predicting changes in composite stiffness arising from damage.

The shear behaviour of a unidirectional composite has been investigated and described by *Degallaix et al.* [67] using a modified Basquin relation also based on S-N curves.

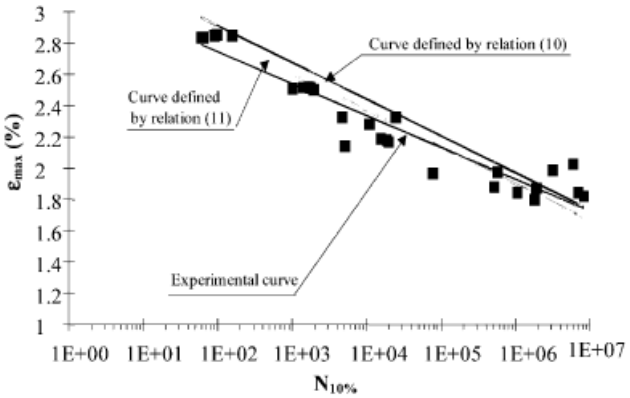

Figure 36. *Experimental and approximate pseudo-Wöhler curves [62]*

In addition to the description of the fatigue damage, some authors have chosen an analytical model to predict the fatigue life. *Kong et al*. [92] have estimated the fatigue life of a wind turbine blade by using the S-N linear damage theory, Goodman's diagram, the load spectrum and Spera's empirical formulae [94]. The Goodman diagram represents the cycles-to-failure as a function of mean stress and range along lines of constant *R*-values (*R* is the ratio minimum stress divided by maximum stress). Using this method, a dynamic structural problem in fatigue can be converted into a static structural problem.

Epaarachchi & Clausen [74] and *Post et al.* [50] have both proposed models to predict the fatigue behaviour of composites based on the strength degradation, while *Shan & Liao* [56] have proposed a phenomenological fatigue model which is capable of estimating the fatigue behaviour of a glass-carbon/epoxy hybrid composite from their parent composites.

In order to define a method for determining safety factors which must be taken into account when designing laminates for long term applications, *Richard & Perreux* [17] have used a meso/macro approach. At the mesoscale, i.e. layer scale, behaviour is time-dependant and a model based on the thermodynamic framework was used. To compute the response at the macroscale, i.e. laminate scale, a non-linear laminate theory based on Love-Kirchoff plate description was applied.

Finally, an analytical model can also be coupled with a statistical approach. *Salvia et al.* [79] have defined from the Weibull statistical analysis a linear regression which describes the fatigue behaviour.

2.4.2. Statistical models

As seen previously, statistical methods can be used to predict the fatigue behaviour, especially the two-parameter Weibull distribution [35, 41, 42]. The Weibull distribution is one of the most widely used lifetime distributions in reliability engineering. It is usually characterized by two parameters. First the shape parameter *k*, which describes the shape of the distribution. The second parameter is the scale parameter of the distribution λ. From $-\infty$ to this value, the area under the normalized probability distribution function is *0.632*. In certain cases, a third parameter is necessary to identify the minimum expected life x_0. *Figure 37* shows distribution curves for various shape parameters of a Weibull random variable *X*. Significantly different shapes can be described by a Weibull function. If the quantify *X* is the "time-to-failure", the Weibull distribution gives a distribution for which the failure rate is proportional to a power time.

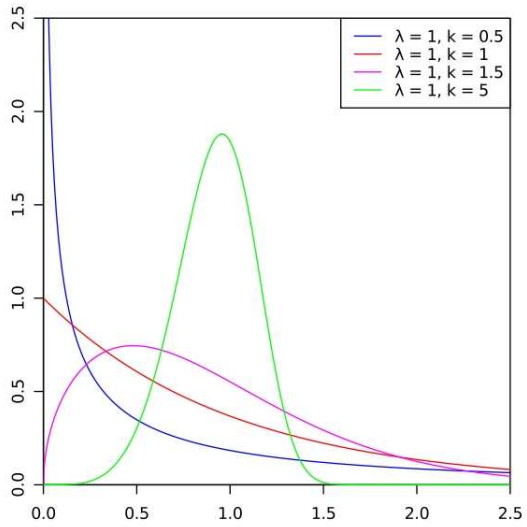

Figure 37. *Probability density function of a Weibull random variable*

Philippidis & Vassilopoulos [35] have defined with a two-parameter Weibull distribution the probability of survival after *N* cycles as :

$$P_S(N) = \exp\left[-\left(\frac{N}{\overline{N}}\right)^{\alpha_f}\right] \qquad \textit{(Eqn. 2)}$$

with α_f a statistical model parameter determined using the experimental data.

A Weibull scaling law can also be used to predict the four-point bending fatigue lives from a three-point bending curve fit and *vice versa* [60].

2.4.3. Models based on the redistribution of stress (cycle jump approach)

In studying the fatigue behaviour of fibre-reinforced composites, it is best to simulate the in-service conditions as nearly as possible.

Sedrakian et al. [77] have shown the interest of modelling with updating of the strain field, as well as the capacity to take into account the load redistribution phenomena during the fatigue behaviour simulation. Their damage model is based on generalised standard material

thermodynamics, a potential dissipation based on Norton's evolution law [95] was implemented.

Van Paepegem & Degrieck [64, 65, 75, 76, 96] have developed a phenomenological residual stiffness model that predicts the stiffness degradation and possible permanent strain in fibre-reinforced polymers under in-plane fatigue loading. This model takes into account the actual stress state at each material point and does not make any assumptions about geometry or boundary conditions of the fatigue loaded specimen. Their fatigue model was implemented both in a mathematical software package (Mathcad©) [64] and in a finite element code (SAMCEF™) [64, 65, 75, 96] by using two different methods.

First, the numerical model implemented in the mathematical software was based on Simpson's rule which is a Newton-Cotes quadrature formula. These numerical integration formulae were chosen to integrate exactly the second degree polynomials. Because the increase of the damage variable *D* during one cycle is so small, the integrations must be very precise indeed, otherwise the relative error on the calculation of the bending stiffness *EI* can be larger than the increase of the damage variable itself. *Figure 38* shows the experimental and simulated results for the $[\pm 45]_8$ specimen.

In the second method, the fatigue damage model was implemented in a finite element code. The integration of the damage growth rate equation for each Gaussian point of the finite element mesh has been made with the *cycle jump* approach. The *cycle jump* (*Figure 39*) approach means that the computation is done for a certain set of loading cycles and deliberately chosen intervals, and that the effect on the stiffness degradation of these loading cycles is extrapolated for each Gaussian point over the corresponding intervals in an appropriate manner.

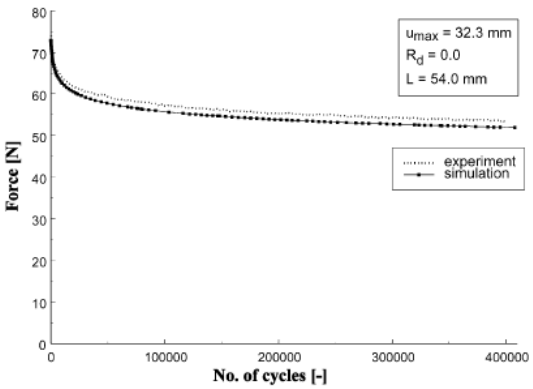

Figure 38. *Degradation of the force versus the number of cycles for a* $[\pm 45]_8$ *specimen [64]*

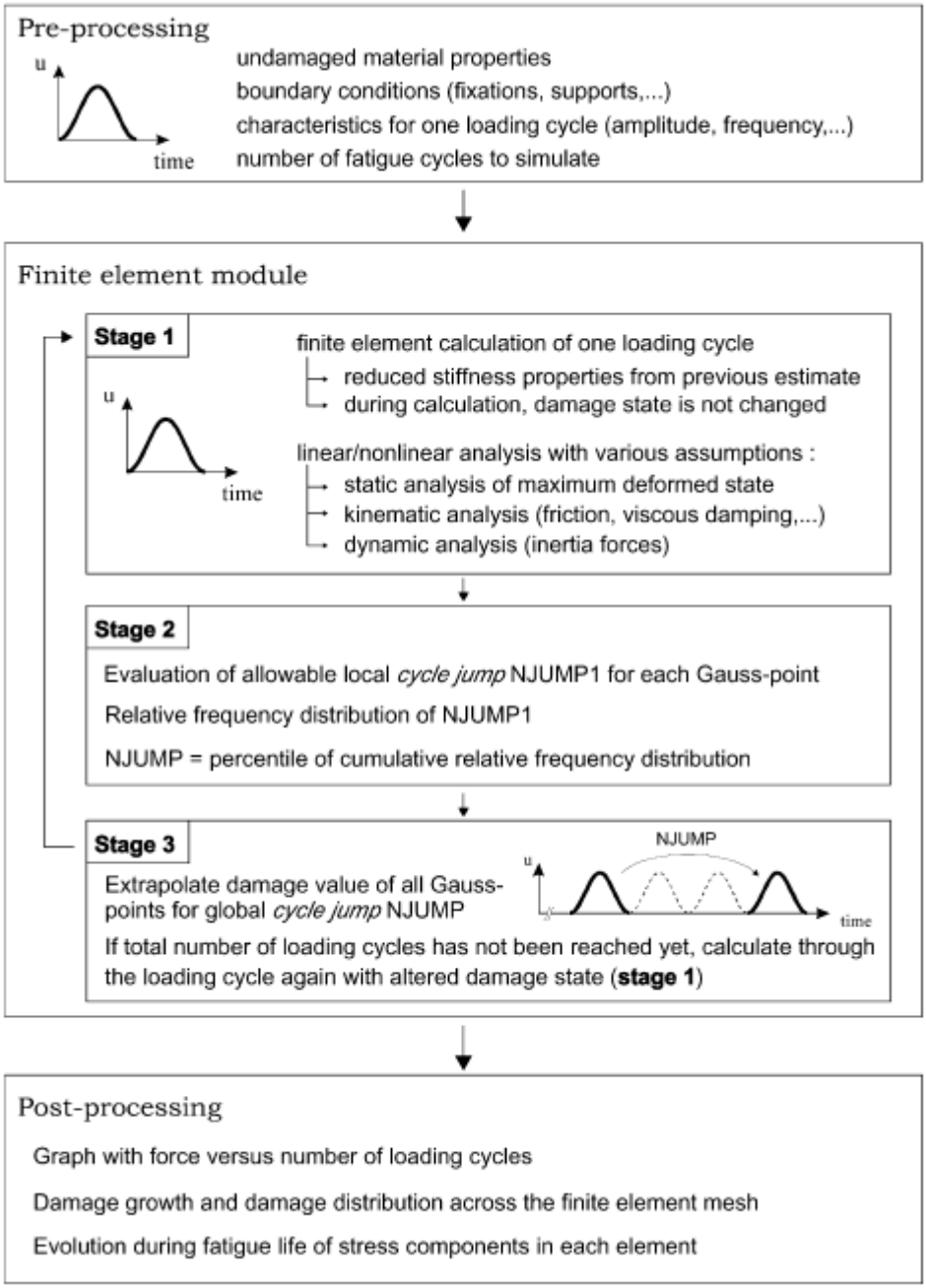

Figure 39. *Flowchart of the finite element implementation of the cycle jump approach [76]*

Attia et al. [84] have proposed a methodology for predicting the fatigue life of fibre-composite components and structures which combines relatively short-term fracture mechanics data, obtained from experimental measurements, with a finite element analysis (ABAQUS) of the component or structures. This approach has been used to study the growth of damage and the cyclic fatigue life of I-beams. The beams were manufactured using carbon-fibre-reinforced-plastic and contained a *60 mm* diameter notch in the web. The agreement between the theoretical results of the model and the experiments was very good, especially when it was considered that there are no “adjustable factors” involved in the modelling studies.

2.4.4. Stress Corrosion Cracking model (SCC model)

It is widely acknowledged that the prediction of the durability of glass fibre reinforced composite systems under mechanical and environmental loading is greatly complicated by the occurrence of several interacting physico-chemical and mechanical degradation mechanisms. However, the two types of model exposed previously do not take into account environmental effects, and in particular the stress corrosion phenomenon. This is a degradation of glass fibres under the combined action of stress and wet environment, and it will be discussed in more details in *Section 2.5.3*.

In order to analyse the flexural fatigue behaviour of water-aged unidirectional glass/epoxy composites, a stress-corrosion-cracking (S.C.C.) model can be applied [38, 81, 82]. For example, the corresponding model developed by *Pauchard et al*. [81] has been derived from a combination of the Weibull statistical distribution of the fibres strength with a classical power law expression for the sub-critical crack growth rate. This model has been satisfactorily applied to fatigue tests carried out at different frequencies and strain ratios. For a given strain level, it has been demonstrated that the time dependence of the stiffness loss can be described using a single parameter depending on the statistical distribution of the fibres surface defects and the sub-critical crack growth rates of these defects within a given physic-chemical environment.

2.4.5. Other types of models

In adition to the four types of models presented above, a large range of other models can be found in the literature to describe or predict the fatigue behaviour of composite materials.

For example, to unify the macro and microscopic behaviour and incorporate multiaxial cases, *El Kadi & Al-Assaf* [52] have chosen to use the strain energy as an input to an artificial neural network (ANN), to predict failure fatigue in unidirectional composite materials. If trained adequately, the ANN can be used to accurately predict the lifetime under a given set of conditions.

Zhifei et al. [97] have simulated the micro mechanical damage of fibre/matrix interfaces under cyclic loading using a model based on a modified power degradation model. This model is based on a degradation function of coefficient of friction [98]. The effects of loading conditions and shear deformation of matrix on interfacial debonding have been considered.

Another type of model develops failure criteria such as the Tsai-Hill failure criterion [51] or the failure tensor polynomial in fatigue (FTPF) criterion [88]. For example, a life prediction methodology which takes into account the laminate behaviour has been proposed by *Nyman* [51]. In his work, the fatigue failure functions, and thus the calculated uniaxial properties, are established on a laminate level, in this case with the Tsai-Hill failure criterion. *Philippidis & Vassilopoulos* [88] have modified the failure tensor polynomial to account for fatigue loading. They called this the failure tensor polynomial in fatigue, and it was shown to successfully predict fatigue strength under reversed complex plane stress states.

To conclude, *Miyano et al.* [99] have proposed an accelerated testing methodology for long term durability of polymer composites based on the time-temperature superposition principle. The long term flexural fatigue life of plain woven glass fibre/vinyl-ester laminates was predicted based on this methodology (*Figure 40*). When all four hypotheses (A-D in *Figure 40*) hold, the methodology can predict lifetime under any loading conditions and temperature. The hypothesis A states and assumes that the failure mechanisms under static, creep and fatigue loading are identical. The hypothesis B states that the same time-temperature superposition principle applies for the three types of strength (static, creep

and fatigue). Hypothesis C states that the linear cumulative damage law can be used for monotonic loadings. Hypothesis D assumes the linear dependence of fatigue strength upon the stress ratio *R* (minimal stress on maximal stress). They have confirmed that the methodology is applicable to their composite material, plain woven glass fibre/vinyl-ester laminates for conventional marine use.

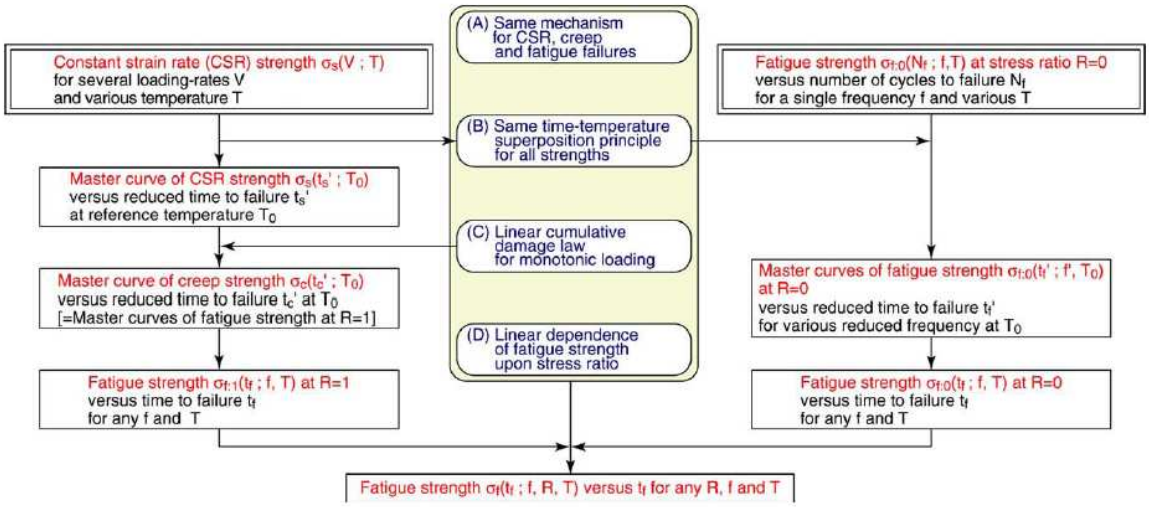

Figure 40. *Prediction procedure of fatigue strength for polymer composites [99]*

2.5- Sea water ageing

Polymers are permeable, whilst ceramics, glasses and metals are generally impermeable. This may be a disadvantage because aggressive substances such as water will diffuse into polymeric structures such as adhesive joints or fibre-reinforced composites and degrade them.

Due to the context of the study, the aim of this section is first to present briefly the characteristics of sea water and the notion of accelerated ageing. Then, the water diffusion mechanisms and their fundamental aspects [100, 101] are explained. In addition, an overview of the analytical formulation of the phenomena is proposed, as well as the effects induced in a composite material by water absorption.

2.5.1. Natural sea water characteristics and accelerated ageing

In a liquid environment, the water content at equilibrium is linked to the chemical activity of water. When the concentration of dissolved matter in water increases, salt for example, the saturation level decreases.

Whilst only pressure and temperature determine the physical properties of pure water, for sea water temperature, pressure and salinity, are needed to determine its physical properties. On average, sea water in the world's ocean has a salinity of between *3.5 %* and *3.8 %*, *i.e.* every kilogram of sea water contains approximately between *35 g* and *38 g* of dissolved salts. Some authors [102-104] showed that the relative composition of sea salts is constant and is governed by Marcet's law. The sea salts mainly consist of Chloride Cl^- (≈ *55 %*), Sodium Na^+ (≈ *30.6 %*) and Sulfate SO_4^{2-} (≈ *7.7 %*) [105] as presented on *Figure 41*.

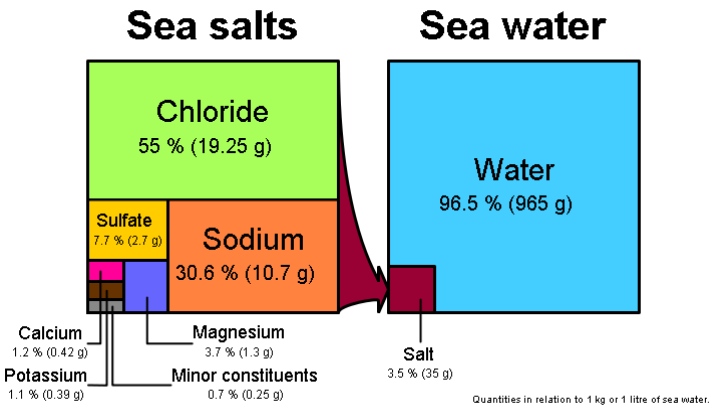

Figure 41. *Diagram showing concentrations of various salt in sea water*

Accelerated ageing is a test method that uses aggravated conditions of heat, oxygen, sunlight, *etc.* to speed up the normal ageing processes of samples. *Verdu* has provided an introduction to this subject [106]. The difficulty with this approach is to verify that increasing the temperature does not introduce mechanisms which do not operate at the lower temperatures, and this may require considerable effort. Other time-temperature equivalence methods are available (the Williams-Landel-Ferry equations for example) and may prove more appropriate [107]. It is used to help determine the long term effects within a reduced time. As the sea water ageing phenomenon is due to chemical reactions, it is thermally activated and the increase of diffusivity with temperature can be described by the Arrhenius equation.

2.5.2. Water diffusion mechanisms

Diffusion is a molecular process in which molecules move as a result of random thermal motion from a region of higher concentration to one of lower concentration. When a sample is immersed in a liquid the surface layer immediately absorbs the liquid and reaches its equilibrium state. As time passes, the liquid penetrates further into the bulk of the material until equilibrium is reached, when the liquid distribution is uniform everywhere throughout the sample. The movement of the liquid obeys the laws of diffusion and the “speed” of movement is characterized by the diffusion coefficient. However, a high diffusion coefficient does not necessarily mean that a lot of liquid is being transported since the latter is governed by the permeability, which is the product of the diffusion coefficient and the solubility of the liquid in the material.

2.5.3. Analytical formulations

The two main laws of diffusion which describe the kinetics of diffusion are Fick’s law and the Langmuir-type law. These two approaches can be described by analytical formulations [100, 101, 108-110] which allow us to determine the diffusion parameters from experimental data.

To describe the kinetics of absorption, Fick’s law is frequently used, but some materials exhibit more complex water absorption kinetics in which case the Langmuir-type model may be more efficient. Both models assume the reversibility of the absorption.

a) The Fickian approach

The fundamental diffusion equations are due to Fick [109], who formulated them in 1855 by adapting the analogous heat conduction equations which had been derived by Fourier [111] some years earlier. The first law of diffusion states that the flux in the *x*-direction (*Fx*) is proportional to the concentration gradient ($\partial c/\partial x$) of the penetrant, that is :

$$F = -D\frac{\partial c}{\partial x} \qquad \textbf{(Eqn. 3)}$$

Flux is the amount of substance diffusing across unit area per unit time, *D* is the diffusion coefficient, *c* is the concentration of the diffusing substance and *x* the space coordinate normal to the section. The first law can only be directly applied to diffusion in the steady state, that is, when concentration is not varying in time. The diffusion coefficient, or diffusivity, *D* is proportional to the squared velocity of the diffusion particles, which depends on the temperature, viscosity of the fluid and the size of the particles.

Fick's second law of diffusion describes the non-steady state and is derived by considering the mass balance of the diffusing substance in an element of volume, and for diffusion in one dimension it may be written as :

$$\frac{\partial c}{\partial t} = D\frac{\partial^2 c}{\partial x^2} \qquad \textbf{(Eqn. 4)}$$

where *t* is the time and *D*, the diffusion coefficient, is assumed constant. However, in the case of vapours and liquids interacting with high polymers, the diffusion coefficient is usually a function of the concentration of the penetrant. In such cases *(Eqn. 4)* is usually rewritten as :

$$\frac{\partial c}{\partial t} = \frac{\partial}{\partial x}\left(D\frac{\partial c}{\partial x}\right) \qquad \textbf{(Eqn. 5)}$$

A simplified approach which utilizes the simplest mathematical solution for a semi-infinite medium has been found to be adequate for many purposes [110]. In this case, it is assumed that the liquid extends to infinity on one side of the boundary interface and that the sample extends to infinity on the other side. In a plane sheet the diffusion behaviour will be the same as that for a semi-infinite sheet, neglecting edge effects, until the liquid reaches the centre of the sheet. The concentration of liquid, *ct* at a time *t*, is related to the distance *x* below the surface by :

$$\frac{c_t - c_0}{c_1 - c_0} = 1 - \frac{4}{\pi}\sum_{n=0}^{\infty}\frac{(-1)^n}{(2n+1)}\exp\left(-D\frac{(2n+1)^2}{4e^2}\pi^2 t\right)\cos\frac{(2n+1)\pi \cdot x}{2e} \qquad \textbf{(Eqn. 6)}$$

where c_0 and c_t are the concentrations of the liquid in the piece respectively at $t=0$ (usually $c_0=0$) and at equilibrium, *D* is the diffusion coefficient and *e* is the half thickness of the sample. M_t represents the total mass of water absorbed by the material at a time *t* and M_∞ is the mass at saturation. Experimentally, the water absorption is proportional to the square

root of time and reaches a plateau value known as the saturation mass as represented on *Figure 42*.

$$\frac{M_t}{M_\infty}=1-\frac{8}{\pi^2}\left[\sum_{n=0}^{\infty}\frac{1}{(2n+1)^2}\exp\left(-\frac{(2n+1)^2}{4e^2}D\pi^2 t\right)\right] \qquad \textbf{(Eqn. 7)}$$

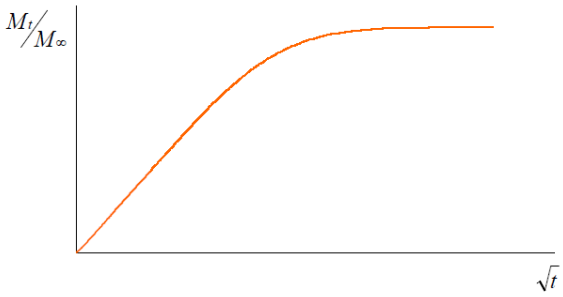

Figure 42. *Kinetics of absorption according to Fick's law*

As the diffusion phenomena are thermo-activated, the diffusion coefficient is related to the temperature according to the Arrhenius law :

$$D=D_0\cdot\exp\left(\frac{-E_a}{RT}\right) \qquad \textbf{(Eqn. 8)}$$

where D_0 is a temperature independent factor, E_a is the activation energy for permeation, R is the gas constant and T is the absolute temperature.

The classic Fickian treatment has often been used to explain water uptake by unreinforced epoxy resins but this is not always adequate for composites. That is the reason why another model has been developed for anomalous moisture diffusion in composites [108], the Langmuir-type model.

b) The Langmuir-type approach

In *1978, Carter & Kibler* [108] developed a new model of diffusion called Langmuir-type because of its similarity to Langmuir adsorption. This anomalous moisture absorption in epoxy materials can be explained quantitatively by assuming that absorbed moisture consists of mobile and bound phases.

Molecules of the mobile phase diffuse with a concentration – and stress – independent diffusion coefficient D and are absorbed (become bound) with a probability per unit time γ at certain sites whose nature is unspecified. Molecules are emitted from the bound phase, thereby becoming mobile, with a probability per unit time β. The diffusion process is therefore described by the same modification of the simple equation which has long been used to describe neutron flux in absorbing and multiplying media. The local weight fraction of moisture approaches an equilibrium value, M_∞, when the number of mobile molecules per unit volume, n, and the number of bound molecules per unit volume, N, approach values such that *(Eqn. 9)*, as in Langmuir adsorption theory.

$$\gamma\cdot n=\beta\cdot N \qquad \textbf{(Eqn. 9)}$$

We assume that the diffusion of mobile molecules conforms to simple diffusion theory augmented by sources and sinks, as in the theory of neutron chain reactions. Thus, for the one dimensional case, the number densities of position *z* and time *t* satisfy the coupled pair of equations :

$$\begin{cases} D\dfrac{\partial^2 n}{\partial z^2}=\dfrac{\partial n}{\partial t}+\dfrac{\partial N}{\partial t} \\ \dfrac{\partial N}{\partial t}=\gamma\cdot n-\beta\cdot N \end{cases} \qquad \textbf{(Eqn. 10)}$$

In the usual experimental case of an initially dry slab of thickness *2e* exposed to a constant moisture environment on both sides at *t=0*, the total mass of water absorbed by the material at a time *t*, M_t, can be presented as *Figure 43* and written as *(Eqn. 11)*. The analytical development of the Langmuir-type formulation is developed in *Annex 1*.

$$\frac{M_t}{M_\infty}=1-\frac{8}{\pi^2}\sum_{p=1}^{\infty(odd)}\frac{\left[r_p^+\exp\left(-r_p^-\cdot t\right)-r_p^-\exp\left(-r_p^+\cdot t\right)\right]}{p^2\left(r_p^+-r_p^-\right)}+\frac{8}{\pi^2}\left(\frac{k\beta}{\gamma+\beta}\right)\sum_{p=1}^{\infty(odd)}\frac{\left[\exp\left(-r_p^-\cdot t\right)-\exp\left(-r_p^+\cdot t\right)\right]}{\left(r_p^+-r_p^-\right)} \qquad \textbf{(Eqn. 11)}$$

With $$r_p^\pm=\frac{1}{2}\left[\left(kp^2+\gamma+\beta\right)\pm\sqrt{\left(kp^2+\gamma+\beta\right)^2-4k\beta p^2}\right] \qquad \textbf{(Eqn. 12)}$$

$$k=\frac{\pi^2 D}{(2e)^2} \qquad \textbf{(Eqn. 13)}$$

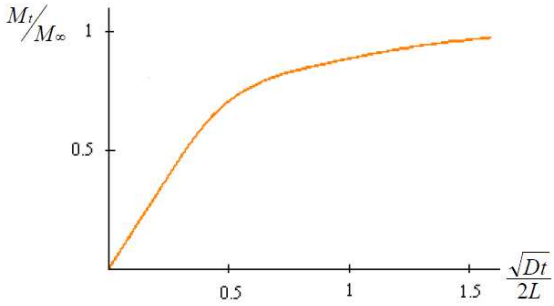

Figure 43. *Kinetics of absorption according to the Langmuir-type model*

2.5.4. Effects of water diffusion on mechanical behaviour

Environmental and mechanical stresses cause degradation of the physical and chemical structures of the composite material. This phenomenon involves two aspects which influence each other, hygrothermal ageing and mechanical damage. The influence of ageing on mechanical properties is observed, for example, the variation of the glass transition temperature and the shear modulus [112]. This is the most commonly studied aspect of coupling, but for some composite materials, stress may also affect diffusion kinetics so a fully coupled model would include both relationships. For glass/epoxy laminate pipes, *Perreux & Suri* [113] have demonstrated that the absorption of a damaged material and the damage of an aged materials are interrelated phenomena. The overall behaviour depends on the water

contents and on the level of damage. So they have proposed a coupling method for simultaneous modelling of the two kinetic processes. On the contrary, *Mercier* [114] have observed no direct relationships between the water absorption and the crack evolution in their glass/epoxy specimens.

In the following section we focus on two phenomena, the Stress Corrosion Cracking of glass fibres, which can occur during wet ageing, and the effects of water absorption on fatigue behaviour.

a) The Stress Corrosion Cracking mechanisms

Stress Corrosion Cracking (*SCC*) is the unexpected sudden failure of glass reinforced composite material subjected to a stress in a corrosive environment. SCC is highly chemically specific in that certain materials are likely to undergo SCC only when exposed to a small number of chemical environments.

Over time, stress corrosion cracking attacks E-glass fibres, which weakens the structure and can lead to premature failure. SCC failure is characterized by flat fracture surfaces perpendicular to the fibres at both the macroscopic and microscopic levels. Prevention of stress corrosion cracking includes proper selection of fibre and resin, and may include use of a protective layer between the glass fibres and the environment [115]. For applications where glass reinforced composites are exposed to aggressive environments special boron-free glass formulations have been developed which are more resistant to SCC [116]. These will be described in more details in *Section II-1*.

b) Fatigue behaviour in water

The interrelationship between the hygrothermal ageing and the fatigue behaviour of composite materials has been investigated by *Chateauminois & Pauchard* [83] and *Pauchard et al.* [81] within the context of the flexural loading of unidirectional glass fibres reinforced plastics. They have detailed the effects of water induced physico-chemical changes on the stress corrosion mechanisms involved during the delayed failure of the glass fibres under fatigue loading. In addition, they have developed a durability model based on the stress corrosion. This model takes into account the combined effects of time, temperature, humidity and applied stress. *Weitsman* has also described fatigue behaviour of carbon reinforced composites in sea water [117], and proposed a specific mechanism which resulted in accelerated degradation of saturated specimens. This involves crack opening during unloading, due to the presence of water.

3- Positioning of the present study

As presented in the context of the study, there is a large experience of composite materials in marine applications, from small boats to submarines. The majority of these structures are not highly loaded, as current regulations result in large safety factors. The high reliability needed to make ocean energy conversion systems cost-effective makes composite materials a natural choice in terms of performance, corrosion resistance and weight. However, the consequences of a combination of the marine environment with mechanical loads have not been completely investigated in previous applications.

During the bibliographic study, an overview of the test methods involving quasi-static and fatigue loads has been presented. Even though this analysis of the literature has been

voluntarily focussed on composite materials reinforced with glass fibres, there is a vast choice of test methods (tension, compression, torsion, bending, in air or in relative humidity) and of specimen geometries (rectangular, dog-bone, cube, rod). However, in all these studies, hardly any tests results for natural circulating sea water have been found. For this reason, in order to fill this gap, our investigations have been performed both in air and in natural circulating sea water. In addition, as a major objective of the study present is to identify and quantify the influence of the glass fibre type, the bibliographic study has enabled us to choose appropriate test methods, i.e. tests which load the fibres.

A review of the different approaches for modelling damage has been presented. This allowed us to define the different types of damage in the composite materials as well as the different criteria used to characterize them, such as residual strength degradation or stiffness degradation. The latter will be used in the experimental study here. A summary of the most common models applied to explain the damage and predict the lifetime of composite materials has also been presented. Based on this part of the bibliographic study, we have chosen to describe the evolution of damage in our composite materials according to a method based on a *cycle jump* approach

The last part of the bibliographic study has been devoted to a brief explanation of the phenomena involved in ageing. This section has allowed us to develop an analytical approach which will be used to describe the kinetics of diffusion in composite materials reinforced with glass fibres. In addition, previous studies on the effects of water diffusion on mechanical behaviour have been discussed, in order to describe the coupling between these phenomena.

CHAPTER II
OUTLINE OF TEST PROGRAMME

II- OUTLINE OF TEST PROGRAMME

The main objective of the study is to perform tests to show the influence of glass fibre type on the response of composites under quasi-static and cyclic loading. In addition, the influence of the environment is investigated by testing the composite materials in air and in natural circulating sea water.

In order to study the influence of the type of fibre, a test procedure has been defined. Three types of test were performed on each material studied, quality control tests, sea water ageing, and mechanical tests (quasi-static and cyclic).

1- Material selected

The reference fibre material is *17 µm* diameter E-glass (*1250 g/m²*) with P196 sizing from OCV™ Reinforcements. Two other grades of glass fibre are also studied, Advantex® glass (*20 µm* diameter, *1250 g/m²*) and High Performance glass, the HiPer-tex™ glass (*20 µm* diameter, *1250 g/m²*). the fibres properties are summarized in *Table 1*.

The reinforcement type is a quasi-unidirectional fabric reference with *90 %* of unidirectional fibres approximately and *10 %* of mat and 90° fibres (*Figure 44*), (*1 150 g/m²* warp, *50 g/m²* weft and *50 g/m²* chopped mat).

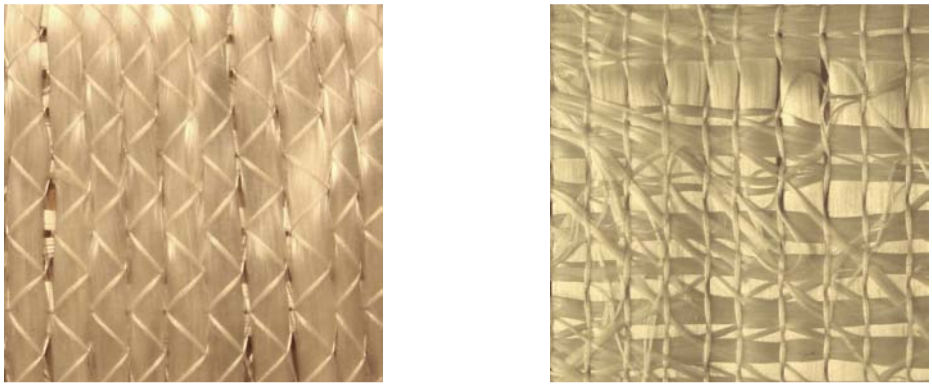

(a) *(b)*

Figure 44. *Details of the two sides of quasi unidirectional fabric :*
a) Unidirectional fibres face, b) Mat and 90° fibres face

Advantex® is formulated to be a boron-free E-glass and possesses significantly improved resistance to the corrosive effects of a range of environments. Advantex® is both a E-CR-glass and a E-glass in accordance with ASTM D578. In all aqueous environments tested to date, the Advantex® glass reinforced composite materials have provided better corrosion-resistance performance than similar materials reinforced with traditional E-glass. The microscopic view of glass fibres in an acidic medium (*Figure 45*) shows the degradation of the E-glass which occurs by an etching process that involves hydration followed by total dissolution of the E-glass, while Advantex® remains undamaged.

The HiPer-tex™ glass, with a boron-free formulation can be classified as a High Strength R-Glass, as defined by the ASTM C-162, DIN 1259 and ISO 2078 standards. This glass is designed for excellent mechanical properties (tensile strength and modulus) and offers significantly better thermal and corrosion resistance properties than E-glass. The initial

product lines include reinforcements specially developed for wind energy, ballistic armour, aerospace and other industrial applications.

The epoxy resin chosen here was specially designed for infusion processes with a very low viscosity. It is the infusion resin MGS© RIM 135 from Hexion™ with amine hardener RIMH137. Moulded parts can be worked and de-moulded after curing at room temperature. Curing at higher temperatures (up to approximately 80°C-100°C) is possible depending on layer thickness and geometry of the parts to be manufactured.

Both resin and fibres are currently used in wind turbine blades.

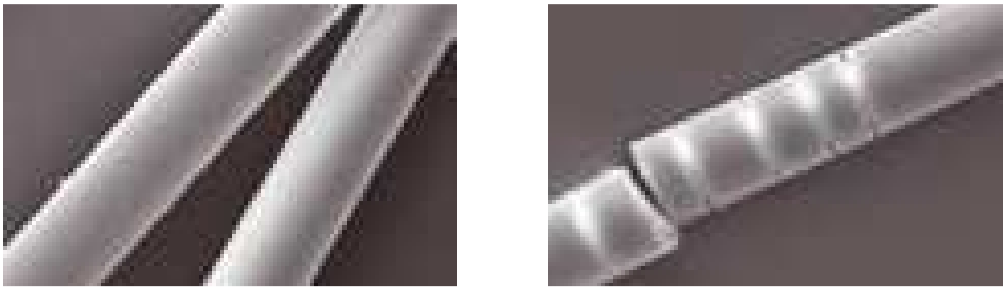

(a) *(b)*

Figure 45. *Advantex® E-glasses in acid for four hours : a) Advantex® glass, b) Traditional E-glass*

Table 1. *Fibre properties*

	Tensile strength ASTM D2343 $[MPa]$	Tensile modulus ASTM D2343 $[GPa]$
E-glass	2 000-2 500	74-80
Advantex®	2 200-2 600	81-83
HiPer-tex™	2 800-2 900	89-91

2- Manufacturing process

In order to obtain relevant results, it is important to manufacture the coupons in a similar way to the application procedure. So, it is crucial to both define a coherent stacking sequence and the conditions of infusion.

2.1- Stacking sequence

According to the preliminary studies to define the test methods, it was decided to work with specimens about *5 mm* thick. As the thickness of each ply is known (almost *0.8 mm*), laminate composites were made with 6 plies distributed symmetrically with respect of the midplane as shown on *Figure 46*. A ply is represented by both the grey and the green parts, the grey part is the face with unidirectional fibres (*Figure 44a*) and the green part is the face with mat and *90°* fibres (*Figure 44b*). All the plies have the same orientation.

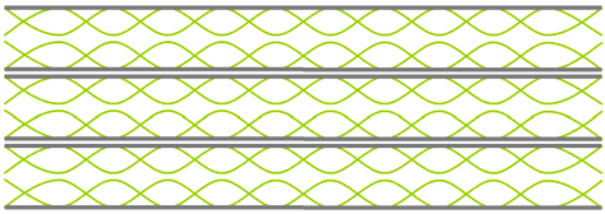

Figure 46. *Stacking sequence used for the coupons*

2.2- Conditions of fabrication

In order to be as close as possible to the industrial manufacturing process, it was decided to produce the specimens by infusion, because it is the principal process currently used to produce large turbine blades. The infusion process offers many benefits compared to hand lay-up techniques. As it is a closed process, it eliminates hazardous emissions. In addition, it results in a higher fibre-to-resin ratio than hand lay-up. The vacuum bag also facilitates good resin distribution and less wasted resin.

Each panel has been infused following the same manufacturing process described in *Annex 2*.

Although there are many variants of the infusion process, the basic principle is always the same. Reinforcements are placed in a mould with a peel ply on it and covered with another peel ply, a perforated plate and a vacuum bag (*Figure 47*). A vacuum is then applied, resin is fed into the mould and the vacuum draws it through the glass fabric until saturation. The vacuum is maintained until the part is cured.

In our case, after preliminary trials we chose to infuse at *35°C* in a climatic chamber with a visual control of the resin progress using a webcam (*Figure 48*). This enabled temperature and humidity to be closely controlled. After infusion the composite plates were left for 12 hours at *35°C* in the mould, then de-moulded and post-cured for 10 hours at *70°C*. As the part is post-cured outside the mould, the temperature increase has to be slower than the development of the glass transition temperature (*Tg*) of the resin, so a temperature increase of *10°C/h* up to *70°C* was applied (*Figure 49*).

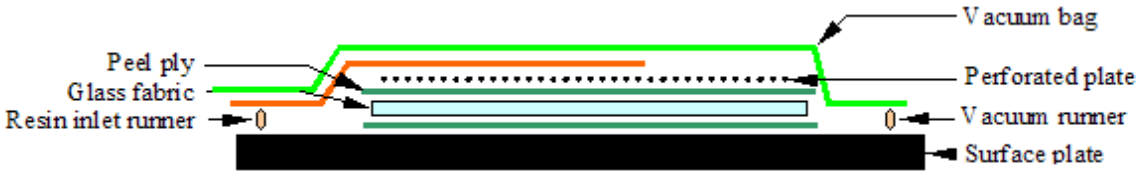

Figure 47. *Diagram of the infusion process*

Figure 48. *Infusion in the climatic chamber and visual control device*

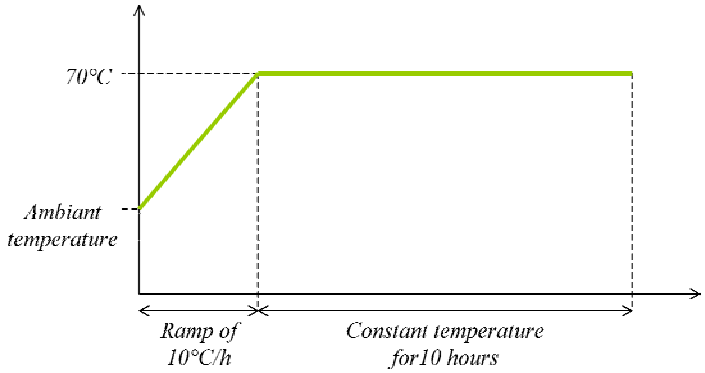

Figure 49. *Post-curing cycle*

2.3- Summary of the different laminates

As mentioned previously, three types of reinforcement have been studied, E-glass, Advantex® glass and HiPer-tex™ glass. In order to avoid confusion, the different plates made with the different reinforcements have been named as follows :

- the first letter refers to the place of fabrication : I for IFREMER, H for Hexion™ and 3B for 3B Fibreglass;
- the second letter represent the type of glass used as reinforcement : E for E-glass, A for Advantex® glass and H for HiPer-tex™ glass;
- the number of the plate (for a given place of fabrication and reinforcement).

For example, the plate HH1 is the plate #1 infused at Hexion™ with HiPer-tex™ glass reinforcement. All the infused laminates are summarized in the *Table 2* with their characteristics (reinforcement, place and date of fabrication).

Table 2. *Summary of the laminates manufactured*

Plate	Place of fabrication	Reinforcement used	Date of fabrication
HE3	Hexion™	E-glass	August 2008
HE4	Hexion™	E-glass	August 2008
HA5*	Hexion™	Advantex®	August 2008
HA6*	Hexion™	Advantex®	August 2008

HH1	Hexion™	HiPer-tex™	March 2009
HA1	Hexion™	Advantex®	March 2009
3BA1**	3B Fibreglass	Advantex®	April 2009
3BA2**	3B Fibreglass	Advantex®	April 2009
3BHd1	3B Fibreglass	HiPer-tex™	April 2009
IE1	IFREMER	E-glass	March 2009
IH1	IFREMER	HiPer-tex™	March 2009
IE2	IFREMER	E-glass	April 2009

** HA5 and HA6 are taken from the same large panel, so for the rest of the study they will be considered to have the same characteristics.*

*** 3BA1 and 3BA2 are also taken from one large panel, so for the rest of the study they will be considered to have the same characteristics.*

3- Test methods

Before reception of the reinforcement and resin for infusion, preliminary tests were performed on hand laminated unidirectional glass/epoxy composite in order to define the test methods to be carried out.

Three types of tests were chosen and performed, quality control tests, natural sea water ageing at different temperatures and mechanical tests (tension and four-point flexure).

3.1- Quality control tests

To check their mechanical integrity, quality control tests were performed on each infused plate.

The quality control tests are of four types, Interlaminar Shear Stress (ILSS), burn-off tests, Modulated Differential Scanning Calorimetry (MDSC) and Optical and Scanning Electron Microscopy (SEM).

3.1.1. Interlaminar Shear Stress (ILSS)

The short beam shear specimen is widely used to check composite quality. In most cases, because of the complexity of the stress state and the variety of failure modes that can occur in a specimen, it is not possible to relate the short-beam strength to any material property. However, failures are normally dominated by resin and fibre/matrix interface properties, and the test results have been found to be repeatable for a given specimen geometry, material system, and stacking sequence.

A series of interlaminar shear stress tests was performed on specimens from the panels. At least five specimens were tested in each case. The specimen is a short beam machined from a flat laminate up to *6 mm* thick. The beam is loaded in three-point bending. Application of this test method is limited to continuous – or discontinuous – fibre-reinforced polymer matrix composites, for which the elastic properties are balanced and symmetric with respect to the longitudinal axis of the beam.

Tests followed the ASTM D2344 procedure, this specifies a distance between supports equal to five times the thickness of the specimens and a test loading rate of *5 mm/min*. According to the following equation, we will be able to determine the interlaminar shear stress of the different composite materials.

$$ILSS = \frac{3}{4}\frac{F}{b \cdot h} \qquad \textbf{(Eqn. 14)}$$

where F is the fracture load, b is the width of the specimen and h its thickness.

3.1.2. Burn-off tests

As the fibre content has a strong influence on the mechanical properties of composite materials [118-120], resin burn-off tests were also used to control the quality of manufacture, by determination of the fibre contents by weight.

Between four and six specimens, with dimensions typically *20 x 20 mm*, were cut from the different infused plates, weighed and placed in an oven. The applied temperature must be higher than the combustion temperature of the resin but lower than the degradation temperature of the glass fibres. In our case, we have chosen *450°C*.

After a total burn-off of the resin, *5* hours at *450°C*, the specimens were re-weighed after a cooling phase in a dessicator.

The fibre contents by weight of each specimen were determined using the following expression :

$$M_f = \frac{m_{burnt}}{m_{initial}} \times 100 \qquad \textbf{(Eqn. 15)}$$

In addition, the fibre volume fraction V_{fibre} can also be determined with the results of the burn-off tests if we consider that there are no voids in the infused composite. The fibre volume fraction is expressed as a function of the mass of fibre and resin respectively M_{fibre} and M_{matrix}, and the density of each components, ρ_{fibre} (*2550 kg/m*^{3}) and ρ_{matrix} (*1 152.3 kg/m*^{3}).

$$V_{fibre} = \frac{M_{fibre}/\rho_{fibre}}{\frac{M_{fibre}}{\rho_{fibre}} + \frac{M_{matrix}}{\rho_{matrix}}} \qquad \textbf{(Eqn. 16)}$$

3.1.3. Modulated Differential Scanning Calorimetry (MDSC)

The main application of Differential Scanning Calorimetry (DSC) is in studying phase transitions, such as melting, glass transitions, or decompositions. These transitions involve energy changes or heat capacity changes that can be detected by DSC with great sensitivity.

DSC is a thermo-analytical technique in which the difference in the amount of heat required to increase the temperature of a sample and a reference is measured as a function of temperature. Both the sample and reference are maintained at nearly the same temperature throughout the experiment. Generally, the temperature program for a DSC analysis is designed such that the sample holder temperature increases linearly as a function of time. The reference sample should have a well-defined heat capacity over the range of temperatures to be scanned.

The basic principle underlying this technique is that, when the sample undergoes a physical transformation such as a phase transition, more or less heat will need to flow to it compared to the reference to maintain both at the same temperature. The amount of heat required depends on whether the process is exothermic or endothermic. For example, as a solid sample melts to a liquid it will require more heat flowing to the sample to increase its

temperature at the same rate as the reference. This is due to the absorption of heat by the sample as it undergoes the endothermic phase transition from solid to liquid. Likewise, as the sample undergoes exothermic processes (such as crystallization) less heat is required to raise the sample temperature. DSC may also be used to observe more subtle second order phase changes, such as glass transitions. It is widely used as a quality control instrument due to its applicability in evaluating sample purity and for studying polymer curing.

The result of a DSC experiment is a curve of heat flux versus temperature or versus time (*Figure 50a*). There are two different conventions : exothermic reactions in the sample shown with a positive or negative peak, depending on the kind of technology used in the experiment. This curve can be used to calculate enthalpies of transitions, by integrating the peak corresponding to a given transition. So, differential scanning calorimetry can be used to measure a number of characteristic properties of a sample. Using this technique it is possible to observe fusion and crystallization events as well as glass transition temperatures T_g. DSC can also be used to study oxidation, and other chemical reactions.

In our case, we used a Modulated DSC (MDSC) to measure the glass transition temperature *Tg*. Whereas DSC measures heat flow as a function of a constant rate of change in temperature, MDSC superimposes a sinusoidal temperature modulation on this rate (*Figure 50b*).

Each MDSC study of specimens was performed according to the following protocol :

- equilibrate at *20°C*;
- modulation of *0.477°C* every *60* seconds;
- isothermal for *5* minutes;
- ramp of *5°C/min* to *200°C*.

The glass transition temperature *Tg* is defined on the reversible heat flow curves as the point of inflexion. At least three samples were analysed for each material.

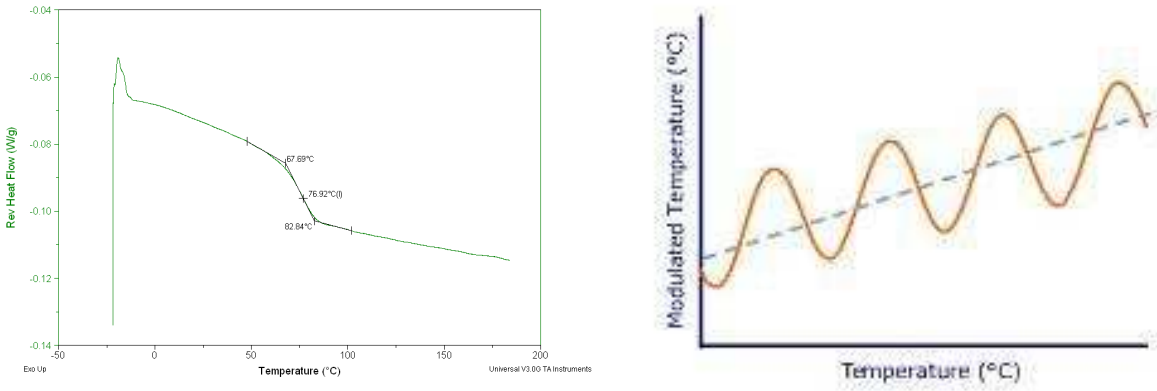

(a) *(b)*

Figure 50. *Representative curves of DSC and MDSC*
a) Common feature of a DSC curve, b) Temperature curve of a MDSC

3.1.4. Imaging techniques

In addition to the burn-off tests, the fibre contents can be measured and overall quality of a composite material controlled by imaging techniques, such as Scanning Electron Microscopy (SEM), optical microscopy and X-ray micro-tomography. These provide some

indications about the surface states and the diameter of the fibres, and resin porosity which all have an influence on the mechanical behaviour of the composite [121].

The Scanning Electron Microscope (SEM) images the sample surface by scanning it with a high-energy beam of electrons in a raster scan pattern. The electrons interact with the atoms that make up the sample producing signals that contain information about the sample's surface topography, composition and other properties such as electrical conductivity.

In a typical SEM, an electron beam is emitted from an electron gun fitted with a tungsten filament cathode. Tungsten is normally used in thermionic electron guns because it has the highest melting point and lowest vapour pressure of all metals, thereby allowing it to be heated for electron emission, and because of its low cost. The electron beam, is focused by one or two condenser lenses to a spot about *0.4 nm* to *5 nm* in diameter. The beam passes through pairs of scanning coils or pairs of deflector plates in the electron column, typically in the final lens, which deflect the beam in the *x* and *y* axes so that it scans in a raster fashion over a rectangular area of the sample surface (*Figure 51*).

All samples must also be of an appropriate size to fit in the specimen chamber and are generally mounted rigidly on a specimen holder called a specimen stub. The SEM used here can examine any part of a *15 cm* long sample. For conventional imaging in the SEM, specimens must be electrically conductive, at least at the surface, and electrically grounded to prevent the accumulation of electrostatic charge at the surface. Because coating prevents the accumulation of static electric charge on the specimen during electron irradiation, all the samples have been coated with gold (*Figure 52a*).

The orientations of the reinforcement, the mean diameter of the fibres and their surface states have been controlled by SEM as presented on *Figure 52b*.

In addition, the distribution of the reinforcement and the resin, which influence the behaviour of the composite, are checked by optical microscopy.

Before microscopy, the specimens are sectioned and polished. The cross-section of the sample is examined in order to control the fibre distribution and reveal porosity. This process also allows us to check the stacking sequence of the laminate.

X-ray micro-tomography uses X-rays to create a cross-sections of a 3D-object that later can be used to recreate a virtual model without destroying the original model [122]. A *GE Phoenix V-TOM-X240* high resolution microfocus computed tomography system was used at CRT Morlaix. The term *micro* is used to indicate that the pixel sizes of the cross-sections are in the micrometer range. *Figure 53* shows the specimens in the tomograph.

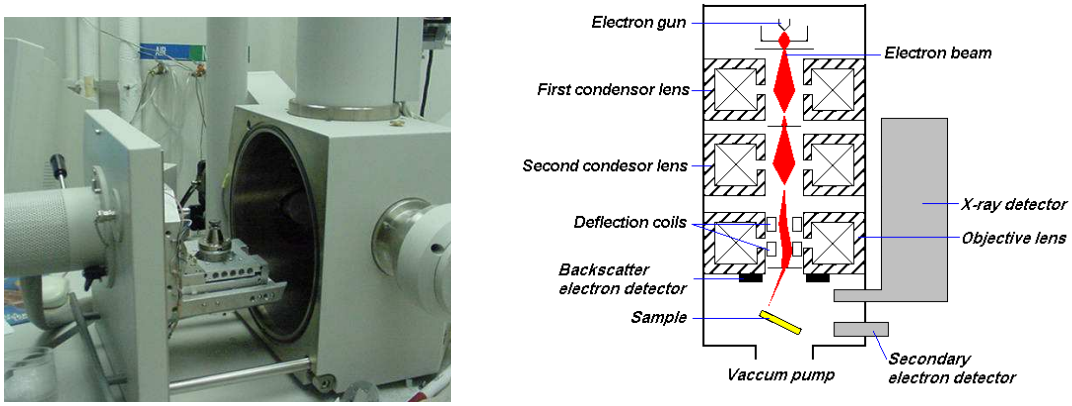

(a) *(b)*

Figure 51. *SEM device and working principle :*
a) SEM opened sample chamber, b) Schematic diagram of a SEM

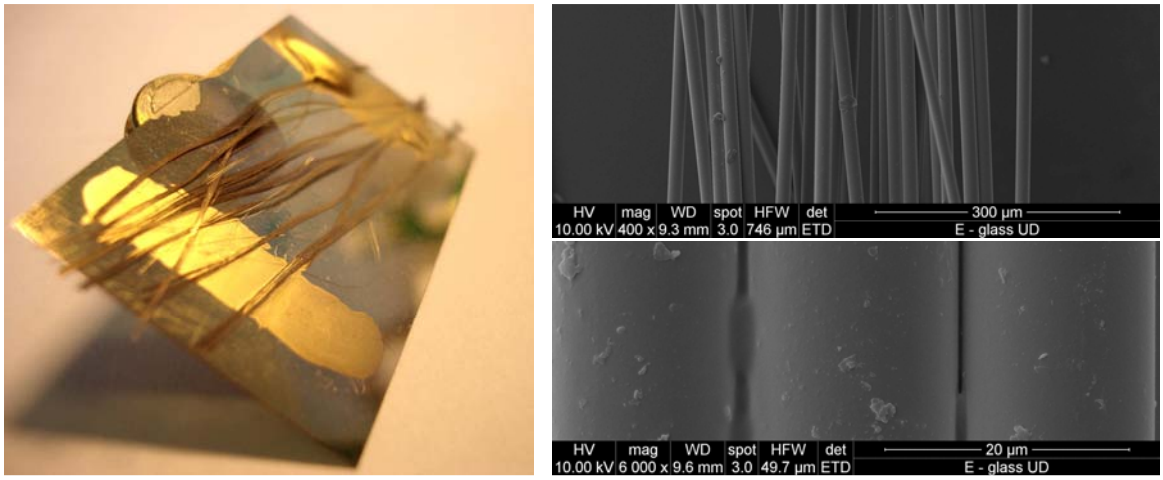

(a) *(b)*

Figure 52. *a) Gold coated glass fibres for viewing with the SEM, b) SEM views of E-glass fibres*

Figure 53. *Four samples during analysis by tomography*

3.2- Natural sea water ageing and gravimetric analysis

Detailed understanding of the mechanisms leading to degradation of mechanical properties, caused by various environmental factors such as temperature and moisture absorption, is essential for durability prediction of composite materials. So, natural sea water ageing was performed on each material at different temperatures.

Experimentally, the water absorption of a specimen is a function of the water absorption of the matrix and of the fibre/matrix interfaces. It is generally assumed that glass fibres do not absorb water. So, in order to have a detailed understanding of the mechanisms of diffusion in a composite material, it is important to understand the kinetics of diffusion in the matrix. For this reason the natural sea water ageing was performed not only on infused E-glass (plate #HE4), Advantex® (plate #HA5) and HiPer-tex ™ (plate #3BHd1) specimens, but also on pure resin specimens infused using the same process parameters and cure cycle (plate #CR).

Thirty specimens of each material have been used for the sea water ageing. These were cut from the same plates (HE4, HA5, 3BHd1 and CR). The square samples (*Figure 54*) were measured and weighed then placed in circulating sea water tanks (*Figure 55*).

In a given environment, in our case natural sea water, the kinetics of diffusion depend on the temperature. So, the thirty specimens have been randomly distributed between the six circulating natural sea water tanks at different temperatures : *4°C*, *20°C*, *40°C*, *60°C*, *70°C* and *80°C*. However, only four of the six specimens at each condition were weighed each time, the fifth and sixth ones were kept for other tests such as calorimetry.

From weight measurements made throughout the ageing process we can define the water content in *%* according to the initial weight of the specimen. Each weighing was performed according to the following protocol :

- remove the specimens from the sea water tanks;
- note the date and the hour of the removal from sea water;
- dry the specimen by wiping the six faces with absorbent paper;
- weigh the specimen;
- replace the specimens in the sea water tanks.

The weight of the specimen will gradually decrease during the time in air, due to evaporation, so it is very important to always use the same procedure.

Figure 54. *View of the sea water ageing specimens (pure resin at 20°C and 40°C)*

Figure 55. *Circulating natural sea water tanks*

3.3- Mechanical tests

The mechanical tests allow us to identify and quantify the influence of the specific environmental conditions, especially natural sea water, and in addition we will be able to quantify the influence of glass fibre type on composite behaviour.

In the mechanical study, both quasi-static and fatigue tests have been performed. Quasi-static tests were performed in order to obtain the intrinsic properties of the material, the elastic constants and strengths. Fatigue tests were performed in order to determine life time of the composite material at different load levels.

These tests were carried out both in air and in natural circulating sea water, on specimens in their initial state and at different stages of ageing or fatigue.

3.3.1. Geometry of the specimens

In order to define the shape of the specimens, a bibliographic study and a preliminary experimental study have been performed on hand laminated specimens. From the preliminary mechanical study the four-point bending method was selected as the main test method, as it introduces both compressive and tensile loads and avoids complicated test fixtures.

Initially, the four-point bending tests were carried out on rectangular specimens, because they are simple to prepare and recommended in test standards [31]. However, the first tests showed that the loading points whatever their radius, caused local damage due to indentation of the upper face of the specimen. As a consequence, this prevents valid lifetime data being obtained. It is interesting to note that few published studies mention this problem, even for tests in three-point flexure which are more sensitive to local indentation.

In order to find a solution and avoid this damage, dog-bone specimens were studied. These are more difficult to manufacture, but they allowed the loads to be spread over a larger area and for our materials resulted in failures in the central sections without crushing.

So all the subsequent mechanical tests, both quasi-static and cyclic, were performed on dog-bone specimens as shown on *Figure 56*. These specimens have been cut in infused plates using a high pressure water jet, which provides an excellent surface finish without heating the specimen. Once the geometry has been programmed on the machine controller exactly the same specimen geometry can be obtained for each plate. Each infused plate provides at least 30 specimens (*Figure 57*).

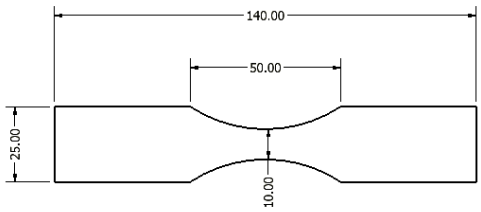

Figure 56. *Test specimens (dimensions in mm)*

Figure 57. *Infused E-glass plate IE1after high pressure water jet cutting*

3.3.2. Quasi-static tests

The initial properties of a composite material can be determined either directly, from tests involving simple loading such as tensile or compression, or indirectly from more complex tests such as three-point or four-point bending. In order to measure the resin properties, specimens were tested in tension, while for the composites we have carried out both “CRP” tests in tension and in compression and failure tests in four-point bending.

a) Resin tensile tests

Dog-bone specimens (*150 mm* long, *20 mm* wide at the ends and *9 mm* in the centre and *5.50* mm thick) were tested in tension at a crosshead displacement rate of *2 mm/min* (*Figure 58*), on an *Instron 5566 10 kN* test machine (*Figure 59*). A digital camera was used to measure central section strain, via the movements of two targets and an in-house image analysis programme.

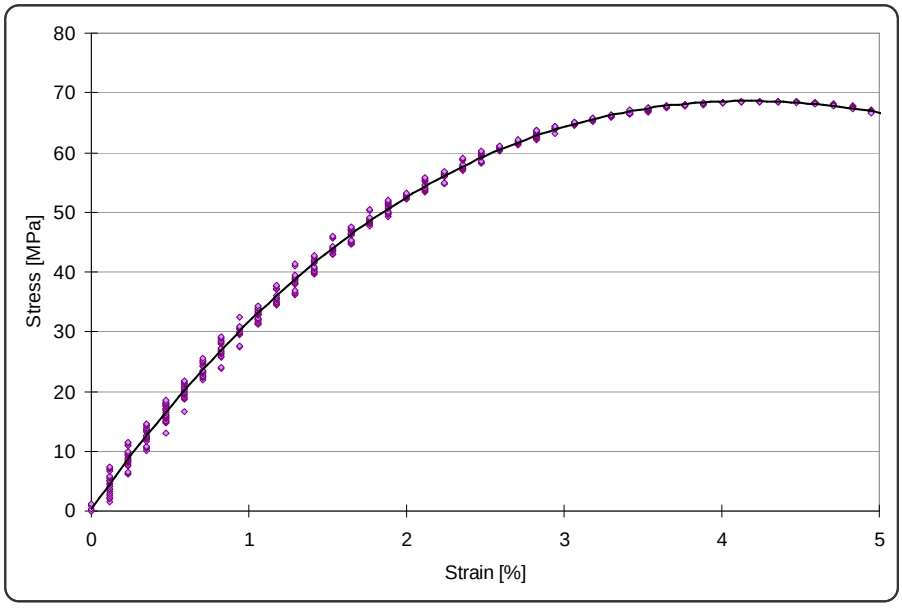

Figure 58. *Example of load and central section strain measurements*

Figure 59. *Load device and instrumentation of resin tensile tests*

b) CRP tests

The principle of "CRP" (Chargement Répété Progressif) tests is to load and unload a dog-bone specimen to load levels which increase progressively until failure, as represented on *Figure 60*. These tests have been performed both in tension and in compression at UFC. A short loading cycle (from *0* to *2.8 kN*) was applied to the specimen after each main cycle in order to define the elastic constants, such as the moduli E_1 and Poisson's ratios v_{12}, by using two extensometers attached to the central part of the specimen (*Figure 61*).

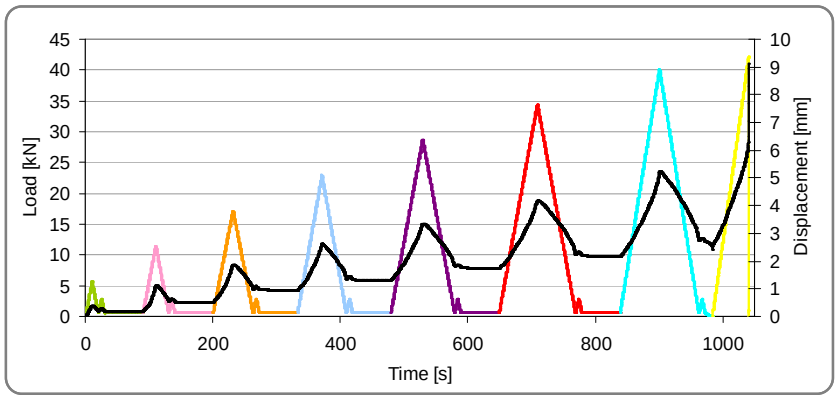

Figure 60. *Applied Load and measured displacement during a "CRP" tensile test*

Figure 61. *Load device and instrumentation of the " CRP" tensile tests*

c) Failure tests

In order to define the fatigue levels for the subsequent part of the study, we have to determine the failure stresses of the three different materials. For this reason we have performed quasi-static flexural tests.

These tests have been carried out on dog-bone specimens with the four-point bending method. The inner span is equal to *60 mm* and the outer span is *120 mm* (*Figure 62*). The specimen is loaded with a displacement controlled bending device with a rate of *5 mm/min* until complete failure. The same test machine and fixtures as those used for subsequent cyclic loading were employed.

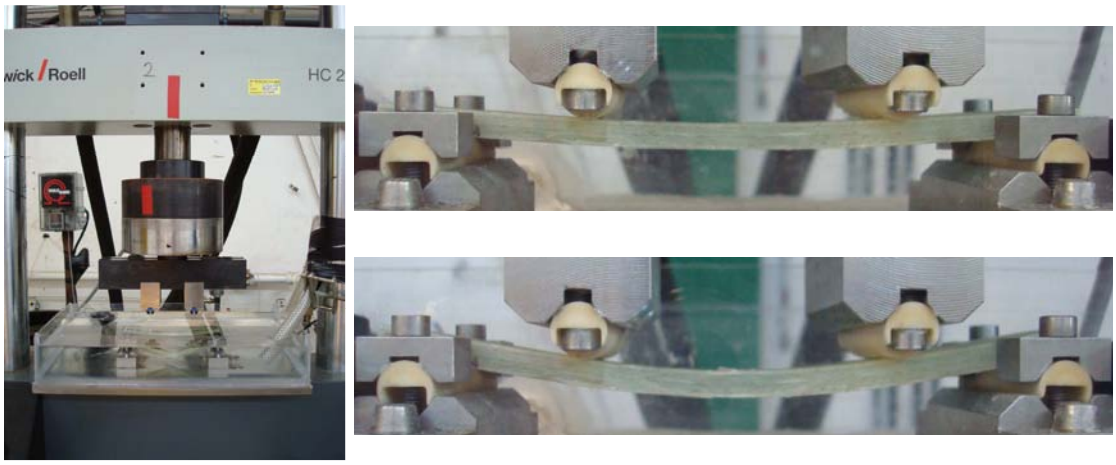

Figure 62. *Four-point bending testing machine*

d) Nanoindentation tests

In an indentation test, a hard tip whose mechanical properties are known is pressed into a sample whose properties are unknown. The nanoindentation technique has been developed to measure the hardness of a small volume of material by using small loads and tip sizes. An indenter with a geometry known to high precision is employed, a Berkovitch tip, which has a three-sided pyramid geometry.

While indenting, various parameters can be measured, such as load and depth of penetration. A record of these values is plotted on a graph to create a load-displacement curve (*Figure 63*). These curves are used to extract mechanical properties of the tested material, such as the Young's modulus, the hardness or the strain-rate sensitivity. In our case, we have focussed on the Young's modulus. The slope of the curve, *dP/dh* during unloading is indicative of the stiffness of the contact *S* which is used to calculate the reduced Young's modulus *Er (Eqn. 17)* [123, 124]. This value generally includes a contribution from both the tested material and the response of the test device itself.

$$Er = \frac{1}{\beta} \cdot \frac{\sqrt{\pi}}{2} \cdot \frac{S}{\sqrt{A_p(h_c)}} \qquad \textbf{(Eqn. 17)}$$

Where $A_p(h_c)$ is the projected area of the indentation at the contact depth h_c, and β is a geometrical constant close to one.

The nanoindentation tests were performed on pure resin specimens after different ageing periods, natural sea water at *60°C*, and a complete drying. The tests were analysed following ISO 14577 [123] and the Oliver and Pharr method [124].

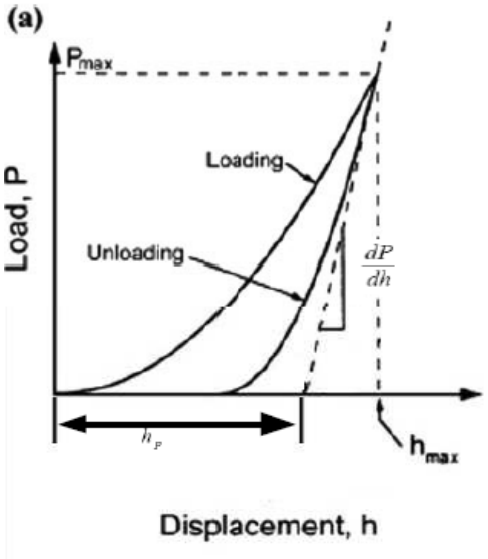

Figure 63. *Schematic of load-displacement curve for an instrumented nanoindentation curve*

3.3.3. Fatigue tests

Fatigue is the progressive and localized structural damage that occurs when a material is subjected to cyclic loading. ASTM defines fatigue life N_f, as the number of stress cycles of a specified character that the specimen sustains before failure of a specified nature occurs.

In our case, we have performed the majority of the fatigue tests in four-point bending, with a small number in tension-tension, both in air and in natural circulating sea water.

a) Flexural fatigue tests

The fatigue tests applied here involve cycling specimens with a constant stress level until failure. The corresponding load applied to the specimen is estimated, according to the beam theory. In four-point bending, the maximal stress in the middle of the beam is written :

$$\sigma = \frac{M_f}{\left(I_{GZ} / v\right)} \qquad \textbf{(Eqn. 18)}$$

where M_f is the bending moment, I_{GZ} is the moment of inertia of the section and v is the distance to the neutral axis, in our case the demi-thickness. The maximal bending moment and the moment of inertia are written as :

$$M_f = \frac{F \cdot L}{8} \qquad I_{GZ} = \frac{b \cdot h^3}{12} \qquad \textbf{(Eqn. 19)}$$

By substituting *(Eqn. 19)* in the *(Eqn. 18)*, we obtain :

$$\sigma = \frac{3}{4} \cdot \frac{F \cdot L}{b \cdot h^2} \qquad \textbf{(Eqn. 20)}$$

If we consider that $R_\sigma = \frac{\sigma}{\sigma_{fail}}$ we can write

$$F = \frac{4}{3} \cdot \frac{\sigma_{fail} \cdot R_\sigma \cdot b \cdot h^2}{L} \qquad \textbf{(Eqn. 21)}$$

where σ_{fail} is the failure stress of the material in four-point bending, $R\sigma$ is the stress level to be applied, b is the width and h is the thickness of the specimen in the centre of the dog-bone and L is the effective length of the specimen, i.e. the outer span.

The stress level $R\sigma$ depends on the quasi-static failure stress of each composite material. The reference stress level $R\sigma$ is 60 % of the failure stress. The reference frequency is *2 Hz* and R, the load ratio ($R = \sigma_{min}/\sigma_{max}$) is equal to *0.1* unless otherwise stated.

The flexural fatigue tests have been performed in air and in natural circulating sea water. The latter required a specific test device as presented on *Figure 64*, in order to avoid corrosion problems.

The first, and the easiest, parameter to determine during these tests is the fatigue life N_f, the number of cycles to failure, which allows us to draw three types of curves. Here failure is defined as a displacement superior to *14 mm*, corresponding to extensive damage and an inability to maintain the load level requested. This is an arbitrary failure criterion based on experience, but load and displacement measurements were made continuously throughout the tests so alternative criteria can be examined.

The first type of curve to be plotted is the classical S-N curve which represents the stress level $R\sigma$ versus the number of cycles N_f. The second one represents the applied stress σ as a function of the logarithm of the fatigue life N_f. The third one represents the stress level $R\sigma$ versus the logarithm of the fatigue life N_f.

The other parameter which will be observed is the evolution of the damage. One indicator of this is given by recording the displacement of the upper loading points throughout the fatigue test. When the ratio of the applied load divided by the displacement is plotted as a function of the ratio number of cycles/fatigue life, we obtain a curve which describes the evolution of the damage.

With these sets of curves, we will be able to compare the influence of the reinforcement as a function of the environment (air or natural circulating sea water). In addition, we will be able to observe and quantify the influence of the environment on the fatigue life for each material.

Figure 64. *Fatigue test set-up in four-point bending in natural circulating sea water*

b) Tension-tension tests

As noted previously, the four-point bending tests involve both tension and compression. So in order to have a better understanding of the phenomena it was initially intended to perform some fatigue tests in tension-tension loading, in air and in natural circulating sea water.

To make these tests possible in natural circulating sea water, it was necessary to develop a new test device [125]. This device needs to be water tight, transparent and resistant to cyclic loading. There are some published examples of fixtures to allow testing wet specimens but there are based on closed water-filled envelopes fixed to the specimens (e.g. *Figure 14* in *Chapter I*). The device developed is shown on *Figure 65a* and *Figure 65b*. In order to provide the joint with the specimen and avoid problems due to leakage, a joint is moulded directly around the specimens before testing (*Figure 65c*). The major advantage of this system is that the complete specimen is wet and that the water can be continuously renewed. The latter is important to leached products during long tests can modify water composition if circulation is not allowed.

Unfortunately due to lack of time it was not possible to perform a full characterization programme with this fixture. A small number were performed on rectangular infused specimens (dimensions *400 x 20 x 5 mm*), with a frequency of *0.5 Hz* and *R* equal to *0.1*. The results will be briefly discussed in *Chapter V*.

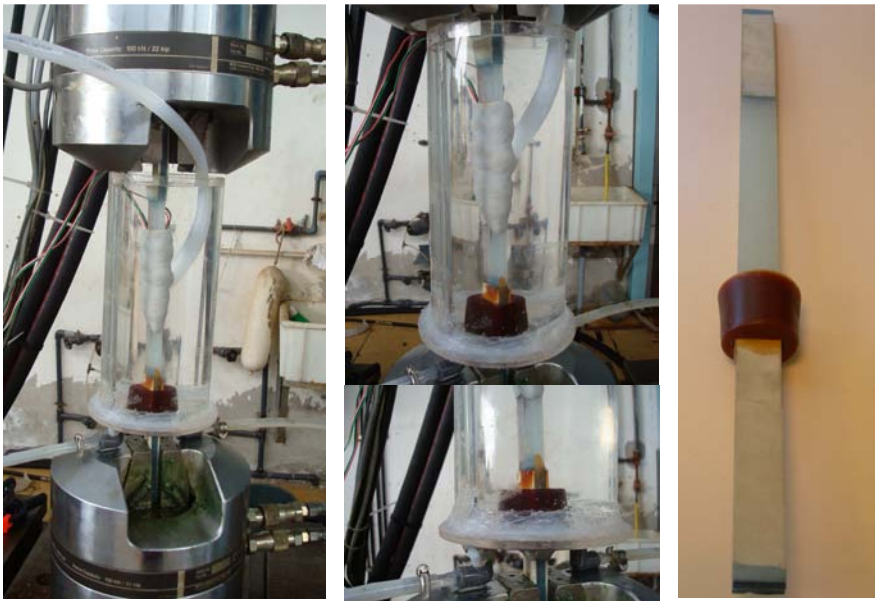

(a) *(b)* *(c)*

Figure 65. *Fatigue test set up in tension-tension in natural circulating sea water : a) overall view of the device, b) details of the device, c) detail of the specimen*

4- Numerical analysis

In order to determine the main characteristics of the infused composite materials, the experimental data have to be analysed. So, based on the sets of experimental data and classical analytical formulations, we were able to define the coefficients which characterize these phenomena, such as the evolution of damage, the water uptake and the fatigue life.

The first tool used is the least squares method. The second tool is a genetic algorithm.

4.1- Least squares method

The least squares method is a standard approach to approximate the solutions of over-determined systems, i.e. sets of equations in which there are more equations than unknowns. “Least squares” means that the overall solution minimizes the sum of the squares of the errors made in solving every single equation.

In our case, we have used the method implemented in the *Matlab*© routine for the data fitting. If we consider a residual as the difference between an observed value and the value provided by a model, the best fit in the least-squares sense minimizes the sum of squared residuals.

The objective is to adjust the parameters of a model to best fit an experimental data set. A simple data set consists of n points (x_i , y_i) with $i=1, 2, \ldots, n$, where x_i is an independent variable and y_i is a dependent variable whose value is found by observation. The model function has the form $f(x , \beta)$, where the m adjustable parameters constitute the vector β. The goal is to find the parameter values for the model which provides the best fit with the experimental data. The least squares method finds its optimum when the sum S *(Eqn. 22)* of squared residuals is a minimum. A residual is defined as the difference between the value of the dependent variable and the model value *(Eqn. 23)*.

$$S=\sum_{i=1}^{n} r_i^2 \qquad \textbf{(Eqn. 22)}$$

$$r_i=y_i-f(x_i,\beta) \qquad \textbf{(Eqn. 23)}$$

The minimum of the sum of squares S is found by setting its gradient to zero. Since the model contains m parameters, there are m gradient equations.

$$\frac{\partial S}{\partial \beta_j}=2\sum_i r_i \frac{\partial r_i}{\partial \beta_j}=0 \qquad \text{with} \quad j=1,2,\ldots,m \qquad \textbf{(Eqn. 24)}$$

By replacing the *(Eqn. 23)* in the *(Eqn. 24)*, we obtain

$$-2\sum_i \frac{\partial f(x_i,\beta)}{\partial \beta_j} r_i=0 \qquad \text{with} \quad j=1,2,\ldots,m \qquad \textbf{(Eqn. 25)}$$

The gradient equations apply to all least squares problems. Each particular problem requires particular expressions for the model and its partial derivatives. Least squares problems can be divided into two categories, linear and non-linear least squares.

4.2- Genetic algorithm

A genetic algorithm (GA) is another search technique used in computing to find exact or approximate solutions to optimization and search problems. Genetic algorithms are categorized as global search heuristics. They are a particular class of evolutionary algorithms (EA) that use techniques inspired by evolutionary biology such as inheritance, mutation, selection, and crossover.

Before using a genetic algorithm to solve a problem, a way must be found to encode any potential solution to the problem. This could be a binary bit string or, in our case, a string of real numbers (*i.e. m* parameters) called a chromosome. At the beginning of a genetic algorithm run, a large population of random chromosomes, each one representing a different solution (individuals) to the problem, is created. Individuals represented by a set of m parameters are sorted according to their fitness, in our case the sum of square residuals as expressed in the least square method. The evolution starts from this population of individuals and proceeds in generations. The algorithm terminates when either a maximum number of generations has been produced, or a satisfactory fitness level has been reached for the population.

In each generation, the fitness of every individual of the population is assessed, multiple individuals are stochastically selected from the current population according to their fitness, and modified by recombination and random mutations, to form a new population. This new population is then used in the next iteration of the algorithm.

This approach was used in a previous study to optimise the lay-up of composite cylinders [126, 127].

CHAPTER III
EXPERIMENTAL CHARCTERIZATION OF THE COMPOSITE MATERIALS

III- EXPERIMENTAL CHARACTERIZATION OF THE COMPOSITE MATERIALS

The main objective of the experimental study described in the previous chapter is to determine the properties of the infused composite materials. This results will be presented in three main parts, the material characterization, the definition of the kinetics of diffusion and the mechanical characterization. Then in *Chapter IV*, with the experimental data obtained we will be able to investigate and verify the model predictions of the behaviour of the materials.

1- Material characterization

The material characterization is based on the quality control tests performed on the infused composite plates. As mentioned previously, this part of the study is divided into four sections, Interlaminar Shear Stress tests (ILSS) in order to determine the shear stress at failure, burn-off tests in order to determine the fibre contents of the plates, Modulated Differential Scanning Calorimetry (MDSC) in order to determine the glass transition temperatures and imaging techniques in order to check the surface states, the distribution of the reinforcement and the porosity.

1.1- Interlaminar shear failure stress

Each panel was investigated by testing *5* specimens cut in the unidirectional fibre direction. *Table 3* and *Figure 66* show the results for the infused E-glass, Advantex® and HiPer-tex™ panels.

When we compare the results for the three materials (*Figure 66*), we can observe that there is a significant difference between the experimental values obtained for E-glass and Advantex© specimens. The mean ILSS of all the infused Advantex© panels tested is around *36 MPa* compared to *50 MPa* for the infused E-glass, a difference of *25 %*. This suggests there is a material problem, either with the reinforcement, the resin or the interface, because these results do not change with the place of manufacturing. In addition, the experimental results are different from results obtained previously during tests at the *Risø Institute* in another project, being almost *20 %* lower. The panels HE4 and 3BHa1 also gave low results, so they were not used for fatigue tests.

There is little difference between the experimental values obtained for the other E-glass and HiPer-tex™ specimens. The mean ILSS of all the infused HiPer-tex™ panels is around *50 MPa* which is very similar to that measured for the infused E-glass. For this material, the experimental results obtained here are about *10 %* higher than the results obtained at *Risø*. The latter value of *45 MPa* was taken (arbitrarily) as an acceptable value for all the material tested here.

Although none of Advantex® panels satisfied this criterion specimens were nevertheless tested even though this is recognized to be a sub-quality material. At the very end of the thesis satisfactory panels were produced (with *ILSS=52.1(1.4) MPa*) and these will be discussed in *Chapter V*.

Table 3. *Experimental data obtained with ILSS test for the three infused composite specimens*

Reinforcement	Infused panel	Mean ILSS (SD) $[MPa]$
E-glass	HE3	53.5 (1.3)
	HE4	43.9 (2.2)*
	IE1	50.8 (1.3)
	IE2	48.8 (1.3)
	Mean (SD)	**51.0 (2.4)**
Advantex®	HA5 & HA6	32.5 (1.4)
	HA1	38.0 (2.1)
	3BA1 & 3BA2	37.1 (1.5)
	Mean (SD)	**35.9 (2.9)**
HiPer-tex™	HH1	51.2 (1.8)
	3BHa1	37.9 (2.7)*
	3BHc1	49.3 (1.2)
	3BHd1	47.7 (1.2)
	IH1	52.3 (0.9)
	Mean (SD)**	**50.2 (2.8)**

** Too low values not take into account in the mean value*
*** Mean value for HH1, 3BHd1 and IH1*

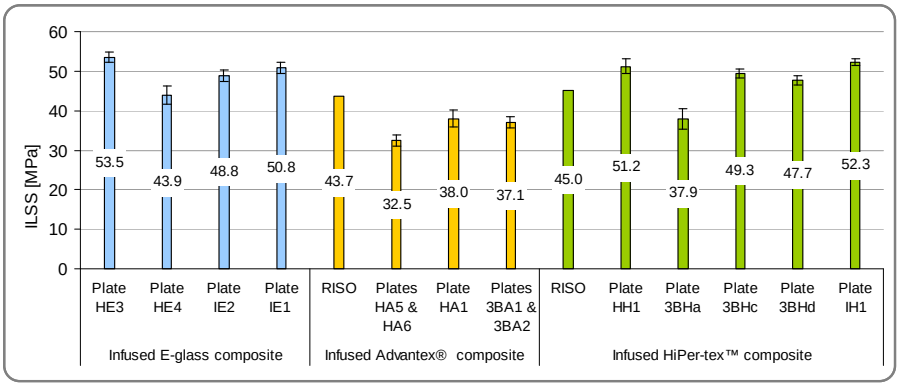

Figure 66. *Comparative plot of ILSS data for the three infused composites*

1.2- Fibre contents

Burn-off tests have been carried out on each infused panel. The results are summarized in *Table 4* for the infused E-glass, Advantex® and HiPer-tex™ panels.

When we compare the mean results obtain for the three infused composites, we can see that all the values are very similar. The mean value obtained for the E-glass reinforcement is *73 %* by weight compared with *73.5 %* and almost *75 %* by weight respectively for the Advantex® and HiPer-tex™ reinforcement. These values are much higher than those obtained by hand lay-up (typically *40-50 %* by weight), and scatter is very low suggesting a repeatable processing procedure.

Table 4. *Experimental data obtained with burn-off test for the three infused composite specimens*

Reinforcement	Infused panel	Mean fibre contents by weight (SD) [%]	Mean fibre contents by volume (SD) [%]
E-glass	HE3	70.8 (0.6)	52.3 (0.8)
	HE4	71.1 (0.7)	52.6 (0.9)
	IE1	74.4 (0.3)	56.8 (0.4)
	IE2	75.7 (0.2)	58.5 (0.3)
	Mean (SD)	**73.0 (2.4)**	**55.1 (3.1)**
Advantex®	HA5 & HA6	72.4 (0.2)	54.3 (0.3)
	HA1	72.9 (1.3)	54.9 (1.6)
	3BA1 & 3BA2	75.2 (0.3)	57.9 (0.4)
	Mean (SD)	**73.5 (1.5)**	**55.7 (1.9)**
HiPer-tex™	HH1	73.2 (0.4)	55.3 (0.5)
	3BHd1	75.1 (0.5)	57.7 (0.7)
	IH1	76.4 (0.3)	59.5 (0.4)
	Mean (SD)	**74.9 (1.6)**	**57.5 (2.1)**

1.3- Glass transition temperatures

Table 5 shows the results from MDSC analyses.

The mean value of *Tg* obtained is equal to *76°C* for the Advantex® specimens against *77°C* for the E-glass specimens. These values are very similar and suggest that the lower ILSS results noted for Advantex® (*Section 1.1*) are not caused by a curing problem.

In addition, the mean value of *Tg* obtained for the HiPer-tex™ is equal to *82°C* compared to *77°C* for the E-glass specimens and *76°C* for the Advantex® specimens. Given the variability of these measurements (*77-87°C* here, made on very small samples) these values are quite similar.

Besides, the mean value of *Tg* obtained for the pure resin, *72°C*, is less than those obtained for the three infused composite materials

Table 5. *Experimental data obtained with MDSC tests for the three infused composite specimens*

Reinforcement	Infused panel	Mean Tg (SD) $[°C]$
E-glass	HE3	75
	HE4	83
	IE1	77
	IE2	74
	Mean (SD)	**77 (4)**
Advantex®	HA5 & HA6	76
	HA1	77
	3BA1 & 3BA2	76
	Mean (SD)	**76 (1)**
HiPer-tex™	HH1	77
	3BHd1	81
	IH1	87
	Mean (SD)	**82 (5)**
Pure resin		**72 (3)**

1.4- Surface state of the fibres and distribution of the reinforcement and the resin

The mean diameters of each type of fibre were measured and their surface states were checked using Scanning Electron Microscopy (SEM). The views obtained are presented in *Annex 3*.

The mean diameters of the E-glass, Advantex® and HiPer-tex™ fibres were measured to be respectively approximately *16 µm, 20 µm* and *19 µm.* In addition, we have observed that the mat fibres of each reinforcement have much smaller diameter (around *10-12 µm*) and appear to be coated periodically.

The distribution of the reinforcement and the resin through the laminate thickness can influence the mechanical behaviour of the composite, particularly when tested in flexure. This was also checked by microscopy, together with the stacking sequence. The *Annex 3* show the views obtained for E-glass, Advantex® and HiPer-tex™ specimens.

As presented in *Annex 3*, some porosity has been detected in the different laminates, particularly in the HiPer-tex™ specimens. Porosity is one of the most common imperfections in composites reinforced with continuous fibres, because of air bubbles trapped during resin mixing and impregnation and volatile substances liberated during curing. Even though the composite panels were manufactured following nominally the same process, both at IFREMER and by the material suppliers, they can have different degrees of porosity. In many cases, insufficient pressure or vacuum leaks during curing are the most important factors that affect formation of porosity in composite laminates, but the porosity in the finished infused plate is a consequence of many factors which are difficult to control. The distribution and the density of porosity can affect the mechanical properties of unidirectional laminates significantly, and a percentage void content is quite insufficient to characterize this [128-130]. *Olivier et al.* [128, 129] showed for aeronautical composites that even if two laminates show the same void content, their respective response to an identical mechanical loading can be

very different, which is mainly due to the void sizes and locations. *Maurin* [131] provided a recent overview of the influence of porosity on mechanical properties in marine composites.

X-ray micro-tomography is an interesting technique to characterize larges pores ($> 20\ \mu m$) as it allows both the geometry and the distribution of defects to be quantified. The figures presented in *Annex 3* show examples for each of the three composite materials.

In the present study the translucent nature of the materials enabled specimens with large defects to be rejected, but a detailed quantitative characterization was not performed.

2- Kinetics of diffusion

In order to have a better understanding of the kinetics of diffusion in the infused composite materials and to obtain the coefficients to be used in a numerical model, natural sea water ageing tests have been performed following the procedure described in the previous chapter.

As the water absorption of a composite material depends on the water absorption of the matrix, the fibre contents in volume and the fibre/matrix interfaces, natural sea water ageing has been performed not only on infused composite specimens but also on pure resin specimens.

In this section, experimental data will be provided. Then, the analytical approach will be explained and the results obtained will be presented.

2.1- Experimental data

2.1.1. Pure resin material

As for the infused composite materials, it is important to manufacture the coupons of pure resin in a similar way to the application procedure, so the infusion method was chosen. The pure resin plate (*MGS© RIM 135* from Hexion™ noted plate #CR), was subjected to the same cure cycle as the infused composite, as presented in *Section 2.2, Chapter II*.

Then thirty specimens have been cut, measured and weighed (see *Annex 4*) before being distributed in the sea water tanks. For these pure resin specimens, tests have been carried out at six different temperatures, *4°C*, *20°C*, *40°C*, *60°C*, *70°C* and *80°C*.

The resin samples have been immersed in sea water for almost *700* days (almost *2* years) and the weight gains have been measured and plotted versus the square root of time. The first experimental results exhibited a curious shape for the weight gain of the specimen at *60°C* (*Figure 67*). For that reason a second series of specimens was subjected to sea water ageing at *60°C* and *70°C*, in order to be sure of the diffusion kinetics (*Figure 68*). The second series of specimens at *60°C* and *70°C* has been in sea water for more than *200* days (almost *7* months).

When the weight gain is plotted versus the square root of time (*Figure 67* and *Figure 68*), it appears that the diffusion in the material follows Fick's law. As a consequence, we can use a *Matlab©* fitting routine, based on the least squares method, to determine the diffusion characteristics according to the analytical formula of Fick's law and the experimental data for *4°C*, *20°C*, *40°C* and *60°C* (see following paragraph).

The anomaly at *60°C* is not yet completely explained, but at that temperature the drop in *Tg* due to moisture absorption may result in a switch from $T_{ageing}<Tg$ to $T_{ageing}>Tg$. When the ageing temperature exceeds the material *Tg*, increased molecular mobility may modify the diffusion behaviour. If curing continues at *60°C* this will affect the water content as observed by *Perrin et al.* [132]. It is curious however that the initial weight gain at *60°C* is lower than that at *40°C* and then accelerates after about *3* weeks to reach the expected level. More analyses are required to confirm this, as there may also be a resin degradation mechanism under these conditions, and an error in the bath temperature regulation might also be invoked. It should also be noted that at *80°C* the bath temperature exceeds the resin *Tg* from the start of immersion.

The second series of tests at *60°C* and *70°C* appear more consistent during the initial phase but it is interesting to note that the saturation level for both is then lower (at *2 %*) than that of the *40°C*.

A third series at *60°C*, on dog-bone resin specimen will be described below.

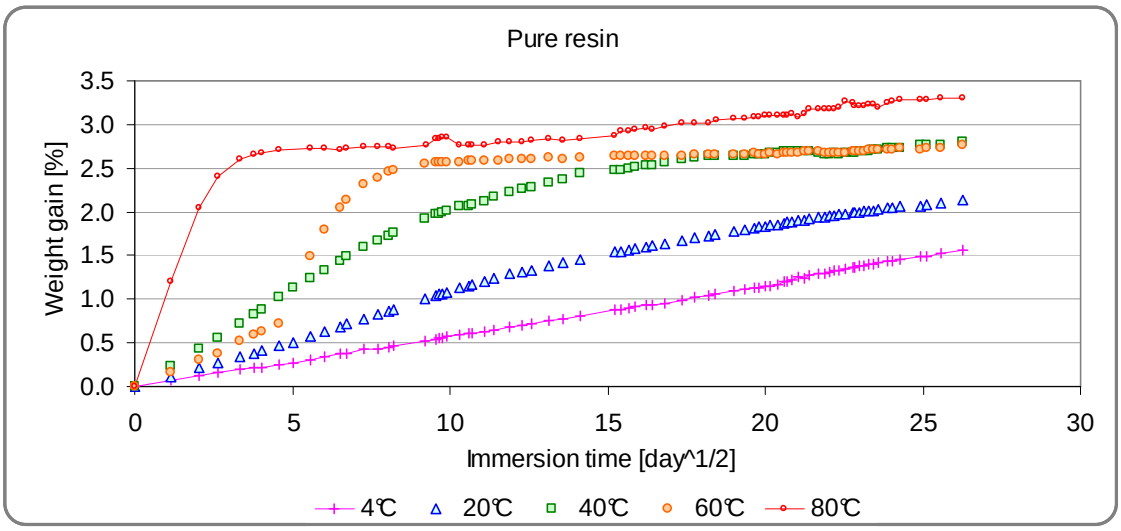

Figure 67. *Comparative curves of the kinetics of diffusion of the pure resin specimens at five temperatures in natural circulating sea water*

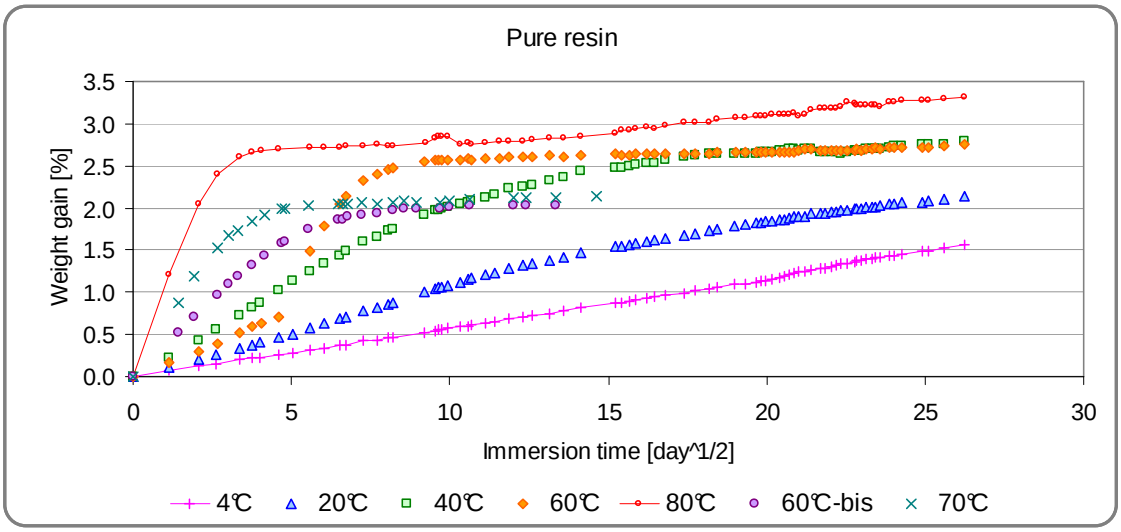

Figure 68. *Comparative curves of the kinetics of diffusion of the pure resin specimens at six temperatures in natural circulating sea water, including second series at 60°C and 70°C*

2.1.2. Fibre-reinforced composite material

In this part, the materials studied are quasi-unidirectional E-glass (plate #HE3), Advantex® glass (plate #HA5) and HiPer-tex™ glass (plate #3BHd).

The three sets of thirty specimens have been measured and weighed (see *Annex 4*), the weight gains are plotted versus the square root of time on *Figure 69* for the infused E-glass specimens, *Figure 70* for the infused Advantex® specimens and *Figure 71* for the infused HiPer-tex™ specimens.

The infused E-glass specimens have been immersed for almost *600* days (*20* months), the infused Advantex® specimens for *170* days (almost *6* months) and the infused HiPer-tex™ specimens for *300* days (*10* months).

Once again, as noted for pure resin specimens at *60°C*, a step increase in weight gain is noted after immersion for about *1* year for infused E-glass specimens and *4* months for infused HiPer-tex™ specimens (*Figure 72a*). But when the weight gains of these two composite materials are plotted as a function of the dates, as presented on *Figure 72b*, we observe that the drops take place at the same time. So we can conclude that these anomalies in the water uptake must be due to the experimental device. For the rest of the study, only the results from immersions before this anomaly are analysed.

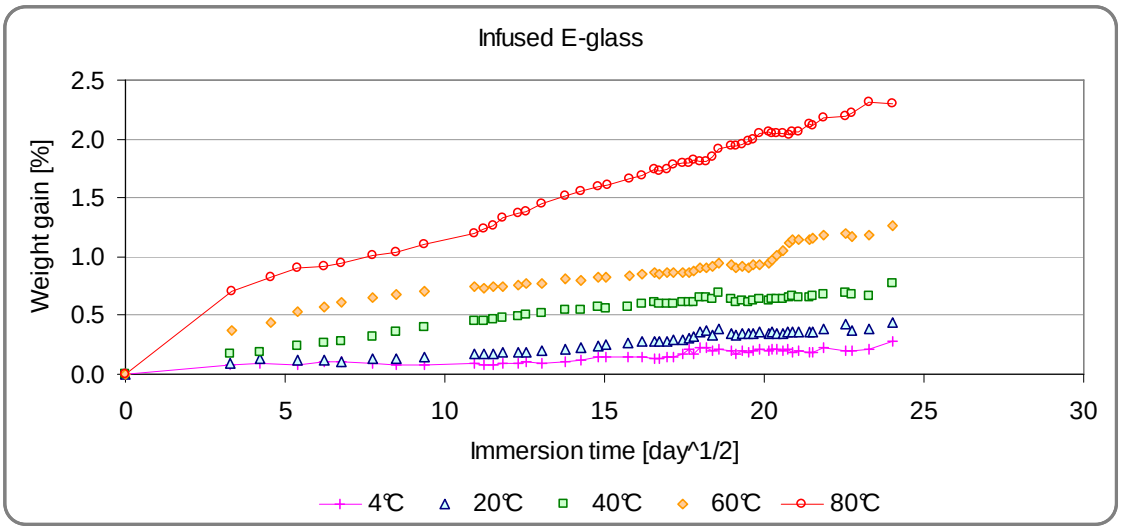

Figure 69. *Comparative curves of the kinetics of diffusion of the infused E-glass specimens at five temperatures in natural circulating sea water*

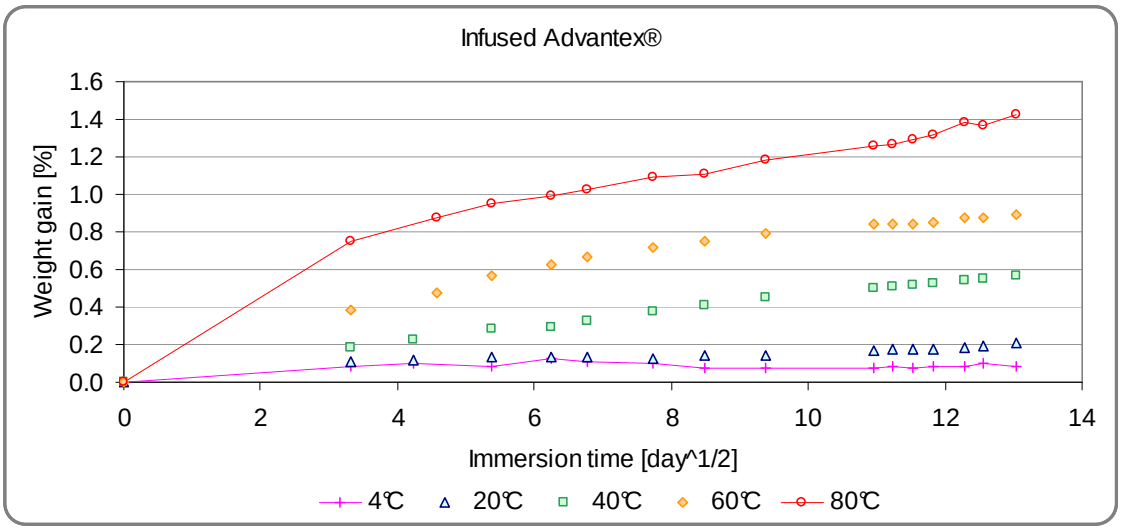

Figure 70. *Comparative curves of the kinetics of diffusion of the infused Advantex® specimens at five temperatures in natural circulating sea water*

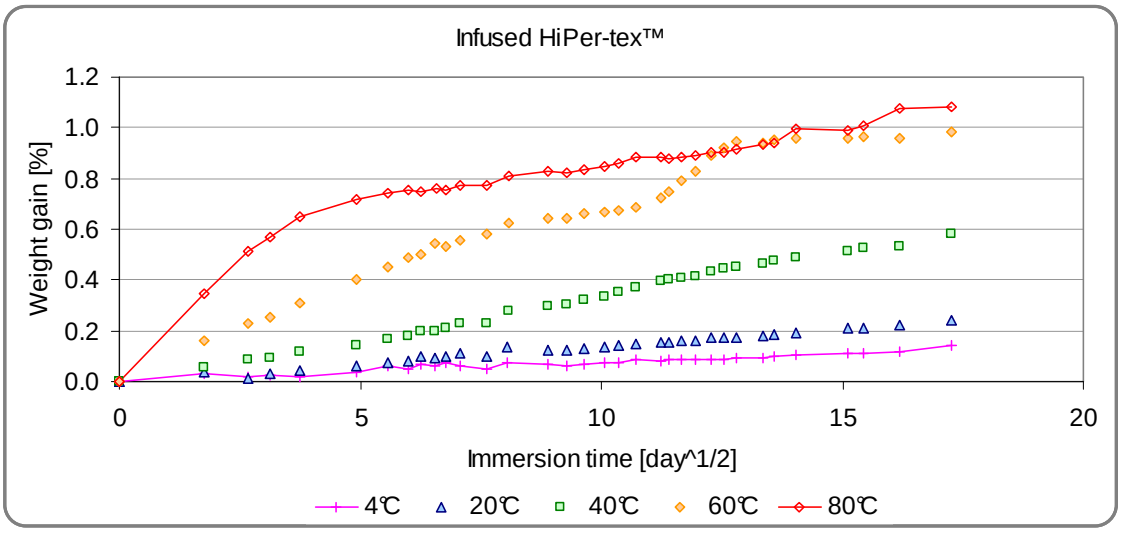

Figure 71. *Comparative curves of the kinetics of diffusion of infused HiPer-tex™ specimens at five temperatures in natural circulating sea water*

(a)

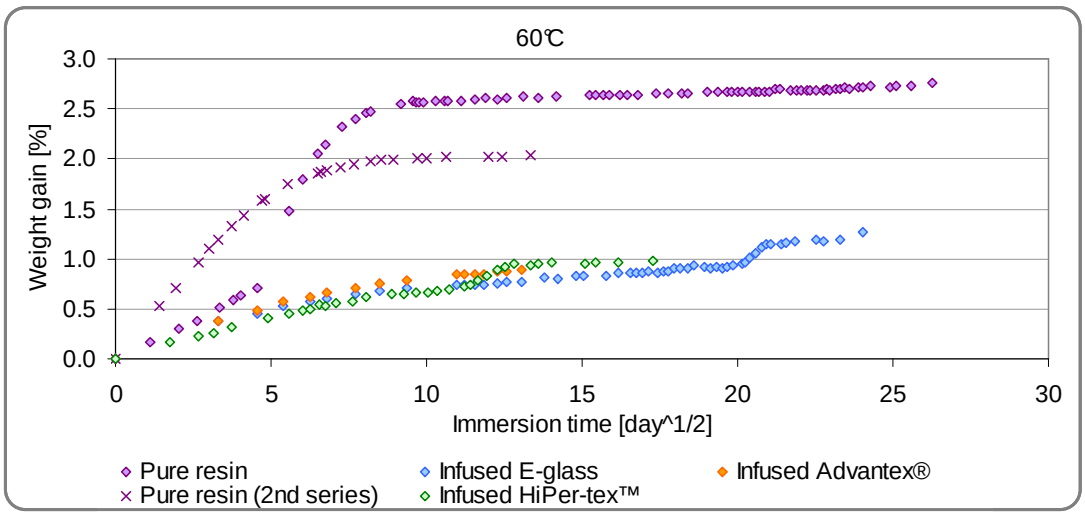

(b)

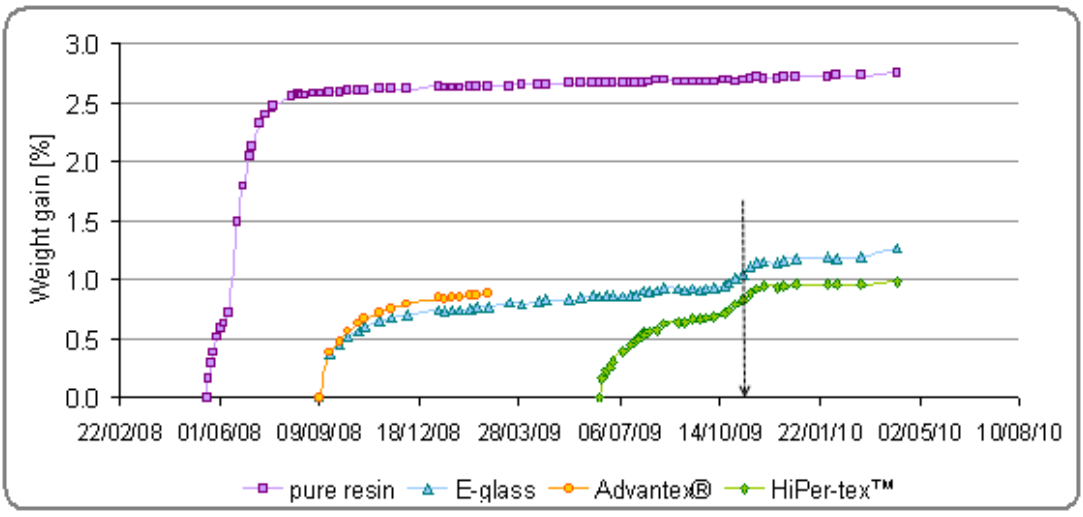

Figure 72. *Comparative curves of the kinetics of diffusion of the four materials specimens at 60°C in natural circulating sea water, a) as a function of the immersion time, b) as a function of the date*

2.2- Analytical approach

For each composite material and at each sea water temperature, the optimization routine provides the diffusion coefficient *D*, using the experimental data and the analytical formulation of Fick's law, by considering the dimensions of the specimen and the mass at saturation.

For a material immersed in liquid the mass at saturation M_∞ is a constant [15]. If we consider that the fibres and the interfaces fibres/matrix do not absorb water and there are no voids in the infused composite, we can estimate the weight gain of the infused composites M_{comp} as a function of the weight gain of the pure resin material M_{matrix} and the fibre contents by weight of each composite material W_f using the expression

$$M_{comp} = M_{matrix} \cdot (1 - W_f) \qquad \textbf{(Eqn. 26)}$$

So, by considering that the weight gain at saturation is equal to *2.75 %* for the pure resin specimens, we can estimate that the weight gain in the infused E-glass (*73 %* of fibres), Advantex® (*73.5 %* of fibres) and HiPer-tex™ (*74.9 %* of fibres) composites are respectively equal to *0.75 %*, *0.73 %* and *0.70 %*.

The results of the optimizations are summarized in *Table 6* for the pure resin specimens, in *Table 7* for the infused E-glass specimens, in *Table 8* for the infused Advantex® specimens and in *Table 9* for the infused HiPer-tex™ specimens.

The experimental results obtained for the fibre reinforced composites at *60°C* have been taken into account only until the step observed. The weight gain has been considered constant after this point and equal to the analytical value of the mass at saturation obtained with *(Eqn. 26)* as presented on *Figure 73* for the pure resin specimens, *Figure 74* for the infused E-glass specimens, *Figure 75* for the infused Advantex® specimens and *Figure 76* for the infused HiPer-tex™ specimens. We can observe that the Fick's law does not fit accurately the weight gain results at *60°C*, especially for the infused E-glass and HiPer-tex™ composites. This suggests that the diffusion kinetics may be different for high and low temperatures.

In addition, the experimental results obtained at *80°C* have not been used because this temperature is very close to or higher than the glass transition temperature of the dry materials (*72°C* for the pure resin, *77°C* for the infused E-glass, *76*°C for the infused Advantex® and *82°C* for the infused HiPer-tex™).

It is often noted that the diffusion coefficient *D* depends on the temperature of the environment according to an Arrhenius law. The results obtained for the pure resin, the infused E-glass, Advantex® and HiPertex™ specimens, are presented respectively on *Figure 77*, *Figure 78*, *Figure 79* and *Figure 80*.

The linear fits are not very good, again suggesting that there may be more than one mechanism involved at these different temperatures.

This section provides the first input for a durability model, namely the diffusion coefficients which will allow the water content at any point in the specimen to be calculated.

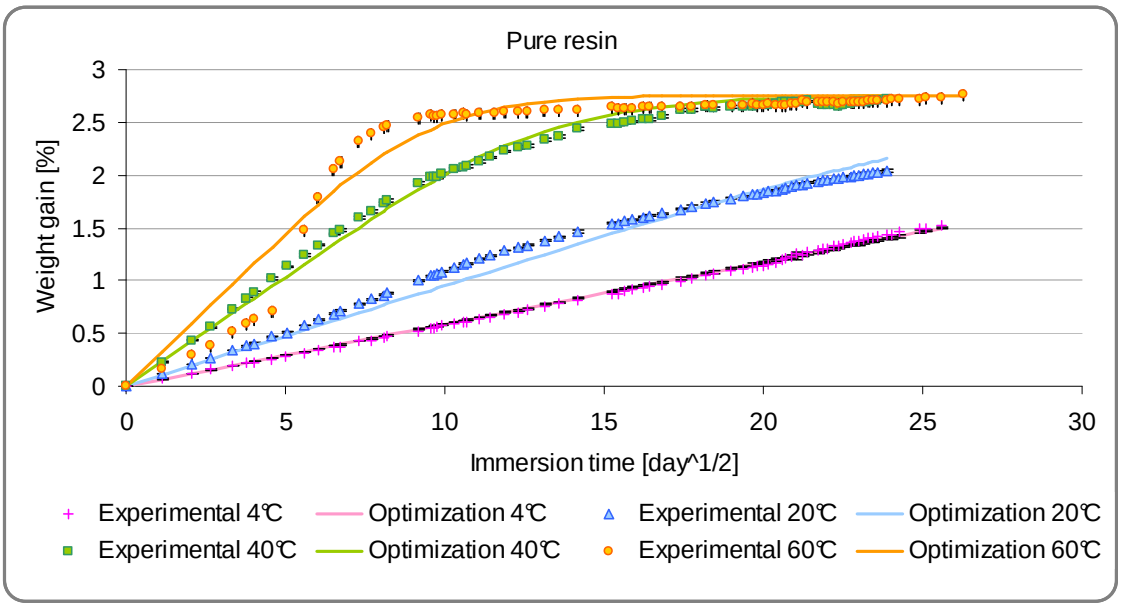

Figure 73. *Comparative curves between experimental data and optimization for pure resin specimens*

Table 6. *Summary of the natural sea water ageing data obtained for pure resin material*

Temperature [°C]	Mean thickness (SD) [mm]	Mean diffusion coefficient D (SD) [mm^2/day]	Mean diffusion coefficient D (SD) [m^2/s]
4	4.99 (0.03)	0.0022 (0.0001)	2.58E-14 (5.79E-16)
20	4.96 (0.06)	0.0058 (0.0002)	6.66E-14 (2.00E-15)
40	4.99 (0.03)	0.0275 (0.0003)	3.18E-13 (3.66E-15)
60	4.96 (0.04)	0.0517 (0.0012)	6.15E-13 (1.33E-14)

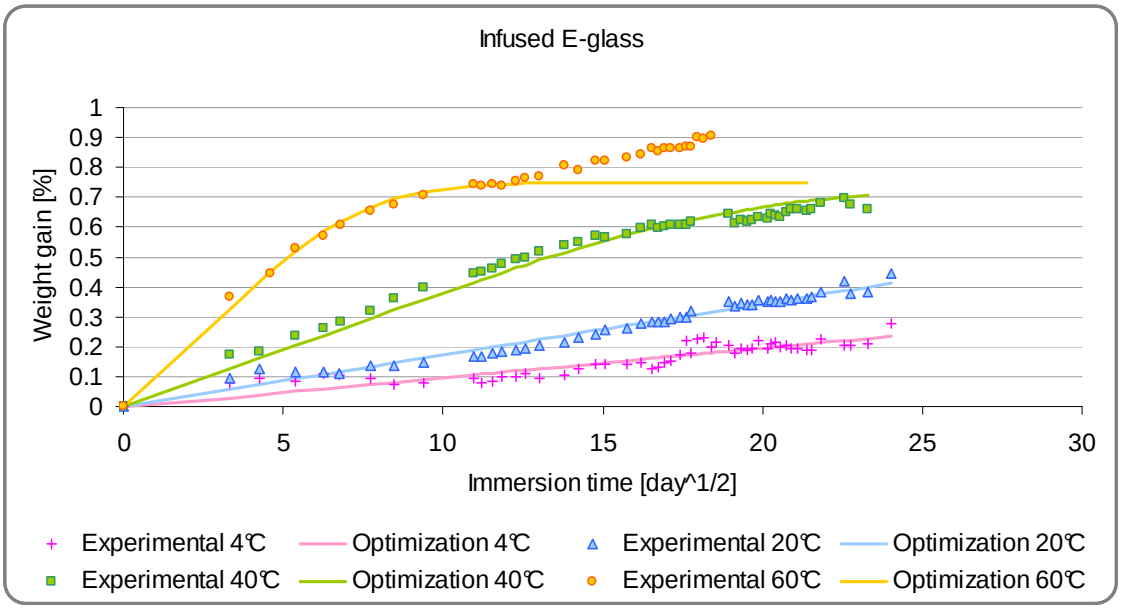

Figure 74. *Comparative curves between experimental data and optimization for infused E-glass specimens*

Table 7. *Summary of the natural sea water ageing data obtained for infused E-glass material*

Temperature [°C]	Mean thickness (SD) [mm]	Mean diffusion coefficient D (SD) [mm²/day]	Mean diffusion coefficient D (SD) [m²/s]
4	5.45 (0.06)	0.0010 (0.0001)	1.16E-14 (8.47E-16)
20	5.50 (0.06)	0.0031 (0.0001)	3.59E-14 (1.34E-15)
40	5.44 (0.04)	0.0150 (0.0009)	1.34E-13 (7.81E-14)
60	5.52 (0.10)	0.1031 (0.0060)	1.19E-12 (6.99E-14)

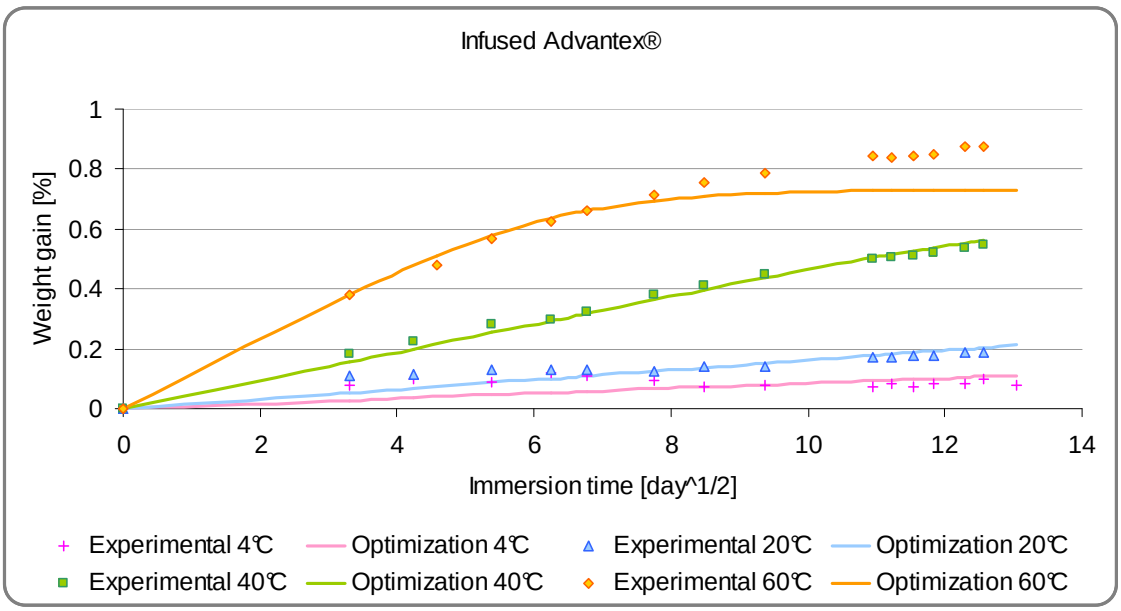

Figure 75. *Comparative curves between experimental data and optimization for infused Advantex® specimens*

Table 8. *Summary of the natural sea water ageing data obtained for infused Advantex® material*

Temperature [°C]	Mean thickness (SD) [mm]	Mean diffusion coefficient D (SD) [mm²/day]	Mean diffusion coefficient D (SD) [m²/s]
4	5.57 (0.11)	0.0008 (0.0002)	9.65E-15 (2.44E-15)
20	5.60 (0.06)	0.0030 (0.0004)	3.50E-14 (4.86E-15)
40	5.45 (0.10)	0.0242 (0.0019)	2.80E-13 (2.20E-14)
60	5.57 (0.10)	0.1501 (0.0181)	1.74E-12 (2.10E-13)

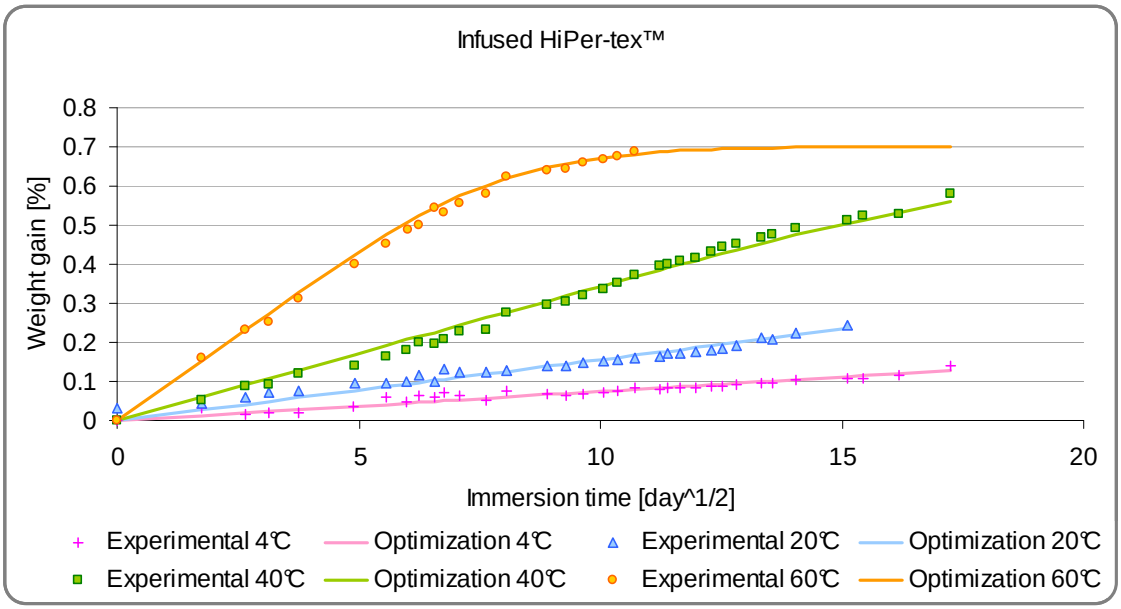

Figure 76. *Comparative curves between experimental data and optimization for infused HiPer-tex™ specimens*

Table 9. *Summary of the natural sea water ageing data obtained for infused HiPer-tex™ material*

Temperature [°C]	Mean thickness (SD) [mm]	Mean diffusion coefficient D (SD) [mm²/day]	Mean diffusion coefficient D (SD) [m²/s]
4	5.26 (0.18)	0.0006 (0.0001)	7.21E-15 (8.01E-16)
20	5.37 (0.09)	0.0029 (0.0008)	2.82E-14 (1.07E-14)
40	5.46 (0.03)	0.0141 (0.0007)	1.63E-13 (7.91E-15)
60	5.47 (0.05)	0.0914 (0.0067)	1.06E-12 (7.74E-14)

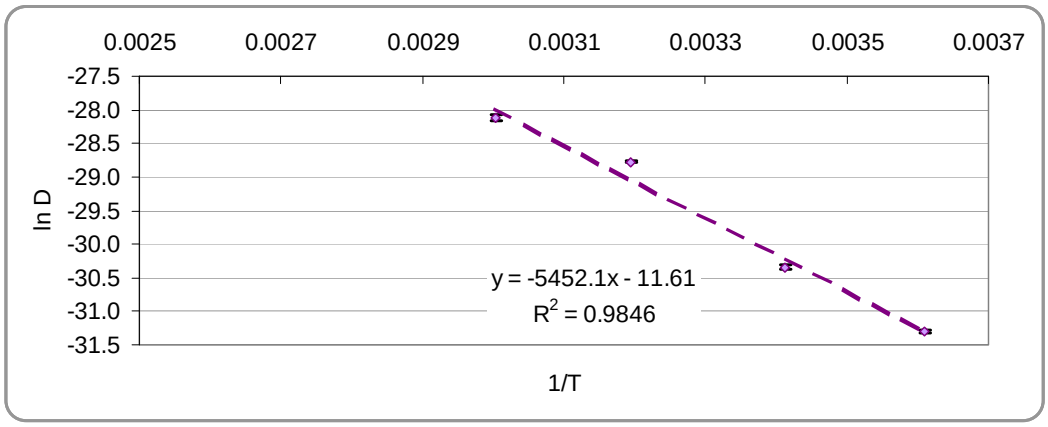

Figure 77. *Graphical view of the Arrhenius law for the pure resin specimens*

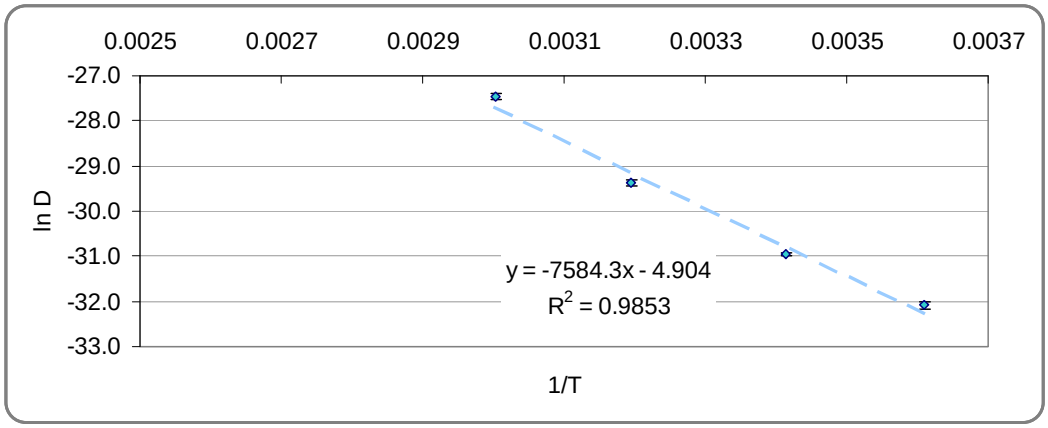

Figure 78. *Graphical view of the Arrhenius law for the infused E-glass specimens*

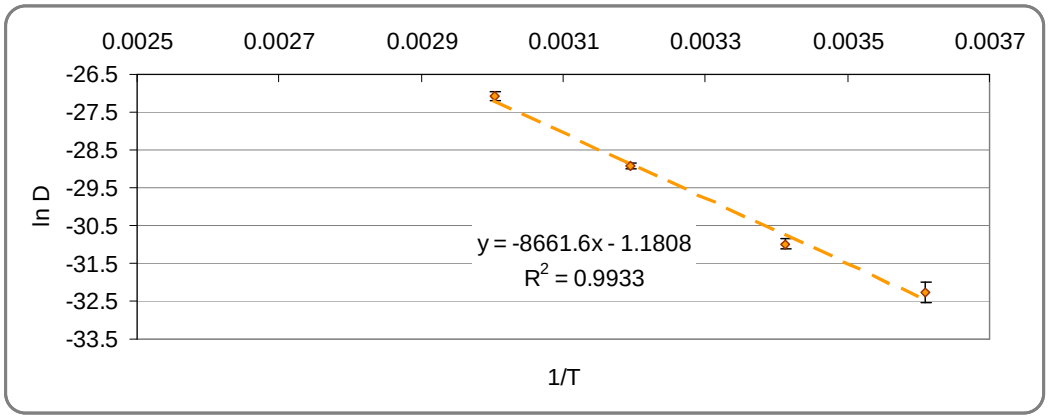

Figure 79. *Graphical view of the Arrhenius' law for the infused Advantex® specimens*

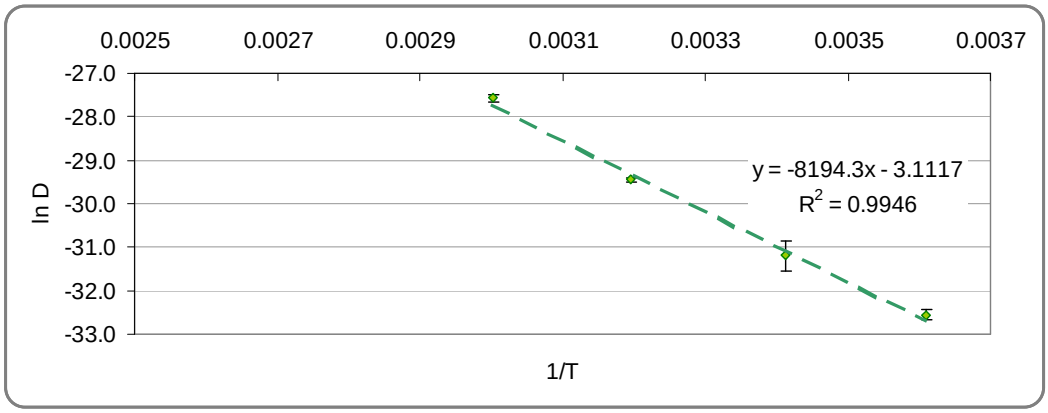

Figure 80. *Graphical view of the Arrhenius law for the infused HiPer-tex™ specimens*

3- Mechanical characterization

For the mechanical characterization quasi-static and fatigue tests have been performed.

3.1- Initial properties of the fibre-reinforced composite materials

3.1.1. Quasi-static properties

Quasi-static tests were performed in order to obtain the initial properties of the material : "CRP" tests in tension and in compression and four-point bending. These tests have been presented previously in *Section 3.3.2, Chapter II*.

a) CRP tests

The experimental results obtained for infused E-glass, Advantex® and HiPer-tex™ composites are presented and compared in order to quantify the influence of the fibre type in this loading case.

The first parameters used to compare the materials and quantify the influence of the fibre type, are the failure stresses in tension and in compression, which can be obtained directly (*Table 10*). A second value is the Young's modulus in the main reinforcement direction defined by the slope of the stress-strain curve between *0* and *2.8 kN* (*Figure 81*). These moduli, summarized in *Table 11*, vary according to the maximum load applied to the specimens. So we can compare their initial values for each type of composite and we can also observe their evolution during the test.

Table 10. *Experimental data for failure stress in tension and in compression for the three infused composite materials*

Failure stress σ_{fail}	σ_{fail} in tension (SD) $[MPa]$	σ_{fail} in compression (SD) $[MPa]$
E-glass	750.4 (23.8)	472.5 (10.8)
Advantex®	798.1 (0.4)	431.3 (14.8)
HiPer-tex™	891.7 (49.4)	506.7 (10.6)

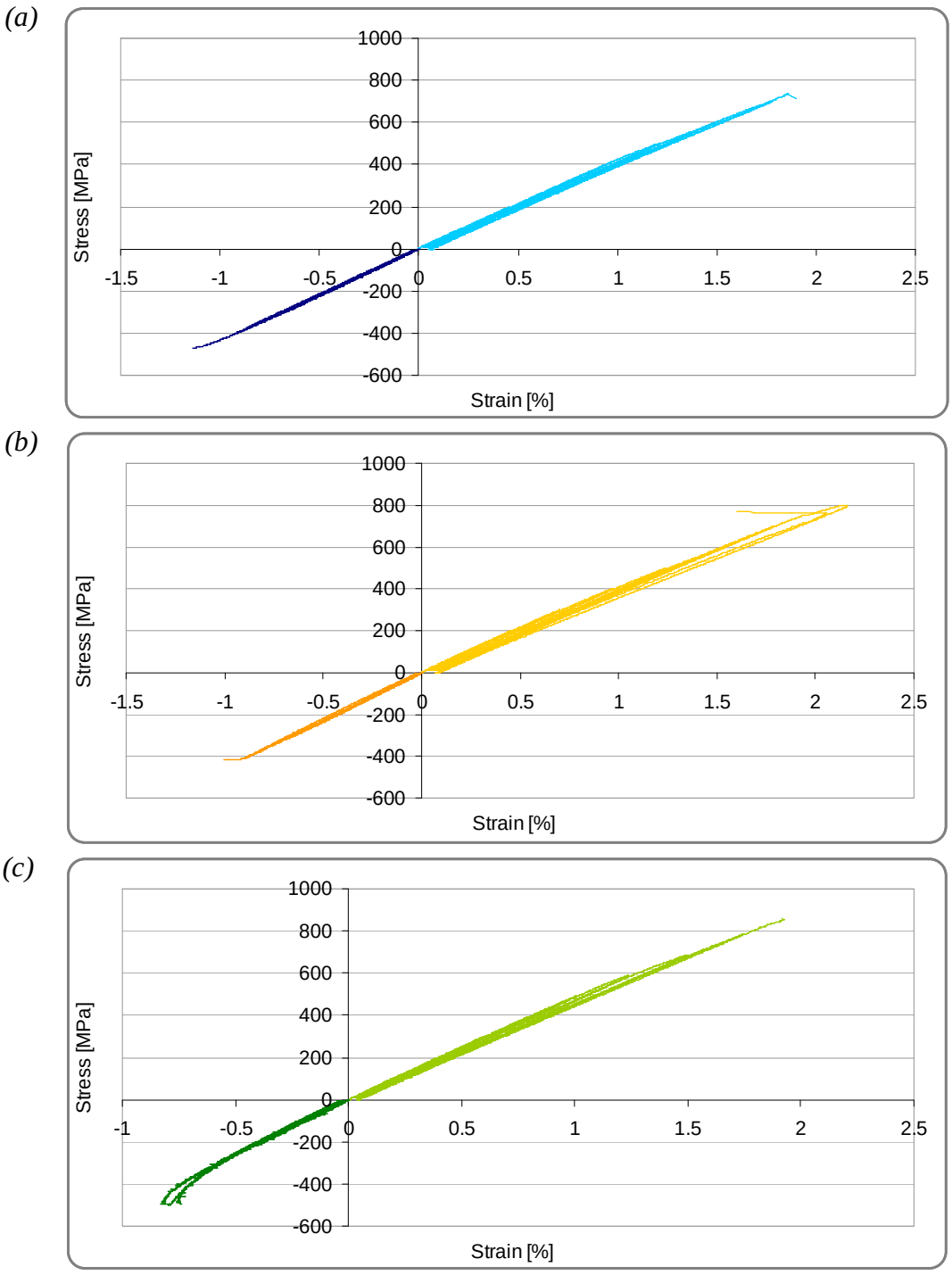

Figure 81. *Stress-strain curves obtained in tension or compression during "CRP" tests : a) Infused E-glass specimen, b) Infused Advantex® specimen, c) Infused HiPer-tex™ specimen*

Table 11. *Experimental data for the initial Young's modulus for the three infused composite materials*

Initial Young's modulus E_I	E_I in tension (SD) $[GPa]$	E_I in compression (SD) $[GPa]$
E-glass	46.9 (0.8)	45.2 (2.1)
Advantex®	45.0 (0.4)	46.4 (0.8)
HiPer-tex™	55.9 (4.1)	48.8 (1.6)

Tensile and compression slopes are quite similar but the strengths are very different for the three materials. Compression strength is significantly lower than tensile strength for this specimen configuration. For infused E-glass composites, the failure stress in compression is *37 %* lower than the failure stress in tension. For the infused Advantex® composite, the difference is equal to *46 %* and for the infused HiPer-tex™ composite, this value is almost *43 %*.

When we compare the different materials, we can observe that their experimental strengths in tension or in compression are quite similar. The difference between infused E-glass and Advantex® is equal to *6 %* in tension and *8 %* in compression. Between infused E-glass and HiPer-tex™, this variation is more important and is equal to *19 %* in tension and *7 %* in compression. It is very interesting to note however, that the low ILSS values measured for Advantex®, suggesting a material quality problem, do not affect the tensile strength, which is higher than that measured on E-glass. Compression values are lower than those of E-glass composites however. This suggests that it may be the fibre/resin interface in the mat layer which is not optimised, as this would not affect tensile behaviour but influence local support to fibres in compression.

As mentioned previously, the tensile and compression slopes are quite similar for each material. The differences observed between tension and compression are only *4 %* for infused E-glass, *3 %* for Advantex® reinforcement. For the infused HiPer-tex™ composite this difference is more important and equal to *13 %*. In addition, the initial values of the tensile modulus are quite similar from one material to another. Between infused E-glass and Advantex® modulus, the difference is equal to *4 %* in tension and *3 %* in compression. Between E-glass and HiPer-tex™ reinforcement, the difference is equal to 19 % in tension and *8 %* in compression. The HiPer-tex™ fibres have a higher tensile modulus according to the fibre datasheets (*90* compared to *79 GPa*), but this improvement is not measured in compression.

There is a small change in initial modulus E_I and modulus before final failure E_F for all of the three materials. *Figure 82* and *Table 12* show the results, which are dominated by the fibre response in these tests. For the infused E-glass specimens, the modulus values vary only by about *5 %* during the cycles in tension and *1 %* in compression. For the infused Advantex® specimens, the variation is equal to *7 %* in tension and less than *1 %* in compression. The composite reinforced with HiPer-tex™ fibre shows the most important variation between initial and final modulus, *8 %* in tension and *9 %* in compression.

These experimental values of stiffness are dominated by the fibre volume fraction. Simple law-of-mixture expressions *(Eqn. 27)* [133] can be used to estimate them, (*Table 13*) according to the values of modulus for the fibres and the resin and the fibre volume fraction.

$$E_{comp} = E_{fibre} \cdot V_{fibre} + E_{matrix} \cdot (1 - V_{fibre}) \qquad \textbf{(Eqn. 27)}$$

where E_{comp}, E_{fibre} and E_{matrix} are respectively the Young's modulus of the composite material, of the fibre (taken to be *79 GPa* for the E-glass fibres, *82 GPa* for the Advantex® fibres and *90 GPa* for the HiPer-tex™ fibres) and of the resin (taken to be *3 GPa*) and V_{fibre} is the measured fibre volume fraction.

The calculated values are quite close to measured values (from *– 3.4 %* for the infused Advantex® composite to *+ 6.3 %* for the infused HiPer-tex™ composite). It should be noted however, that the expression used neglects the fact that a part of the fibres are oriented

off-axis (mat and *90°* fibres). If *100 g/m²* of the *1250 g/m²* reinforcement makes a reduced contribution to axial modulus one might anticipate a drop in the estimated modulus of up to *8 %*.

However, the strength values determined on these specimens are lower than would be expected from simple "law-of-mixtures" approach for an ideal unidirectional composite *(Eqn. 28)*. *Table 14* shows the nominal fibre strengths and the calculated composite tensile strengths.

$$\sigma_{comp}=\sigma_{fibre}\cdot V_{fibre}+\sigma_{matrix}\cdot(1-V_{fibre}) \qquad \textbf{(Eqn. 28)}$$

where σ_{comp}, σ_{fibre} and σ_{matrix} are respectively the tensile strength of the composite material, of the fibre (taken to be *2 000 MPa* for the E-glass fibres, *2 400 MPa* for the Advantex® fibres and *2 850 MPa* for the HiPer-tex™ fibres) and of the resin (taken to be *68 MPa*) and V_{fibre} is the fibre volume fraction.

The calculated composite strengths are higher than measured values but there may be a number of reasons for this. First, the fibres are stitched, which can introduce premature damage during loading. Second, the laminate is not completely unidirectional, about *8 %* by weight of *90°* and mat fibres are attached to each layer, and damage in these layers may initiate early failure. Third, manufacturing defects may reduce this value. Nevertheless to check this a few tests were performed on parallel-sided specimens with and without end tabs. *Figure 83* shows the test set-up, composite end-tabs were bonded under vacuum.

The results without and with end-tabs indicated respectively a failure in tension at around *700 MPa* and *1 100 MPa* (*Table 15*). The dog-bone specimens give values intermediate between the tabbed and untabbed specimens.

(a)

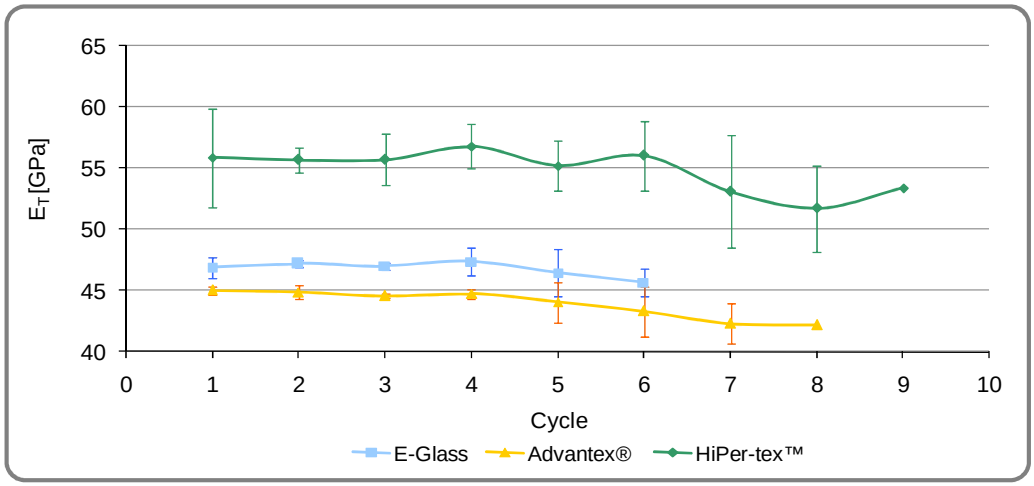

(b)

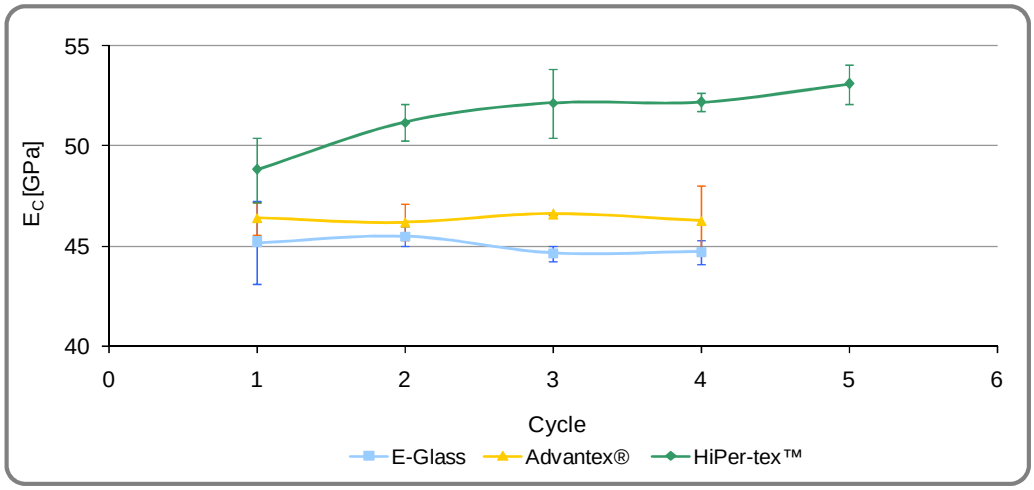

Figure 82. *Evolution of the Young's modulus of the specimens during the "CRP" tests : a) tests in tension, b) tests in compression*

Table 12. *Experimental data for the initial and final Young's modulus for the three infused composite materials*

Young's modulus in tension	Initial E_I (min-max range) [*GPa*]	Final E_F (min-max range) [*GPa*]
E-glass	46.9 (0.8)	44.4 (0.6)
Advantex®	45.0 (0.4)	41.7 (0.7)
HiPer-tex™	55.9 (4.1)	51.3 (2.9)
Young's modulus in compression		
E-glass	45.2 (2.1)	44.7 (0.6)
Advantex®	46.4 (0.8)	46.3 (1.8)
HiPer-tex™	48.8 (1.6)	53.11(1.0)

Table 13. *Summary of the experimental and theoretical data of Young's moduli for infused E-glass, Advantex® and HiPer-tex™ composites*

Young's modulus in tension	V_f (by volume) [%]	Experimental E_I (min-max range) [*GPa*]	Theoretical E_I [*GPa*]	Difference [%]
E-glass	55.1	46.9 (0.8)	44.9	+ 4.5
Advantex®	55.7	45.0 (0.4)	47.0	- 4.3
HiPer-tex™	57.5	55.9 (4.1)	53.0	+ 5.5

Table 14. *Summary of the experimental and theoretical data of tensile strength for infused E-glass, Advantex® and HiPer-tex™ composites*

Tensile strength	Nominal fibre strength [*MPa*]	Experimental strength (min-max range) [*MPa*]	Calculated ideal composite strength [*MPa*]	Difference [%]
E-glass	2 000	750.4 (23.8)	1 132.5	- 33.7
Advantex®	2 400	798.1 (0.4)	1 366.9	- 41.6
HiPer-tex™	2 850	891.7 (49.4)	1 667.7	- 46.5

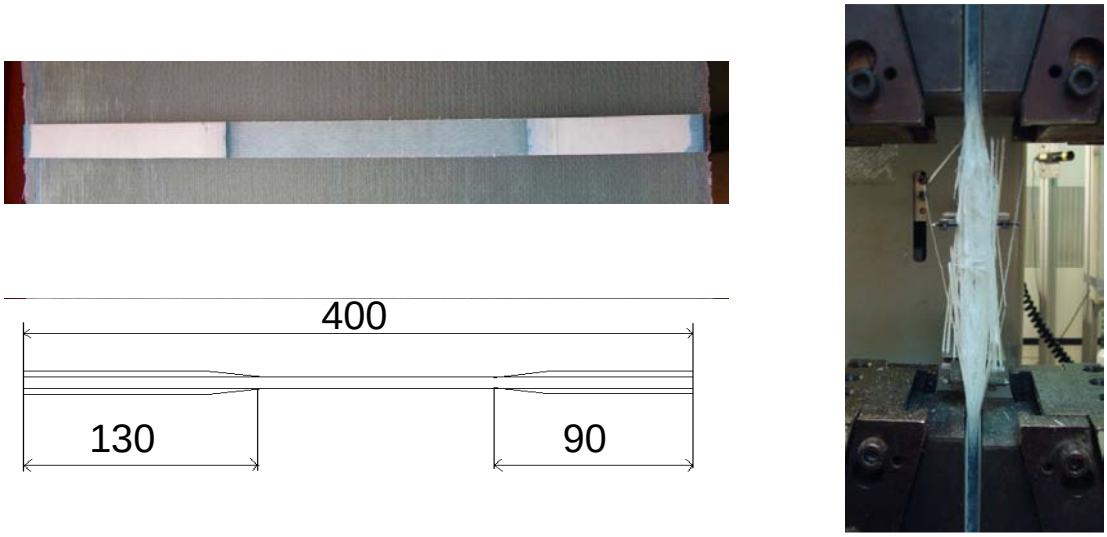

Figure 83. *Tensile specimen and sample after failure*

Table 15. *HiPer-tex™ tensile strengths*

Specimen type	Tensile strength $[MPa]$
CRP dog-bone	891
Parallel (no tabs)	701 758 663
Mean (SD)	***707 (48)***
Parallel (with end-tabs)	1 099 1 137
Mean (SD)	***1 118 (27)***

b) Flexural tests

Quasi-static flexural tests have been performed in order to determine the failure stresses in four-point bending of the different composite materials. These values of failure stresses will be used in the study of the effect of fatigue to define the cyclic stress levels.

The results obtained for the failure stresses in four-point flexure are summarized in *Figure 84* and *Table 16*. Here, the infused Advantex® composite shows lower results than the two other materials, but failure is in compression so this is consistent with the previous results. The difference between the composite reinforced with E-glass and Advantex® is equal to *24 %* in terms of stress. This suggests that the ILSS tests provides a useful check on properties.

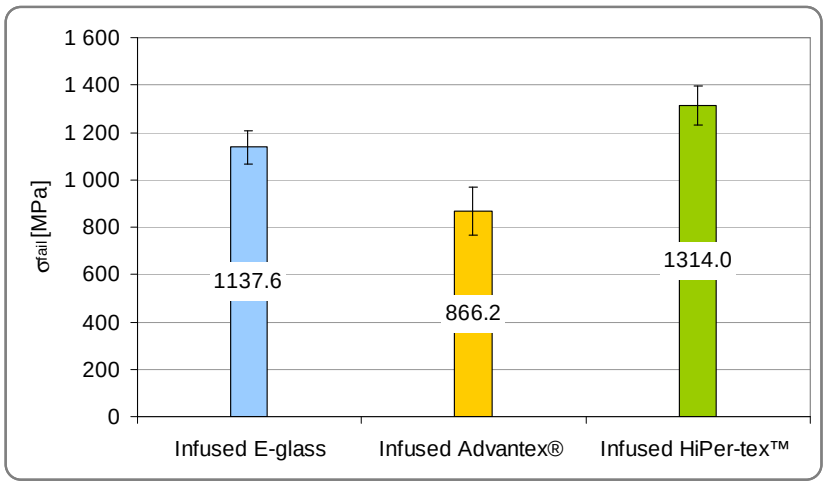

Figure 84. *Comparison of the failure stresses in flexure for the three composite materials*

Table 16. *Experimental data for the failure stresses in flexure for the three infused composite materials*

Failure stress σ_{fail}	σ_{fail} (SD) $[MPa]$
E-glass	1137.6 (69.3)
Advantex®	866.2 (102.4)
HiPer-tex™	1314.0 (83.6)

3.1.2. Fatigue behaviour

Four-point bending was selected for cyclic tests. These flexural fatigue tests involved cycling specimens with a constant stress level until failure. The corresponding load applied to the specimen was estimated by using a formula *(Eqn. 29)* which takes into account the dimensions of the specimen, the failure stress of the material in four-point bending and the stress level applied.

$$F = \frac{4}{3} \cdot \frac{\sigma_{fail} \cdot R\sigma \cdot b \cdot h^2}{L} \qquad \textbf{(Eqn. 29)}$$

The reference stress level was *60 %*, the reference frequency was *2 Hz* and the ratio between the minimal and the maximal stress *R* was equal to *0.1* unless otherwise stated. The stress level *Rσ* depends on the failure stress of each composite material. The main stress levels used are summarized in *Table 17*.

The flexural fatigue tests have been carried out in air and in natural circulating sea water on *31* infused E-glass specimens (*12* in air and *19* in natural sea water), *19* infused Advantex® specimens in natural sea water (given the results from the quality control and static tests this material was less extensively studied) and *29* infused HiPer-tex™ specimens (*10* in air and *19* in natural sea water), at *9* different loading levels ($45\% \leq R\sigma \leq 85\%$). All the experimental data are summarized in *Annex 6*.

The first, and the easiest, parameter to determine is the fatigue life N_f, the second parameter to note is the evolution of the damage.

Table 17. *Summary of the experimental data of failure stress and stress levels for the three composite materials*

	Infused E-glass	Infused Advantex®	Infused HiPer-tex™
Failure stress σ_{fail} (SD) $[MPa]$	**1 137.6 (69.3)**	**866.2 (102.5)**	**1 314.0 (83.6)**
Applied stress for $R\sigma=40\%$	455.0	346.5	525.6
Applied stress for $R\sigma=50\%$	568.8	433.1	657.0
Applied stress for $R\sigma=60\%$	**682.6**	**519.7**	**788.4**
Applied stress for $R\sigma=70\%$	796.3	606.3	919.8
Applied stress for $R\sigma=80\%$	910.1	693.0	1 051.2

a) Fatigue life in air and in natural circulating sea water

These tests allow us to draw three type of curves. The first one is a classical S-N curve which represents the stress level $R\sigma$ versus the number of cycles N_f. The second one represents the applied stress σ in *MPa* as a function of the logarithm of the fatigue life N_f. The third one represents the stress level $R\sigma$ versus the logarithm of the fatigue life N_f.

With these curves we will be able to compare the influence of the reinforcement as a function of the environment. In addition, we will be able to observe and quantify the influence of the environment on the fatigue life for each material. All the experimental data are summarized in *Annex 6* for the three infused composite specimens.

- Stress level versus fatigue life

The first curves obtained are classical S-N curves, which represent the fatigue life N_f of the specimen on the abscissa and the stress level $R\sigma$ on ordinate (*Figure 85* and *Figure 86*).

A number of equations have been proposed to characterise the S-N curves of a composite, as discussed previously in *Section 2.2.2* of *Chapter I*. These equations are derived using the concept of fatigue modulus and a failure criterion. One such model describes the number of cycles to failure N_f as a function of the applied stress level $R\sigma$ and two material constants B and d.

$$N_f = \left[B \cdot (1 - R\sigma)\right]^{1/d} \qquad \textbf{(Eqn. 30)}$$

In order to define the two material constants B and d, the experimental results, represented by the points on the *Figure 85* and *Figure 86*, and the *(Eqn. 30)* are used in an optimization routine in *Matlab*© using the least squares method (*Section 4.1*, *Chapter II*) represented with the dashed lines. So, these constants can be defined as a function of the material, infused E-glass, Advantex® or HiPer-tex™, in a given environment, air or natural circulating sea water. This set of constants, summarized in *Table 18*, will be integrated in a numerical model in order to predict the behaviour of a composite material.

By comparing the results obtained, we can see that for a given number of cycles before failure, especially at high cycles, the corresponding normalized stress level is higher for the infused Advantex® composite than for the HiPer-tex™ composite, which is higher than the infused E-glass composite in natural circulating sea water (*Figure 85a*). In air (*Figure 85b*), the results are better for the infused HiPer-tex™ composite than for the infused E-glass composite. However, this is a misleading presentation, as the significantly lower failure stress of the Advantex® material means that much lower stresses are applied.

When we compare the results obtained for one composite in different environments, we can see that for a given number of cycles before failure, the corresponding stress level is reduced in natural sea water compared to in air, both for infused E-glass specimens (*Figure 86a)* and infused HiPer-tex™ specimens (*Figure 86b*).

(a)

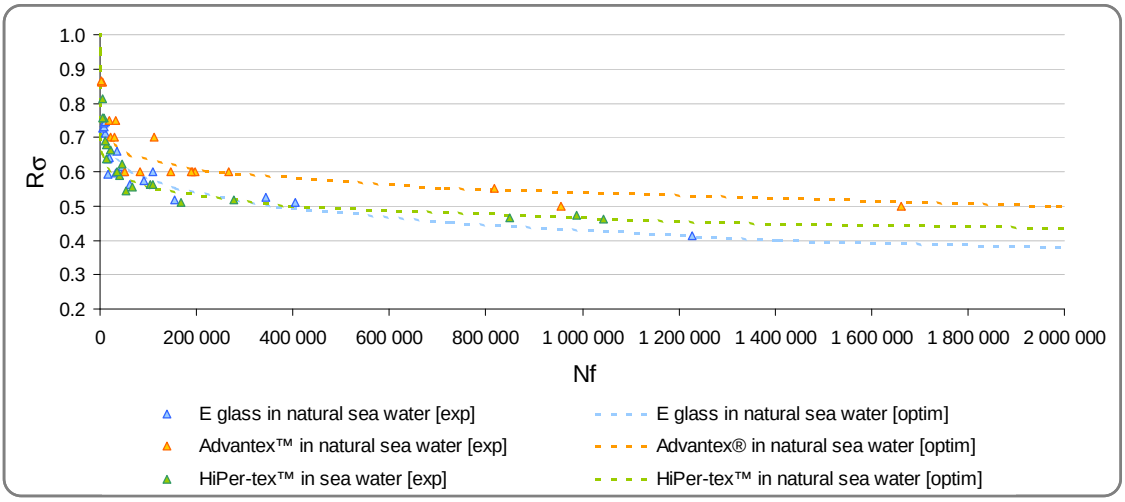

(b)

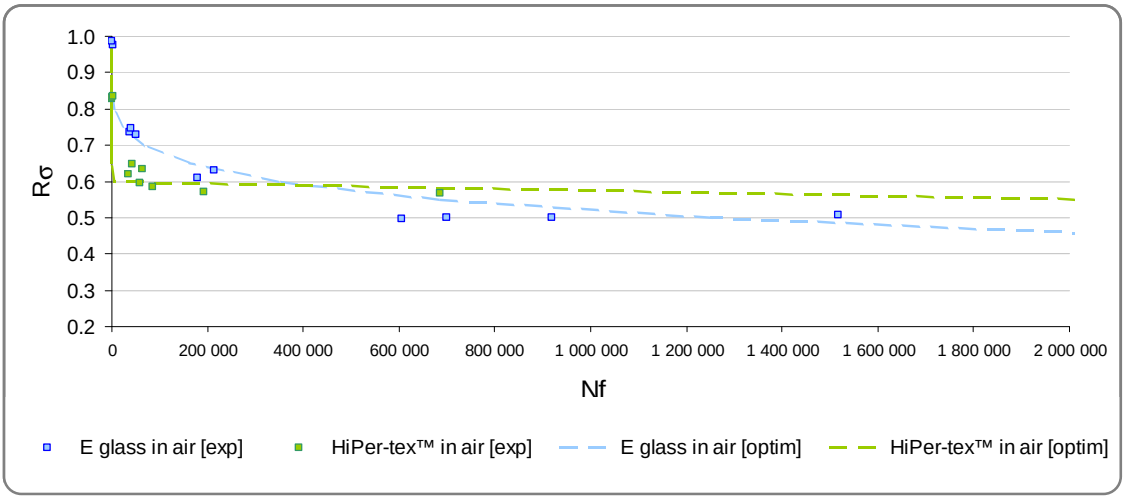

Figure 85. *Comparative curves for infused E-glass, Advantex® and HiPer-tex™ specimens, Rσ versus Nf : a) in natural circulating sea water, b) in air*

(a)

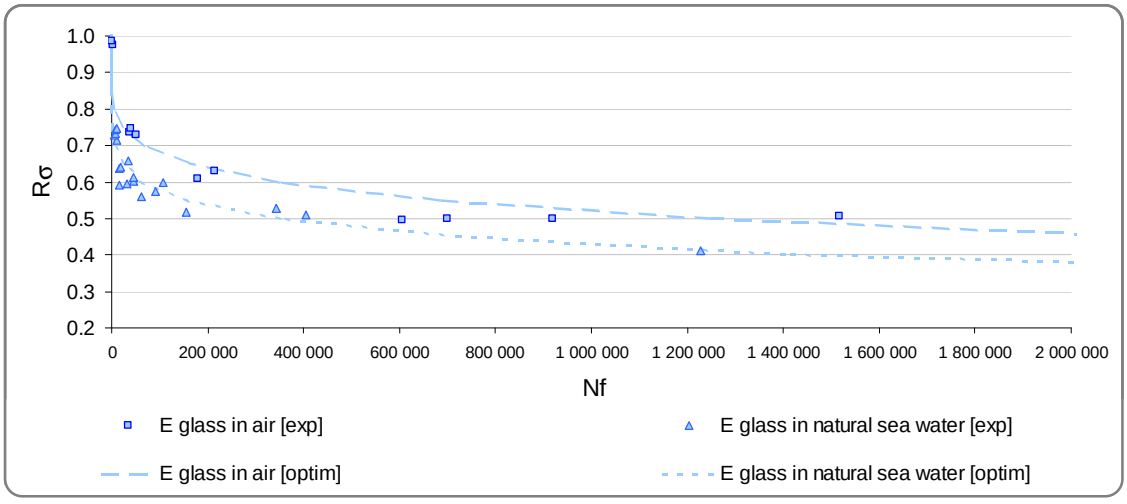

(b)

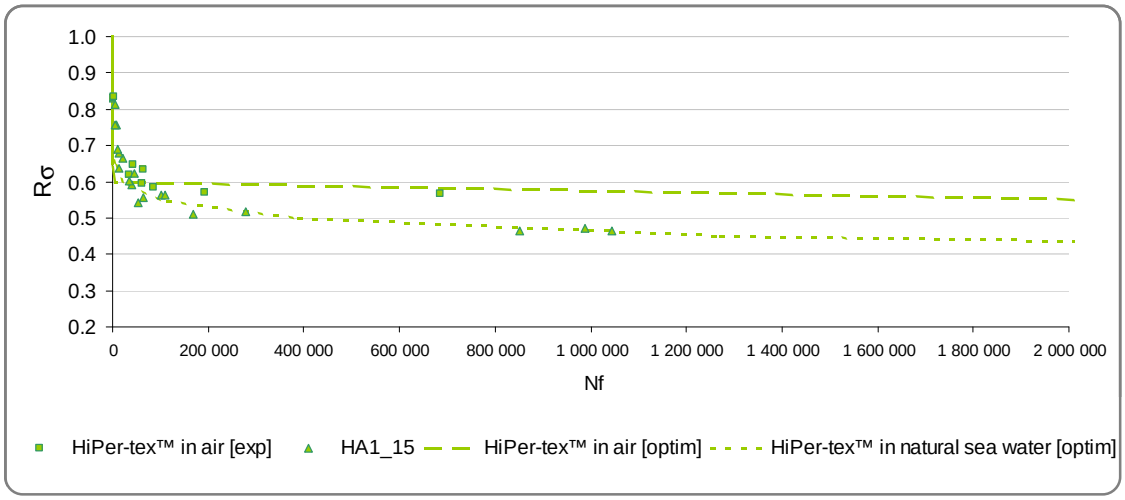

Figure 86. *Comparative curves in air and in natural circulating sea water, Rσ versus Nf : a) infused E-glass specimens, b) infused HiPer-tex™ specimens*

Table 18. *Material constants of infused E-glass, Advantex® and HiPer-tex™ composite in air and in natural circulating sea water*

Material constants *B* and *d*		In air	In natural circulating sea water
Infused E-glass specimens	B	23.3046	10.7801
	d	0.1749	0.1319
Infused Advantex® specimens	B		8.8088
	d		0.1023
Infused HiPer-tex™ specimens	B	2.9724	5.5312
	d	0.0200	0.0792

- Applied stress versus the logarithm of fatigue life

The second type of curve represents the stress applied to the specimen σ on the ordinate and the logarithm of the fatigue life N_f on abscissa (*Figure 87* and *Figure 88*).

This set of experimental curves allows us to quantify the influence of the fibre type, E-glass, Advantex® and HiPer-tex™, in fatigue in natural circulating sea water. So we can see that the fibre type has an important influence on the behaviour of the composite material. For a given applied stress, the fatigue life is shorter for the infused Advantex® composite than for the two other composite materials. However, given the low ILSS values for this material it may be that higher values could be obtained if manufacturing is optimised. This point is discussed in *Chapter V*.

This plots clearly indicate an effect of test in natural sea water for E-glass but not for HiPer-tex™.

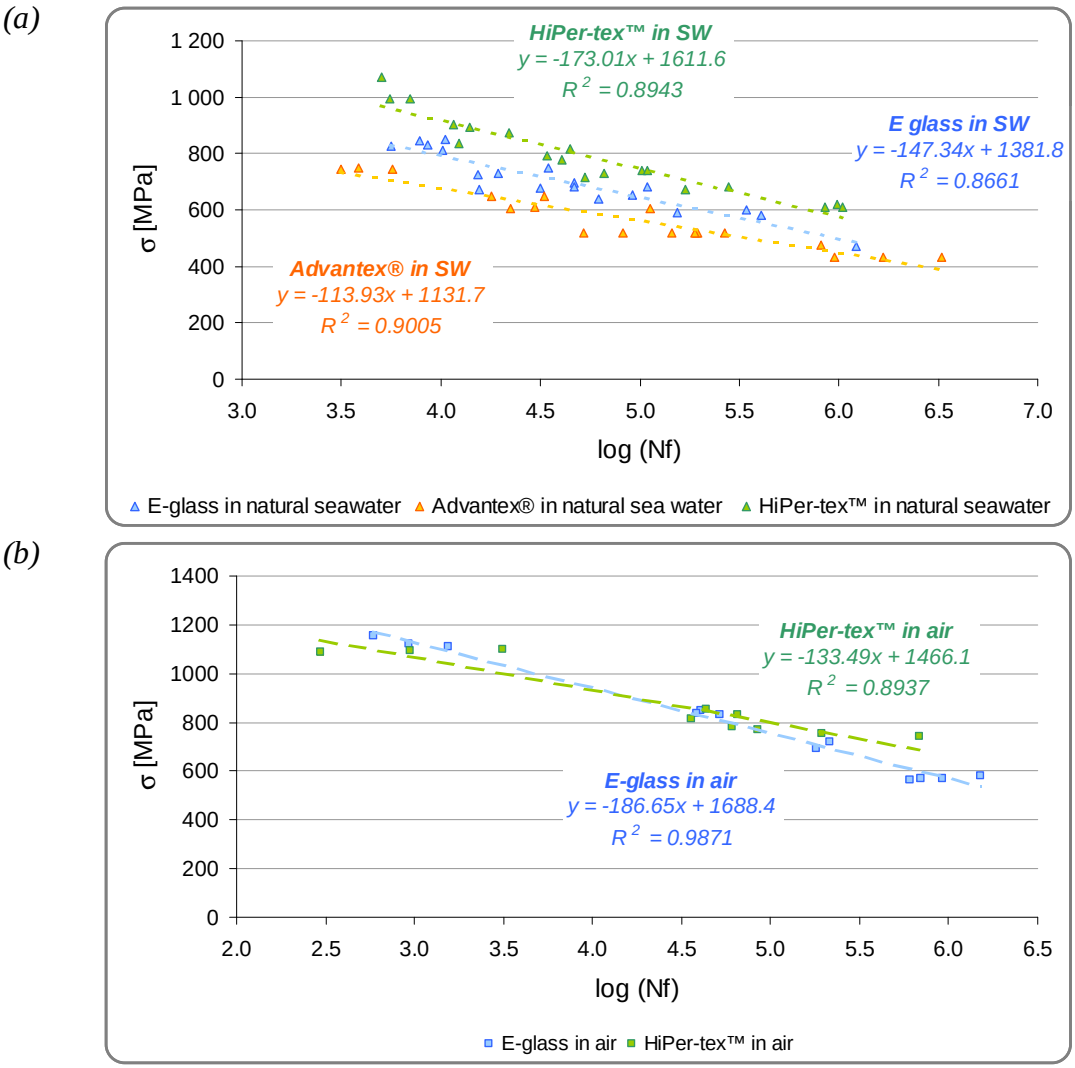

Figure 87. *Comparative curves for infused E-glass, Advantex® and HiPer-tex™ specimens, σ versus log(Nf) : a) in natural circulating sea water, b) in air*

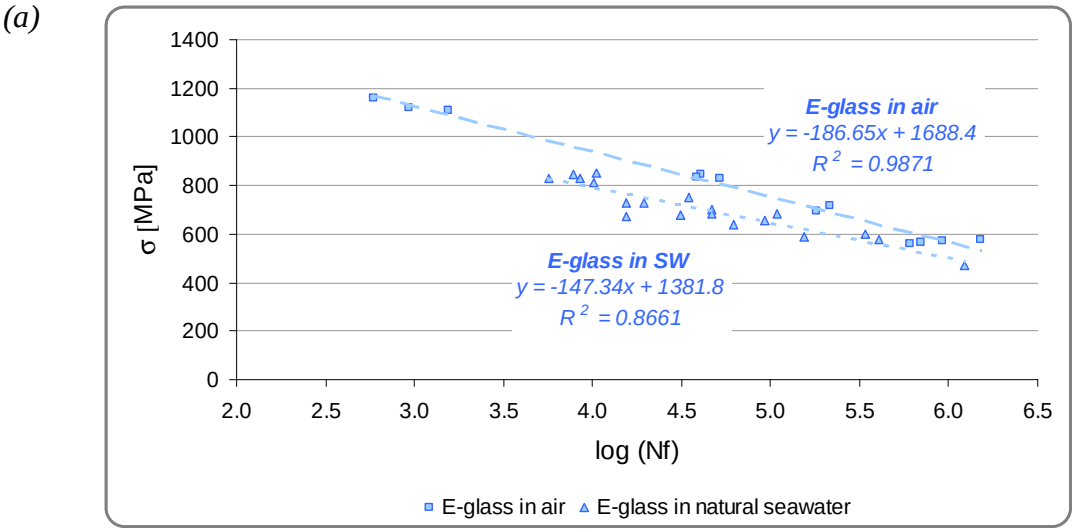

(b)

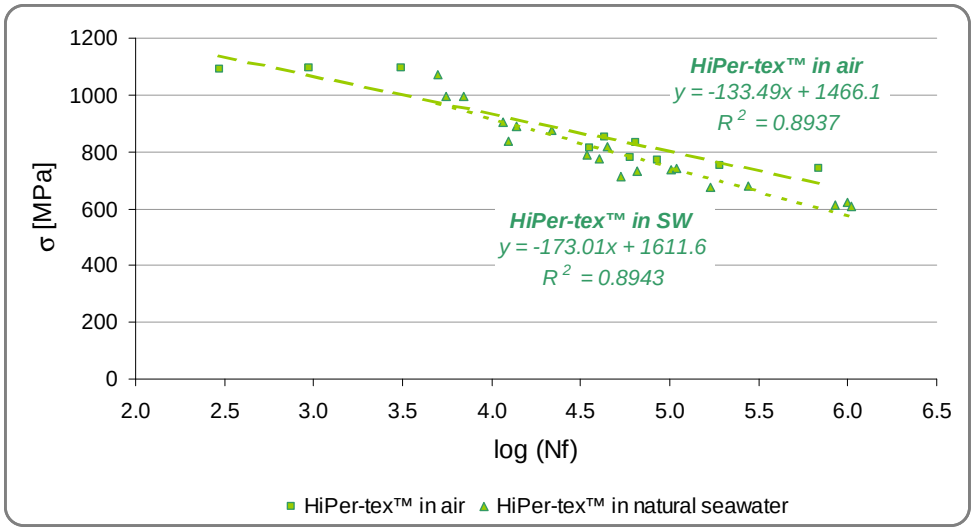

Figure 88. *Comparative curves in air and in natural circulating sea water, σ versus Nf : a) infused E-glass specimens, b) infused HiPer-tex™ specimens*

- Stress level versus the logarithm of fatigue life

The third type of curve represents the stress level applied to the specimen $R\sigma$ in ordinate and the logarithm of the fatigue life N_f in abscissa (*Figure 89* and *Figure 90*). These curves are the normalized form of the ones presented previously.

By observing the results, we can see that the slopes obtained for the infused E-glass, Advantex® and HiPer-tex™ specimens are quite similar in natural circulating sea water.

In addition when we compare the curves presented on *Figure 87* and those presented on *Figure 89*, we can see that for a given applied stress the infused Advantex® specimens seem to have a shorter fatigue life than infused E-glass and HiPer-tex™ specimens, but in terms of relative applied stress level, its fatigue life is longer than those of the infused E-glass and HiPer-tex™ specimens.

(a)

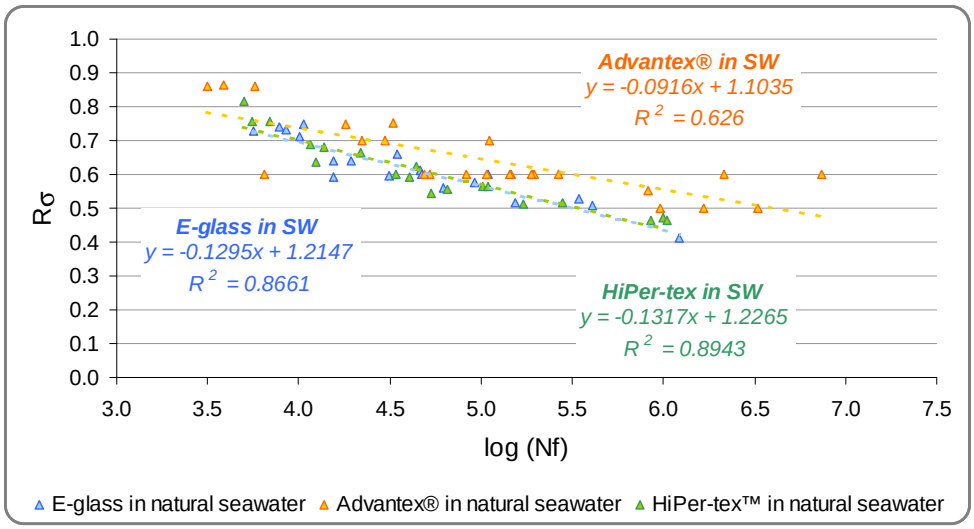

(b)

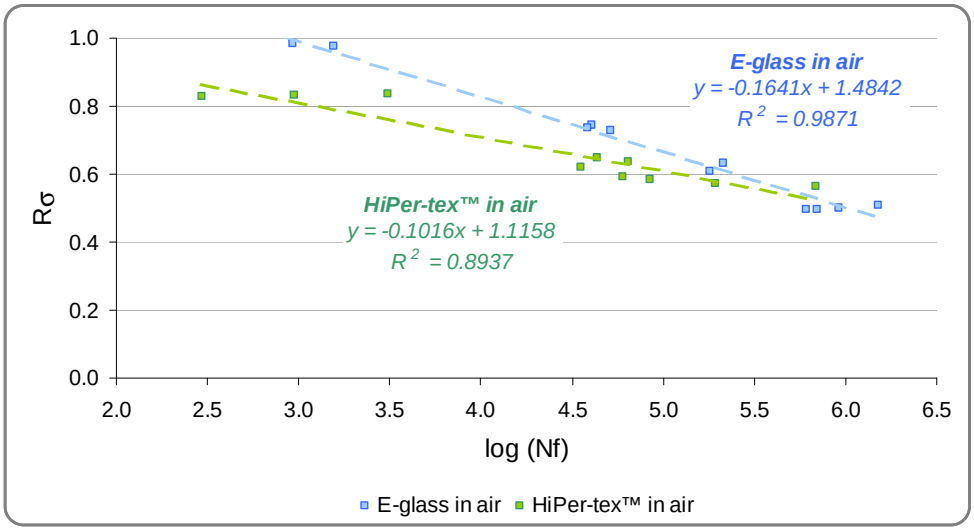

Figure 89. *Comparative curves for infused E-glass, Advantex® and HiPer-tex™ specimens, Rσ versus log(Nf) : a) in natural circulating sea water, b) in air*

(a)

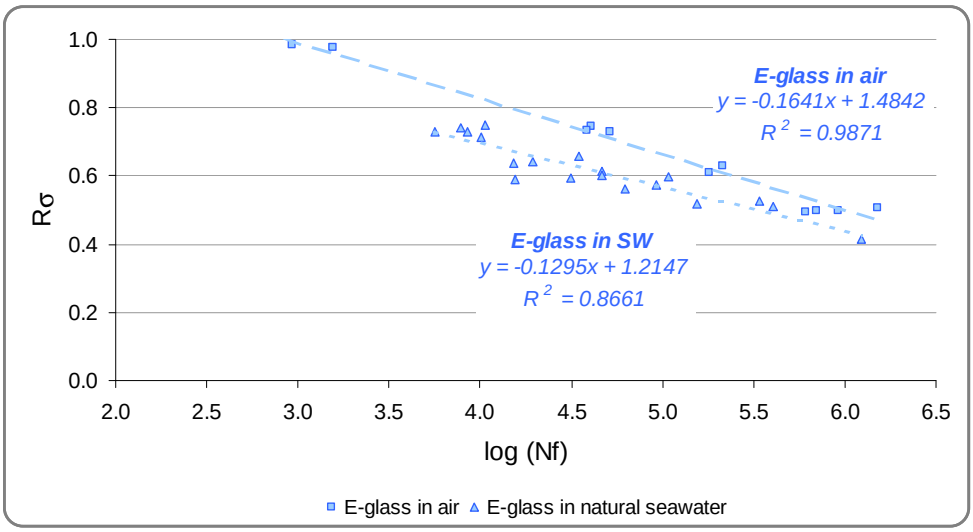

(b)

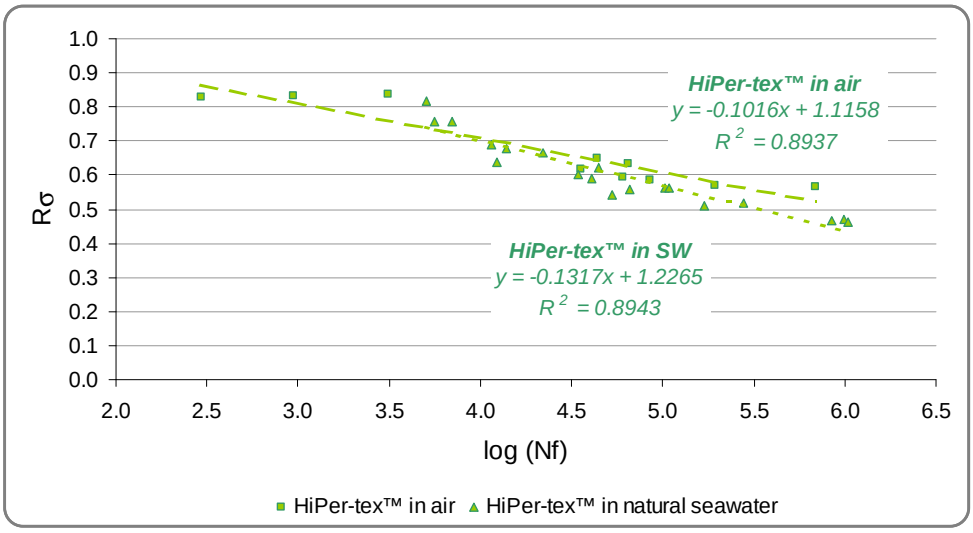

Figure 90. *Comparative curves in air and in natural circulating sea water, Rσ versus Nf : a) infused E-glass specimens, b) infused HiPer-tex™ specimens*

b) Evolution of the damage in air and in natural circulating sea water

One indicator of the evolution of the damage during the fatigue life is given by recording the displacement of the upper loading points throughout the fatigue test. This measured displacement includes both local movements (indentation at the loading points, which will be discussed below in *Section 3.4.3*) and global movements caused by distributed damage within the specimen. It may also include movements due to creep. The latter were not studied in detail, as it was assumed that the unidirectional fibres dominated the response and these do not creep at these low temperatures. A constant load test was performed at *60 %* of failure stress (*i.e. 2 800 N*), the results are presented on *Figure 91*.

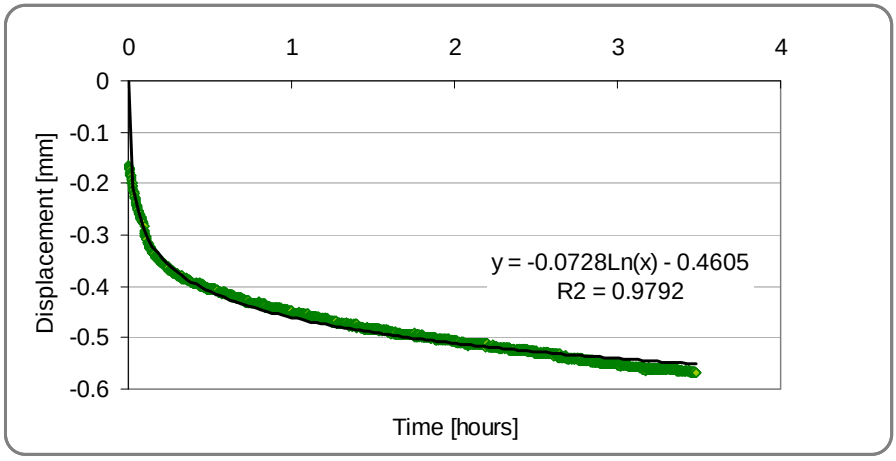

Figure 91. *Creep test plot for infused HiPer-tex™ specimen*

When the ratio of the applied load divided by the displacement is plotted as a function of the ratio number of cycles/fatigue life, we obtain a curve which describes the evolution of the damage. With these curves, we are able to compare the influence of the reinforcement as a function of the environment (air or natural circulating sea water). In addition, an analytical formulation of these experimental curves has been determined in order to define these behaviours in a numerical model.

- Experimental results

The experimental curves are presented on *Figure 92* and *Figure 93*. *Figure 92* shows the influence of the reinforcement in a given environment (air or natural circulating sea water) and *Figure 93* shows the influence of the environment on a given composite material (reinforced with E-glass or HiPer-tex™) .

For each composite material and each environment, two curves are represented. The dark coloured one is for a specimen which has supported a high stress level (HSL with $R\sigma$ varying between *0.75* and *0.83*) and the light coloured one is for a specimen which has supported a lower stress level (LSL with $R\sigma$ varying between *0.51* and *0.60*). We can see that whatever the stress level applied and the environment, the three composite materials have a similar behaviour. There is a strong drop of the ratio *F/disp* at the beginning of the life, which is caused by the settling-in of the specimen and the appearance of longitudinal cracks, then a long gradual slope until the last drop beyond *80 %* of the lifetime, which represents the final failure.

By comparing the measured displacements obtained during these fatigue tests with those obtained during creep tests, we can note that the displacement due to the time-dependent behaviour is not significant (*Figure 94*).

(a)

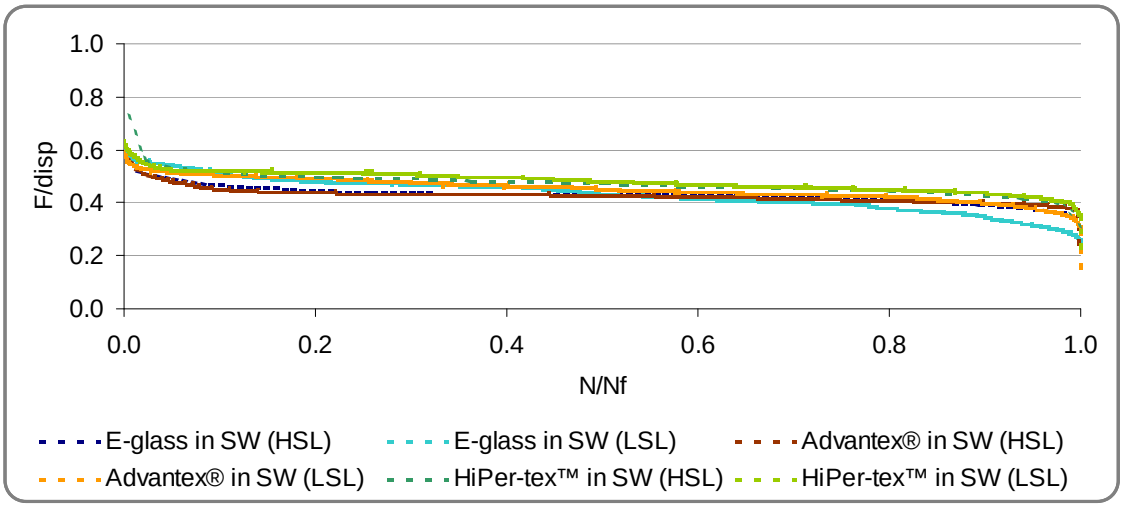

(b)

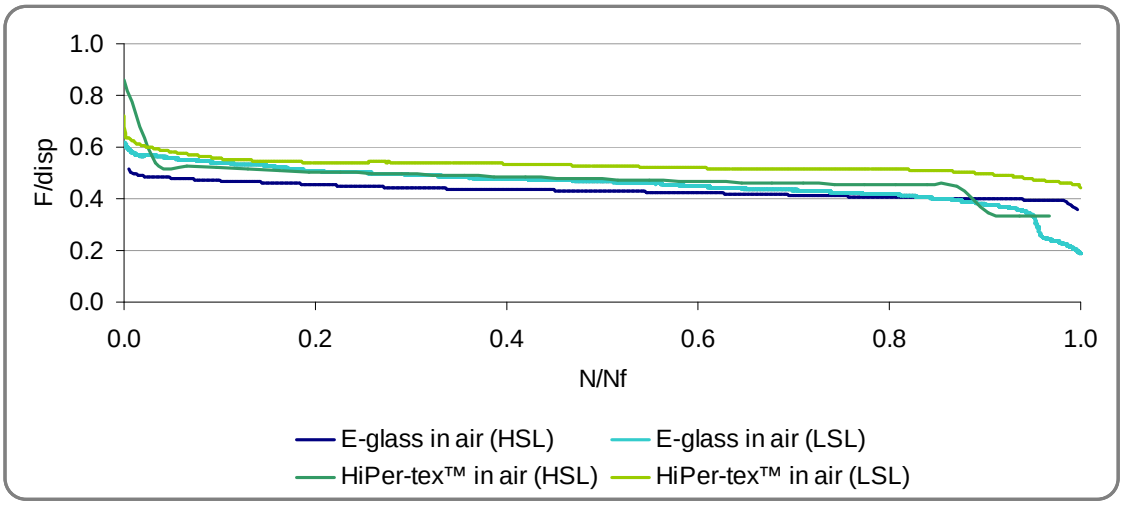

Figure 92. *Comparative curves for infused E-glass, Advantex® and HiPer-tex™ composite : a) in natural circulating sea water, b) in air*

(a)

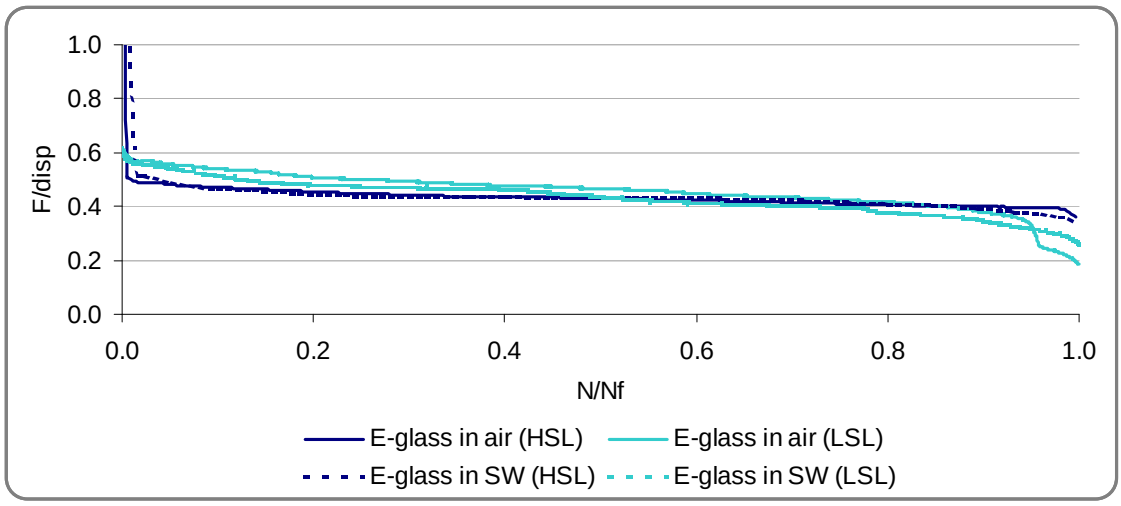

(b)

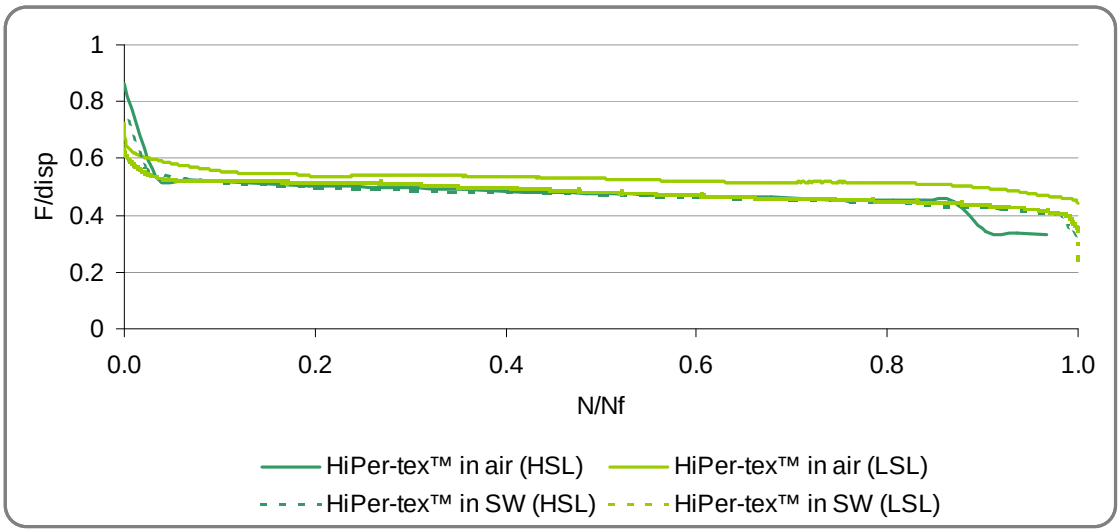

Figure 93. *Comparative curves in air and in natural circulating sea water : a) infused E-glass specimens, b) infused HiPer-tex™ specimens*

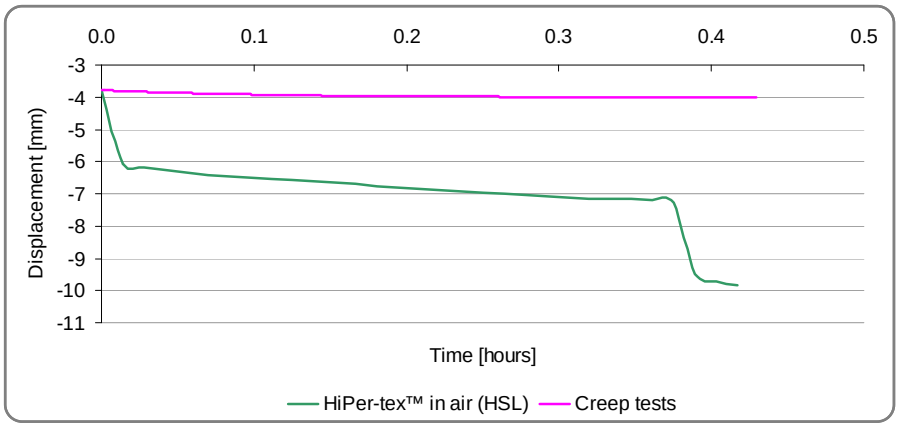

Figure 94. *Comparative curves of displacements during fatigue and creep tests*

- Analytical formulation

In order to describe the evolution of damage and integrate these phenomena in a numerical model, an analytical study has been performed based on the experimental results and empirical formulations. As the evolution of the damage does not follow a known law, the analytical study was based on the general shape of the experimental curves. For this reason we have evaluated several formulations with several coefficients to solve using either a *Matlab*© least squares fitting routine or a genetic algorithm. The genetic algorithm method has been developed to control the accuracy of the results obtained by the least squares method. Indeed, the least squares method gives optimum solutions for the coefficients of the function but without any sensitive coefficient to control the optimization. On the contrary, the genetic algorithm approach gives a family of possible solutions. In addition, one of the formulations, the hyperbolic function, cannot be examined by using the least squares method because its formulation is not compatible with this computing method.

So if we consider

$$y=\frac{F}{Displacement} \qquad x=\frac{N}{N_f}$$

We can write the evolution of the ratio of the applied load divided by the displacement as a function of the ratio number of cycles/fatigue life, using the following four equations.

$$y = D - \frac{A \cdot x \cdot (1 + x^B) - A \cdot (1 - x)^C}{1 + A} \qquad \textit{(Eqn. 31)}$$

$$y = C \cdot \left(\arccos\left(2x^A - 1\right)\right)^B \qquad \textit{(Eqn. 32)}$$

$$y = C \cdot \left(1 - x^A\right)^B \qquad \textit{(Eqn. 33)}$$

$$y = C \cdot \frac{1 - x^A}{1 + x^B} \qquad \textit{(Eqn. 34)}$$

All the results obtained for the different coefficients and with the different numerical tools (least squares method in *Matlab*© or genetic algorithm) are summarized in *Annex 7*. Some graphical representations of the fittings are presented on *Figure 95*. We can observe that the four optimization functions all fit the experimental results quite well. These results will be used in *Section 5* of *Chapter IV*.

The choice between the four analytical formulations is motivated by several criteria. The first one is the number of coefficients (Occam's razor principle), the more coefficients to determine, the more difficult it is to optimise. The second criterion is the dispersion of the results. The dispersion can be due to two main reasons, either the parameter is linked to another one, or the experimental data are not sufficient to determine this parameter especially the shape factor of the initial slope. The third criterion is the capability of integrating the optimised function in a numerical model. So, in the following section, the power function *(Eqn. 33)* will be used, as it is simple but provides a good representation of the results.

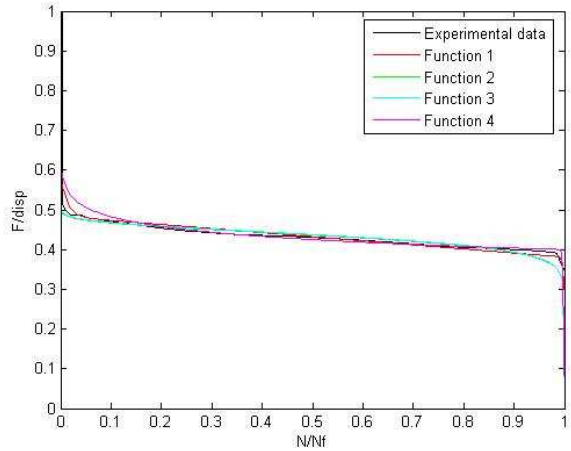

(a)

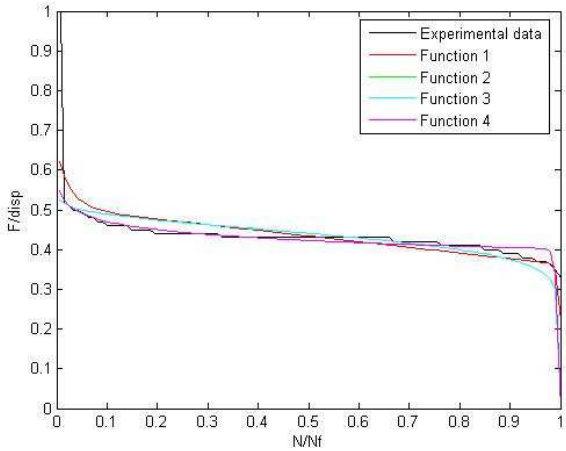

(b)

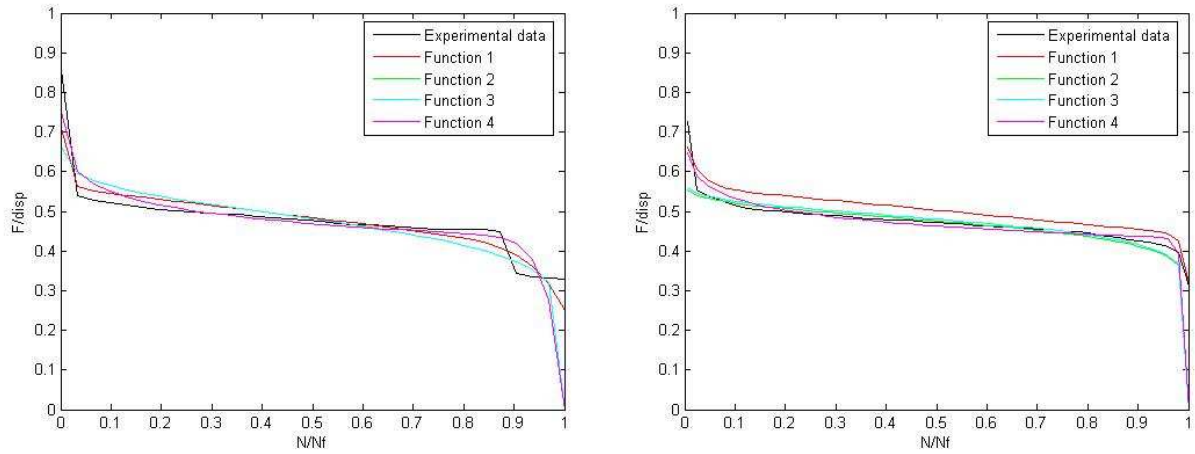

(c) *(d)*

Figure 95. *Comparative curves of the experimental data (in black) and the optimisation (in colour) : Infused E-glass specimen (a) in air, (b) in natural circulating sea water and infused HiPer-tex™ specimen (c) in air, (d) in natural circulating sea water*

3.2- Effects of wet ageing on the mechanical properties of the materials

In order to develop a better understanding of the phenomena of sea water ageing and its consequence on the composite material studied, quasi-static tests were performed at different stages of wet ageing. Two series of tests have been performed, first on the unreinforced resin then on the composites. These series of tests provide information about the evolution of the moduli and the failure and the damage mechanisms which develop during natural sea water ageing.

3.2.1. Tests on pure resin specimens

In order to distinguish the changes in resin properties with ageing from those of the composite an extra panel was produced, by casting under vacuum, and cured following the same cycle as the composites. Eighteen specimens were placed in natural sea water at *60°C* and specimens were removed after different periods and tested. Tensile tests have been performed on wet specimens (within *30* minutes of removal from water) and some nanoindentation tests were performed on dried specimens. The degree of sea water ageing is defined by the immersion time in hours (*Figure 96*) and the weight gain obtained by gravimetric analysis. The ageing stages performed in natural sea water at *60°C* have been defined as follows :

- *31 hours* (≈ *1* day)
- *96 hours* (= *4* days)
- *177 hours* (≈ *7* days)
- *361 hours* (≈ *15* days)
- *529 hours* (≈ *22* days)
- *1 275 hours* (≈ *53* days)
- *2 140 hours* (≈ *90* days)

a) Tensile tests

The parameters observed are the stresses, strains and Young's moduli (defined between *0* and *2 kN*) and their variations with respect to the experimental results obtained at the initial state (*Table 19*). These comparisons between the different ageing stages can be made because no changes in failure mode, especially changes in cross section, have been observed during experiments. *Figure 97* shows how failure stress evolves with ageing time and weight gain and *Figure 98* shows how modulus changes. These curves are represented as a function of the root square of the ratio days of immersion divided by thickness of the specimens, because of the large variability of the geometric parameters of the specimens (*see Annex 4*)

We can see that both the failure stress and the Young's modulus are strongly influenced by immersion in natural sea water at *60°C*.

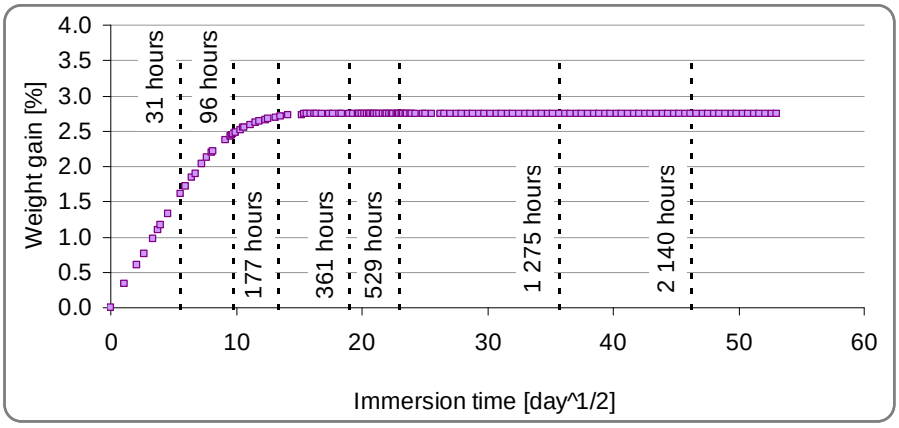

Figure 96. *Graphical representation of the weight gain of the pure resin materials and the different sea water ageing stages at 60°C*

Table 19. *Summary of the experimental data obtained in tensile tests and variations of the failure stresses, strains and Young's moduli after ageing for pure resin specimens*

	σ_{fail} (min-max range) [*MPa*]		ε_{fail} (min-max range) [%]		E (min-max range) [*GPa*]	
Initial state	68.4 (1.6)		4.94 (0.1)		2.8 (0.2)	
31 h at 60°C	66.7 (1.8)	- 3 %	5.33 (0.08)	+ 8 %	2.5 (0.2)	- 10 %
96 h at 60°C	64.9 (3.8)	- 5 %	4.80 (1.24)	- 3 %	2.4 (0.2)	- 15 %
177 h at 60°C	63.4 (1.0)	- 7 %	4.73 (0.90)	- 4 %	2.7 (0.02)	- 4 %
361 h at 60°C	54.9 (13.4)	- 20 %	3.55 (1.90)	- 28 %	2.2 (0.4)	- 23 %
529 h at 60°C	55.3 (9.6)	- 19 %	4.83 (3.80)	- 4 %	2.0 (0.1)	- 31 %
1 275 h at 60°C	56.2 (2.8)	- 18 %				
2 140 hours at 60°C	54.2 (2.4)	- 21 %	4.94 (2.80)	0 %	1.8 (0.2)	- 34 %

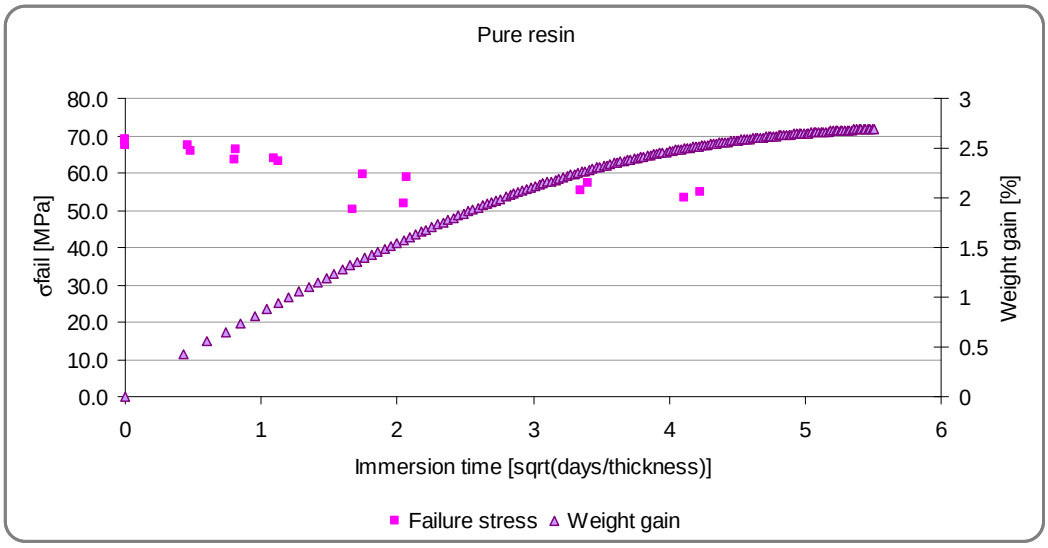

Figure 97. *Evolution of the failure stresses and the weight gain for pure resin specimens as a function of the immersion time*

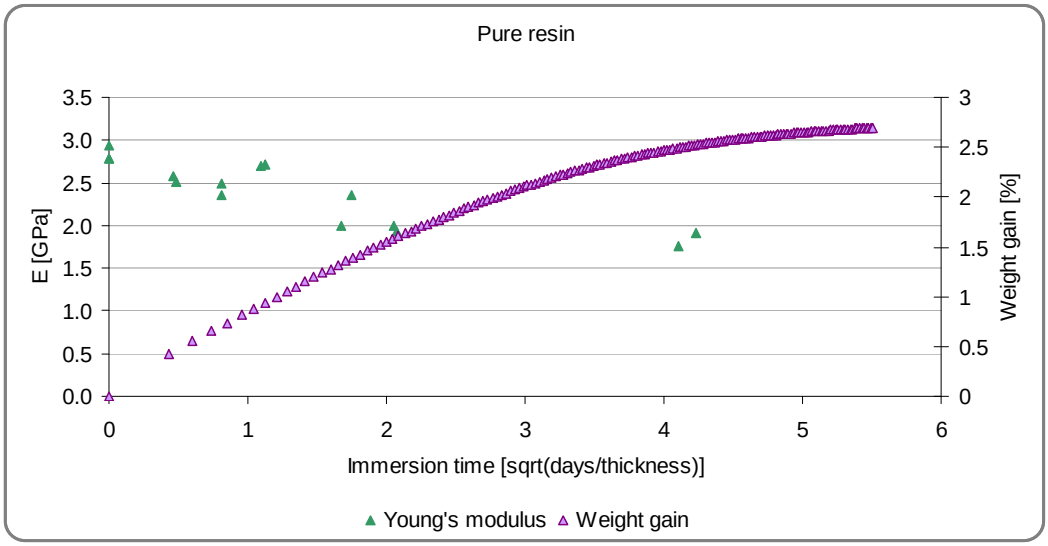

Figure 98. *Evolution of the modulus and the weight gain for pure resin specimens as a function of the immersion time*

b) Nanoindentation tests

The nanoindentation tests were performed by *Alain Bourmaud* at the *Université de Bretagne Sud, Lorient*, on two pure resin specimens, in the initial state and after *1 275 hours* in natural sea water at *60°C* and drying. Two lines of *25* points have been performed in the sections of the two specimens in order to obtain their mechanical properties. Each indentation is *1 000 nm* deep and the distance between two indentations is *240 µm* for the specimen at initial state and *194 µm* for the aged specimen. *Figure 99* shows the measured moduli as a function of the position in the section of the specimens. We can observe that the two sets of data are similar. So, the evolution of moduli observed in tensile tests at different ageing stages due to the water absorption is probably reversible. In order to be sure of these results, nanoindentation tests should be performed on wet aged specimens, but these tests are long to

perform and moisture control during the test is not easy. Absolute values of nanoindentation modulus are slightly higher than those from tensile tests (*2.8 GPa*), as is usually noted [131].

From these pure resin tests we can conclude that although changes in modulus are reversible, for an application in water both modulus and strength of the epoxy resin decrease with immersion time.

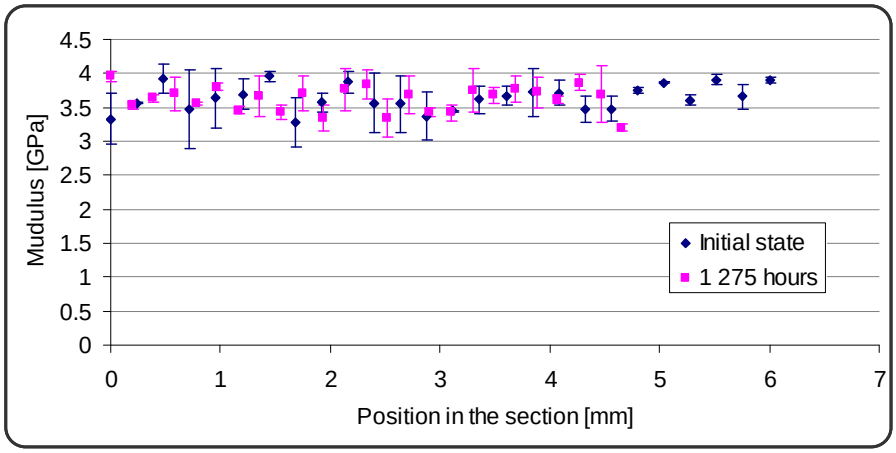

Figure 99. *Graphical representation of the moduli as a function of the position in the section*

3.2.2. Tests on infused composite specimens

The degree of sea water ageing is defined by the immersion time in hours (*Figure 100*) and the weight gain obtained by gravimetric analysis. The ageing stages performed in natural sea water at *60°C* have been defined as follows :

- *168 hours* (*1* week)
- *672 hours* (*4* weeks)
- *1 008 hours* (*6* weeks)
- *1 344 hours* (*8* weeks)
- *2 016 hours* (*12* weeks)
- *2 352 hours* (*14* weeks)
- *2 688 hours* (*16* weeks)
- *3 024 hours* (*18* weeks) followed by a complete drying
- *5 040 hours* (*30* weeks)

All the specimens have been weighed before the tests and were tested wet unless otherwise stated.

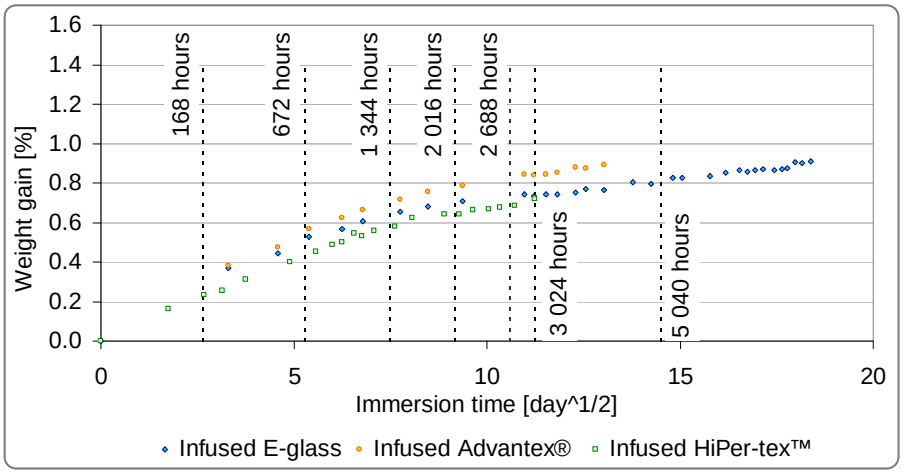

Figure 100. *Graphical representation of the weight gain of the composite materials and the different sea water ageing stages*

a) CRP tests

First, the changes in properties were determined directly, from tests involving simple tensile or compressive loading at different stages of sea water ageing on infused E-glass specimens. These tests are intended to identify the influence of sea water ageing on the material properties for subsequent modelling.

The first parameters to observe are the experimental values of failure stresses in tension and in compression, obtained at different stages of ageing. These results and their variations are summarized in *Table 20* and *Figure 101*. We can observe a correlation between the variation of the failure stresses and the weight gain of the composite materials. The comparison between tension and compression is very interesting, tensile strengths drop significantly with ageing while compression strengths are lower initially but change very little.

The other parameters are the modulus values defined by the slope of the strain-stress curve between *0* and *2.8 kN*. These moduli, summarized in *Table 21* and *Figure 102*, do not seem to be influenced by the evolution of the water absorption of the composite material. Thus although the pure resin modulus drops the axial modulus is dominated by the fibres, and their stiffness is not sensitive to water.

Table 20. *Summary of the experimental data obtained in "CRP" tests and variations of the failure stresses after ageing for infused E-glass specimens*

Failure stress σ_{fail}	σ_{fail} in tension (min-max range) $[MPa]$		σ_{fail} in compression (min-max range) $[MPa]$	
Initial state	750.4 (47.6)		472.5 (21.6)	
672 h at 60°C	589.5 (24.6)	- 21 %	395.4 (13.4)	- 16 %
1 008 h at 60°C	595.0 (9.6)	- 21 %	386.2 (0.6)	- 18 %
1 344 h at 60°C	555.0 (36.0)	- 26 %	382.0 (16.0)	- 19 %
2 352 h at 60°C	427.1 (84.6)	- 43 %	415.3 (14.4)	- 12 %

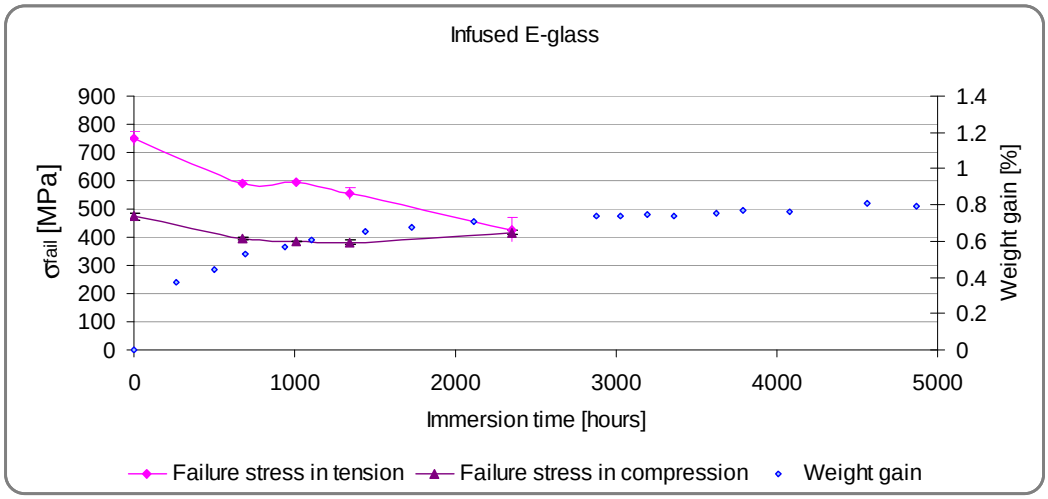

Figure 101. *Evolution of the failure stresses and the weight gain for infused E-glass specimens as a function of the immersion time*

Table 21. *Summary of the experimental data obtained in "CRP" tests and variations of initial Young's modulus after ageing for infused E-glass specimens*

Initial Young's modulus E_I	E_I in tension (min-max range) $[GPa]$		E_I in compression (min-max range) $[GPa]$	
Initial state	46.9 (1.6)		45.2 (4.2)	
672 h at 60°C	48.4 (6.4)	+ 3 %	52.7 (10.0)	+ 17 %
1 008 h at 60°C	48.3 (4.8)	+ 3 %	51.1 (4.0)	+ 13 %
1 344 h at 60°C	48.1 (2.4)	+ 3 %	47.5 (1.4)	+ 5 %
2 352 h at 60°C	51.7 (2.8)	+ 10 %	45.8 (3.6)	+ 1 %

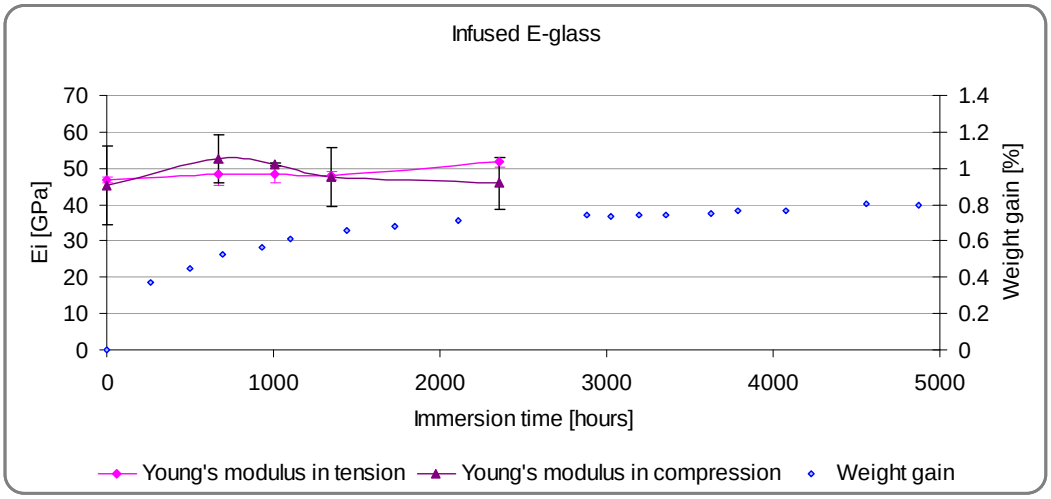

Figure 102. *Evolution of the initial Young's modulus and the weight gain for infused E-glass specimens as a function of the immersion time*

b) Flexural tests

Flexural tests were also performed at different stages of ageing. After a given immersion time, the specimens have been removed from sea water, weighed (*Table 22*) and tested wet in four-point bending. The experimental results are summarized in *Table 23* and presented on *Figure 103*. These tests will be used to validate the coupled water-mechanical properties model which will be presented in *Chapter IV*.

We can observe that sea water ageing has a large influence on the flexural failure stress, especially for the infused E-glass composite. The failure stress decreases by *5 %* during the first week of sea water ageing for the infused E-glass composite and by almost *40* % after *30* weeks for the two composite materials. All the variations of the failure stress are summarized in *Table 23*. For the infused E-glass composite, the evolution of the failure stress seems to be more rapid during the early stages of sea water ageing and reaches a plateau, as presented on *Figure 104*. As presented on *Figure 105*, we can observe a correlation between the evolution of the weight gain and the variation of the failure stress for the infused E-glass specimens.

In order to complete these results, the flexural stiffness of the different specimens has been compared by superposing the experimental curves obtained for the different ageing stages (*Figure 106*). We do not observe any significant difference in flexural stiffness between the seven ageing stages, as expected from the tensile and compressive results.

In addition, flexural tests performed on aged and dried E-glass and HiPer-tex™ specimens show that the phenomena involved in sea water ageing are not completely reversible. Even after drying the failure stress loss is *30 %* for the E-glass composite and *16 %* for the HiPer-tex™ composite.

Table 22. *Summary of the sea water ageing stages in terms of weight gain*

Ageing stages (Weight gain in %)	Infused E-glass	Infused HiPer-tex™
168 h at 60°C	0.2956 (0.0035)	
672 h at 60°C	0.5319 (0.0076)	
1 344 h at 60°C	0.6695 (0.0030)	
2 016 h at 60°C	0.7424 (0.0025)	
2 688 h at 60°C	0.6785 (0.0125)	0.7104 (0.0031)
3 024 h at 60°C	0.6580 (0.0230)*	0.6647 (0.0101)*
	0.1511 (0.0061)**	0.2136 (0.0096)**
5 040 h at 60°C	0.7443 (0.0051)	0.7292 (0.0114)

** before drying*
*** after drying*

Table 23. *Summary of the experimental data obtained in flexural tests and variations of the failure stress after ageing*

Failure stress $[MPa]$	Infused E-glass		Infused HiPer-tex™	
Initial state	1 137.6 (69.3)		1 314.0 (83.6)	
168 h at 60°C	1 085.0 (72.1)	- 4.6 %		
672 h at 60°C	946.0 (49.9)	- 16.8 %		
1 344 h at 60°C	799.2 (29.1)	- 29.7 %		
2 016 h at 60°C	728.4 (16.1)	- 36.0 %		
2 688 h at 60°C	665.0 (16.2)	- 41.5 %	924.0 (69.0)	- 28.3 %
3 024 h at 60°C + drying	789.1 (45.2)	- 30.6 %	1 103.1 (85.3)	- 16.0 %
5 040 h at 60°C	683.9 (46.4)	- 39.9 %	746.4 (44.3)	- 41.3 %

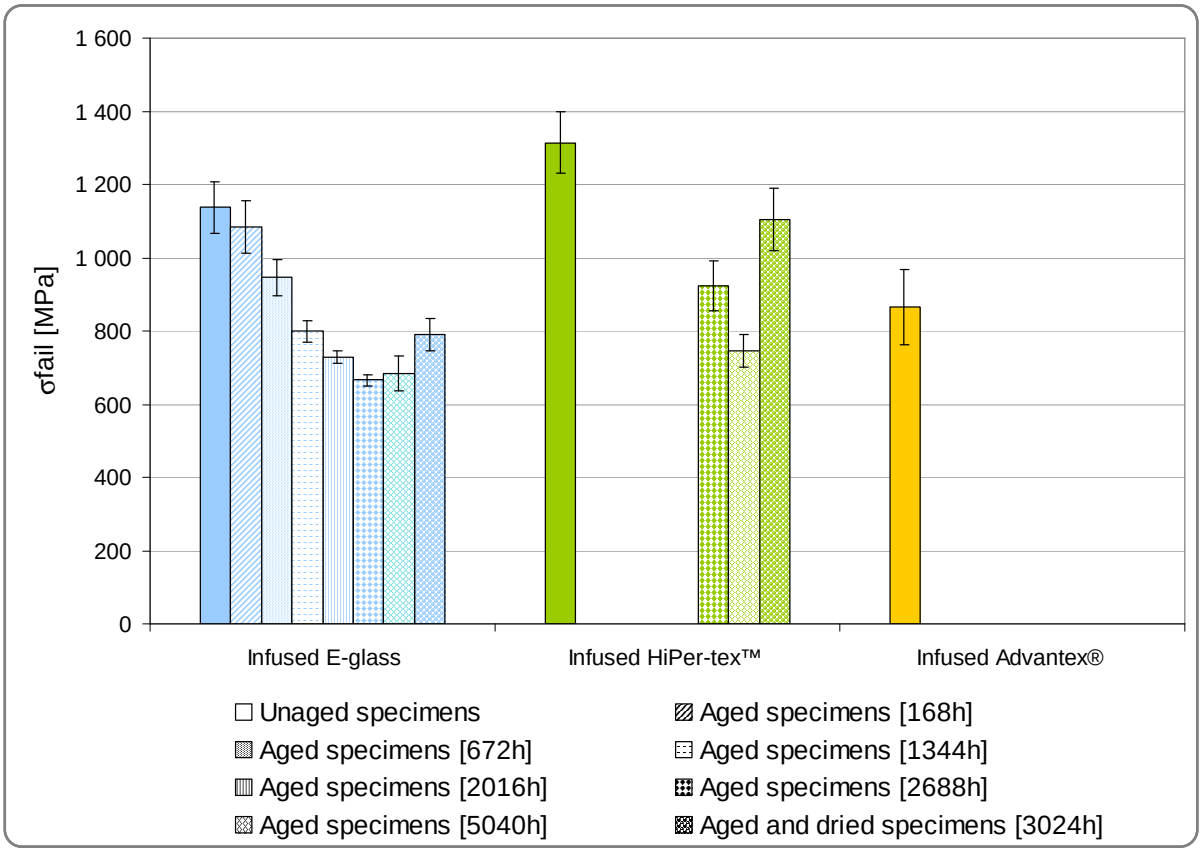

Figure 103. *Comparative curves of the experimental data obtained in flexural tests for infused E-glass, Advantex® and HiPer-tex™ specimens at different stages of sea water ageing*

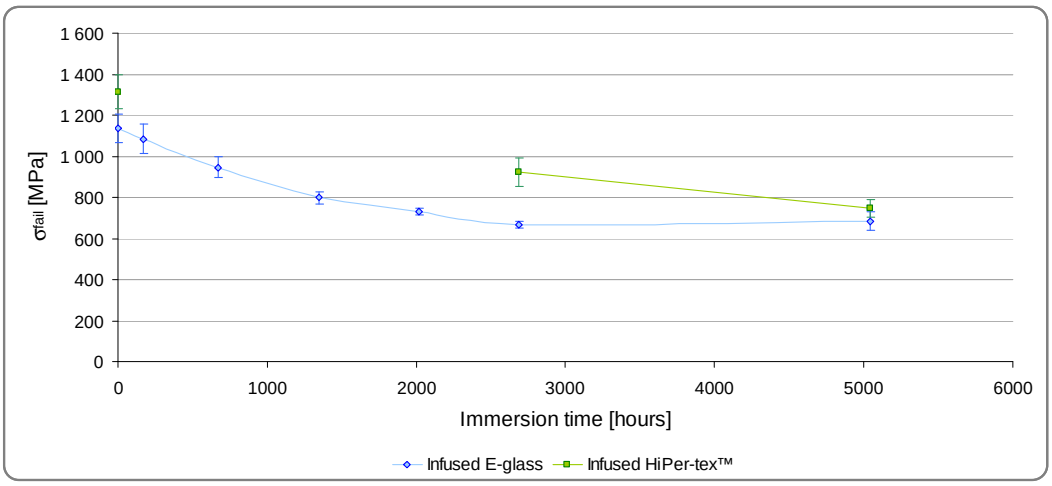

Figure 104. *Evolution of the failure stress for infused E-glass and HiPertex™ specimens as a function of the immersion time*

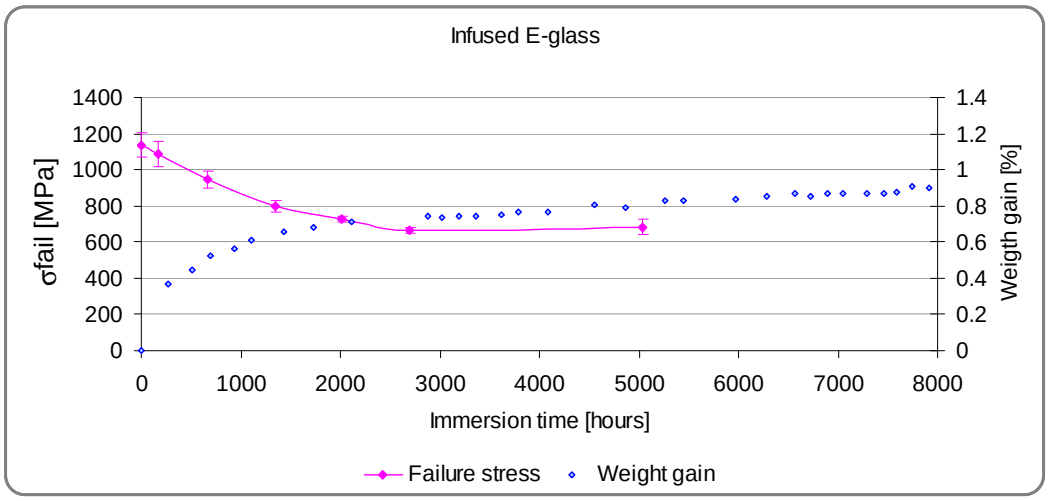

Figure 105. *Evolution of the failure stress and the weight gain for infused E-glass specimens as a function of the immersion time*

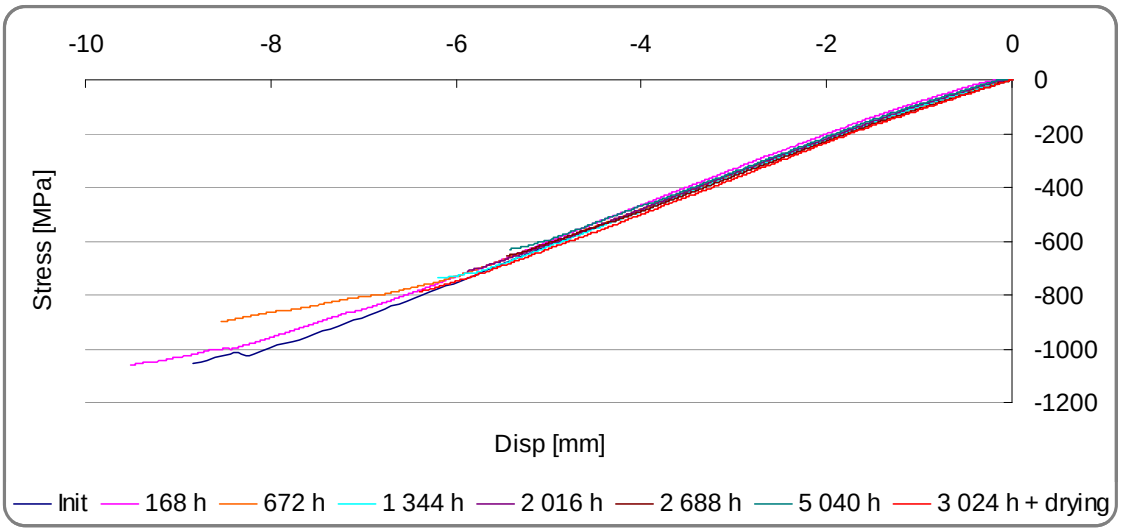

Figure 106. *Evolution of the stress-displacement plots for different ageing stages for infused E-glass*

c) Interlaminar Shear Stress tests (ILSS)

Another series of tests, to determine ILSS values, was also performed on aged E-glass specimens but after drying in air between *7* and *9* months. *Table 24* and *Figure 107* show the results for at least *4* specimens per condition. When we observe the results it appears that up to *2 000 hours* there is a gradual drop in ILSS, and the values, while still reasonably high, drop below the quality criterion we have used to accept our panels. This suggests that the degradation of the fibre/matrix interface may contribute to the large drop in flexural strength after ageing shown in *Table 23*. Nevertheless, the values after longer periods and for the dried specimens are close to initial values, suggesting that another mechanism, post-curing for example, may operate at longer time.

Table 24. *Summary of the experimental data obtained in ILSS tests and variations after ageing for infused E-glass specimens*

	ILSS (SD) $[MPa]$	
Initial state	48.7 (0.8)	
168 h at 60°C	45.5 (1.8)	- 7 %
672 h at 60°C	45.1 (1.0)	- 7 %
1 344 h at 60°C	41.9 (0.6)	- 14 %
2 016 h at 60°C	39.6 (1.7)	- 24 %
2 688 h at 60°C	46.2 (1.3)	- 5 %
3 024 h at 60°C + drying	47.6 (1.8)	- 2 %
5 040 h at 60°C	41.0 (2.1)	- 15.8 %

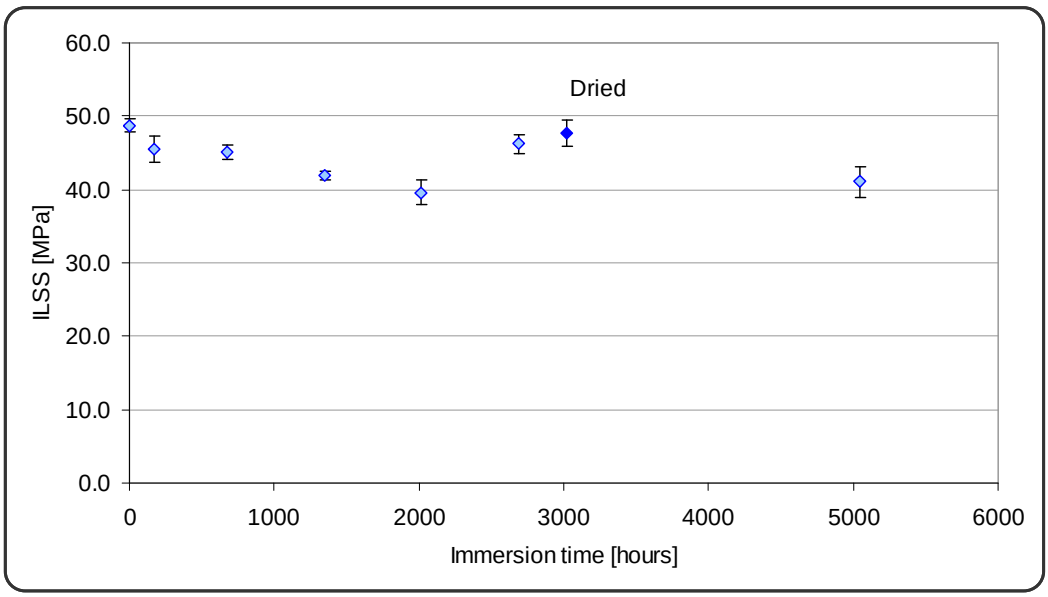

Figure 107. *Evolution of the ILSS data for infused E-glass specimens as a function of the immersion time*

3.2.3. Summary of ageing effect

When we compare the results obtained in tension with the resin (*Figure 97*) and the infused E-glass composite (*Figure 101*), we can notice that their properties decrease as a function of the weight gain. When we plot the variation of their failure stresses as a function of the square root of the ratio days of immersion divided by the thickness of the specimen (*Figure 108*), we can see that the evolutions of the failure stresses of the two materials are similar in the early stages of immersion.

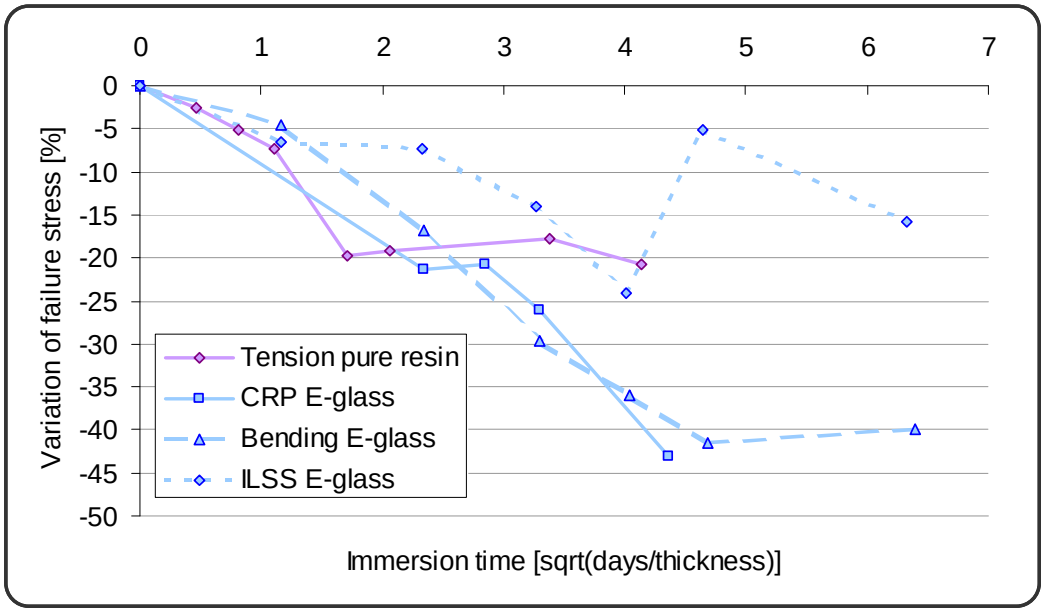

Figure 108. *Variations of the failure stresses observed for pure resin and infused E-glass composite*

3.3- Effects of fatigue on the mechanical properties of the fibre-reinforced composite materials in flexion

As for the sea water ageing, the influence of fatigue load cycles on the composite materials has been investigated by performing flexural tests. Fatigue sequences have been defined according to the results obtained during the fatigue tests in natural circulating sea water at the reference stress level $R\sigma = 60\ \%$. The fatigue sequences are summarized in *Figure 109* and *Table 25*. This series of tests provides information about the evolution of the residual failure stress and damage mechanisms due to fatigue. The experimental results are summarized in *Table 26* and presented on *Figure 110*.

As shown on *Figure 110*, the fatigue cycling up to $N/N_f=0.6$ does not seem to have a negative effect on the flexural failure stress of the infused E-glass, Advantex® and HiPer-tex™ composites. On the contrary, failure stresses tend to increase slightly after fatigue cycles for E-glass and HiPer-tex™ composites, while for Advantex® composite the increases are much larger, *15 %*, and remain constant after more cycles. This is very interesting as cycling appears to increase the Advantex® failure stresses to values close to those which would be expected based on the fibre properties, around *1 100 MPa*. *Figure 111a* and *Figure 111b*, show the changes in failure stress for the three materials.

Most studies on residual strength of fatigued composite materials [134, 135] show that the residual strength after fatigue drops below the static strength. Indeed, this is often used in

fatigue modelling (*Section 2.3.1*, *Chapter I*). An increase in the residual fatigue strength is sometimes observed on notched composites [136-139], but this phenomenon is due to the mechanisms of redistribution and relaxation of the stresses around the notch area. In the present case, a redistribution of the stresses during fatigue cycling might explain the increase of failure stress observed. This redistribution can be due to the modification of the geometry involved by the crack propagation along the specimen during the early stages of fatigue.

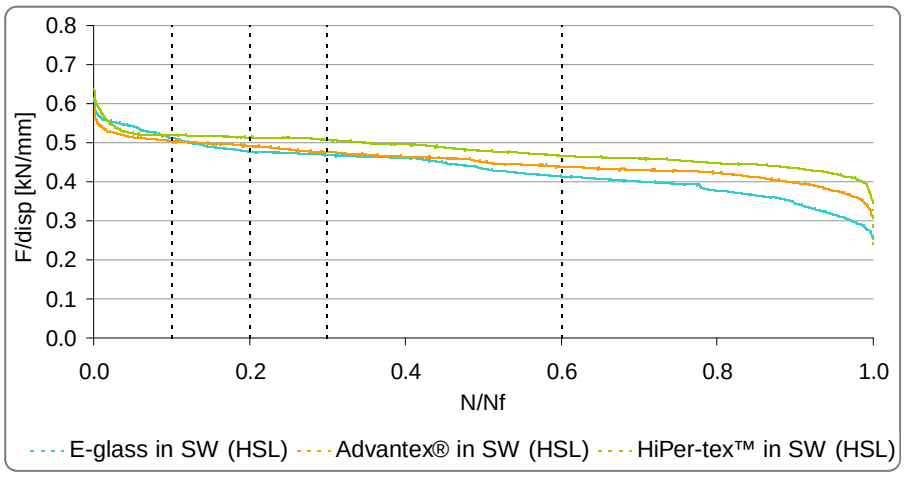

Figure 109. *Graphical representation of the damage curves and the different fatigue sequences*

Table 25.*Summary of the fatigue sequences in terms of number of cycles*

Fatigue stages (Number of cycles)	Infused E glass	Infused Advantex®	Infused HiPer-tex™
N_f at Rσ = 60%.	46 427	180 624	39 639
N/N_f = 0.1	4 600	18 000	4 000
N/N_f = 0.2	9 200	36 000	8 000
N/N_f = 0.3	13 800	54 000	12 000
N/N_f = 0.6	27 600	108 000	24 000

Table 26. *Summary of the experimental data obtained in flexural tests and variations of the failure stress after fatigue*

Failure stress after fatigue [*MPa*]	Infused E-glass		Infused Advantex®		Infused HiPer-tex™	
Initial state	1 138 (69)		960 (88)*		1 314 (84)	
N/N_f = 0.1	1 293 (52)	+ 13.7 %	1 104.1 (66)	+ 15.0 %	1 436 (101)	+ 9.3 %
N/N_f = 0.2	1 223 (91)	+ 7.5 %	1 093 (81)	+ 13.8 %	1 437 (63)	+ 9.4 %
N/N_f = 0.3	1 120 (72)	- 1.6 %	1 035 (82)	+ 7.8 %	1 374 (96)	+ 4.5 %
N/N_f = 0.6	1 175 (47)	+ 3.3 %	1 108 (171)	+ 15.4 %	1 432 (36)	+ 8.9 %

** This initial value of failure stress is issued from the experimental data of the plate #HA1*

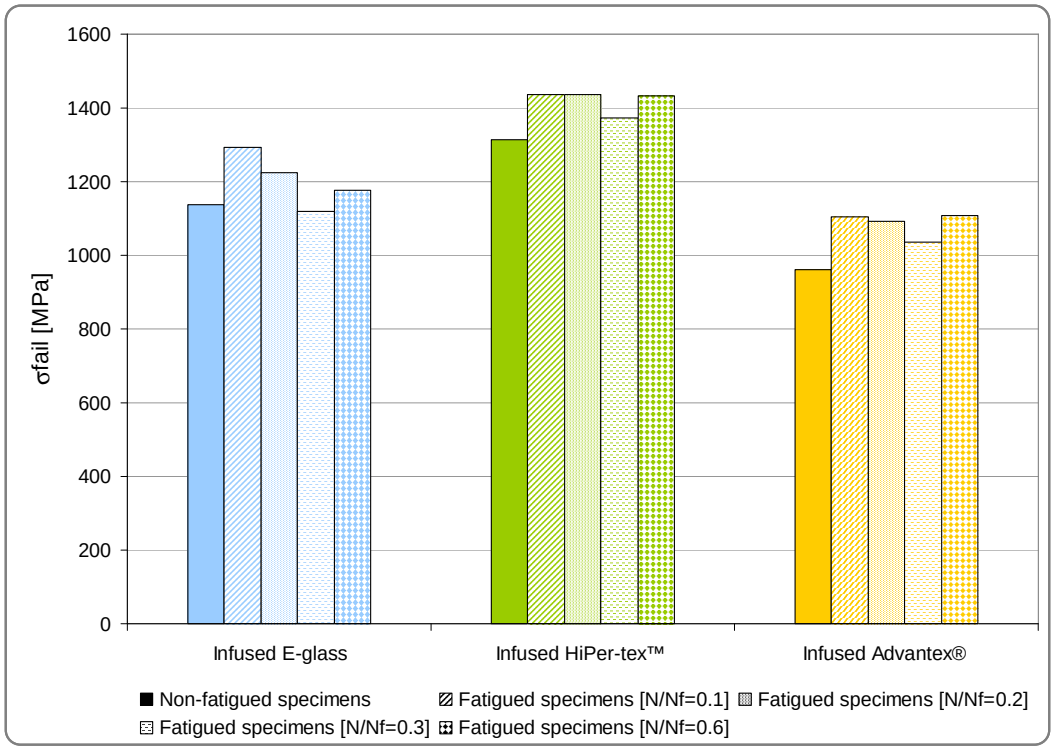

Figure 110. *Comparative curves of the experimental data obtained in flexural tests for infused E-glass, Advantex® and HiPer-tex™ specimens at different stages of fatigue*

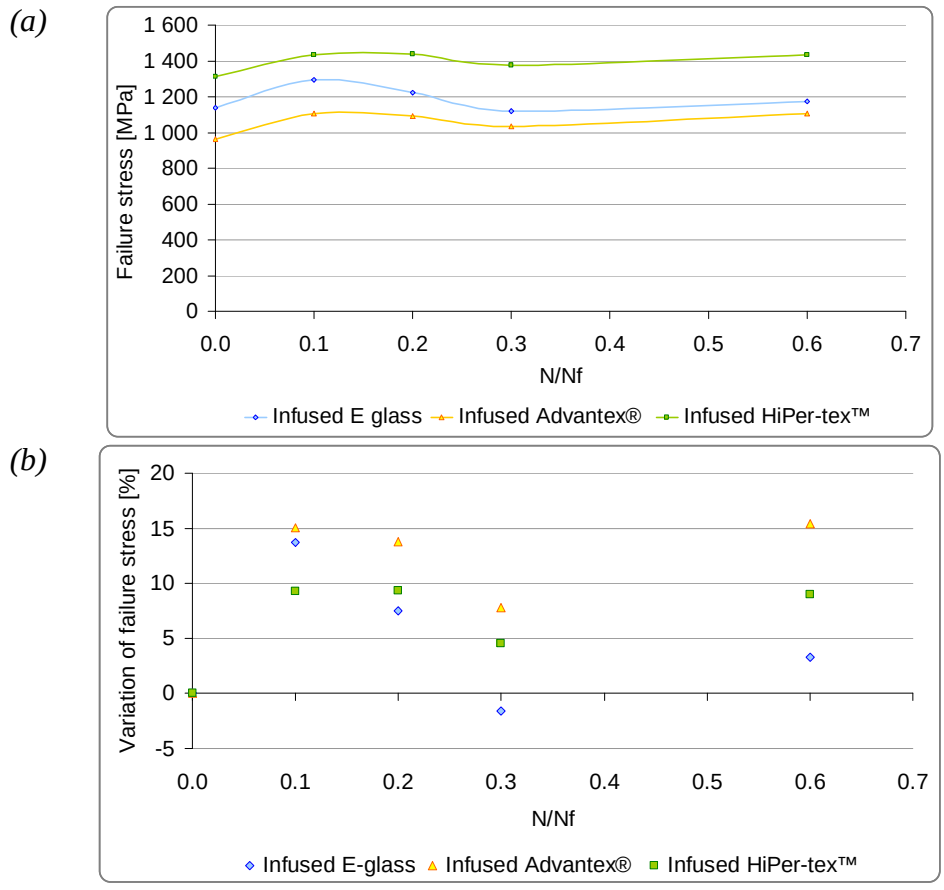

Figure 111. *a) Evolution of the failure stress, b) Variation of the failure stress for infused E-glass, Advantex® and HiPer-tex™ specimens at different stages of fatigue*

3.4- Damage mechanisms

Damage mechanisms in unidirectional composites depend on the loading mode, for example tensile or compressive, and on whether the loading is parallel to or inclined to the fibre direction. Four-point bending tests are complex, involving tensile, compressive and shear stresses, so it is important to understand the damage mechanisms.

The first investigation technique involves simply observing the failure mode of the specimen after flexural tests. Then, we have studied the evolution of the damage using X-ray micro-tomography on samples from interrupted tests at one stress level. Finally, the effect of the loading points on the specimens during flexural fatigue tests has been investigated.

3.4.1. Failure mode during flexural tests

The first and easiest sign of damage to observe is the failure mode of the specimen after flexural tests. Results and pictures of infused E-glass specimens after quasi-static flexural tests are summarized in *Table 27*.

The evolution of the failure mode is presented as a function of both the wet ageing and the fatigue stage. In the initial state, the specimen fails in compression (C) as expected according to the measured values of the strengths in tension and compression. During the natural sea water ageing process, the failure mode of the specimen under flexural loading changes from compression (C) to traction (T). This change, which may be due to a stress corrosion mechanism in the E-glass [37, 81, 82], occurs between *672 hours* and *1 344 hours* of immersion in natural circulating sea water at *60°C*. In order to confirm these results by following the evolution of the properties in tension and compression separately, “CRP” tests were carried out at different ageing stages distributed between *672 hours* (*4* weeks) and *1 344 hours* (*8* weeks). After *5 040 hours* the failure is very localized in the specimen centre, and during ageing a change in colour of the specimen was also noted.

Further analysis has been performed on the resin. A set of pure resin samples immersed in natural circulating sea water at *5* temperatures (*4°C*, *20°C*, *40°C*, *60°C* and *80°C*) for almost *250 days* has been analysed using a Fourier transform infrared (FTIR) spectrometer. The results are presented on *Figure 112*. We can observe the reduction until disappearance of one of the additives of the resin (antioxidant, plasticizer, …) located by the arrow. This result suggests that the temperature of the sea water has an influence on the resin chemical composition. Further chemical analyses are necessary to identify the exact changes. In addition, the results from tensile tests on unreinforced resin samples (*Figure 97* and *Figure 98*), indicate that both modulus and strength decrease as a function of the immersion time.

By contrast, the fatigue cycling does not appear to influence the failure mode of the infused E-glass specimens subjected to flexural load. All the specimens failed in compression (C) whatever the fatigue sequence applied. This suggests that the time-temperature conditions during wet cyclic tests are insufficient to initiate a stress corrosion mechanism, but does not explain why fatigue lifetimes are shorter in sea water than in air. The influence of water on the matrix in the outer layers of the composite may explain this reduction of lifetime, which will be examined in the modelling section below (*Section 4*, *Chapter IV*).

Table 27. *Summary of the typical failure mode during flexural tests*

Failure mode		Face in compression	Face in tension	Failure mode
Initial state				C
Failure mode after natural sea water ageing (60°C)	168 hours			C
	672 hours			C + T
	1 344 hours			T
	2 016 hours			T
	2 688 hours			T
	5 040 hours			T
Failure mode after fatigue sequences	N/Nf = 0.1			C
	N/Nf = 0.2			C
	N/Nf = 0.3			C
	N/Nf = 0.6			C

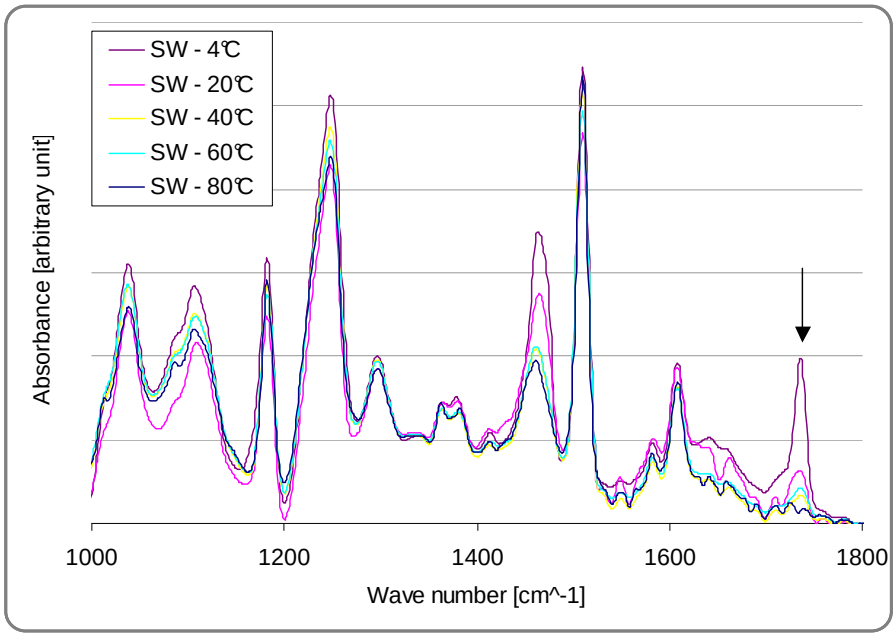

Figure 112. *FTIR spectra for the 5 pure resin specimens after250 days ageing*

3.4.2. Evolution of the damage during flexural fatigue tests (X-ray tomography)

Some tests have also been performed using X-ray micro-tomography, which uses X-rays to create a cross-section of a 3D-object without the need for sectioning and polishing. This appears to be a very promising technique to examine the initiation and the evolution of the damage during the fatigue life of a specimen.

In order to have a realistic representation of the damage evolution, we have performed two interrupted flexural fatigue tests on infused E-glass specimens (N/N_f=*0.1* and N/N_f = *0.6*) following the fatigue sequences presented previously. These two fatigued specimens were compared to a specimen at the initial state and a failed specimen. *Figure 113* shows the samples analysed. Some examples of the images obtained are shown on *Figure 114*.

Figure 114a represents a global view of the four specimens observed with on the right the undamaged sample and on the left side the failed sample. The damage phenomena are more visible on the *Figure 114c*, which shows a section at one point, but the data set generated using this technique allows us to step through each sample and visualize damage at any point. It appears that small cracks occur early in fatigue tests in the shoulder of the specimen, but then remain stable for the majority of lifetime. Extensive delaminations are only observed in the central section when damage introduced at the specimen radius in the form of cracks at *45°* coalesce at final failure, when fibre breakage is noted.

Figure 113. *The four infused E-glass samples analysed*
(from bottom to up : at initial state, after 4 600 cycles, after 27 600 cycles, after failure)

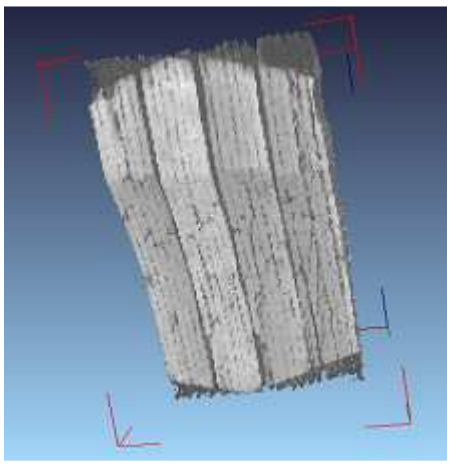

(a)

(b)

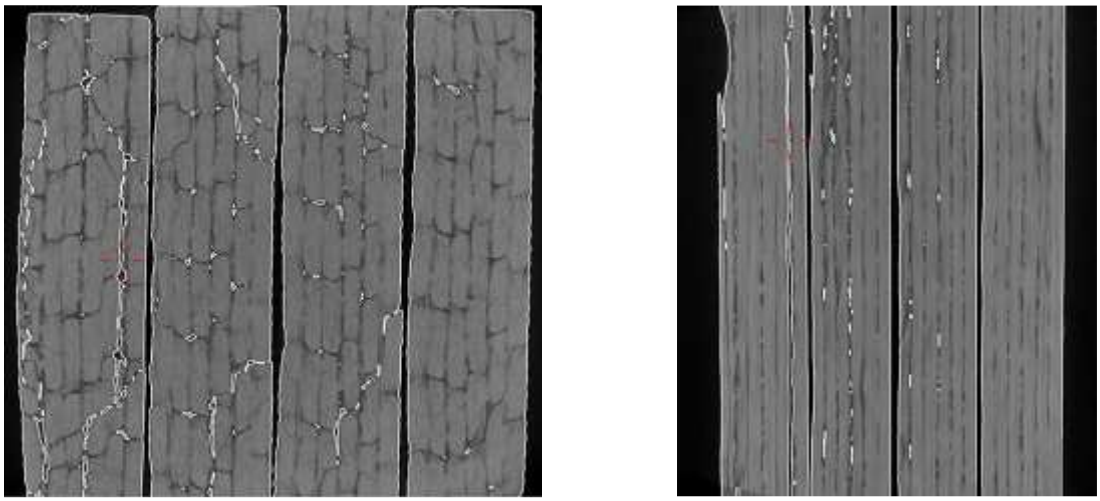

(c) *(d)*

Figure 114. *Graphical representation of the X-ray tomography :*
a) global image, b)-d) sections in three perpendicular planes, indicated by red cross

3.4.3. Effects of the loading points on the specimens during flexural fatigue tests

During the fatigue tests, we have observed small indentations on the upper faces of the specimens due to the ceramic loading points (diameter *10 mm*). So, in order to quantify this phenomenon, we have measured the profile of the specimens using a laser profiler. First, quasi-static tests were interrupted at different load levels up to just before failure. No indentation was detected under these conditions.

Then infused HiPer-tex™ specimens were tested under cyclic loading at different stress levels until failure in natural circulating sea water and profiles were measured. Examples of results are presented on *Figure 115* and *Table 28*.

In fatigue, we can observe an evolution of the depth and the length of the indentation as a function of the lifetime of the specimen. These indentations are caused by wear due to relative movement and friction between the loading points and the specimens.

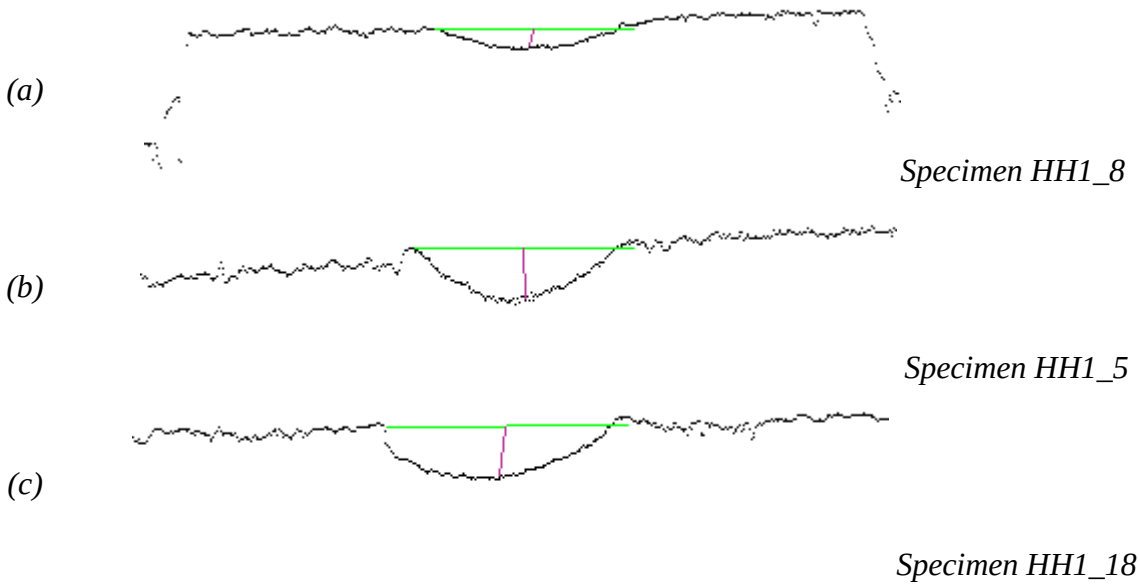

Figure 115. *Graphical representation of the specimen profile*

The indentation of the specimen, although it does not appear to initiate the damage which results in final failure, will affect the values of displacement recorded by the displacement transducer in the piston, used to calculate the change in specimen stiffness during fatigue. It may also affect the stress state calculated by the expression *(Eqn. 35)*. It is therefore important to examine these two points.

$$R_\sigma = \frac{3}{4}\cdot\frac{F\cdot L}{\sigma_{fail}\cdot b\cdot h^2} \qquad \textbf{(Eqn. 35)}$$

In order to determine the influence of the indentation on the calculated stiffness and stress level, the Guide to the Expression of Uncertainty in Measurement (GUM) approach has been used [140]. The GUM approach is to express the results of a measurement, here the stiffness or the stress level, as a best estimate of the measurement, here the displacement or the thickness of the specimen, with an associated measurement uncertainty, here the indentation. In general cases, the knowledge about an input quantity can be deduced in two ways ; from repeated measured values (Type A evaluation of uncertainty), or scientific judgement or other information concerning the possible values of the quantity (Type B evaluation of uncertainty). In our case, we are concerned by the type B evaluation.

First, the uncertainty on the stiffness, *U(K)*, can be written as a function of the combined standard uncertainty, $u_c(K)$, as follows

$$U(K) = 2\cdot u_c(K) \qquad \textbf{(Eqn. 36)}$$

In addition, the combined standard uncertainty $u_c(K)$ is defined by the law of propagation of uncertainty, which is a function of the partial derivative of first order of *K* with respect to *disp*, and the standard uncertainty *u(disp)* associated with *disp*.

$$u_c(K) = \left(\frac{\partial K}{\partial disp}\right)\cdot u(disp) \qquad \text{With} \quad K = \frac{F}{disp} \qquad \textbf{(Eqn. 37)}$$

If we consider that the standard uncertainty associated with *disp*, *u(disp)*, follows an asymmetric right angled triangular distribution with a range, noted Δi, which is equal to the maximal indentation value, then *u(disp)* can be expressed as :

$$u(disp) = \frac{\Delta i}{\sqrt{18}} \qquad \textbf{(Eqn. 38)}$$

So, by integrating *(Eqn. 38)* in *(Eqn. 37)*, we obtain the expression of the combined standard uncertainty $u_c(K)$ *(Eqn. 39)* and the uncertainty on the stiffness *U(K)* *(Eqn. 40)*.

$$u_c(K) = \left(-\frac{F}{disp^2}\right)\cdot\frac{\Delta i}{\sqrt{18}} \qquad \textbf{(Eqn. 39)}$$

$$U(K) = -\left(\frac{2}{\sqrt{18}}\right)\cdot K\cdot\frac{\Delta i}{disp} \qquad \textbf{(Eqn. 40)}$$

Figure 116 represents the evolution of the measured damage during the fatigue test of the specimen HH1_18 and the associated uncertainty by considering the indentation value.

So, with the same method, we can define the expression of the uncertainty on the stress level $U(R\sigma)$ as a function of the stress level itself $R\sigma$, the thickness of the specimen h and the range distribution Δi.

$$U(R\sigma) = \left(\frac{4}{\sqrt{18}}\right) \cdot R\sigma \cdot \frac{\Delta i}{disp} \qquad \textbf{(Eqn. 41)}$$

If we consider the specimen #HH1_18, the uncertainty on the calculated stress level is equal to *11.30 %* of $R\sigma$ in the worst case, *i.e.* with the maximal value of indentation.

Table 28. *Summary of the results obtained for indentation after cyclic loading*

Specimen	Applied stress $[MPa]$	Stress level Rσ	Lifetime	Length of the indentation $[mm]$	Depth of the indentation $[mm]$
HH1_8 *(a)*	904.695	0.69	11 576	4.12	0.24
HH1_5 *(b)*	874.024	0.67	21 858	4.85	0.38
HH1_18 *(c)*	680.144	0.52	278 083	5.27	0.65

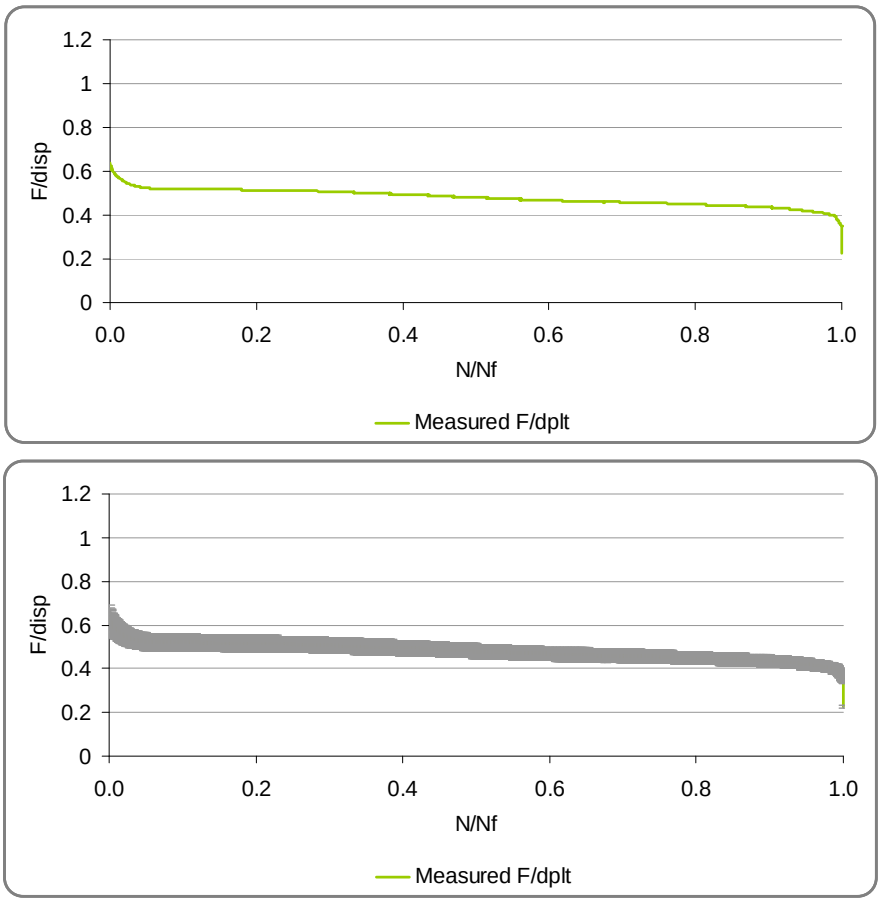

Figure 116. *Evolution of damage measured and corrected with the indentation value obtained for the HiPer-tex™ specimen HH1_18*

3.5- Summary and conclusion of the mechanical characterization

The mechanical characterization has been performed to quantify the influence of glass fibre type on composite performance and behaviour and to identify and quantify the influence of the specific environmental conditions, especially natural sea water.

In order to obtain information about the influence of the environment, quasi-static (CRP and flexural tests) and fatigue tests have been carried out, both in air and in natural circulating sea water. In addition, several tests have been performed on aged and fatigued specimens. To study the influence of the type of reinforcement, the experimental study has been performed on composite materials reinforced with three types of glass fibres and their results have been compared. The main experimental data (failure stresses and moduli) are summarized in *Table 29*.

By performing fatigue tests in air and in natural circulating sea water, we have noticed that sea water has a significant influence on the fatigue behaviour of E-glass composites, while HiPer-tex™ are less sensitive to the environment fatigue life. For a given number of cycles before failure, the corresponding stress level is reduced in natural sea water compared to in air. Nevertheless, sea water does not appear to have any influence in terms of the shape of the evolution of damage during the fatigue life. In addition, quasi-static tests performed on aged specimens have established that the sea water absorption strongly influences the mechanical properties of the composite materials in terms of failure stress but hardly affects moduli. To have a better understanding of the phenomena involved in these drops of mechanical properties, tensile tests on aged pure resin specimens and interlaminar shear stress tests on aged infused composites have been performed. These allow us to highlight the influence of the matrix, the fibres and the interface fibre/matrix on the behaviour of the aged composite.

To complete this study, quasi-static tests have been performed on specimens which have been subjected to cycles of fatigue. The experimental results indicate that fatigue loading up to $N/N_f=0.6$ has a little effect on residual properties.

Table 29. *Summary of the main experimental results obtained for the three infused composite materials*

Infused E-glass composite				
Failure stress $[MPa]$		Tension	Compression	Bending
Initial state		750	473	1 138
Aged states	168 hours			1 085
	672 hours	590	395	946
	1 008 hours	595	386	
	1 344 hours	555	382	799
	2 016 hours			728
	2 352 hours	427	415	
	2 688 hours			665
	5 040 hours			684
	3 024 hours + drying			789
Fatigued states	$N/N_f = 0.1$			1 293
	$N/N_f = 0.2$			1 223
	$N/N_f = 0.3$			1 120
	$N/N_f = 0.6$			1 175
Axial modulus $[GPa]$				
Initial state		46.0	45.2	
Aged states	672 hours	48.4	52.7	
	1 008 hours	48.3	51.1	
	1 344 hours	48.1	47.5	
	2 352 hours	51.7	45.8	
Infused Advantex® composite				
Failure stress $[MPa]$		Tension	Compression	Bending
Initial state		798	431	866 960*
Fatigued states	$N/N_f = 0.1$			1 104
	$N/N_f = 0.2$			1 092
	$N/N_f = 0.3$			1 035
	$N/N_f = 0.6$			1 108
Axial modulus $[GPa]$				
Initial state		45.0	46.4	
** This initial value of failure stress is issued from the experimental data of the plate #HA1*				
Infused HiPer-tex™ composite				
Failure stress $[MPa]$		Tension	Compression	Bending
Initial state				1 314
Aged states	2 688 hours			924
	5 040 hours			1 103
	3 024 hours + drying			746
Fatigued states	$N/N_f = 0.1$			1 436
	$N/N_f = 0.2$			1 437
	$N/N_f = 0.3$			1 374
	$N/N_f = 0.6$			1 432
Axial modulus $[GPa]$				
Initial state		55.9	48.8	

CHAPTER IV
MODELLING THE INFLUENCE OF WATER ABSORPTION AND FATIGUE LOADING

IV- MODELLING THE INFLUENCE OF WATER ABSORPTION AND FATIGUE LOADING

In order to develop tools to evaluate the long term behaviour of composite structures, numerical modelling has been performed. This is based on the finite element method together with the experimental results presented in the previous sections. By considering the low results obtained by the infused Advantex® composite during the experimental study, this material was not taken into account in the numerical modelling study.

The finite element analysis (FEA) is a numerical technique used to find approximate solutions of partial differential equations (PDE). The solution approach is based either on eliminating the differential equation completely, for steady state problems, or integrating the PDE into an approximating system of ordinary differential equations, which are numerically solved using standard techniques (Euler's method, Runge-Kutta, …).

The finite element method (FEM) is a good choice for solving partial differential equations on complex domains which change or move during the study or which need different precision states over them. In addition the FEM allows detailed visualisation of where structures bend or twist and represents the displacements or the distribution of stresses.

The numerical part of this study is divided into four main parts. The first one is the numerical modelling of the water absorption in the specimens. The second part is the numerical modelling of the mechanical behaviour of composite material specimens subjected to simple loads, such as tension or bending. The third is the numerical modelling of the coupling between the water absorption and the mechanical damage of composite specimens. Finally the last part is the numerical modelling of the evolution of damage during fatigue tests. The main objective of this study is to obtain tools to simulate a complex structure, a tidal turbine blade, subjected to complex loads in sea water. The sequence of the numerical modelling is presented in *Figure 117*.

Before defining the different numerical models, a short introduction to the numerical modelling tool is given.

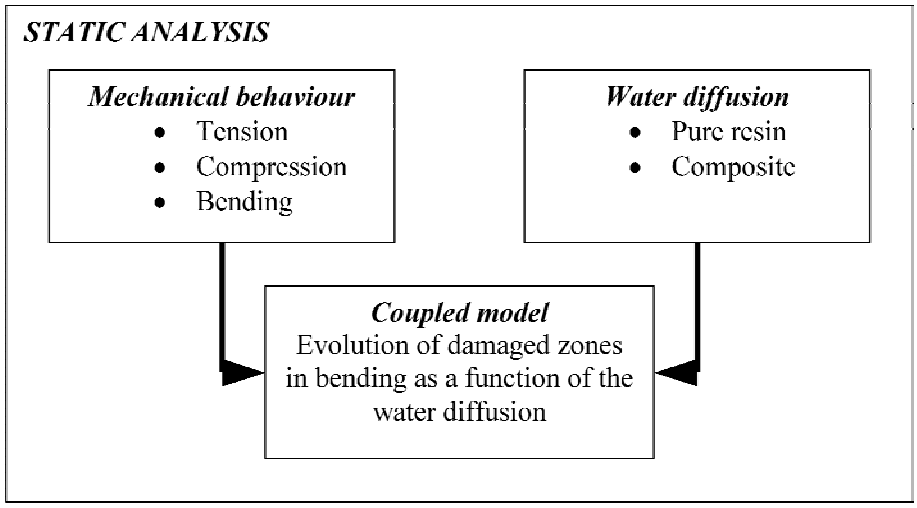

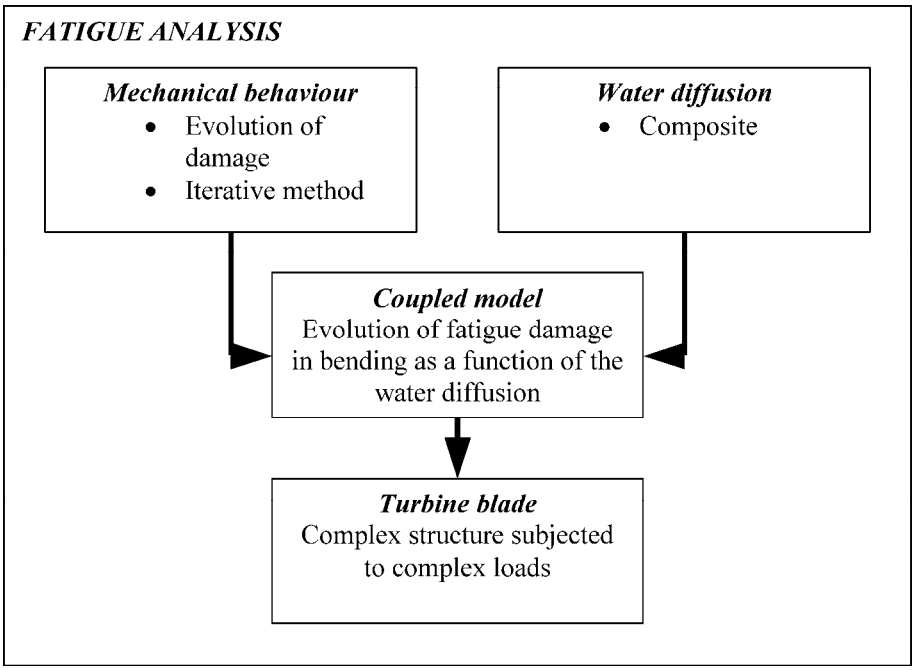

Figure 117. *Modelling procedure used in the study*

1- Introduction to the numerical modelling tool

Due to the complexity of the phenomena to be modelled, namely mechanical behaviour with evolution of damage, water absorption and coupling between them, the software *COMSOL Multiphysics*™ has been chosen.

COMSOL Multiphysics™ is an interactive environment for modelling and solving all kinds of scientific and engineering problems based on partial differential equations (PDE). In addition, with this software we have the possibility to extend for one type of physics into multiphysics models that solve coupled phenomena simultaneously. *COMSOL Multiphysics*™ compiles sets of PDE which represent entire models. It provides three ways of describing PDE through three mathematical application modes. The first one, suitable for linear or nearly linear models is the coefficient form. The second one is the general form which is suitable for the nonlinear models. The third one is for models with PDE on boundaries, edges or points or for models using terms with mixed space and time derivatives, it is the weak form. Using these different approaches stationary and time dependent analysis, linear and nonlinear analysis and eigenfrequency and modal analysis can be performed.

COMSOL Multiphysics™ uses the finite element method (FEM) to solve the PDE. The software runs the finite element analysis both with adaptive meshing and error control using different numerical solvers. PDE describe a wide range of scientific and engineering phenomena, so *COMSOL Multiphysics*™ can be used in many applications. In our study, we have used the Structural mechanics and the Chemical engineering modules.

1.1- Definition of diffusion models

In the diffusion application of the Chemical Engineering module, Fick's law describes the diffusive transport in the flux vector. This application mode is available in 1D, 2D and 3D as well as in axisymmetric formulations in 1D and 2D. The dependent variable is the concentration *c*.

The equation which describes the diffusion in *COMSOL Multiphysics*™ has the same form as the heat equation and is written as :

$$\delta_{ts}\frac{\partial c}{\partial t}+\nabla\cdot(-D\nabla c)=R \qquad \textit{(Eqn. 42)}$$

where δ_{ts} is the time-scaling coefficient, c is the concentration, D is the diffusion coefficient and R is the reaction rate which describes the volume density of mass creation. The diffusion process can be anisotropic, in which case D is a tensor.

The numerical modelling is divided into four steps. First, the geometry modelling with the definition of the global shape and the dimensions. Second, the physics settings with the definition of the sub-domains settings, the definition of the boundaries and initial conditions. Third, the mesh generation, with the choice of the finite element and its size. Fourth, the computing, the post-processing and the visualization of the results.

1.2- Definition of structural mechanics models

The Structural Mechanics module in *COMSOL Multiphysics*™ allows us to solve problems in the fields of structural and solid mechanics, adding special elements such as beams, shells and plates. It provides static, quasi-static transient, time dependent, parametric, linear buckling, eigenfrenquency and frequency-response analysis capabilities. In addition, both linear and nonlinear material models can be used such as elasto-plastic models, large deformation effects can be included in the analysis and materials can be isotropic, orthotropic or fully anisotropic.

As for the diffusion model, several steps are needed to create a model. First, the geometry, then the physics settings (load and constraints), the mesh and the computing. The last step is again the post-processing and the visualization of the results.

2- Water absorption modelling

In order to have a better understanding of the water absorption phenomena and the evolution of the water uptake in a infused composite structure, a numerical model has been developed. The process of water absorption has been modelled and analysed using the diffusion laws and the finite element approach.

This study is divided into two parts, first the definition of the diffusion models and the presentation of the results, and then the evaluation of the model by comparison with the experimental results.

2.1- Definition of the diffusion models

The diffusion process can be defined following various models but Fick's and Langmuir-type laws are the most popular. According to the experimental data and the analytical treatment, the two formulations can be used for our composite materials. So the two numerical models have been developed in parallel in order to compare their results.

In addition, a study concerning the influence of the variations on the parameters has been performed. It is presented in *Annex 8*.

2.1.1. Kinetics of diffusion following a Fickian model

The pure resin material and two infused composite materials (E-glass and HiPer-tex™) have been modelled.

a) Geometry modelling

As the experimental weight gain data have been obtained on square specimens, the numerical models have also been defined with square specimens. The dimensions have been chosen to be the mean values of the real dimensions for each infused composite for each environment (natural circulating sea water at *4°C*, *20°C*, *40°C* and *60°C*). The geometrical data are summarized in *Table 30*.

As the model presents a symmetry in the geometry (square) and in the boundary conditions (total immersion), the numerical model has been defined as one eighth of a coupon

Table 30. *Mean dimensions of the square specimens used for modelling the water absorption of pure resin, infused E-glass and HiPer-tex™ composite*

Pure resin	***4°C***	***20°C***	***40°C***	***60°C***
Length (SD) [*mm*]	50.91 (1.25)	50.53 (0.28)	50.74 (0.39)	50.78 (0.38)
Thickness (SD) [*mm*]	4.99 (0.03)	4.96 (0.06)	4.99 (0.03)	4.96 (0.04)
Infused E-glass	***4°C***	***20°C***	***40°C***	***60°C***
Length (SD) [*mm*]	49.98 (0.11)	49.86 (0.17)	49.80 (0.13)	49.89 (0.12)
Thickness (SD) [*mm*]	5.45 (0.06)	5.50 (0.06)	5.44 (0.04)	5.52 (0.10)
Infused HiPer-tex™	***4°C***	***20°C***	***40°C***	***60°C***
Length (SD) [*mm*]	50.81 (0.17)	50.89 (0.42)	50.75 (0.26)	51.02 (0.21)
Thickness (SD) [*mm*]	5.26 (0.18)	5.37 (0.09)	5.46 0.03)	5.47 (0.05)

b) Physics settings

The sub-domain settings describe the material properties, in our case the diffusion coefficients obtained according to the analytical formulation and the experimental data for each material in each environment (*Section 2.2*, *Chapter III*) (*Table 31*).

The boundary conditions are defined to take into account the symmetry conditions on three faces and an applied concentration on the three other faces. This applied concentration which represents the total immersion of the coupon, is defined as a function of the mass at saturation of the composite material, the initial weight of the specimen and its volume.

In addition, constants and global expressions are defined (*Table 32*), as well as integration coupling variables such as *m* which represents the water uptake as a function of the time. *m* is the integration on the volume of the concentration *c* of the coupon at each time. All the constants and global expressions for each material in each environment are summarized in *Annex 9*.

Table 31. *Summary of the diffusion coefficient values used for the Fickian diffusion modelling*

Pure resin	***4°C***	***20°C***	***40°C***	***60°C***
Diffusion coefficient D $[m^2/s]$ (Stand. Dev.)	2.58E-14 (5.79E-16)	6.66E-14 (2.00E-15)	3.18E-13 (3.66E-15)	6.15E-13 (1.33E-14)
Infused E-glass	***4°C***	***20°C***	***40°C***	***60°C***
Diffusion coefficient D $[m^2/s]$ (Stand. Dev.)	1.16E-14 (8.47E-16)	3.59E-14 (1.34E-15)	1.73E-13 (1.07E-14)	1.19E-12 (6.99E-14)
Infused HiPer-tex™	***4°C***	***20°C***	***40°C***	***60°C***
Diffusion coefficient D $[m^2/s]$ (Stand. Dev.)	7.21E-15 (8.01E-16)	3.33E-14 (8.98E-15)	1.63E-13 (7.91E-15)	1.06E-12 (7.74E-14)

Table 32. *Constants and expressions defined for modelling the water absorption*

Constants		
M_inf		Mass at saturation in $[\%]$
D		Diffusion coefficient in SW in $[m^2/s]$
M0		Initial mass of the specimen in $[kg]$
length		Length of the specimen in $[m]$
thickness		Thickness of the specimen in $[m]$
Global expression		
m_tot	8*m	Water uptake in $[kg]$
V	length^2*thickness_4	Volume of the specimen in $[m^3]$
m_abs	M_inf*M0	Maximal water uptake in $[kg]$
c0	m_abs/V	Initial applied concentration in $[kg/m^3]$

c) Mesh generation

Two type of mesh are distinguished, the unstructured and the structured mesh. The first one refers to an arbitrary distribution of mesh points, where the points are connected by triangles, quadrilaterals or polygons in 2D or by various polyhedrals in 3D. On the contrary, a structured mesh is composed of families of intersecting lines, one for each space dimension (two families in 2D and three in 3D), where each mesh point is located at the intersection of one line, and only one line, of each family.

So, the first mesh to be defined consists of tetrahedral Lagrange quadratic elements as presented on *Figure 118a*. But when we observe the evolution of the concentration on the coupon at a given time step for different mesh sizes, as presented on *Figure 119*, we can note that it varies. In some cases, it happens that concentration is negative which is impossible. These results are due to the boundary effect. So, in order to block this effect, a new mesh has to be defined.

The second mesh to be defined consists of uniform mapped Lagrange quadratic elements as presented on *Figure 118b*. But in this case, we have also observed small boundary effects.

In order to avoid these effects, a new distributed mesh has been defined (*Figure 118c*). By keeping the same number of edge elements as in the previous version, smaller elements

have been placed on external edges and bigger elements on internal edges. So, when we compare the results obtained for the concentration at a given time step for the different mesh cases (*Figure 120*), we observe that the boundary effect has disappeared with the distributed mapped mesh. So, this mesh case has been conserved for the rest of the numerical study of the diffusion.

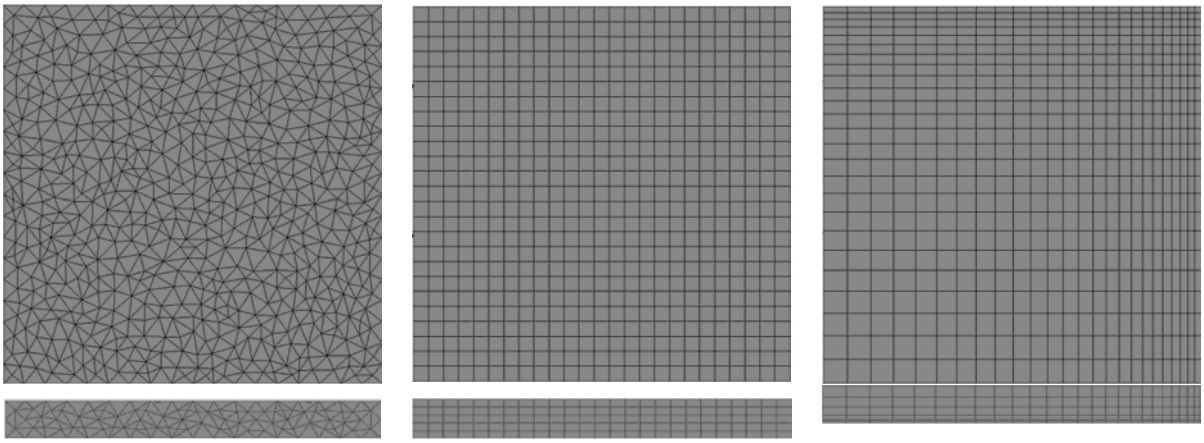

(a) *(b)* *(c)*

Figure 118. *Graphical representation of the different meshes :*
a) Tetrahedral elements, b) Uniform mapped mesh, c) Distributed mapped mesh

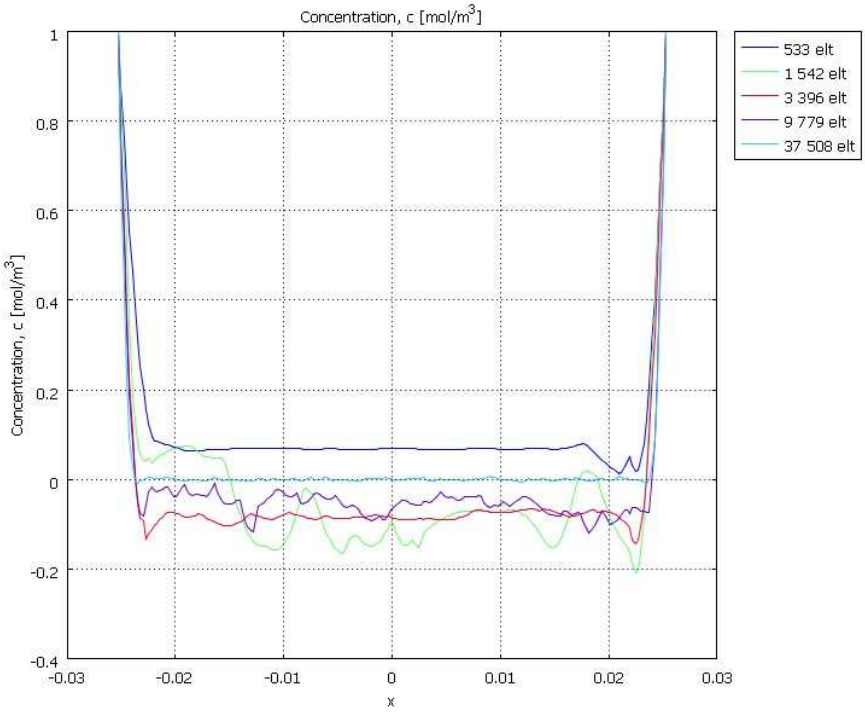

Figure 119. *Comparative curves of the concentration at a given time step for different tetrahedral mesh sizes*

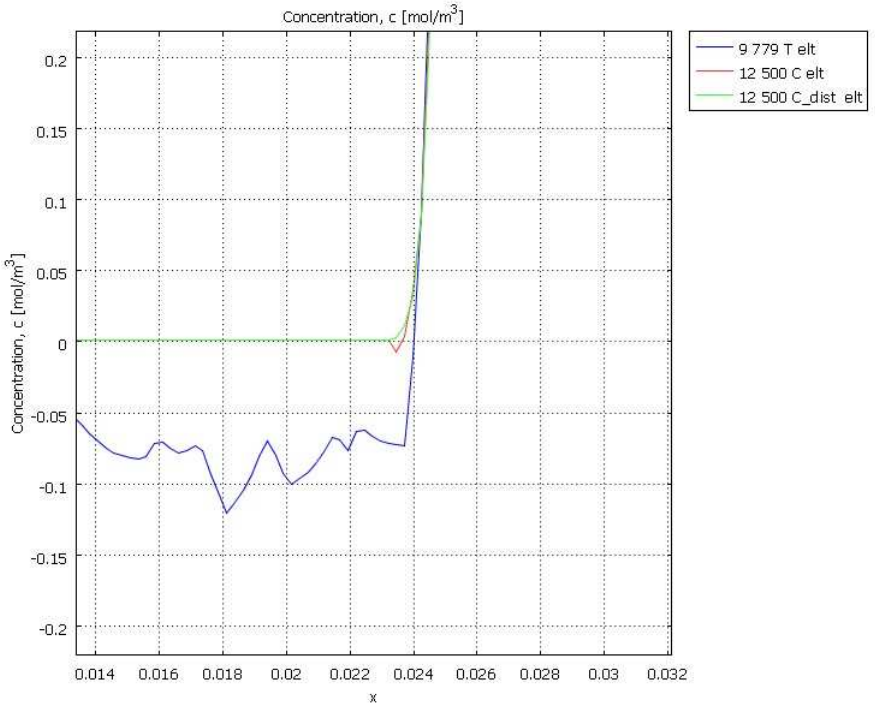

Figure 120. *Comparative curves of the concentration at a given time step for tetrahedral mesh (blue), regular mapped mesh (red) and distributed mapped mesh (green)*

d) Computing and visualization of the results

COMSOL Multiphysics™ includes a large set of solvers for PDE-based models such as stationary linear or non linear, time-dependent, eigenvalue or parametric. In our case, we have chosen to perform a transient analysis by using a time-dependent solver. The calculation goes from *0* to *700 days* with a time step of *1 week.*

The main numerical results observed are the evolution of the weight gain as a function of the square root of time for each material in each environment and the distribution of the water concentration in the coupon. All these results are presented on *Figure 121* for the weight gain and *Figure 122* for the concentration at *t=15 weeks*.

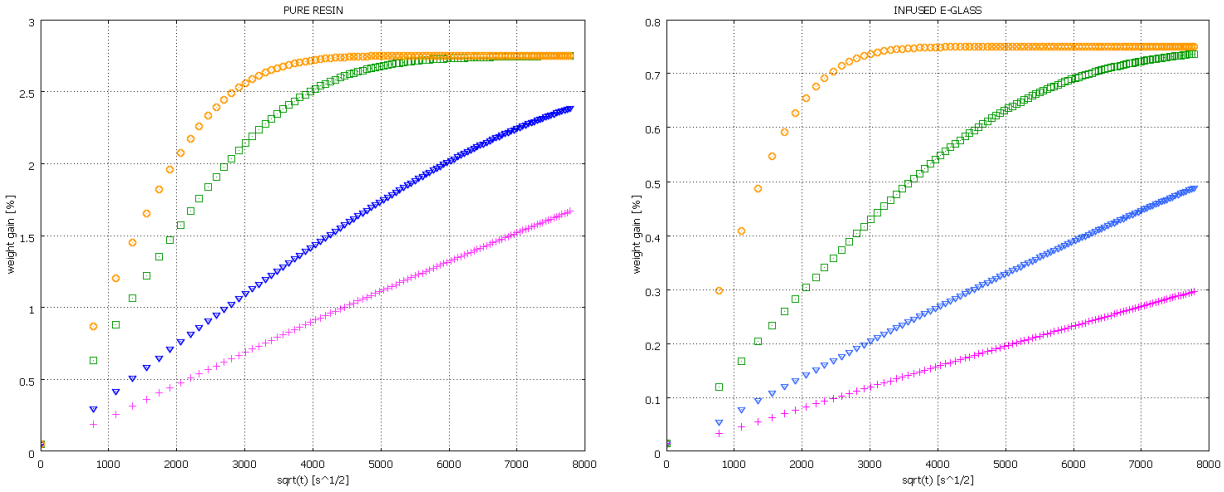

(a) *(b)*

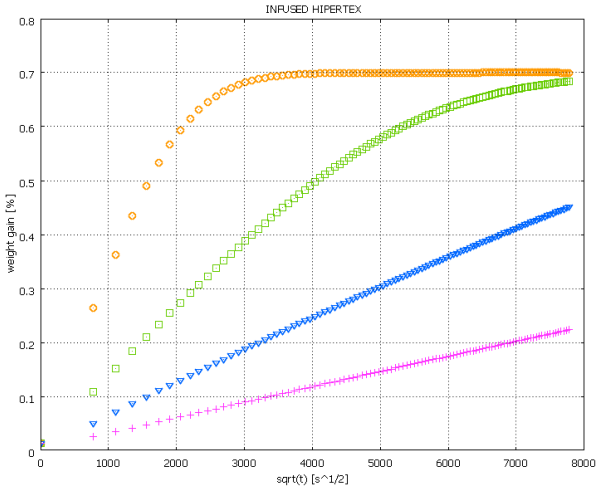

(c)

Figure 121. *Comparatives curves of the calculated weight gain at each temperature (4°C in pink, 20°C in blue, 40°C in green and 60°C in orange) for each material :*
a) pure resin, b) infused E-glass and c) infused HiPer-tex™

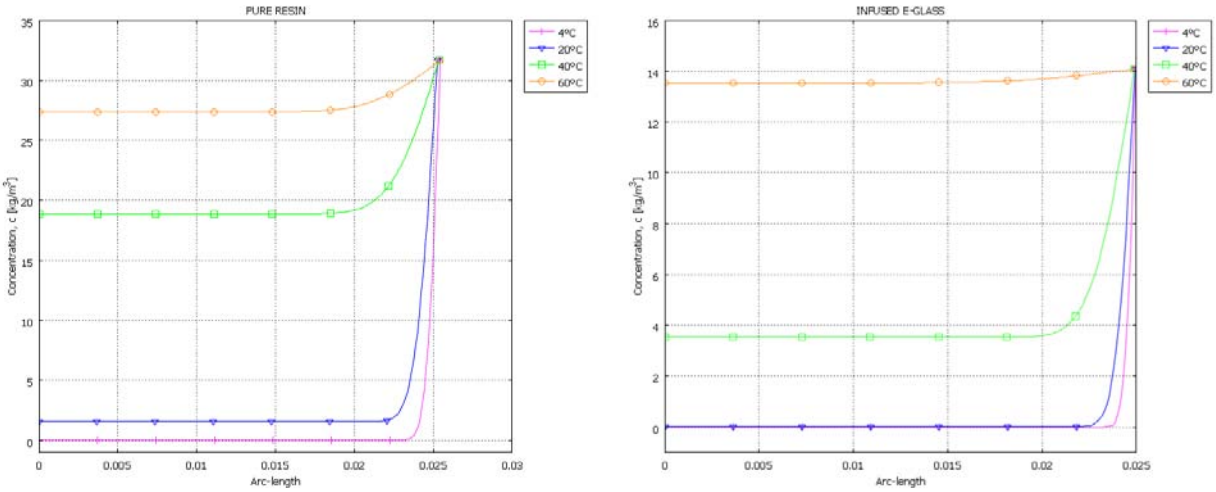

(a) *(b)*

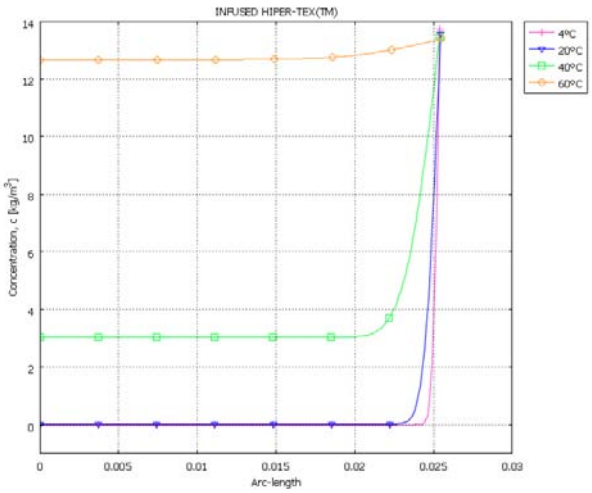

(c)

Figure 122. *Comparatives curves of the calculated concentration for t=15 weeks at each temperature (4°C in pink, 20°C in blue, 40°C in green and 60°C in orange) for each material :*
a) pure resin, b) infused E-glass and c) infused HiPer-tex™

2.1.2. Kinetics of diffusion following a Langmuir-type model

Even if the diffusion defined in *COMSOL Multiphysics*™ follows a Fick's law, it is possible to specify a Langmuir-type model by coupling two diffusions. One of the diffusions represents the free phase and the other the bound phase of the Langmuir-type diffusion. These diffusions are linked by the reaction rate *R*.

In order to be sure of the kinetics of diffusion, a Langmuir-type model has been developed in parallel. This model has only been developed for one case, the pure resin material in natural sea water at *40*°C.

a) Geometry modelling

As the experimental results are the same as those used for the Fickian model, the geometries are also the same. So, one eighth of square specimens have been modelled with the same dimensions as those used for the Fickian model and summarized in *Table 30*.

b) Physics settings

The sub-domain settings describe the material properties, in our case the diffusion coefficients, *D*, β and γ obtained according to the analytical formulation. The experimental data for each material in each environment are given (*Table 33*). In addition, the reaction rate *R* is defined as a function of the coefficients β and γ and the concentration of the free and the bound phase (*c_free* and *c_bound*).

$$R=\pm(\gamma \cdot c\_free-\beta \cdot c\_bound) \qquad \textbf{(Eqn. 43)}$$

As for the Fickian model, the boundary conditions have been defined to take into account the symmetry conditions on three faces and an applied concentration on the three other faces. The applied concentration is also defined as a function of the mass at saturation of the composite material, the initial weight of the specimen and its volume.

Besides, constants, global expressions and integration coupling variables are defined, in the same way as for the Fickian model.

Table 33. *Summary of the diffusion coefficient values used for the Langmuir-type diffusion modelling*

Pure resin at 40°C	
Coefficient diffusion D (SD) $[m^2/s]$	3.39E-13 (6.34E-15)
Coefficient β (SD) $[s^{-1}]$	1.16E-5 (0)
Coefficient γ (SD) $[s^{-1}]$	7.28E-7 (1.06E-7)

c) Mesh generation

In this case, the mesh has been chosen to avoid the boundary effects. The mesh consists of distributed mapped Lagrange quadratic elements.

d) Computing and visualization of the results

As the diffusion is a transient phenomenon, a time-dependent solver has been used to compute the solution.

As for the Fickian model, the evolution of the weight gain as a function of the square root of time has been observed (*Figure 123a*), as well as the distribution of the concentration in the coupon at a given time step (*Figure 123b*).

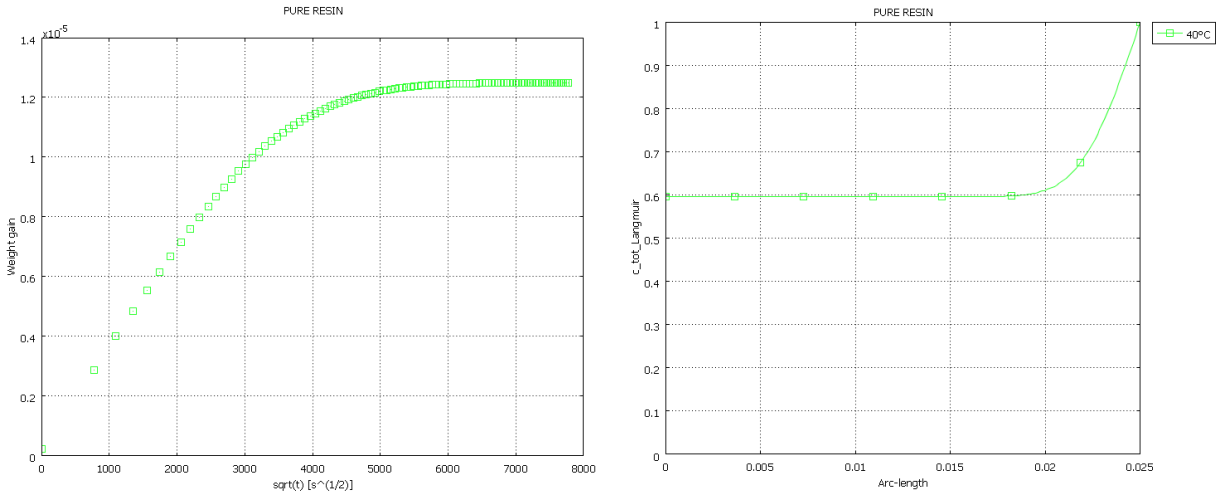

(a) *(b)*

Figure 123. *Graphical representation of the calculated weight gain at 40°C a) and the distribution of the concentration at t=15 weeks b) in pure resin material according to the Langmuir-type model*

2.1.3. Comparison of the two diffusion models

From the experimental data it is not immediately clear whether a Fickian model, will be sufficient to model the diffusion behaviour, as there is a tendency for the weight gain at *60°C* to continue to increase after the "knee". In order to choose the appropriate modelling of water diffusion for the rest of the study, the Fickian and the Langmuir-type models have been compared. *Figure 124* shows the weight gain of the pure resin materials in natural sea water at *40°C* by considering a Fickian model or a Langmuir-type model. *Figure 125* represents the distribution of the concentration in the coupon at different times by considering a Fickian or a Langmuir-type model. When we compare the results, we observe that there is no important difference between the two formulations either for the weight gain or the distribution of the concentration.

This similarity between the two diffusion formulations is probably due to the experimental data, which do not provide enough information to describe accurately the Langmuir-type model. In order to have an accurate description of the diffusion, experimental data should cover a longer immersion time at lower temperatures.

So, for the remainder of the study, the Fickian model has been chosen to describe the kinetics of diffusion in the pure resin materials and in the three infused composite materials.

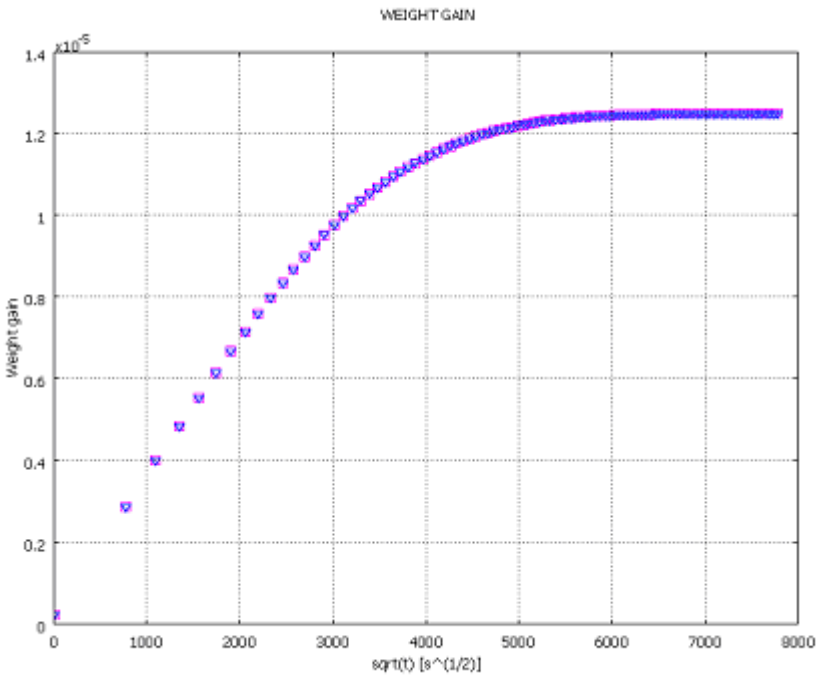

Figure 124. *Comparative curves of the water uptake by considering a Fickian model (squares) and a Langmuir-type model (triangles)*

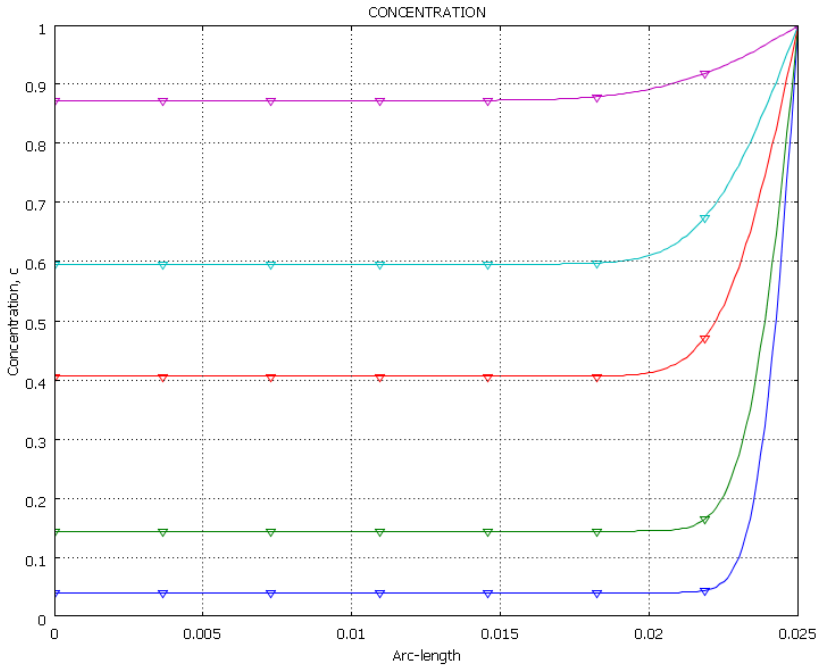

Figure 125. *Comparative curves of the distribution of the concentration in the coupon by considering a Fickian model (continuous line) and a Langmuir-type model (triangles)*

2.2- Evaluation of the model and comparison with the experimental results

A numerical model is a complex system of equations with boundary conditions. So, in order to make sure that the computational results are reliable and consistent with the investigated phenomenon, the results issued from the numerical model have to be confirmed.

So, the experimental data obtained for the weight gain have been compared to the computed values, as presented on *Figure 126* for the pure resin material, *Figure 127* for the infused E-glass, and *Figure 128* for the infused HiPer-tex™ composite.

For the pure resin material, the computed results follow the experimental ones in the early stages of immersion, except for the tests carried out at *60°C* (the anomalous shape of curve at *60°C* has been already discussed in *Section 2.1, Chapter III*). For the three infused composites, the computed solutions seem to follow the experimental data but these materials are still in the early stages of ageing by comparison with the pure resin material. Beyond about *4* months the weight gain at *60°C* of the infused E-glass composite appears to increase, the Fickian model is not appropriate beyond this time.

According to the experimental data available for the moment, we can consider that the numerical modelling of the water diffusion in the composite materials using a Fickian model is reasonably consistent with the measured behaviour.

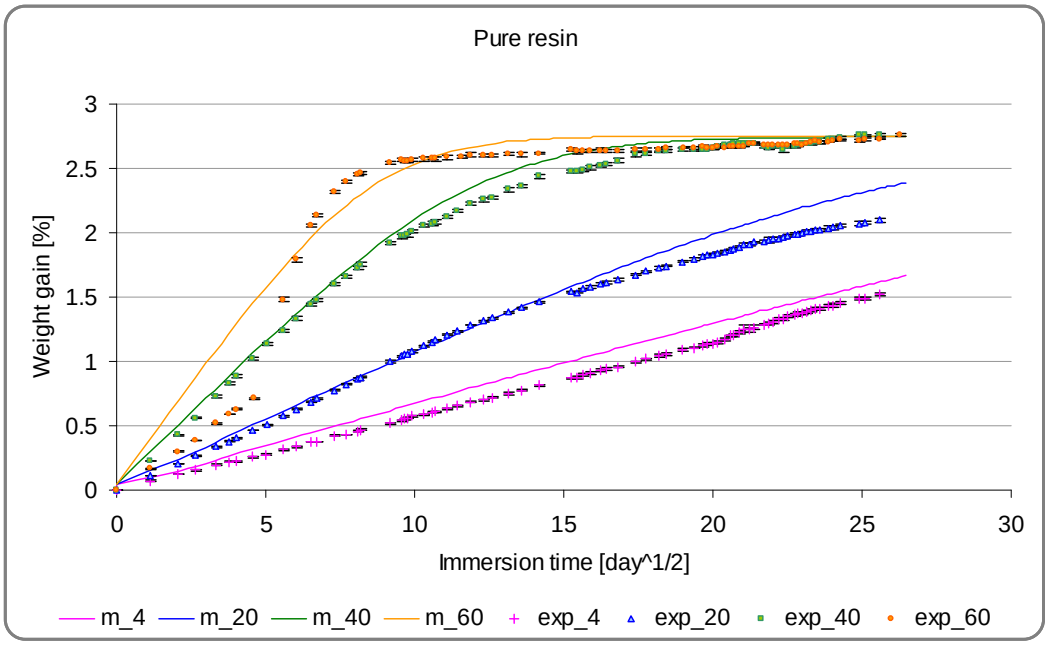

Figure 126. *Comparative curves of the experimental (points) and computed (lines) weight gain for pure resin in natural circulating sea water at four temperatures*

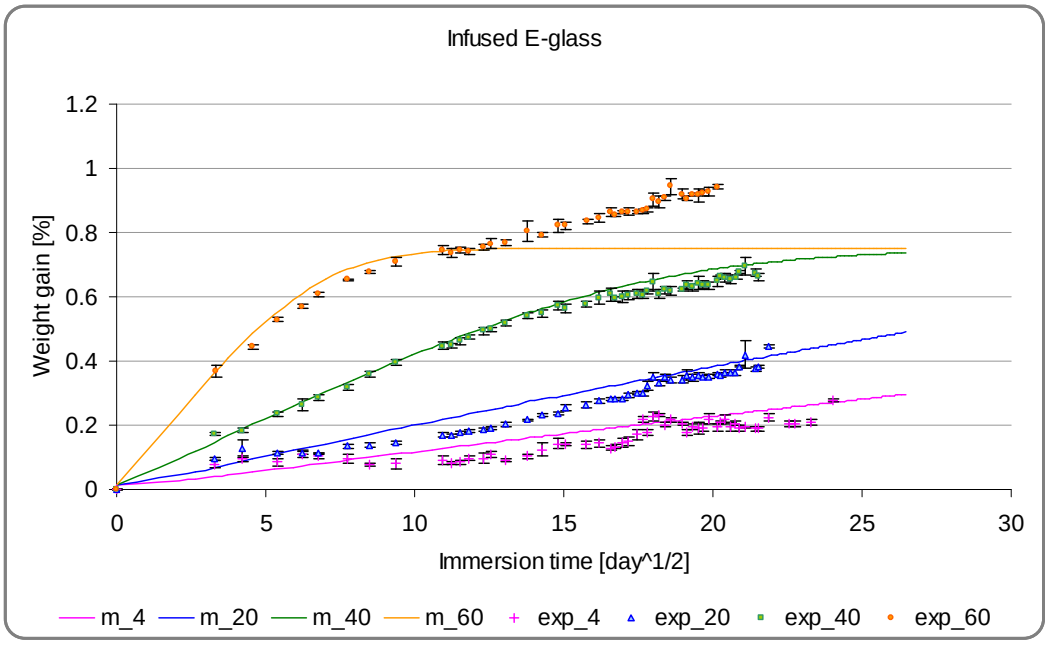

Figure 127. *Comparative curves of the experimental (points) and computed (lines) weight gain for infused E-glass composite in natural circulating sea water at four temperatures*

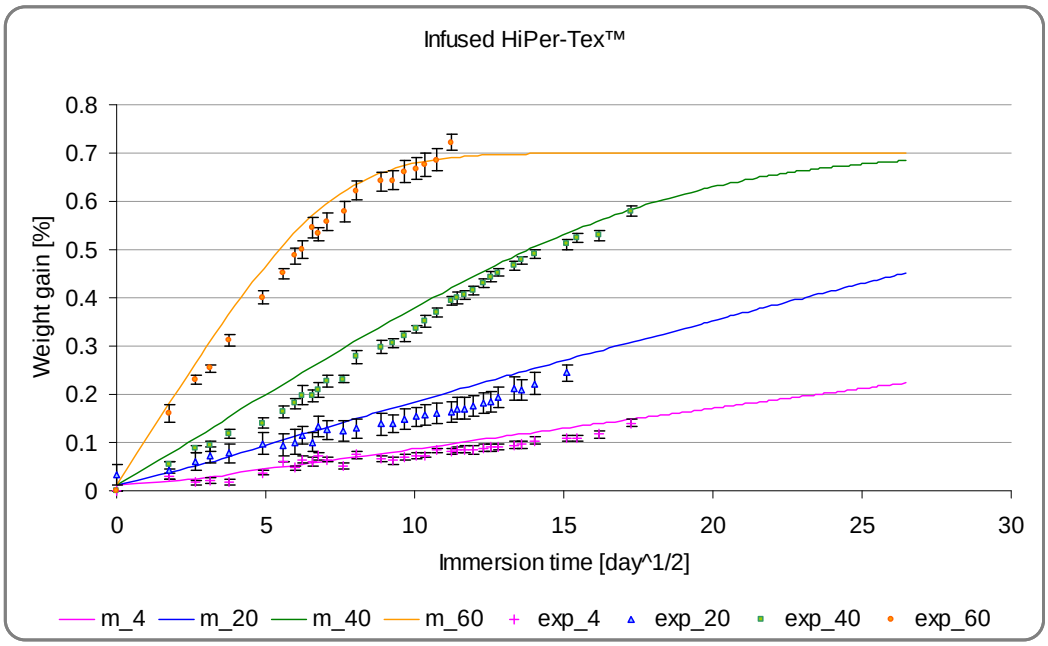

Figure 128. *Comparative curves of the experimental (points) and computed (lines) weight gain for infused HiPer-tex™ composite in natural circulating sea water at four temperatures*

3- Mechanical behaviour modelling

In order to have a better understanding of the mechanical behaviour of the composite materials studied here, several numerical models have been defined using the finite element approach. This part of the study is focused on the mechanical behaviour of the infused E-glass and HiPer-tex™ composites.

A preliminary study, presented in *Annex 10*, was performed in order to define the influence of the variations of the geometry and the elastic moduli on the mechanical response of the specimens. It showed that the most influent parameter in the mechanical response of a dog-bone specimen is the thickness for the geometrical parameters and axial modulus for the material parameters.

The first step in the numerical modelling of the mechanical behaviour is to define a model to simulate elastic behaviour for simple loading cases on composite dog-bone specimens. Three numerical models have been created, in tension, in compression and in bending. The three models defined for each composite materials are presented in this part and assessed by comparison with the experimental results.

3.1- Dog-bone specimen in tension and in compression

The mechanical behaviour in tension and in compression (CRP tests) has been examined first.

3.1.1. Geometry modelling

As experimental data have been obtained on dog-bone specimens, the numerical models have also been defined for this shape. The chosen dimensions are equal to the mean values of the real dimensions for each composite material. The geometrical data are summarized in *Table 34*. L_T is the total length, b the width at the end of the loading jaws of the test machine, b_0 the width in the centre of the specimen and h the thickness.

As the model presents a symmetry in the geometry and in the boundary conditions both in tension and in compression, the numerical models have been defined as a half of a specimen as presented on *Figure 129*.

Table 34. *Mean dimensions of the dog-bone specimens used for tension and compression modelling*

	Modelling in tension		***Modelling in compression***	
	E-glass	HiPer-tex™	E-glass	HiPer-tex™
L_T [*mm*] (SD)	140.26 (0.18)	139.92 (0.02)	140.11 (0.01)	139.90 (0.03)
b [*mm*] (SD)	25.27 (0.22)	25.00 (0.02)	25.08 (0.01)	25.00 (0.01)
b_0 [*mm*] (SD)	10.23 (0.17)	10.04 (0.01)	10.11 (0.01)	10.03 (0.01)
h [*mm*] (SD)	5.50 (0.07)	5.55 (0.10)	5.56 (0.03)	5.50 (0.04)

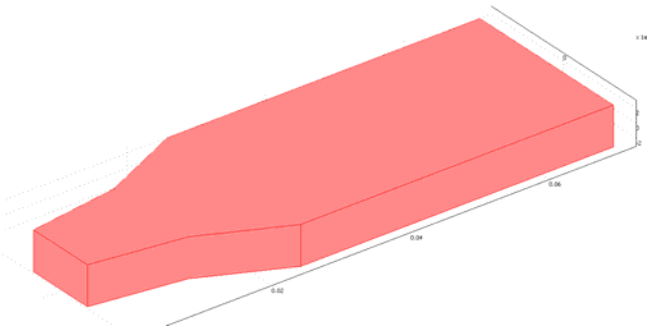

Figure 129. *View of the half-specimen used for tension and compression modelling*

3.1.2. Physics settings

The sub-domain settings describe the material properties, in our case the elastic moduli (summarized in *Table 35*) issued from the experimental data in tension and in compression. The preliminary study presented in *Annex 10* indicated that the mechanical response is dominated by the longitudinal modulus. The two composite materials, considered as homogeneous materials, are defined as transversely isotropic materials.

The boundary conditions describe the symmetry condition (in blue on *Figure 130*), the constraints, and the loads applied to the specimens (represented with green arrows on *Figure 130*). These conditions are defined according to the experimental set up.

Table 35. *Summary of the axial moduli used for the tension and compression modelling*

Axial moduli	E-glass	HiPer-tex™
E in tension $[GPa]$	46.9	55.9
E in compression $[GPa]$	45.2	48.8

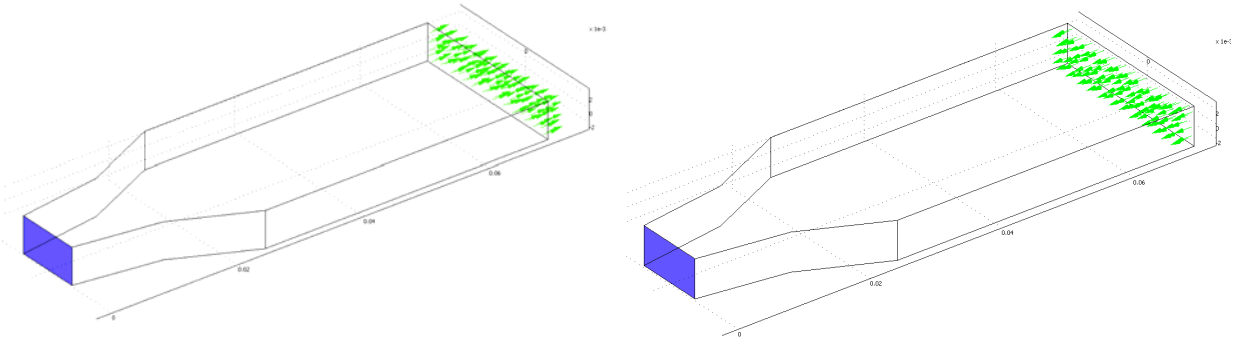

(a) *(b)*

Figure 130. *Representation of the boundary conditions defined : a) in tension, b) in compression*

3.1.3. Mesh generation

Because the specimen is subjected to tension and compression and due to the specific shape of the coupon, a mesh constituted of tetrahedral Lagrange quadratic elements was chosen (*Figure 131*).

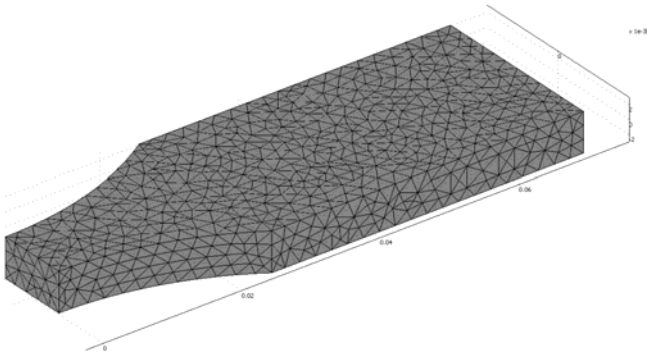

Figure 131. *View of the mesh used for tension and compression modelling*

3.1.4. Computing, results and evaluation

In order to determine the evolution of the mechanical response as a function of the applied load, we have chosen a parametric solver. The applied load has been defined to vary from *0* to *5 500 N* with a load step of *50 N*.

The main numerical results observed are the deformed shape and the distribution of longitudinal stress in the specimen for each loading case (tension or compression) presented on *Figure 132* for a given value of load (*F=5 500 N*). In addition, the evolutions of stress and strain are exported.

As mentioned in the previous section, a numerical model needs to be evaluated by comparing the numerical results with experimental data. So the experimental stress-strain curves obtained for each composite material both in tension and in compression have been compared to the computed data exported. The comparative curves are presented on *Figure 133a* for tension and on *Figure 133b* for compression. The blue curves represent the infused E-glass composite and the green curves represent the infused HiPer-tex™ composite.

These results indicate that the numerical models defined in tension and in compression are in good agreement with the experimental response, as expected given that the measured modulus values are used as input to the model. However, the model also provides information on the extent of the highly loaded region in the centre of the dog-bone specimen (important to define the extensometer measurement accuracy) and an indication of stress concentrations at the ends of the reduced section of the specimen. For the former a uniform zone (stress change *<6 %*) extends over *10 mm*. The fact that modulus values from the tension tests are similar to flexural moduli also suggest that the central stress field covered by the extensometer is reasonably uniform. In addition, the maximum values of stress at the ends of the reduced section are less than *5 %* of the central load. It is clear that modifications could be made to these regions to further reduce these concentrations, but this geometry was retained for ease of machining.

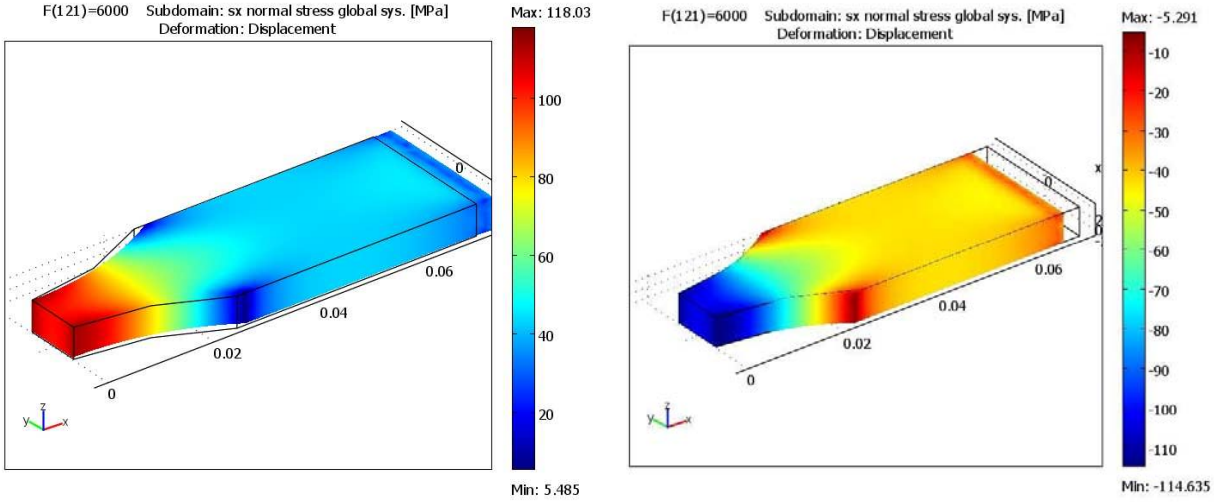

(a) *(b)*

Figure 132. *Representation of the stress and the deformed shape obtained : a) in tension, b) in compression*

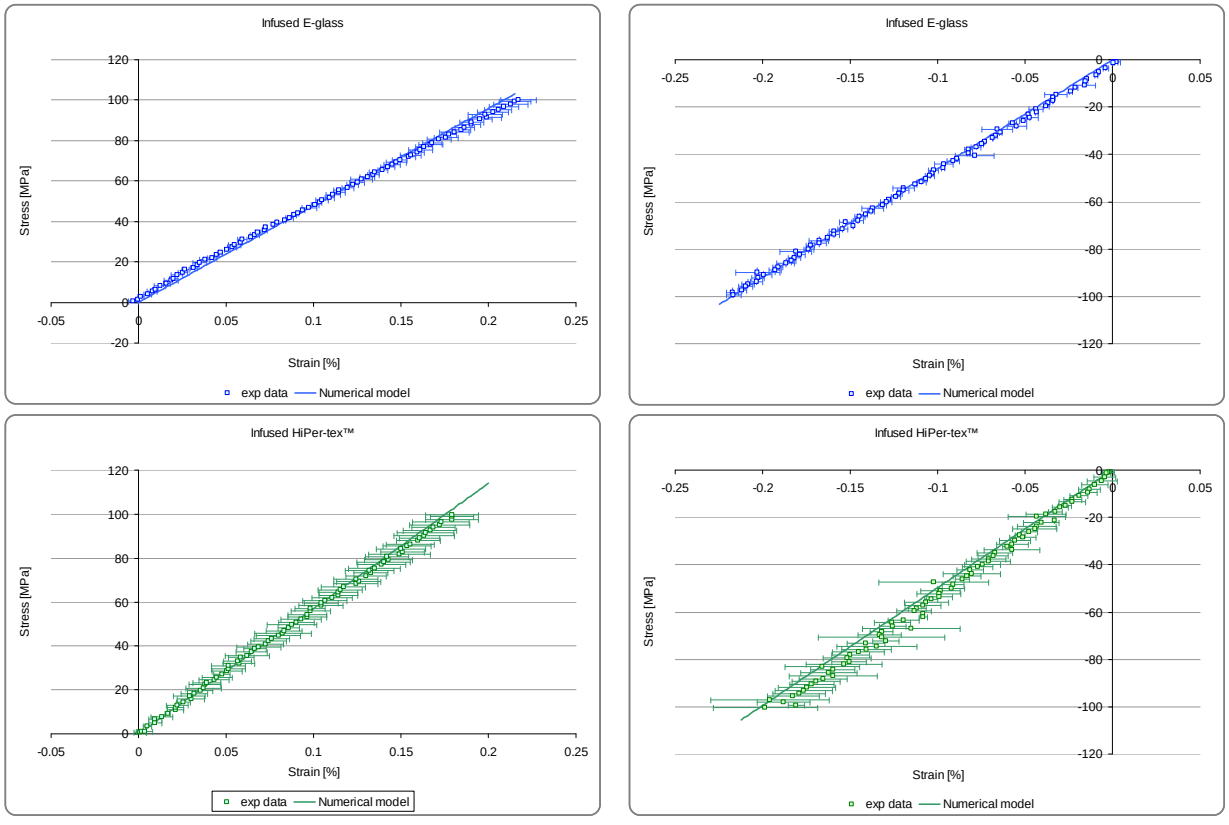

(a) *(b)*

Figure 133. *Comparative curves of all the experimental data (points) and numerical results(lines) : a) in tension, b) in compression*

3.2- Dog-bone specimen in bending

The flexural responses of the two composite materials were modelled based on the four-point bending tests performed. As mentioned in *Section 3.3.1* of the *Chapter II*, dog-bone specimens have been chosen to avoid local damage during the flexural tests due to

indentation of the upper face of the specimen. This choice has been motivated by a bibliographic study and a preliminary experimental study.

3.2.1. Geometry modelling

As previously, the dimensions chosen are equal to the real dimensions for each composite material. This is particularly important for the thicknesses. The geometrical data are summarized in *Table 36*. L_T is the total length, b the width under the loading points, b_0 the width in the centre of the specimen and h the thickness.

As the model presents two symmetries in the geometry and in the boundary conditions, the numerical models have been defined as a quarter of a specimen as presented on *Figure 134*.

Table 36. *Mean dimensions of the dog-bone specimens used for bending modelling*

	E-glass	HiPer-tex™
L_T $[mm]$	139.90	139.86
b $[mm]$	24.90	24.86
b_0 $[mm]$	9.91	9.95
h $[mm]$	5.12	5.16

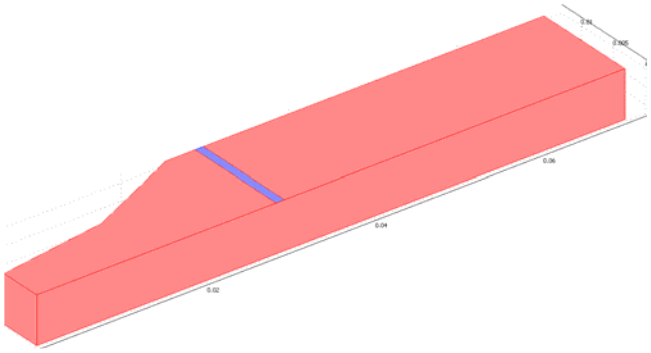

Figure 134. *View of the quarter-specimen used for bending model*

3.2.2. Physics settings

In order to simulate as closely as possible the physical phenomena, the hypothesis of large deformations has been applied. The load is defined as a following load distributed on a surface representing the surface contact between the loading points and the specimen. This contact surface was defined according to the experimental measures of indentation (*Section 3.4.3, Chapter III*) and was fixed with a thickness of *1 mm*. The loading points have not been modelled because results from the preliminary study presented in *Annex 11* indicated that the complexity of the contact conditions could be avoided by modelling only the effects of the loading points on the specimen.

The sub-domain settings describe the material properties. Two cases have been modelled. For the first, the elastic moduli (summarized in *Table 37*) issued from the experimental data from the quasi static flexural tests performed on the two composite

materials are used. For the second, the axial moduli obtained in tension and compression tests (*Table 37*) are entered.

The symmetry condition (in blue on *Figure 135*) and the constraints and loads applied to the specimens (represented with green arrows on *Figure 135*) are described by the boundary conditions of the experimental set up.

Table 37. *Summary of the moduli used for the bending modelling*

Elastic moduli	E-glass	HiPer-tex™
Case #1		
E in bending $[GPa]$	49.6	56.6
Case #2		
E in tension $[GPa]$	46.9	55.9
E in compression $[GPa]$	45.2	48.8

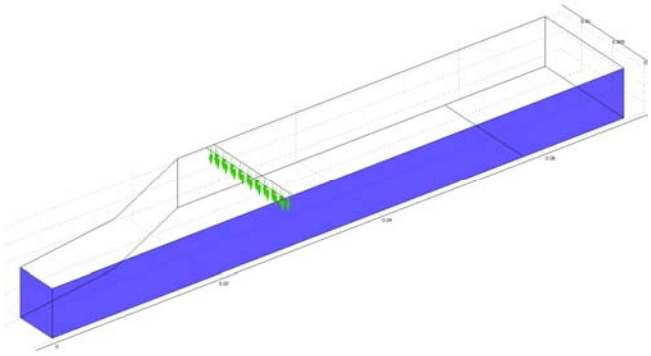

Figure 135. *Representation of the boundary conditions defined : symmetry in blue and load in green*

3.2.3. Mesh generation

As defined previously, the mesh consists of tetrahedral Lagrange elements as presented on *Figure 136*.

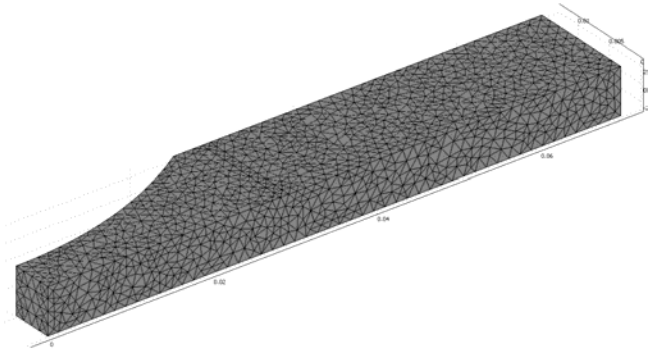

Figure 136. *View of the mesh used for bending model*

3.2.4. Computing, results and evaluation

A parametric solver has again been chosen to compute the numerical model. The applied load is varied from *0* to *4 000 N* with 50 steps for the two infused composites.

The main numerical results observed are the deformed shape, the distribution of longitudinal stress in the specimen for each loading step (*Figure 137*) and the evolutions of stress and strain.

In order to evaluate the numerical model, the experimental data have been compared to the computed results. The comparative curves for the two infused composite materials defined with the bending moduli are presented on *Figure 138a* for the infused E-glass composite and *Figure 138b* for the infused HiPer-tex™ composite. The computed results obtained with the tensile and compressive moduli input values are presented on *Figure 139a* for the infused E-glass and on *Figure 139b* for the infused HiPer-tex™ composite.

The numerical models defined in bending fit reasonably closely to the experimental response, even when the tensile and compressive moduli from independent tests are used as input data.

It is interesting to note that the large displacement results in a slightly non-linear response in spite of the elastic material properties, showing the need to include this option in the model due to the low stiffness of the glass reinforced composites.

The loading points introduce a local stress concentration which appears to be lower than the stress at mid-span, but more detailed modelling would be required to confirm this. Various authors have examined indentation of composites [141-143] but this is a very complex subject. Even if a Hertzian contact law can describe the initial response well [141], composite laminates have several failure modes under static indentation. Different indentation force amplitudes can result in a change from one failure mode to another. To fully investigate this phenomenon, a detailed experimental investigation would be required, but the reduced specimen mid-section adopted here ensures that final failure occurs in the centre.

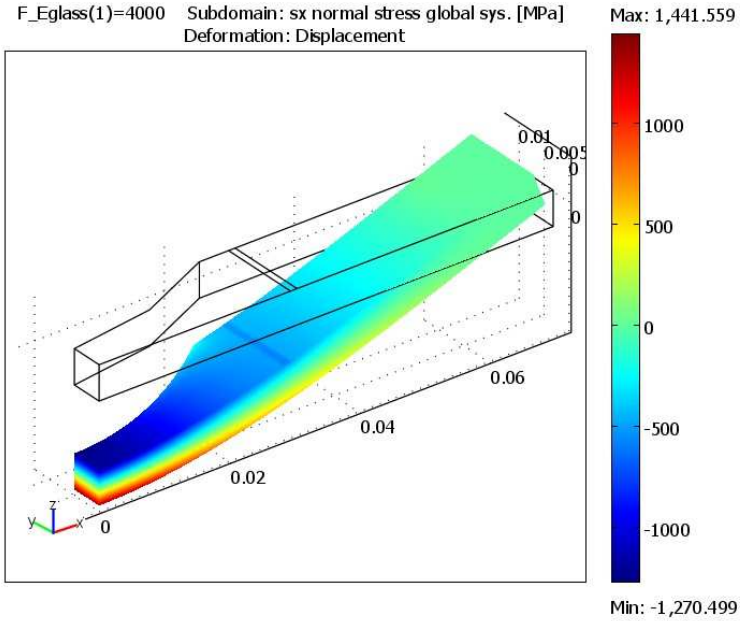

Figure 137. *Representation of the stress and the deformed shape obtained*

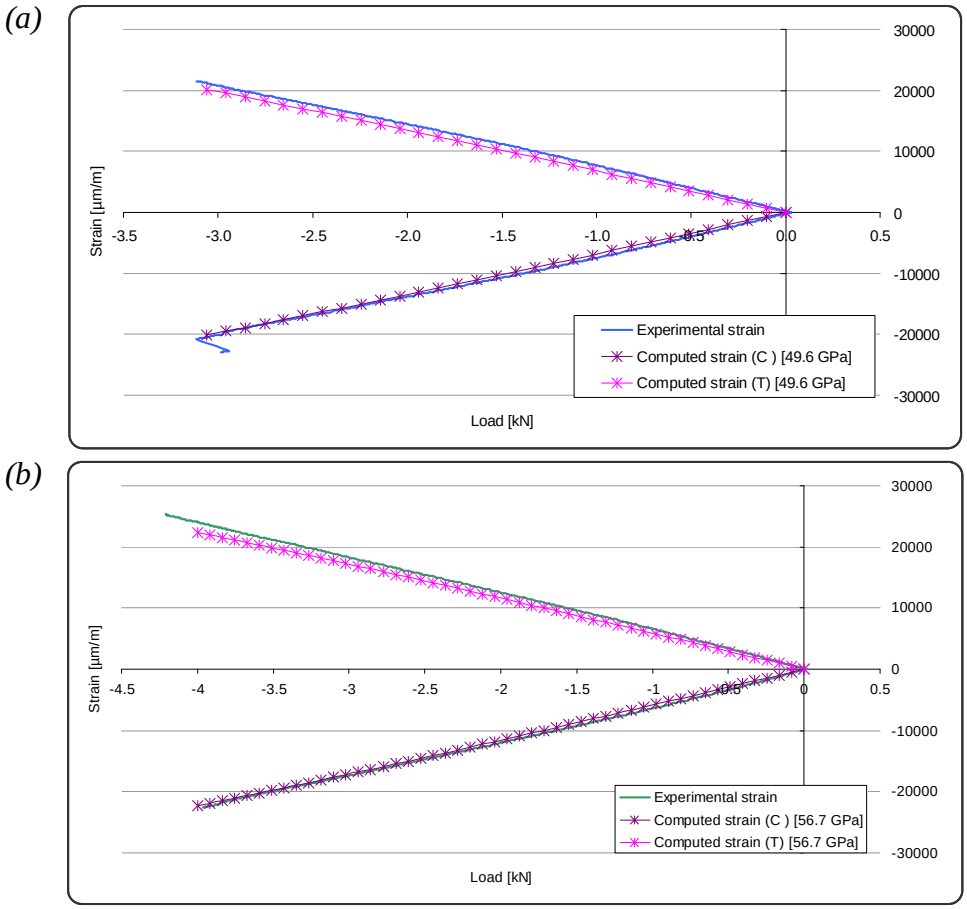

Figure 138. *Comparative curves of the experimental data and numerical results in bending (flexural moduli) : a) Infused E-glass composite, b) Infused HiPer-tex™ composite*

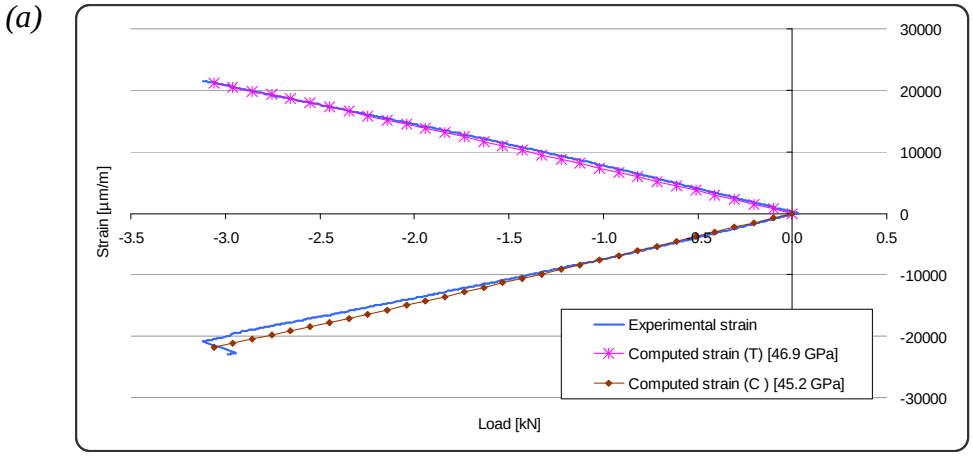

(b)

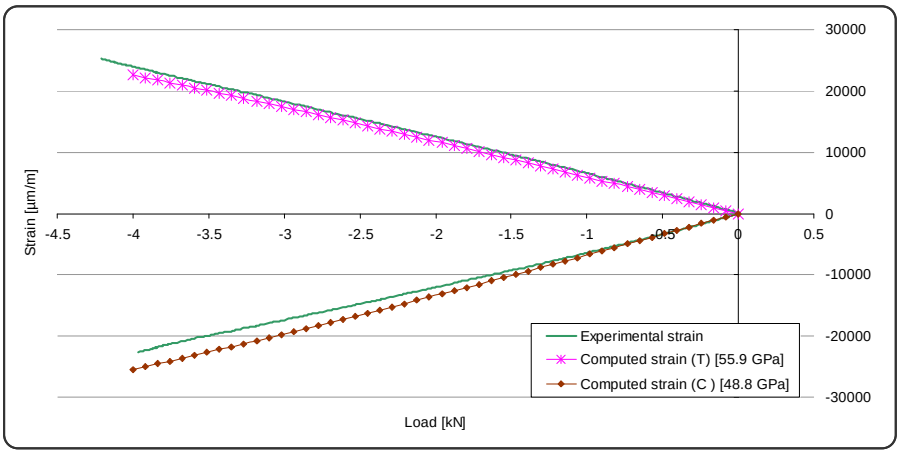

Figure 139. *Comparative curves of the experimental data and numerical results in bending (tensile and compressive moduli input data) : a) Infused E-glass composite, b) Infused HiPer-tex™ composite*

4- Coupling between water absorption and mechanical behaviour

In tidal turbines, the composite materials are subjected simultaneously to a wet environment and mechanical loads. So a model which takes into account the coupling of both phenomena is necessary. In fact, this model is a combination of the models presented in the previous sections, but for a complete model both the dependence of the material properties on water and the dependence of diffusion kinetics on applied stress would be required.

In the present study only the relationships between the water absorption and the mechanical behaviour have been examined, as the experimental data were measured by mechanical testing on specimens previously aged in natural sea water for different periods without applied load. A coupled numerical model has been created and evaluated by comparison with experimental results. This part of the study is focussed on the infused E-glass composite behaviour.

4.1- Definition of the relation between water absorption and the mechanical damage

As shown in the previous sections (*Section 3.2, Chapter III*), the wet ageing has an influence on the mechanical behaviour of the infused composite materials. The mechanical parameters which are most affected by the wet ageing are the failure stresses in tension, compression and bending as presented on *Figure 140* for the infused E-glass material. The moduli change very little for the same ageing conditions (by less than *10 %*) so we can assume them to be constant. This simplifies the coupling as it means for a given load the stress state is unchanged by water entry (at least for the predominantly unidirectional material and over the range of conditions examined here). By comparing the evolutions of the failure stresses and the weight gain, we can see a close correlation between them. The values of failures stresses decrease when the weight gain increases and seem to reach a plateau when the weight gain reach its maximal value.

If we consider to a first approximation that the three failure stresses are varying linearly as a function of the concentration of sea water in the specimen *c* (*Figure 141*), at least over

the first *200 hours*, their evolutions can be written as a function of the ratio of water concentration to the maximal concentration in the specimen c/c_{max}.

$$\sigma_{fail} = -\frac{323.3}{c_{max}} \cdot c + 750.4$$ for the failure stress in tension ***(Eqn. 44)***

$$\sigma_{fail} = -\frac{57.2}{c_{max}} \cdot c + 472.5$$ for the failure stress in compression ***(Eqn. 45)***

$$\sigma_{fail} = -\frac{463.1}{c_{max}} \cdot c + 1137.6$$ for the failure stress in bending ***(Eqn. 46)***

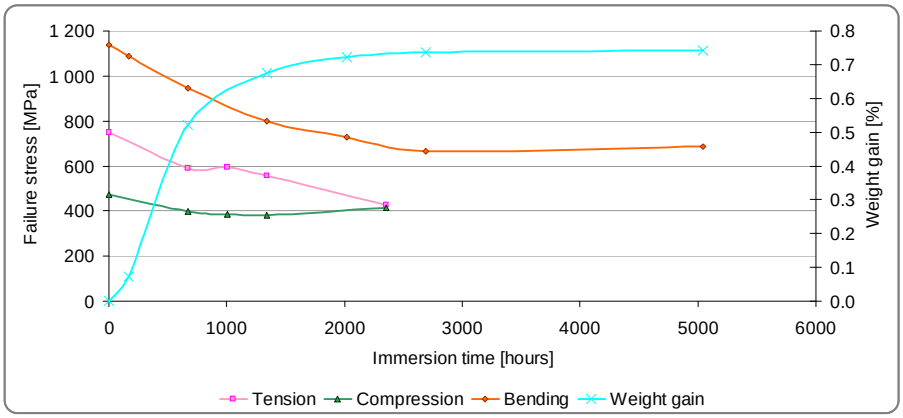

Figure 140. *Evolution of the failure stresses and weight gain of E-glass composite as a function of the immersion time*

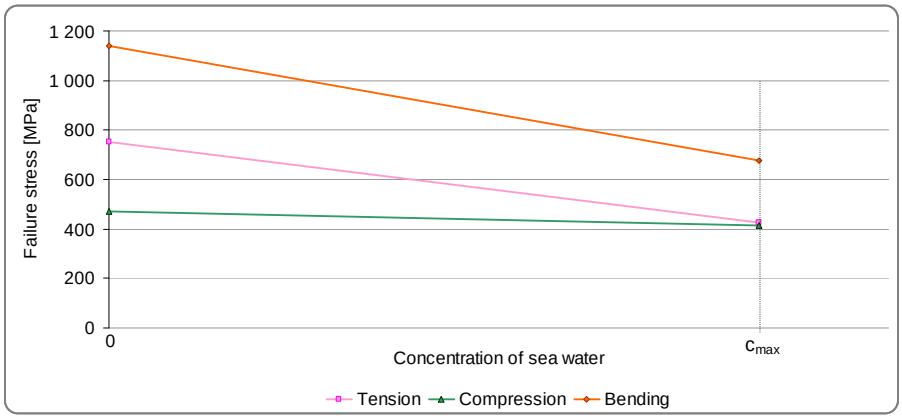

Figure 141. *Simplified evolution of the failure stresses of E-glass composite as a function of the concentration of sea water in the specimen used in coupled model*

4.2- Definition of the coupled model

In order to create a model which takes into account the evolution of the mechanical properties as a function of the water content at all points in the specimen, the Multiphysics module of *COMSOL Multiphysics*™ has been used.

4.2.1. Geometry modelling

The dog-bone shape with the mean dimensions of the specimens is modelled, the geometrical data are summarized in *Table 38*.

The numerical model has again been defined as a quarter of a specimen as presented on *Figure 142*.

Table 38. *Mean dimensions of the dog-bone specimens used for the coupled model*

	E-glass
L_T $[mm]$ (SD)	139.99 (0.10)
b $[mm]$ (SD)	25.01 (0.08)
b_0 $[mm]$ (SD)	10.05 (0.05)
h $[mm]$ (SD)	5.46 (0.21)

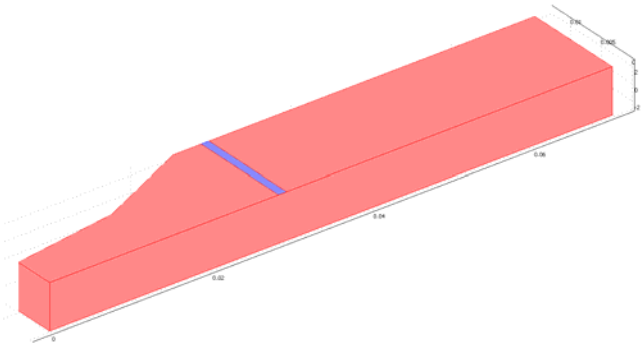

Figure 142. *View of the quarter-specimen used for the coupled model*

4.2.2. Physics settings

In order to simulate as closely as possible the water absorption and the mechanical behaviour, the physics settings for both phenomena have been defined as in the previous sections (*Section 2.1.1* for the water diffusion and *Section 3.2* for the mechanical behaviour).

For the material properties, the diffusion coefficient has been defined equal to *1.19E-12 m²/s* (infused E-glass in natural sea water at *60°C*) and the axial modulus has been defined equal to *49.6 GPa* (Infused E-glass in bending).

4.2.3. Mesh generation

As defined previously for this specimen shape, the mesh consists of tetrahedral Lagrange elements as presented on *Figure 143*. In order to reduce the boundary effects observed in water diffusion modelling (*Section 2.1.1*), the mesh has been chosen as fine as possible on the external boundaries and edges.

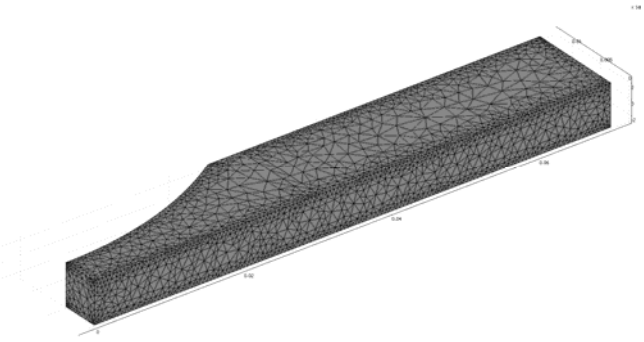

Figure 143. *View of the mesh used for the coupled model*

4.2.4. Computing, results and evaluation

A time dependent solver has been chosen to compute the numerical model. The calculated time goes from *0* to *4 000 hours* with a time step of *5 hours*. The applied load is equal to *2 000 N*.

The main numerical results obtained are the distribution of the water concentration in the specimen and the zones where the computed longitudinal stresses are superior to the failure stresses (either in tension or in compression) which decrease locally as the water diffuses in the specimen. These results are presented on *Figure 144* and *Figure 145*.

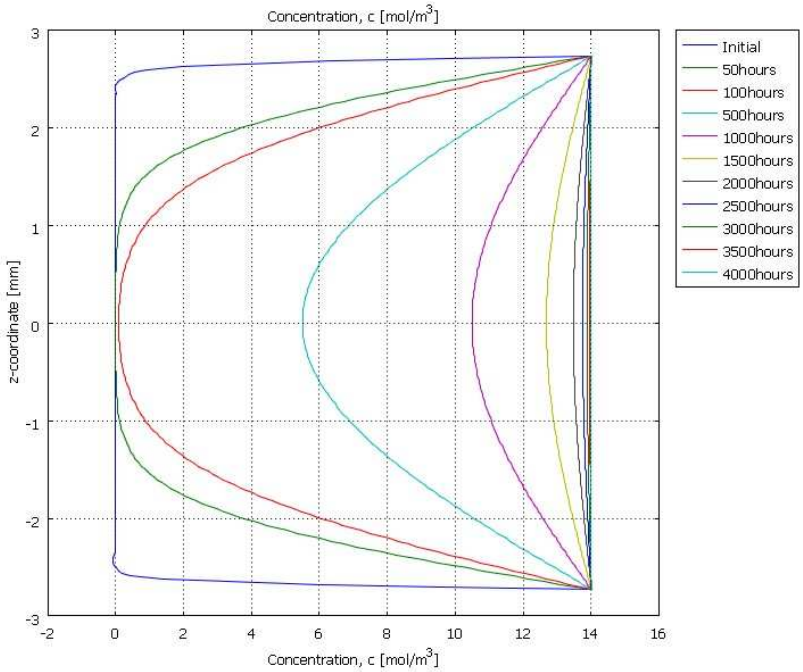

Figure 144. *Evolution of the water concentration in the thickness of the specimen at different times*

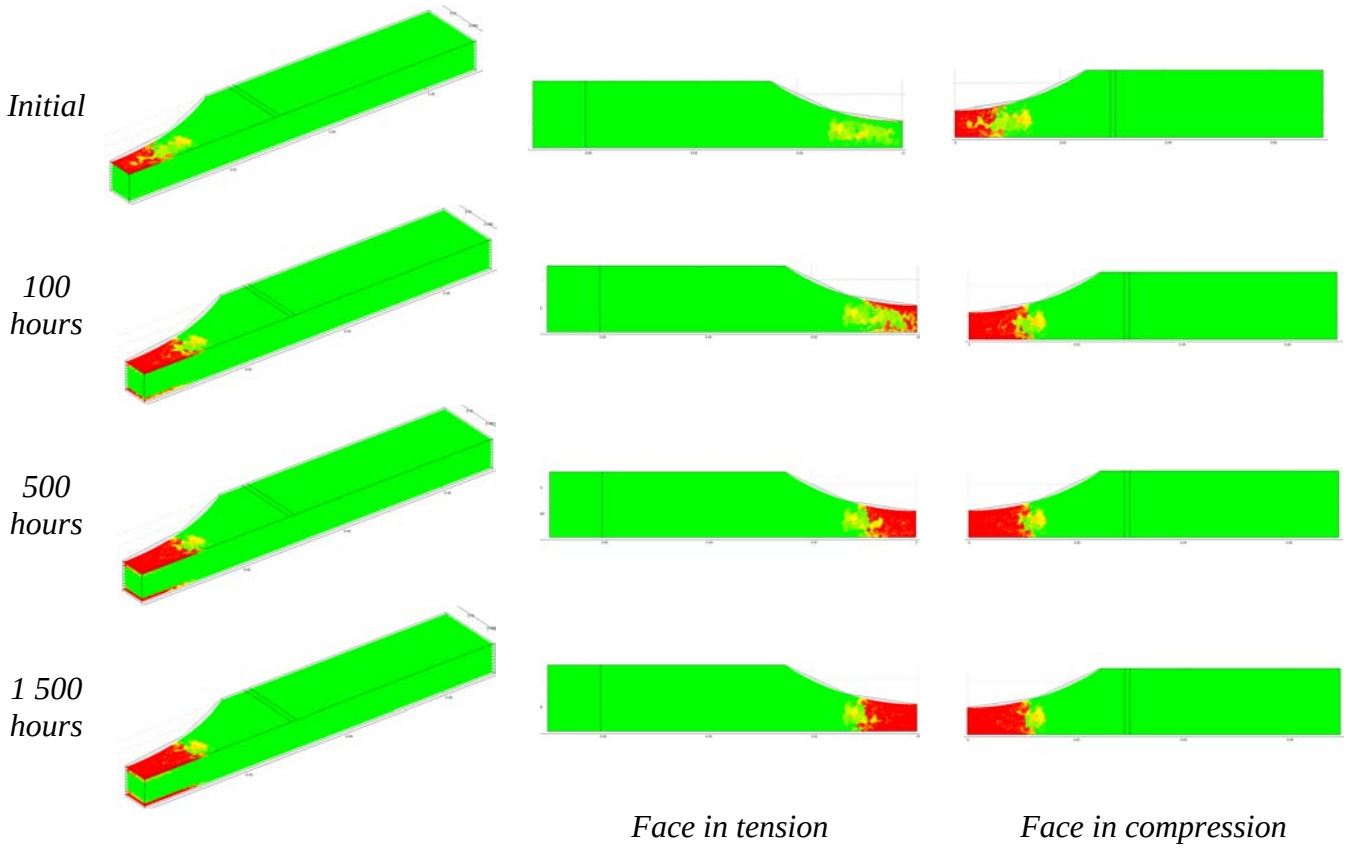

Figure 145. *Evolution of the damaged zones (in red) as a function of the immersion time*

We can see that during the early stages of ageing, the zone initially damaged in bending is on the upper face of the specimen (in red) which is loaded in compression. As the water concentration in the specimen increases with the time, the damaged zone on the upper face expands and progresses in the thickness of the specimen. After a given time (around *150 hours*), a large damaged zone on the lower face of the specimen loaded in tension appears as the tensile properties drop.

As shown in a previous section (*Section 3.4.*1, *Chapter III*), the failure modes observed during flexural tests change from compression to traction as a function of the immersion time. This change occurs between *168 hours* and *1 344 hours* according to the experimental observations. After *168 hours* failure is clearly compressive, after *1 344 hours* it has become tensile, and in the intermediate period after *672 hours* it can be described as mixed, as extensive damage in both the tensile and compression regions is noted. The simplified numerical model developed here shows that the damaged zones become almost symmetrical around *500 hours* which is consistent with the experimental observations. Further intermediate ageing tests would be needed to refine the correlation.

For the latter stages of ageing, a very local failure in tension is noted, suggesting that a stress corrosion phenomenon in the E-glass fibres is the main damage mechanism. *Pauchard et al.* have developed a model based on this phenomenon [81, 82] which could be included in the numerical model. The analytical expressions for the SCC model were derived by considering that the macroscopic stiffness is linearly related to the accumulation of broken fibres within an elementary volume of the composite. So, this model would require further experimental investigations by microscopic observations of the fibre failure process in order to identify the parameters as the materials are slightly different here.

This model can also be used to investigate the difference between fatigue behaviour in air and in natural sea water. There is a significant shortening of E-glass composite lifetimes when cycled in natural sea water (*Figure 88a, Section 3.1.2, Chapter III*) which suggest that sea water at the highly loaded specimen surfaces is accelerating degradation. However, the tests are performed at room temperature (*15-20°C*) and the water concentration profiles for tests at this temperature lasting between a few hours and two weeks are very small as presented on *Figure 146*.

Nevertheless, a small amount of water is present in the most highly loaded region of the specimen, and it may be that the mechanism suggested by *Weitsman* [117], accelerated damage of aged composites which contain water due to local stress concentrations, is responsible here. It should be noted that there is no global change in failure mechanism between tests cycled in air and in natural sea water. The water present is not sufficient to reduce tensile strength significantly, but local stress corrosion may occur and create damage which accelerates the final compression failure. The HiPer-tex™ fibre composites certainly appear less sensitive to testing in sea water, results are similar to those of specimens tested in air (*Figure 88b, Section 3.1.2, Chapter III*).

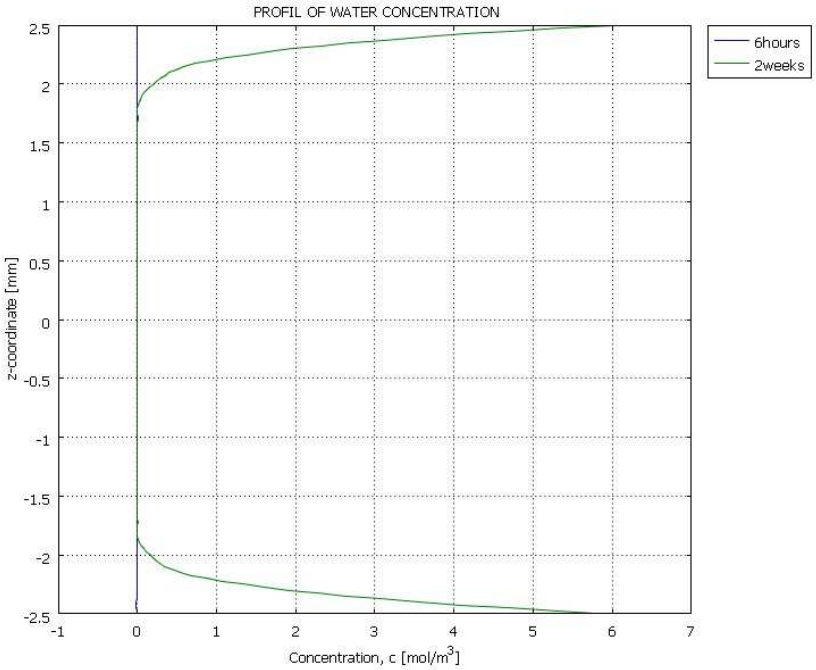

Figure 146. *Profiles of water concentration in the thickness of the specimen after 6 hours and 2 weeks at 20°C*

5- Modelling the evolution of fatigue damage

Composite materials are inhomogeneous and anisotropic and their fatigue behaviour is complex. The first stage of deterioration in fatigue is observable by the formation of more or less extended damage zones, which contain a multitude of forms of damage (microscopic cracks, debonding, initial fracture of fibres, …). This early stage is followed by a second stage of more gradual deterioration of the material characterized by a reduction of the stiffness. More serious damage appears finally in the third stage, such as fibre breakage and delaminations, leading to an accelerated stiffness drop and finally to failure.

The numerical model developed in this section aims to take into account the evolution of damage induced by fatigue loading. First the modelling procedure is described, and then the numerical model is defined and the results presented.

5.1- Modelling procedure applied to describe the evolution of damage

In order to describe the evolution of the damage in an infused composite specimen subjected to fatigue loading in flexion, an iterative method has been chosen. This method takes into account the evolution of the material properties as a function of the number of cycles and the distribution of stress in the specimen.

The finite element model used to simulate the evolution of the damage consists of ten independent layers, as defined in the preliminary study (*Annex 11*). Each layer has its own material properties and is divided into three sections. At the beginning of the simulation the ten layers are considered as identical *i.e.* with undamaged material properties. Then a first calculation is performed with a given loading. The stress distribution in the thickness of the specimen and the vertical displacement of the specimen are evaluated. These values will be used to determine a new set of material properties for each layer and then a new finite element iteration can be launched. This loop, presented on *Figure 147*, will be repeated until the failure criterion is reached.

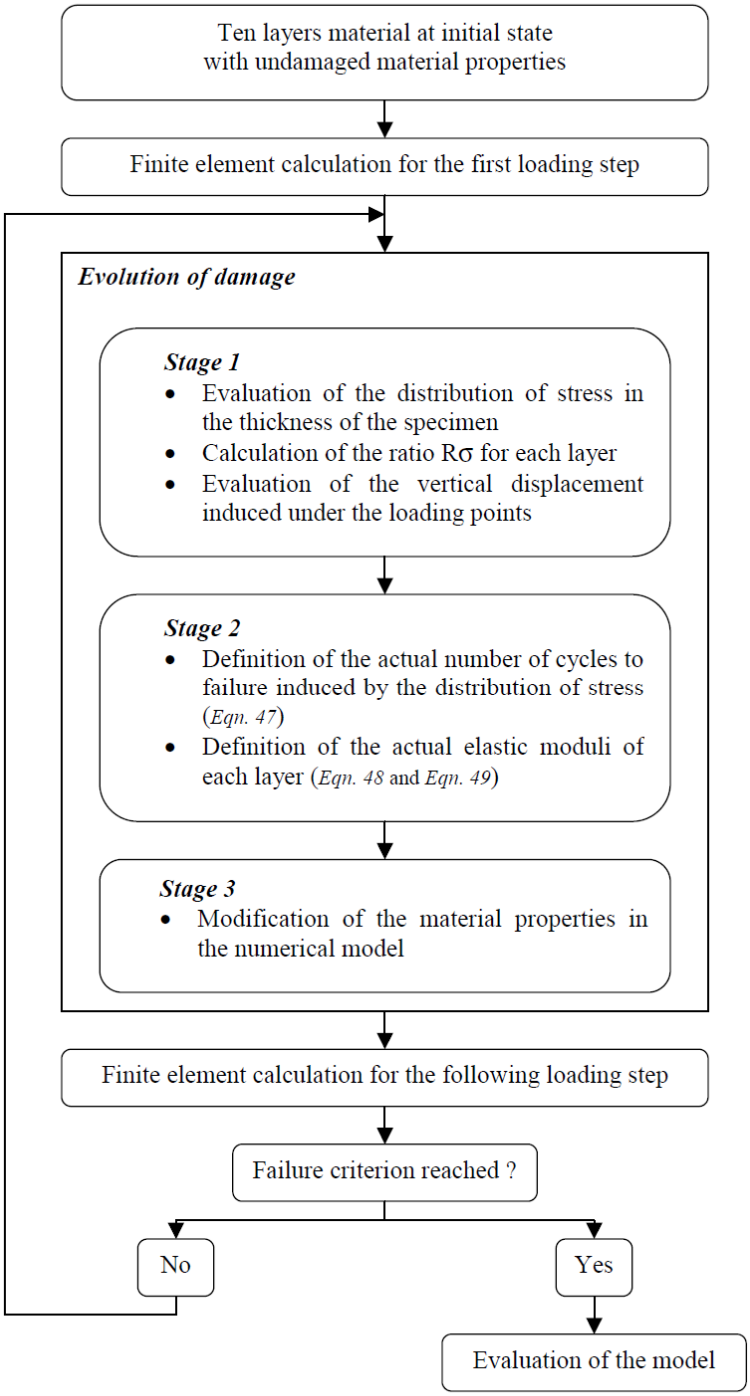

Figure 147. *Flowchart of finite element implementation of the iterative approach*

Based on the experimental data, the fatigue behaviour of the two infused composites in air and in natural circulating sea water have been characterized in terms of their S-N curves and the corresponding analytical formulation (*Figure 148*). The number of cycles to failure N_f can be expressed based on the stress level $R\sigma$ and two constants B and d *(Eqn. 47)*. The constants depend on the material and the environment.

$$N_f = \left[B \cdot (1 - R_\sigma)\right]^{1/d} \qquad \textbf{(Eqn. 47)}$$

If we consider that the stiffness varies only as a function of the ratio number of cycles/fatigue life, we can express it at a given step. This variation can be defined according to two different hypotheses. The first and easiest one is to consider that its values are varying linearly as a function of the ratio N/N_f *(Eqn. 48)*. The second hypothesis is to consider that the elastic modulus is varying according to the damage law defined in *Section 3.1.2*, *Chapter III (Eqn. 49)*. This evolution is based on the evolution of rigidity of the composite materials as a function of the ratio number of cycles/fatigue life observed during the fatigue experiments (*Figure 149*).

$$E = E_i \cdot \left(1 - \frac{N}{Nf}\right) \qquad \textbf{(Eqn. 48)}$$

$$E = E_i \cdot \left(1 - \left(\frac{N}{Nf}\right)^A\right)^B \qquad \textbf{(Eqn. 49)}$$

The mechanical properties in the central part of the specimen (*a*), presented *Figure 150*, are subjected to changes according to the procedure presented above. The mechanical properties in the sections located at the end of the specimen (*c*) are fixed. The mechanical properties of points in the third section (*b*) are assumed to vary linearly as a function of their positions, between the values calculated in section (*a*) and the values in section (*c*).

The finite element approach described above is not limited to the fatigue modelling of these composite materials reinforced with glass fibres, and can be applied to other materials. The material dependence is expressed only by the equations and the coefficients which describe the fatigue process. For other materials, other fatigue laws can be implemented in the procedure. It is a phenomenological approach, which does not require knowledge of failure mechanisms, but these could be included by applying an appropriate criterion (e.g. first matrix cracking, onset of delamination) if sufficient test data are available to define these.

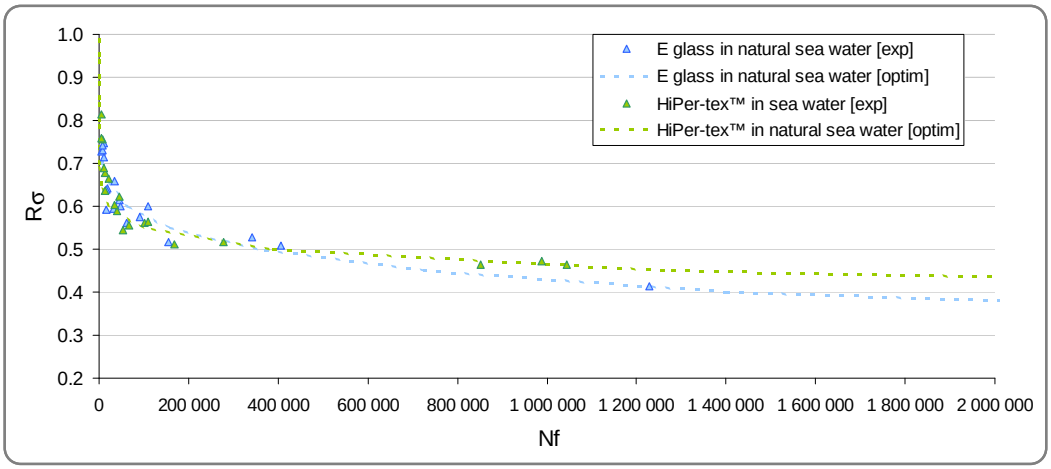

Figure 148. *S-N curves obtained for the two infused composites in natural circulating sea water*

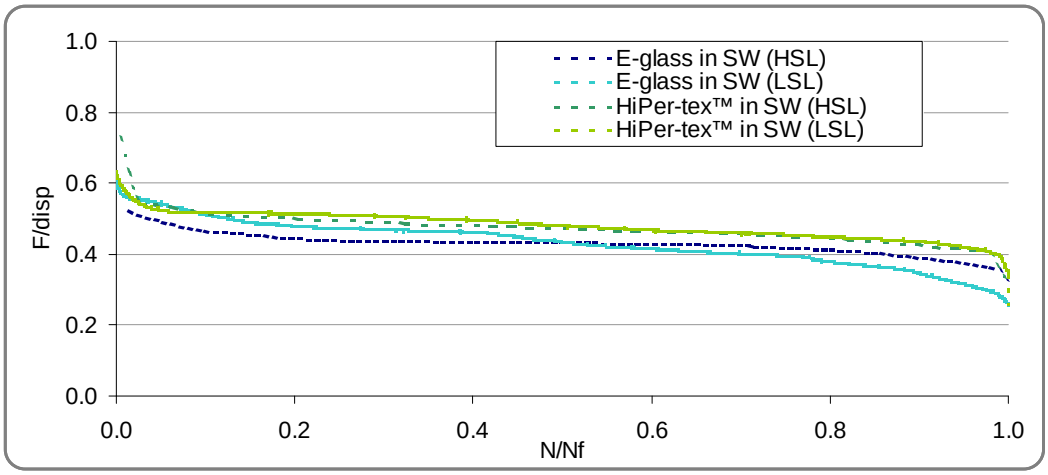

Figure 149. *Evolution of damage during the fatigue life for the two infused composites in natural circulating sea water*

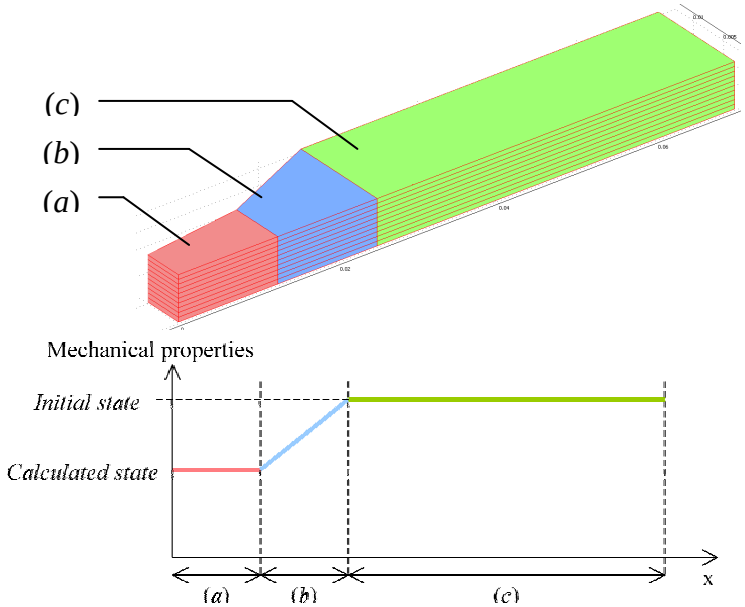

Figure 150. *Representation of the different specimens zones in the numerical model of damage evolution*

5.2- Definition of the model

This numerical model has only been applied to the infused E-glass composite material.

5.2.1. Geometry modelling

As mentioned previously, in order to describe the evolution of the damage in a specimen loaded in bending, a material divided in ten layers has been chosen with the dimensions summarized in *Table 39*.

As the model presents two symmetries in geometry and in the boundary conditions, the numerical model has been defined as a quarter of a specimen as presented on *Figure 151*.

Table 39. *Mean dimensions of the dog-bone specimens used for the modelling of the evolution of damage*

	E-glass
L_T $[mm]$ (SD)	139.99 (0.10)
b $[mm]$ (SD)	25.01 (0.08)
b_0 $[mm]$ (SD)	10.05 (0.05)
h $[mm]$ (SD)	5.46 (0.21)

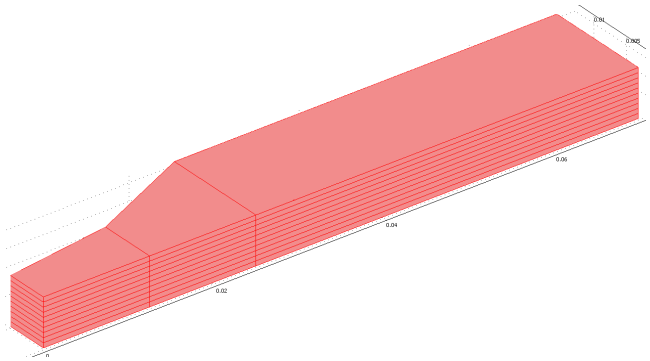

Figure 151. *View of the quarter-specimen used for the modelling of the evolution of damage*

5.2.2. Physics settings

The physics settings have been defined to simulate as closely as possible the fatigue experiments. These settings have been presented in *Section 3.2.2*. At the initial state, the *10* layers have each an axial modulus equal to *49.6 GPa*. The expressions of the material properties for the layer #1 (upper face of the specimen) are summarized in *Table 40*. The calculated values of the elastic moduli are issued from the two hypotheses mentioned above, either *(Eqn. 48)* or *(Eqn. 49)* are used. For the second formulation, the coefficients *A* and *B* (summarized in *Table 41*) are those corresponding to the infused E-glass composite tested in fatigue in air. These coefficients were defined in two ways, a least square method and a genetic algorithm method described previously (*Section 3.1.2*, *Chapter III*).

The applied load has been chosen to correspond with a stress level equal to *60 %* and is defined as a following distributed load across the specimen width.

Table 40. *Summary of the material properties defined for the layer #1 at initial state*

Name	***Location***	***Expression***
E_1_1	Section (a)	49.554 $[GPa]$ (*CALCULATED*)
E_1_2	Section (b)	((E_1_3-E_1_1)/12.5E-3)*(x-12.5E-3)+E_1_1
E_1_3	Section (c)	49.554 $[GPa]$ (*FIXED*)

Table 41. *Summary of the coefficients used to describe the elastic moduli evolution*

	Least squares method	***Genetic algorithm method***
A	1.5E-5	0.053
B	0.0563	0.050

5.2.3. Mesh generation

As defined previously (*Section 3.2*), the mesh consists of tetrahedral Lagrange elements randomly distributed.

5.2.4. Computing and results

The failure criterion applied here is based on the values of the elastic moduli. A layer is considered to be failed when its axial modulus is inferior to half of its initial value. As the final failure of the specimen can not be simulated, the iterative method is considered to be finished when the stiffness of the specimen, *i.e.* the mean of the stiffnesses of the three sections, is too low to compute the model.

As the stress level is considered here to be equal to *60 %*, the mean fatigue life of infused E-glass in air is *180 000 cycles*.

The main computed result is the evolution of the vertical displacement of the specimen under the upper span. The stiffness, which is defined as the ratio applied load divided by vertical displacement, is plotted as a function of the ratio N/N_f as presented on *Figure 152*.

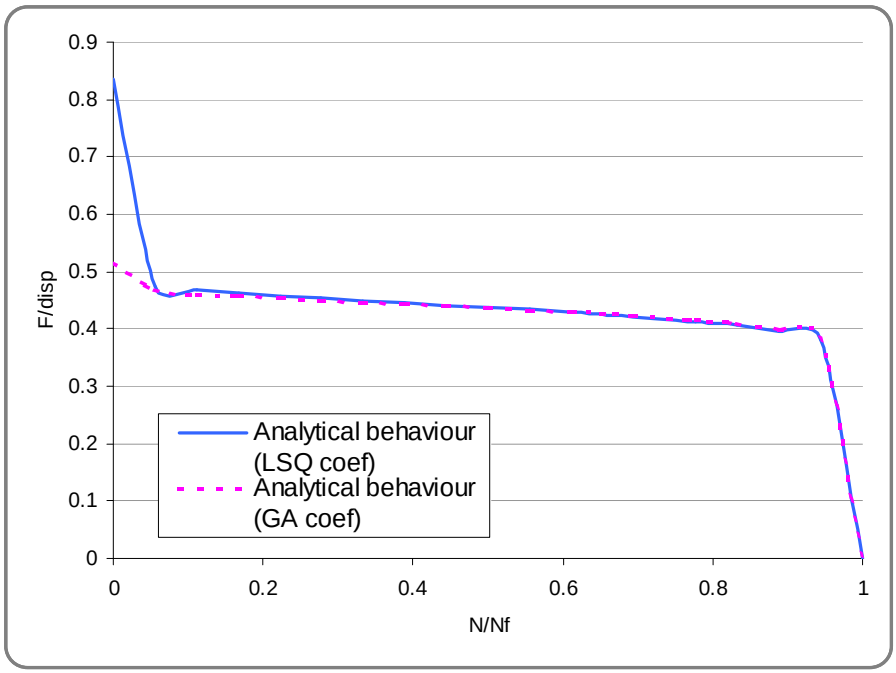

Figure 152. *Analytical fits to fatigue behaviour according to the different optimization methods*

5.3- Evaluation of the models and comparison with the experimental results

As mentioned in the previous section, three models have been used to calculate how the specimens stiffness changes during fatigue cycling. The three computed evolutions of stiffness are presented on *Figure 153*. *Figure 154* presents the comparison between the computed and the analytical behaviour for each case.

When we compare the three evolutions, we can observe that the linear evolution does not simulate the same behaviour as the two other evolutions because its slope is too high compared with the non-linear evolutions. In addition, the two non-linear evolutions are different and do not simulate the early stages of damage in the same way, this difference leads to a gap between them in the damage simulation.

When we compare the computed results obtained with these three evolutions to the analytical formulations of the evolution of damage issued from the fatigue experiments, we note that the linear evolution (*Figure 154a*) does not give a good fit, while the two non-linear models provides a reasonable correlation and reproduce the first drop observed in the early stages of damage.

This model provides a first approach to determine stiffness changes in the fatigue specimen. Further work is needed to refine the approach, and a future step will be to couple this model with the diffusion model.

Among the possible improvements, one aspect to be improved is to include a more precise material analysis. Indeed so far the aim has been to simplify at all steps, in order to develop a model which can be used as an input for analysis of a structural element such as a tidal blade. As will be shown in the Discussion (*Chapter V*) this is a very complex calculation, so the material model must be as simple as can be justified. The simplifications have included describing the composite as a transversely isotropic elastic material, and this will clearly not be adequate for more complex lay-ups with off-axis plies. For example, the delamination damage mechanism cannot be modelled in the present approach. This was justified as delamination was not observed experimentally, but a full orthotropic ply by ply analysis would be required to explore this.

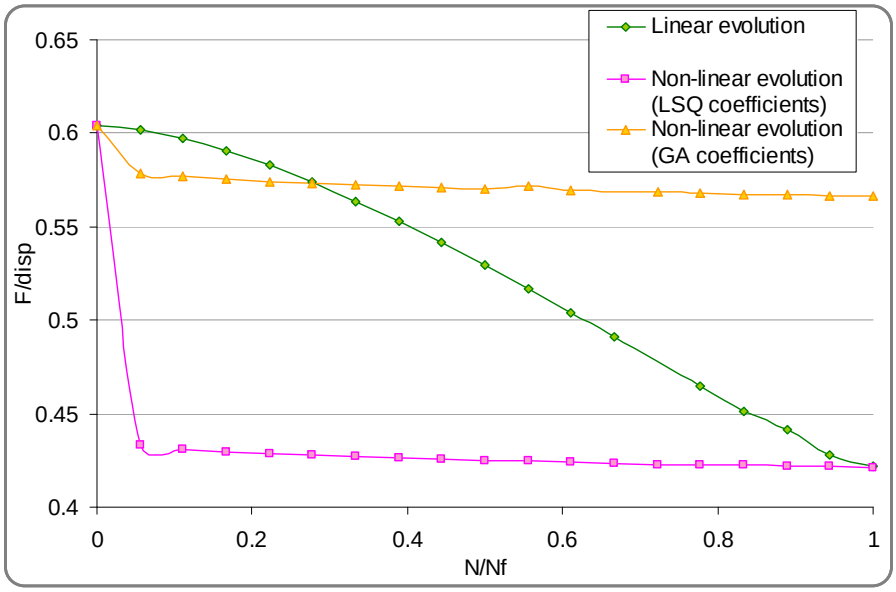

Figure 153. *Comparative curves of the computed behaviour for the three types of stiffness evolution*

(a)

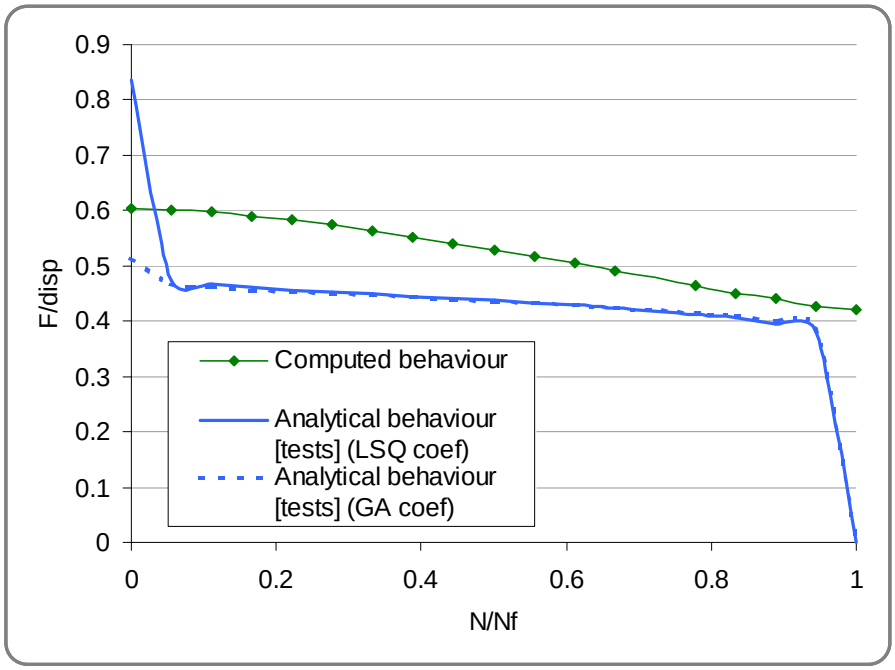
0.9
0.8
0.7
0.6
0.5
0.4
0.3
0.2
0.1
0
F/disp
0
0.2
0.4
0.6
0.8
1
N/Nf
Computed behaviour
Analytical behaviour [tests] (LSQ coef)
Analytical behaviour [tests] (GA coef)

(b)

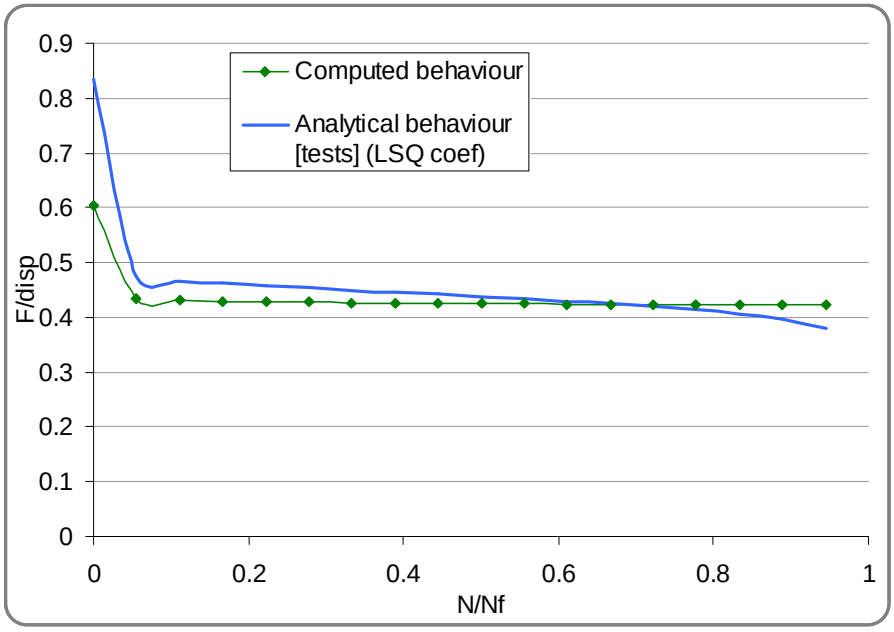
0.9
0.8
0.7
0.6
0.5
0.4
0.3
0.2
0.1
0
F/disp
0
0.2
0.4
0.6
0.8
1
N/Nf
Computed behaviour
Analytical behaviour [tests] (LSQ coef)

(c)

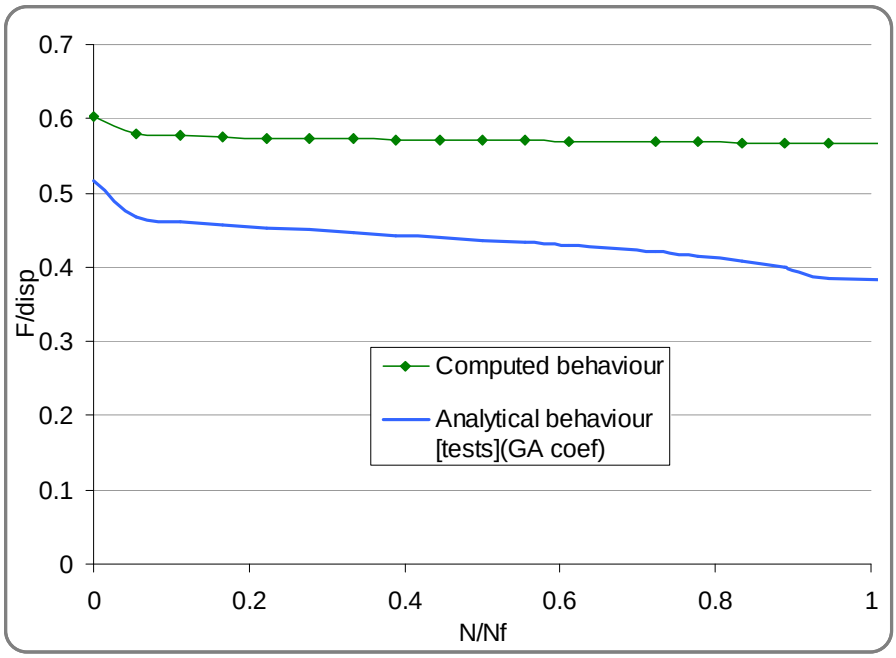

Figure 154. *Evolution of computed stiffness : a) linear evolution, b) non-linear evolution (LSQ coefficients), c) non-linear evolution (GA coefficients)*

6- Summary and conclusion of the numerical modelling

In this study, numerical modelling, based on the finite element method coupled with the experimental data, has been performed in order to develop tools to evaluate the long term behaviour of composite structures.

In order to simulate the wet fatigue behaviour of a glass fibre composite, several steps in the numerical modelling are necessary. The first step is to define the water absorption in the specimen. The second step is to define the mechanical response of a specimen subjected to simple loading such as tension, compression and bending. The third step is to simulate the coupling between the water absorption and the mechanical damage. The following step is to define the evolution of damage during fatigue life. In the future this could also be coupled with the water absorption. In addition, preliminary studies have been performed to quantify the influence of the numerical parameters in the model results and the influence of the model definition.

By performing the numerical study of the water absorption, the importance of the mesh size and distribution has been highlighted. In addition, the numerical modelling of water absorption in composite specimens using a Fickian model has been shown to be reasonably consistent with the measured behaviour.

Three numerical models have been created to simulate the mechanical behaviour of a composite specimen subjected to tension, compression or bending loads and the computed results correspond reasonably closely to the experimental response observed. These results indicate that the basic uncoupled diffusion and mechanical models, while simplified, are adequate to describe the specimen behaviour.

The coupling between the water absorption and the mechanical behaviour has been modelled for a composite reinforced with E-glass fibres subjected to a static four-point flexural load. This simplified numerical model indicates that the damaged zones predicted after a given immersion time are consistent with the experimental results, but further

investigations are required to simulate the real behaviour which is more complex, and to take into account phenomena such as stress corrosion.

The last step of the numerical modelling studied here, is the simulation of the evolution of damage using an iterative model based on the evolution of the stiffness in the specimen due to the distribution of stress. The evolution of the stiffness has been defined according to two different hypotheses, and the computed results obtained have been compared to the experimental behaviour. This model is a first simplified approach to determine the stiffness loss of a specimen during flexural fatigue loading.

The “engineering” approach adopted here could be developed further by taking into account some more local information on the state of the material, such as non-linear strain response, transient moisture concentrations and stress-moisture coupling. The latter are being examined in studies elsewhere e.g. [144]. A more fundamental coupling approach, which includes chemical reaction kinetics, based on work at ENSAM and ENSMA [145-148], would also be interesting, as it could include physico-chemical changes directly related to resin plasticity and hydrolysis rather than the empirical damage approach applied here.

CHAPTER V
DISCUSSION

V- DISCUSSION

During this study a large amount of data has been provided for composites reinforced with glass fibres. These data allow us to determine relationships between reinforcements, environment and mechanical behaviour. However, some questions still need to be addressed concerning the influence of the material parameters, such as the fibre type, the matrix resin and the interface fibre/matrix, and the influence of the test parameters such as the frequency of fatigue tests and the R-ratio. These points will be discussed here, followed by a discussion of the accelerated ageing and the step from specimen to full tidal turbine modelling.

1- Influence of material parameters

In this study, three types of composite materials have been studied, more precisely, one epoxy resin reinforced with three different glass fibres. But what would be the experimental results if the fibres or the resin were different ? What are the influences of material parameters on mechanical behaviour in our specific marine context ?

1.1- Fibre type

In this project only glass fibres have been studied, as for cost reasons they are widely used in all but the longest wind turbine blades. E-glass and HiPer-tex™ have been discussed in some detail while a problem with the batch of Advantex® reinforcement meant that satisfactory properties were only obtained at the very end of the study, but *Figure 155* shows that when quality control criteria are satisfied (*ILSS > 45 MPa*) the Advantex® composites show good fatigue behaviour. This underlines the crucial role of quality control, as the difference between fatigue lifetimes for poor and acceptable quality specimens reaches a decade at high stresses.

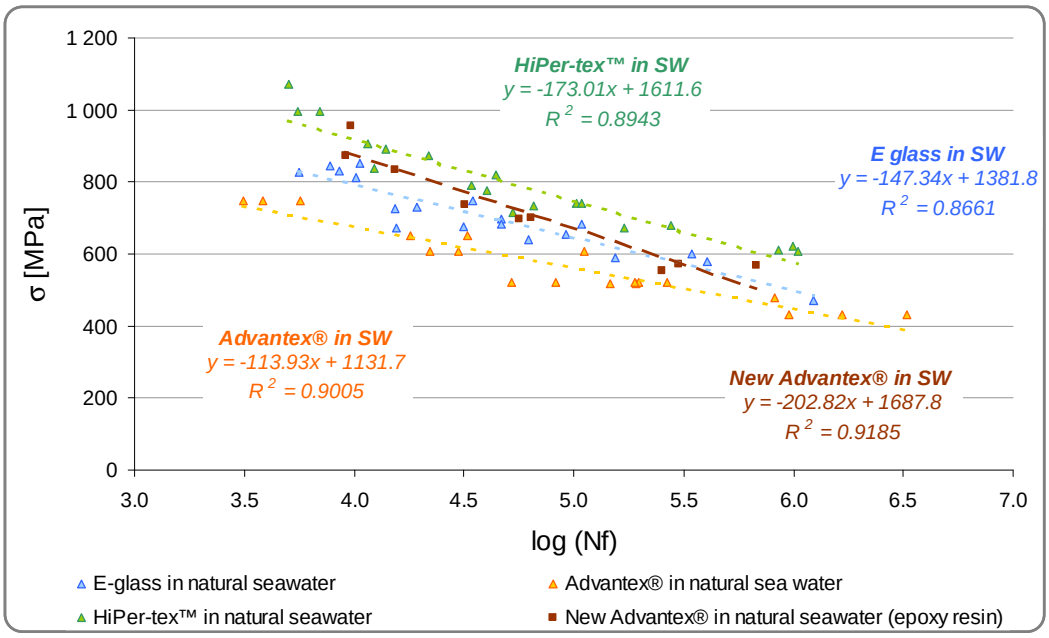

Figure 155. *First results for wet fatigue of new batch of Advantex®/epoxy (October 2010)*

The type of glass fibre has been shown to affect durability in sea water, and grades developed to limit stress corrosion are clearly preferable for marine energy applications.

However, if fatigue is the dimensioning factor it may be interesting to examine alternative fibres such as carbon. There have been many studies in which fatigue of carbon has been directly compared with E-glass but *Smith & Weitsman* [149] clearly indicate that even with carbon fibres it was noted that saturated coupons fatigued in air exhibited the longest fatigue life and saturated coupons fatigued while immersed in sea water failed after the shortest number of load cycles. Further, reduced transverse cracking and increased delaminations were observed in saturated coupons fatigued while immersed.

It is not clear today whether carbon fibres are needed for the relatively short blades envisaged for tidal turbine (generally lengths below *10* meters are being considered), but carbon is certainly being used in some prototypes. A comparison in which the same resin is tested with glass and carbon fibres would be very instructive, such tests are currently underway.

1.2- Matrix resin selection

The epoxy resin used in this study is widely used in wind turbine blades and is optimised for infusion process. Other resins are available and within the project some tests have been performed on the new batch of Advantex® fibres with a vinyl ester matrix. Such comparisons are delicate as the optimal fibre sizings for vinyl esters and epoxies are not the same, but sizings were optimised for both here.

Static and fatigue flexural tests have been performed using the same experimental set-up as described previously (*Section 3.3*, *Chapter II*). When we compare the experimental results obtained for the two infused composites, static flexural strengths appears to be similar but the S-N plots are significantly poorer for the vinyl ester composites as presented on *Figure 156*. This appears to be related to a delamination mechanism not seen with any of the epoxy composites.

Further tests are underway to evaluate the behaviour of this matrix after sea water ageing, but this does indicate that matrix selection is another important parameter.

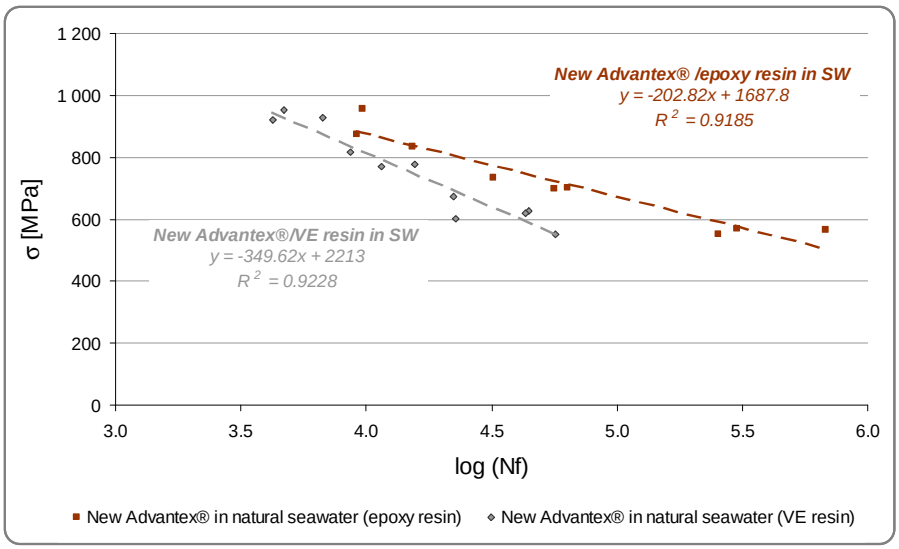

Figure 156. *First results showing influence of matrix resin on wet fatigue performance*

1.3- Fibre sizing

Among the many factors that govern the characteristics of composites involving a fibrous material and a matrix, it is certain that the adhesion between fibre and matrix plays a major role [150]. The stress transfer at the interface requires an efficient coupling between fibre and matrix. So, characterization of the mechanical properties of interfacial zones is necessary for understanding mechanical behaviour of the composite material. This was not studied in detail in this project but a small number of tests underline the importance of the interface properties.

Interlaminar shear stress, static and fatigue tests have been performed on two infused composites reinforced with two types of HiPer-tex™ fibres. The first fibre type is coated with the optimal sizing for an epoxy resin, the second one has a more general purpose sizing. The results obtained during interlaminar shear stress and static tests are presented on *Figure 157a* and *Figure 157b*. The results obtained during fatigue tests in natural sea water (*f=2 Hz, R=0.1* and *Rσ=60 %)* are presented on *Figure 157c*. It is clear that the fibre/matrix interface has a large influence on the mechanical behaviour of the composite material. The ILSS and flexural tests detect the difference in behaviour, while in wet fatigue the mean fatigue life is almost divided by *6*. These results confirm those presented in a recent paper by *Watson* [151], who showed that optimising fibre surface chemistry can increase fatigue life (in air) by a factor of *3*.

(a)

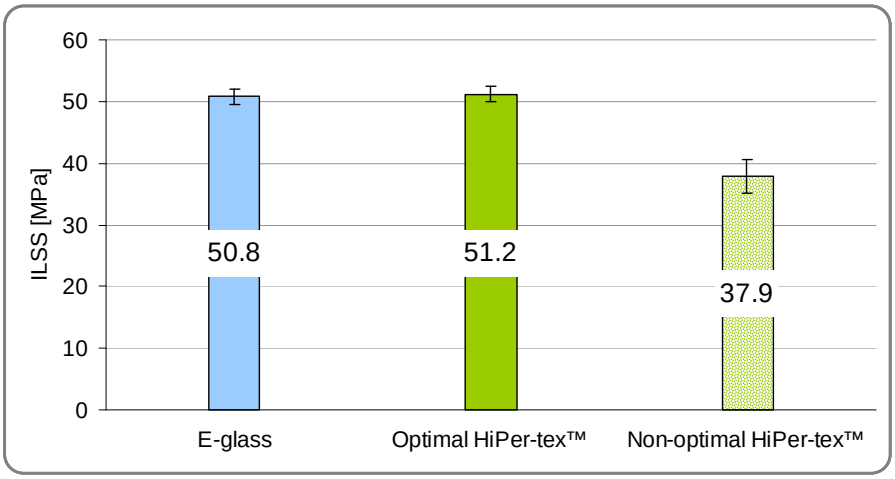

(b)

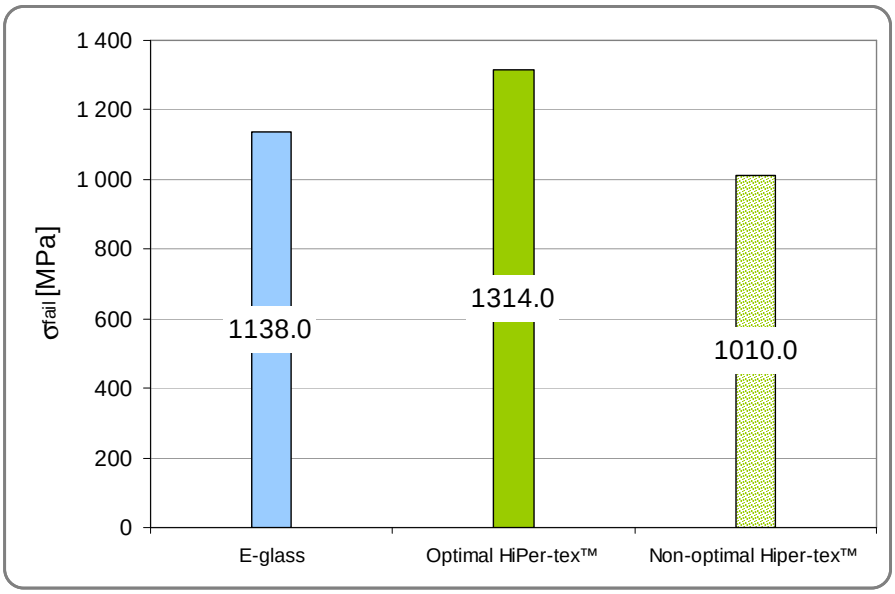

(c)

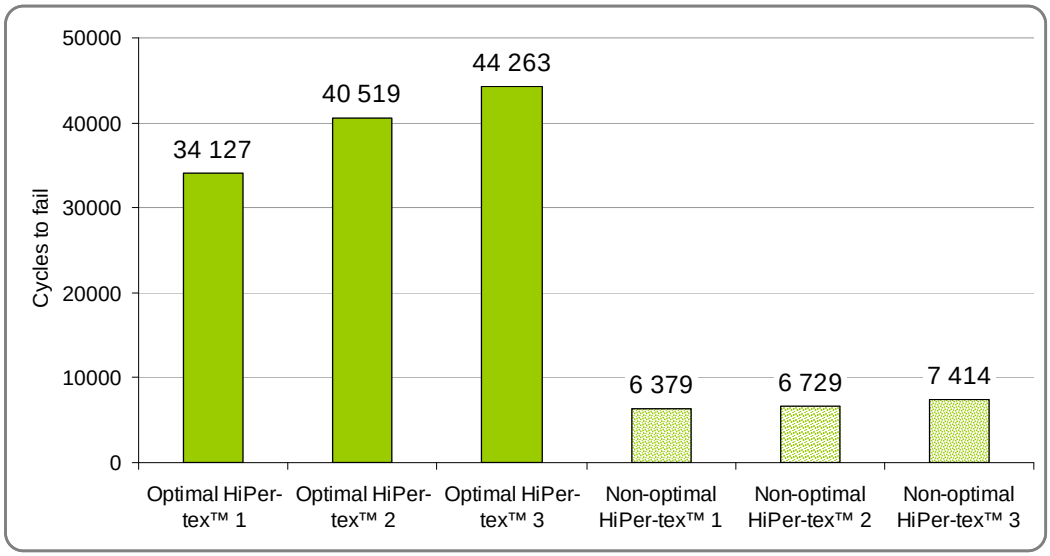

Figure 157. *Influence of fibre sizing on composite properties : a) ILSS, b) Four-point flexure strength, c) Flexural fatigue life time in sea water (results form 3 samples for each material)*

2- Influence of test parameters

In addition to the material parameters, the test parameters selected for this study might have an influence on the experimental results obtained. The aim of the experimental study is to produce data which are relevant to the final application. As mentioned previously (*Section 6, Chapter IV*) there is a wide range of tidal turbine prototypes being developed and they are subjected to very different loading conditions. But what are the sensitivities of results to the test parameters in our study ?

2.1- Frequency

Typically rotation speeds of *10-15 turns/minute* are currently being used for prototype tidal turbines [152], but at these speeds (around *0.25 Hz*) it would not have been possible to produce S-N curves for the three composite materials in the time available. A frequency of *2 Hz* was therefore chosen, but a few tests were performed on infused Advantex® composite at another frequency, *5 Hz*.

The results are presented on *Figure 158* and show that there is considerable scatter at the higher frequency. The mean lifetimes are quite close, slightly lower for the higher frequency. In the future it would be interesting to perform further tests at lower frequencies to have a better understanding of the effect of frequency on fatigue life.

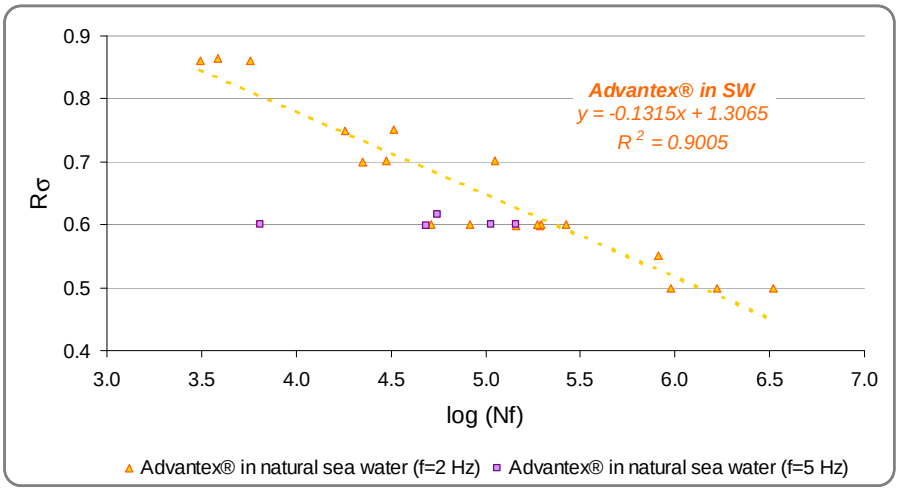

Figure 158. *Influence of the frequency in wet fatigue tests*

2.2- R-ratio

The R-ratio applied in all the tests described above is defined as $\sigma_{min}/\sigma_{max} = 0.1$. However this is misleading in flexural tests, as while this is the case for each of the two sides of the specimen, the complete specimen sees an R-ratio of *–1*.

An alternative approach to S-N plots or Miner damage accumulation lifetime estimation is to use the constant lifetime plots based on different R-ratio tests to establish lifetimes *Figure 160* [153].

In order to study the influence of this parameter on the fatigue behaviour of our materials, a few tests with a different R-ratio have been performed. Infused Advantex® and HiPer-tex™ composites have been tested in wet fatigue with *R=0.5* and *f=2 Hz*. The results are presented on *Figure 159*. It is clear that R-ratio has a strong influence on fatigue lifetime, the higher stress amplitude at *R=0.1* is more severe for both materials. The influence of this ratio must be investigated in future work if variable amplitude loads are to be predicted.

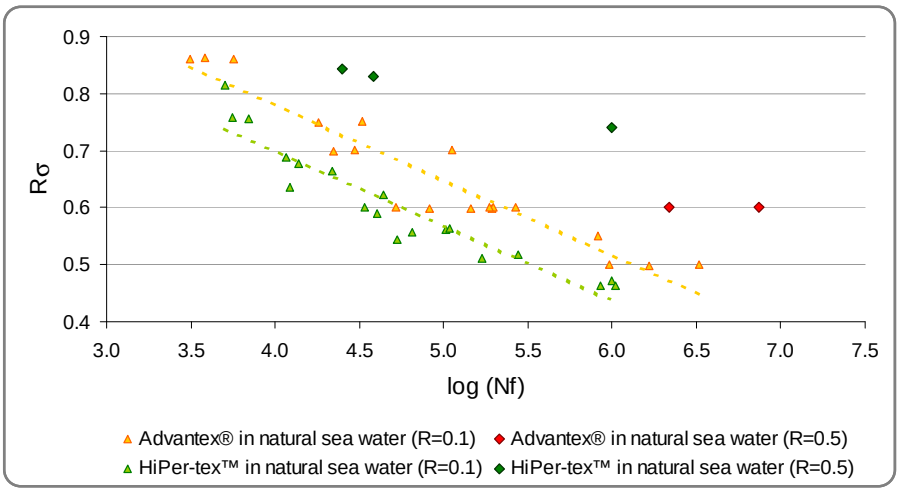

Figure 159. *Influence of the R-ratio in wet fatigue tests*

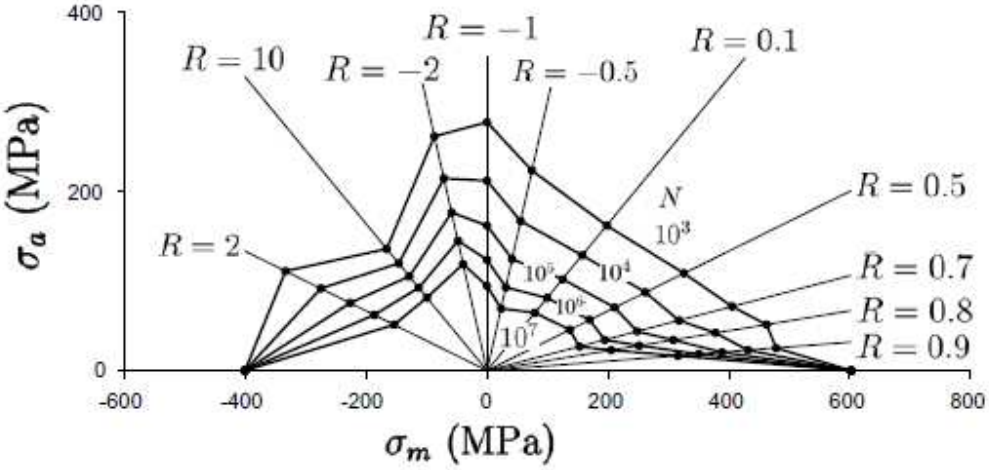

Figure 160. *Example of data from tests on wind turbine material [154] plotted as a constant life diagram, glass/epoxy 0°/±45° sequence [153]*

3- Influence of the shape of the specimen

In order to define the shape of the specimens used in the mechanical study, a bibliographic study and a preliminary experimental study were performed. From the preliminary study, a dog-bone shape was chosen for the specimens in order to avoid the local damage due to the loading points observed on rectangular specimens, without this modification it was not possible to obtain valid fatigue failures. The dimensions of the dog-bone specimen were defined with a large radius of curvature in order to prevent stress concentration in singular points.

Alternative tests such as tension-tension fatigue described in *Section 3.3.3* in *Chapter II*, use a more traditional parallel-sided specimen. A few preliminary tests were performed with this specimen in natural sea water and *Figure 161* shows these plotted on results from tests at *Risø* in air. The values are a little lower. More tests are needed with this new fixture.

Even though the dog-bone specimen gave satisfactory results in our case in fatigue (composites reinforced with glass fibres), more detailed numerical modelling could be used to refine the geometry. In tension the strength are lower than those for specimens with end-tabs (*Table 15*), suggesting that there is a stress concentration in the centre. On the other hand, tests on unidirectional carbon reinforced composites have indicated that parallel sided specimens can be used satisfactorily for those materials in flexural fatigue.

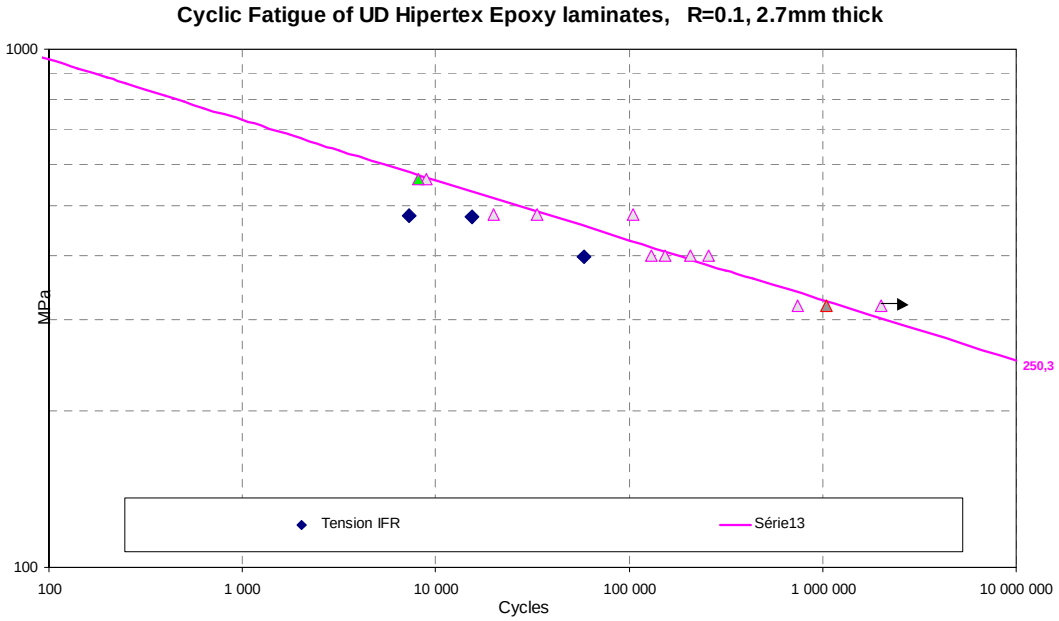

Figure 161. *Tension-tension fatigue tests results*

4- Accelerated ageing

The approach used here to accelerate ageing is to raise the temperature. For the E-glass and HiPer-tex™ materials immersion at *60°C* enables water entry to be accelerated by a factor of *30* to *50* (*Tables 79, Chapter III*) compared to *20°C*. This appears to be an upper temperature limit, immersion at *80°C*, above initial resin *Tg*, resulted in visible colour changes and a different diffusion behaviour. The mechanical properties drop rapidly but appear to reach a plateau after around *16 weeks* at *60°C*.

Three specimens of each material were left in sea water for much longer period (*17 months*) at *60°C*, and residual tests performed on wet specimens revealed that E-glass composite continues to lose strength while HiPer-tex™ remains stable (*Table 42*). This indicates the importance of long term testing to validate material choices, after *30 weeks* the losses were similar for both materials.

These ageing periods would correspond to an immersion of over *30 years* at *20°C*, but it must also be emphasized that the ageing results presented in *Chapter III* represent a worst case of ageing compared to a real structure. A turbine blade is likely to be thicker than the specimens tested here, and protected by at least a gel coat and probably several other coatings (anti-abrasion, anti-fouling paints). Tests on coated specimens would allow diffusion coefficients to be adjusted to account for these.

Table 42. *Residual flexural strengths after ageing, all tested wet*

	Residual strength after 30 weeks (*% loss*)	Residual strength after 70 weeks (*% loss*)
E-glass	684 (- *40 %*)	502 (- *56 %*)
HiPer-tex™	746 (- *43 %*)	788 (- *40 %*)

5- Integration in a structural model of a turbine blade

Once the material has been characterized, the aim is to introduce the behaviour laws into numerical models, which enable the long term behaviour of structures such as tidal turbines to be evaluated. These structures are complex and subjected to combined loading including flexure and torsion, so more complex fatigue damage models could be needed. Nevertheless it is the unidirectional fibres which dominate strength and stiffness so only these were considered in this first approach. On the loading history side we have very few data from prototypes, even though various blades have been instrumented. While mean current speeds are generally known for a particular site, the variable loading component due to waves and/or current fluctuations may be as important in determining critical loads. The development of a range of typical loading spectra, similar to those in use for wind turbines [91, 92], would be very helpful in checking new designs both for geometrical and material optimization. For example, in wind turbine development designers can run simulations based on Wisper or WisperX spectra which include wind loads during installation, normal use and extreme conditions.

The particular design of each structure (*Figure 162*) has an important influence on the dynamic loads observed on the turbine blades. For all these designs the pressure on a stationary immersed structure can be estimated by the expression

$$P = \frac{1}{2} \cdot \rho \cdot C_P \cdot v^2 \qquad \textbf{(Eqn. 50)}$$

where ρ is the water density, C_P a coefficient which depends on the geometry of the structure and v the water speed.

However, to this must be added the cyclic loading caused by rotation of the blades, which move in an area of unknown vertical current profile. When the blades are based on standard aerodynamic geometries (NACA blades) their drag coefficients in the normal and tangential directions are known and detailed calculations can be made based on mean current speeds. The Blade Element Momentum Method (BEM) is often used. However, vibrations due to the natural frequencies of the systems and their supports must also be calculated.

For example, a turbine with an horizontal axis (such as *MCT SeaGen* system [26], *Figure 162a*) will be subjected to high static loads (a recent paper indicate that normal loading at rated power is around *30 tons* per blade [152]) but is moderately solicited in fatigue. It will see reasonably constant tidal forces which fluctuate when the tide direction changes (roughly every *6 hours*) or due to water depth variations in flow caused by wave or seabed interactions. The former may introduce a quite large cyclic amplitude but the number of cycles in *5 years* will be less than 10^5, and the loads should be well known. If the blade pitch can be changed, as is the case with the *SeaGen* turbine, the blades can be oriented to always be loaded in the same direction, minimizing this effect. Load variations due to the water depth on the other hand will probably be of much lower amplitude, but wave periods are usually in the range of *5-10 seconds*, so over *5 years* more than 30×10^6 *cycles* may accumulate. It is clear from the data generated in our tests that such numbers of cycles require careful design.

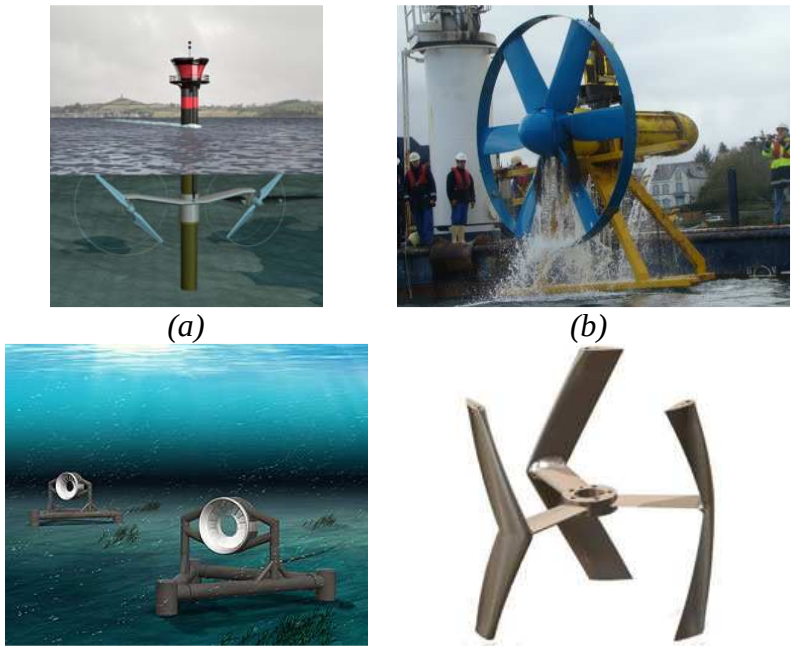

(a) *(b)* *(c)* *(d)*

Figure 162. *Examples of tidal turbine concepts : a)-c) horizontal axis, d) vertical axis*

For a turbine with a vertical axis such as the *Harvest* prototype [155, 156] (*Figure 162d*), the situation is rather different. Here each blade sees a complete load inversion during each cycle, as the blade position rotates with respect to the flow, resulting in a much more severe fatigue loading, as presented on *Figure 163*.

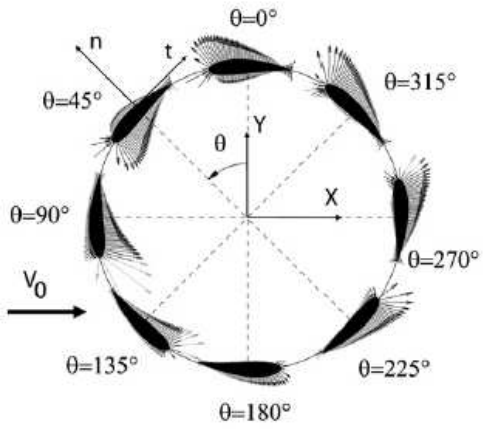

Figure 163. *Changes in pressure field during one rotation of vertical axis tidal turbine blade [156]*

As a result design for fatigue is critical in cross flow (vertical axis) turbines and both materials and structures must be optimised [156].

Another important parameter is the definition of the environment of the structures. Installed depths are usually quite shallow (*< 50 meters*) and both the seabed topography and the influence of waves can create turbulent flows which vary through the water column and will have an impact on the structure and induced loading. An additional loading parameter is related to the length of the blades (up to *10 meters*) which means that they will see pressure differences as they rotate between different water depths. This loading is not large in absolute

terms, $\pm 0.1\ bar$, but depending on design and in particular if foam sandwich is used, may affect durability.

While the aim here is not to design a tidal turbine blade a preliminary study of the modelling of a fixed pitch symmetrical composite blade has been performed. This model is inspired by the geometry of a prototype already in service (*Figure 164a*). The aim was simply to examine how current velocity affects the structural response, in order to examine how the previous material model could be integrated in such calculation. A single symmetrical blade, *1.2 meters* long, is modelled, rigidly fixed at the hub and free at the tip. A distributed load, which is a function of the geometry of the blade and the water speed *(Eqn. 50)* has been applied all over one face to simulate the effect of sea water on the structure (*Figure 164b*) and the deformed shape and the distribution of stress are calculated (*Figure 165*). The material is a solid composite, with the properties of the quasi-unidirectional E-glass/epoxy. The evolution of the global displacement of the structure has been plotted as a function of the water speed (*Figure 166*).

The results of this simple model illustrate various points.

First the pressure load generates twist, so some off-axis reinforcement will be necessary. There are some studies underway to use this flexure/twist coupling to optimise the blade response during service [157].

Second, for this particular design the highest stresses are calculated at the hub. This is not an ideal situation, as the hub/blade region is difficult to design and often involves metal inserts with bolted/bonded interfaces and stress concentrations. By modifying either the boundary conditions, by adding an external ring for example, or the shape and stiffness of the blade it is possible to modify this stress state, to control the design conditions more easily.

Third, the maximum strains (at least in this simple model) depend directly on the current speed. A design can therefore be optimised for a given set of operating conditions provided these and their variations are well known. In order to integrate the fatigue model developed in *Section 5*, *Chapter IV*, the local iterative property degradation approach could then be applied in the critical zone, together with a coupled diffusion model.

In order to validate modelling results there is a clear need for data from instrumented blades, but these are confidential commercial data. Only one very recent example of measured data at sea has been found, from the *SeaFlow* project [158]. This shows the flow inversion over a *12 hours* period and gives a first indication of speed variations, as presented on *Figure 167*. Analysis by these authors also provides an indication of how current profiles may vary through the water depth due to wave/current interactions (*Figure 168*). The authors suggest that these interactions will dominate fatigue loading, but no measured data are available.

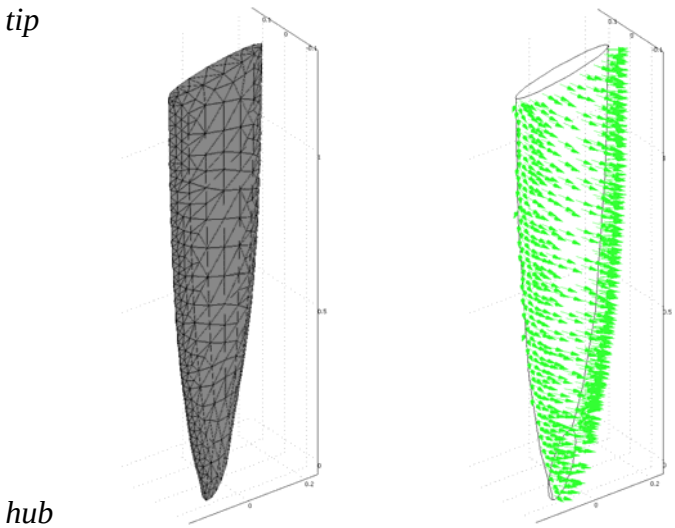

(a) *(b)*

Figure 164. *Structural composite tidal turbine blade model : a) mesh, b) loading applied*

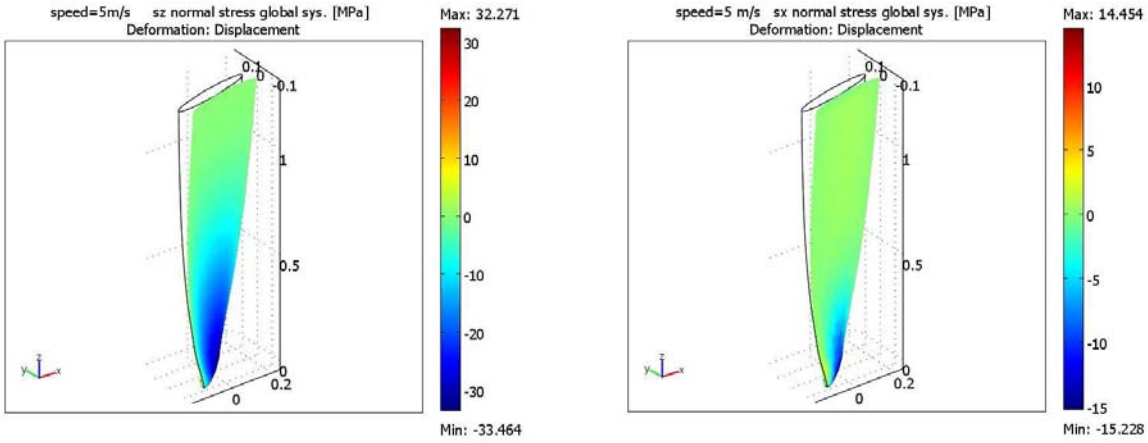

(a) *(b)*

Figure 165. *Deformed shapes and stresses in the tidal turbine blade model*

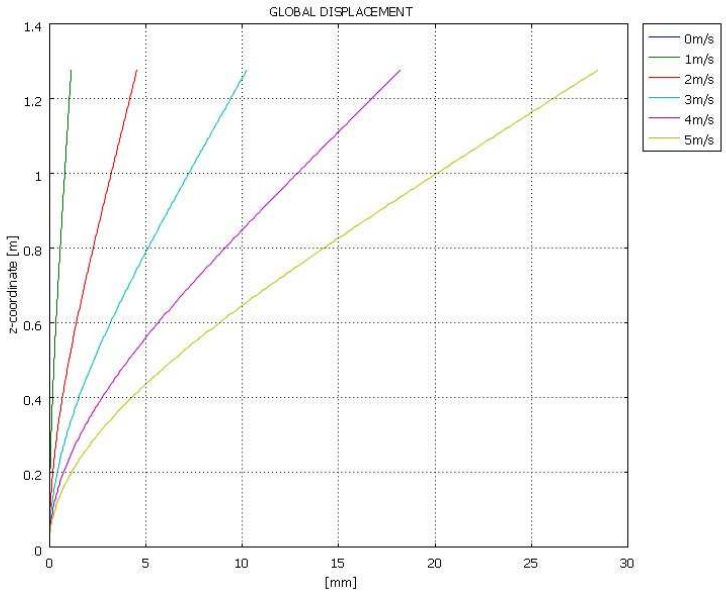

Figure 166. *Comparative curves of the global displacement (y-direction) of the structure as a function of the water speed*

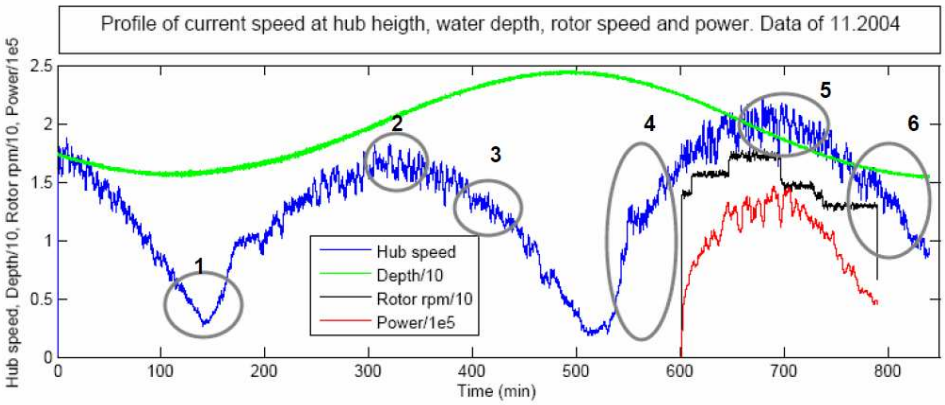

Figure 167. *Variability of current speed and generated power, SeaFlow project (source Fraunhofer Institute [158])*

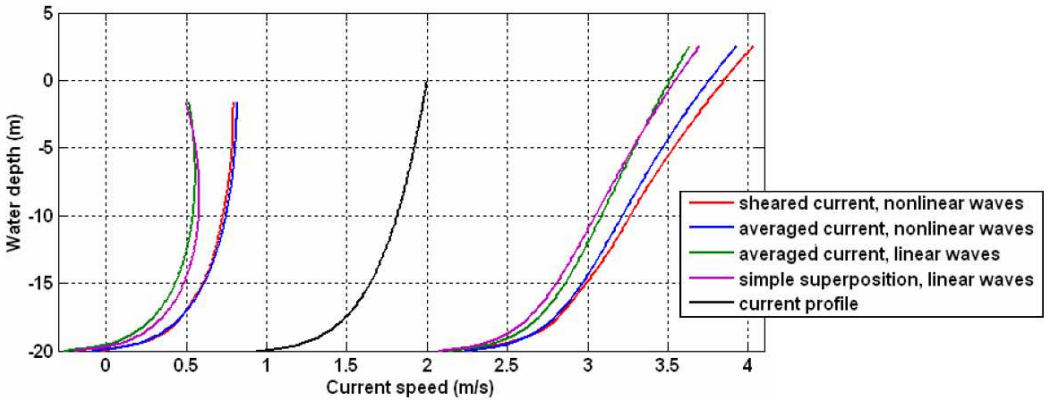

Figure 168. *Variable current speed through water column due to wave/current interactions [158]*

As real measured data are not available, an alternative intermediate step is to work on reduced scale models. Two series of preliminary tests have been performed recently in the hydrodynamics test tanks at the IFREMER Centre in Boulogne on instrumented blades [159], in order to measure directly how the movement of horizontal axis turbine blades in a tidal stream affects strain in the blades. *Figure 169* shows one of the sets of instrumented blades, which were each *300 mm* long. Three materials were used for the blades ; a cast polyurethane, the same with a thin glass mat/epoxy coating, and a third where the mat was replaced by the *1 250 g/m²* quasi-unidirectional E-glass/epoxy of the fatigue study. This resulted in three similar geometries but with very different stiffnesses when they were loaded at the tip in single-point bending (*Figure 170*). Strain gauges on the blades at *100 mm* from the tip allowed strain measurements to be made at *100 Hz*.

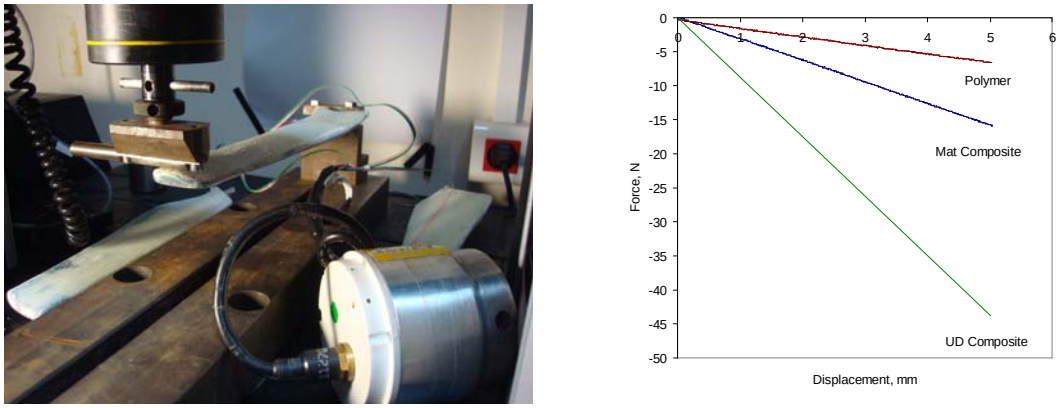

(a) *(b)*

Figure 169. *a) Stiffness measurement set-up, b) Force-displacement plots for three sets of blades*

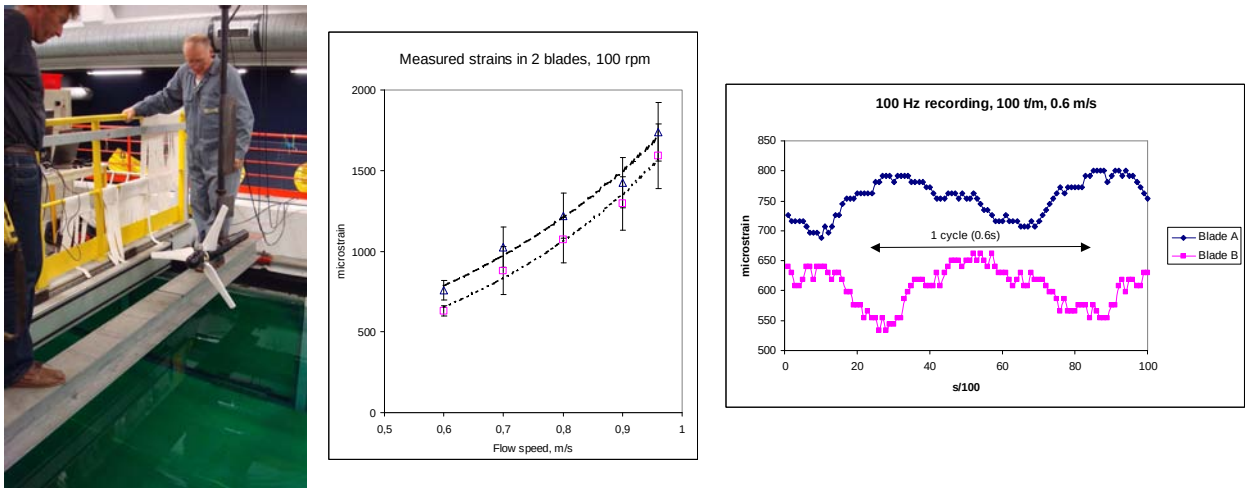

(a) *(b)* *(c)*

Figure 170. *a) Turbine before immersion, b) Strains versus current speed, c) Detail for one rotation [160]*

Figure 170a shows the turbine before immersion and during tests, and *Figure 170b* shows an example of the results for the most flexible blade. Here, the turbine rotation is imposed and the current flow rate is varied. This shows that the strains increase with the square of current velocity as expected.

In *Figure 170c*, a zoom over one second period, we can note that during each cycle the strain varies cyclically. This may be due to the support system, further tests are underway to examine this, but clearly shows a high frequency cyclic component superposed on the pressure-induced strain.

The advantage of such tests is that under closely controlled conditions they allow flow parameters to be varied, and wave-current interactions can also be studied.

They can thus provide data to evaluate more complex structural models. *COMSOL Multiphysics*™ software has been used in this study as it allows coupling to be implemented easily. Moving up from the blade structural analysis shown in the previous section it is possible now to consider a complete turbine system. A complete turbine can now be placed in an imposed flow using weak coupling between solid mechanics and Computational Fluid Dynamics (CFD) modules. Some preliminary studies have been performed with this feature, as it appears to be well-suited to modelling a tidal turbine machine. This has been used to model the wave tank tests described above. The blade geometry was first scanned (*Figure 171a*) and imported (*Figure 171b*). The turbine was then constructed, with three blades around the central generator, and a *120°* section of the flow field was constructed (*Figure 171c*). A *1 m/s* uniform flow was then applied using the CFD module and the resulting flow field around the blade is shown on *Figure 172*. (The slow flow at the model boundary is caused by a non-slip condition which is needed to allow the blade surface to have the same condition, this can be improved). This also allows the pressure field on the blade to be determined for a static blade, which can be used as an input to a mechanical analysis of stresses, strains and deformations, with or without coupling, such as shown on *Figure 173*.

The most recent version of *COMSOL Multiphysics*™ (*version 4.1a*) also includes a new feature which allows a rotating structure to be placed in a flow field (*Figure 174*). This should provide a more realistic representation of the system and allow optimal operating conditions to be studied for different blade configurations, rotations and flow speeds.

These models were developed in collaboration with *S. Savarese* of *COMSOL France* and will be used in the future to evaluate different materials options.

Finally, another key issue in future tidal turbine development is the interaction between turbines in arrays (influence of wake turbulence). As shown on *Figure 172* the zone affected by the presence of a tidal turbine must be well known if parasite loading of downstream turbines is to be avoided. Another PhD study at IFREMER is currently focussed on this problem [161].

Hydrodynamic tank studies, fluid-structure coupling and correlation with real data from instrumented tidal turbines at sea will all be necessary if expensive failures at sea are to be avoided.

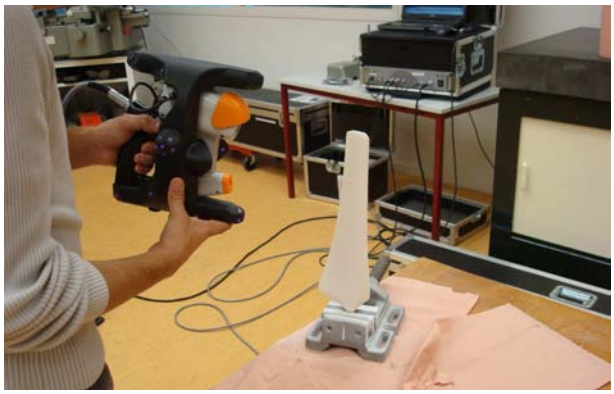

(a)

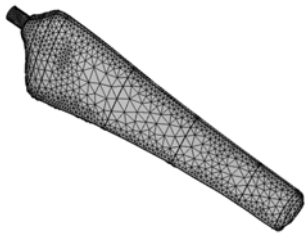

(b)

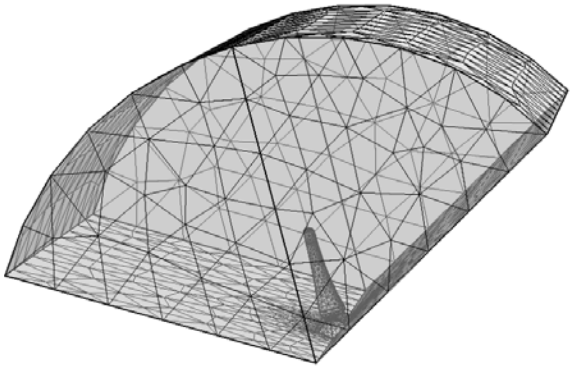

(c)

Figure 171. *a) Laser profiler to measure 3D geometry, b) Blade geometry and mesh, c) one third turbine model in flow field*

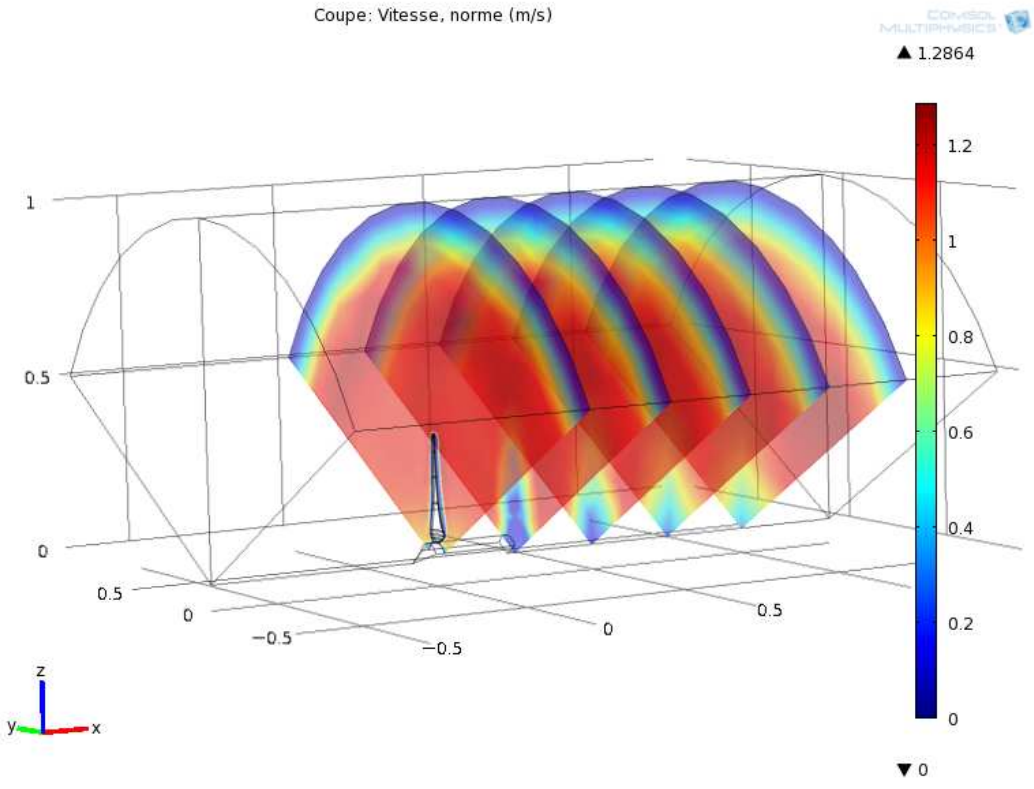

Figure 172. *Flow velocity downstream from turbine, 1 m/s applied at entry (on left)*

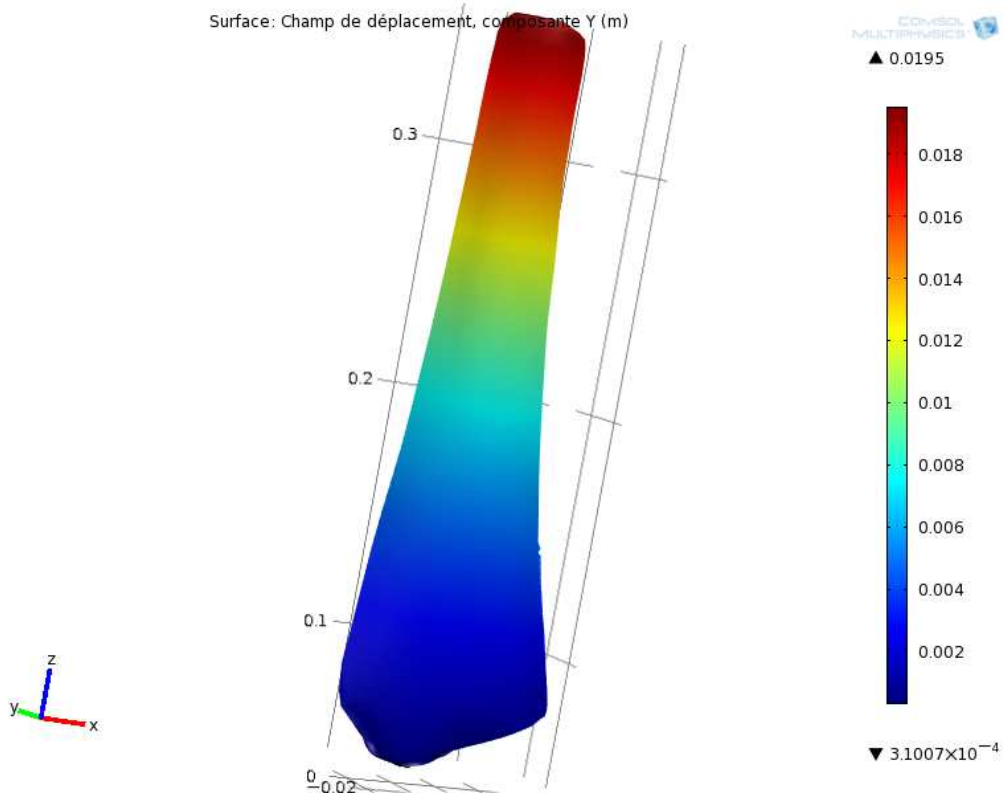

Figure 173. *Deformed shape of blade in 1 m/s flow field*

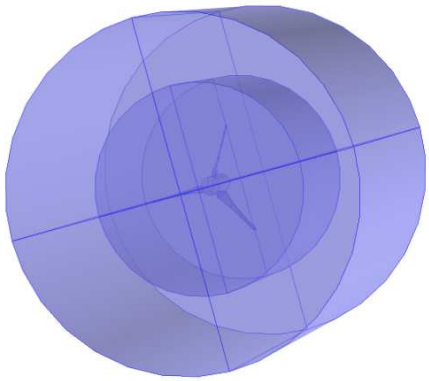

Figure 174. *Model for rotating turbine in flow field*

CONCLUSIONS AND FUTURE WORK

The development of ocean energy conversion systems places more severe requirements on material than similar land-based structures such as wind turbines. Intervention and maintenance at sea are more costly, so for ocean energy supply to become economically viable long term durability must be guaranteed. Composite materials offer many advantages over metallic structures with respect to ease of fabrication of complex profiles and light weight for installation, and many composite marine structures have shown remarkable longevity. Nevertheless material selection is critical. The choice of glass reinforcement is important if stress corrosion is to be avoided, while resin chemistry must be optimized to limit matrix damage and moisture absorption. Fibre/matrix interfaces properties are also critical when composites are immersed for long periods and the know-how of both fibre and resin producers is essential to optimize these.

Ocean energy applications are a new area for composite materials, and the work described in this thesis is a first step toward developing a methodology to design for durability of structures such as tidal turbines.

The main objectives of this study were first to identify and quantify the influence of the type of reinforcement on the composite material behaviour as a function of the environment. A second objective, was to develop a numerical model to simulate the coupling phenomena between the water absorption and the mechanical damage. The overall objective was to contribute to the evaluation of the long term durability of composite structures for ocean energy conversion systems.

At the start of the project reinforcements with three different glass fibres were supplied together with an epoxy resin. In the experimental part it was first necessary to develop an appropriate manufacturing procedure, to define a quality control programme, and to develop appropriate test geometries and procedures, especially in order to perform tests both in air and in natural circulating sea water.

In order to define the influence of the environment and the glass fibre type, a large number of static and fatigue tests have been carried out in different environments, in air and in natural circulating sea water, on three different composite materials reinforced with different glass fibres, E-glass, Advantex® or HiPer-tex™ fibres.

By performing quasi-static (CRP and flexural tests) and fatigue tests both in air and in sea water, the significant influence of sea water on the mechanical properties of these composite materials has been highlighted.

First, a large reduction (*40 %*) in the quasi-static strengths of the composite materials due to sea water absorption has been shown by performing static tests after different ageing periods. The residual failure stresses in tension and bending decrease when the water absorption increases, especially for composite materials reinforced with E-glass. However, the corresponding moduli do not seem to be influenced by the water absorption for these composite materials. In addition, further tests performed on aged and dried specimens have shown that the phenomena involved in sea water absorption are not completely reversible, this last point reveals the damaging role of moisture, which can be added to (or multiply) the mechanical stress contribution.

By comparing the set of experimental results obtained for aged composite materials with those from tests performed on aged pure resin specimens, the influence of the matrix on the behaviour of aged composite has been highlighted. The mechanical properties of both the pure resin material and the infused composites are linked to the water absorption, even if these changes may be reversible, and this must be taken into account in designing tidal turbine blades.

Concerning the fatigue behaviour of these materials in sea water very few data were available at the start of the project, and one of the main results is that the influence of this parameter can now be quantified. For a given stress level, the corresponding number of cycles before failure for E-glass reinforced composites is reduced in natural circulating sea water compared to in air, by a factor of about *3*. However, no change in the evolution of damage (as measured by apparent stiffness changes) was detected during the fatigue life. Composite materials reinforced with HiPer-tex™ fibres are much less sensitive to the sea water environment, suggesting that glass fibre composition plays a role in damage development. This result has been noted previously in creep tests (stress corrosion) but not under cyclic loads.

To complete this set of experimental data, flexural tests have been performed on specimens which were subjected to fatigue cycles, and it appears that fatigue may lead to a redistribution of stress which can induce a small increase in the residual mechanical properties.

In order to be able to evaluate the long term durability of composite structures for ocean energy conversion systems, the complex phenomenon of coupling between water absorption and mechanical damage must be modelled. In the second part of the study a modelling procedure has been defined and several numerical models have been created. These numerical models represent the different steps necessary to simulate the long term behaviour. First, a preliminary study was performed, to define the influence of each of the parameters involved in the different numerical models, such as the geometry, the material properties, and the mesh size and distributions.

Then the first model simulated the water uptake and the evolution of the water concentration in a composite specimen by integrating the kinetics of diffusion in a numerical model defined for each materials (pure resin, infused E-glass and HiPer-tex™) at each experimental temperature (*4°C*, *20°C*, *40°C* and *60°C*). These numerical models, based on the experimental investigations, allowed us to conclude that the modelling of the water diffusion in the composite materials studied using a Fickian model is reasonably consistent with the measured behaviour.

The second set of models described the static mechanical behaviour of the composite materials loaded in tension, compression and bending. These numerical models have been created with respect to the experimental conditions and show, by comparison with the experimental results that the different mechanical behaviours are well represented.

The third step was to create a coupled model, defined for a composite reinforced with E-glass fibres aged in sea water and then subjected to a static four-point flexural load. In order to couple the two phenomena, the relationships between the evolutions of the mechanical properties and the water diffusion have been identified, and integrated in a numerical model taking into account both the water diffusion and the mechanical behaviour. This simplified numerical model reveals the damaged zones after different immersion times, and, more

important it shows how a change in failure mode from compressive to tensile can occur. This change was observed during tests and is important as it indicates that both compressive and tensile properties must be considered in a durability analysis.

The last step investigated in this study was the simulation of the evolution of damage of a composite specimen during a fatigue test. This model developed uses an iterative method based on the evolution of the stiffness of the specimen and the redistribution of the stress during the test. It is a first simplified approach to determine the stiffness loss of a specimen subjected to flexural fatigue loads, and it requires further refinements such as a more precise material definition (ply by ply analysis).

In future work, several points require further study.

From a material point of view it has been shown that many parameters, in particular fibre type, matrix resin selection and fibre sizing affect the durability. Tests are continuing on glass reinforced vinyl ester matrix composites and carbon fibre reinforced composites in order to clarify the role of both. The strong reduction in fatigue life noted during a small number of tests with non-optimized sizing reveal the importance of close collaboration between materials suppliers and designers for these applications. This initial study has focussed on quasi-unidirectional materials but off-axis reinforcements will be needed in a tidal turbine blade, and their role in damage development in water must be examined in detail.

With respect to testing, a limited number of fatigue parameters (frequency and R-ratio) have been studied. The need for preliminary work on a modified test geometry, as the standard specimen did not provide valid results, and the time required to produce satisfactory panels for tests, mean that these parameters have not been explored in details, this is discussed in *Chapter V*. Clearly more work is required, particularly to quantify the rate-dependency. A device to apply tension-tension fatigue loads in sea water has been developed, and this will be used in future to provide additional data on a more conventional specimen geometry.

In the future the materials properties must be also investigated in accordance with the type of stress which occurs in real conditions. From this point of view the experimental and numerical simulation experience of composite wind turbines will be very useful, but the specific loads on underwater structures must also be included. More in-service measurements are urgently needed to quantify these, and the development of embedded instrumentation (strain gauges, Bragg gratings, …) and data transmission methods will be key elements for this. Indeed the role of multiaxial stresses is a natural continuation of this work. For instance the effect of combined tension-torsion loads could affect both the fatigue life and the ageing of the materials.

Finally it is important to consider the integration of the numerical description of the composite material behaviour in a tidal turbine blade model, taking into account the mechanical behaviour of the structure due to the interaction with the fluid. A major recent development means that the same software tool used for the specimen modelling here now enables a complete rotating tidal turbine to be modelled in a flow field. The various steps described in *Chapter V*, (specimen modelling, diffusion, fatigue model, single blade model and full turbine simulation) can thus be followed with the same numerical tool. While this does not replace more complex software specially designed for blade analysis, CFD or mechanical modelling, the ease of coupling the results means that parametric studies can be performed on a PC to examine the consequence of material, structural and environmental changes. This modelling approach has been linked with the first experimental investigations

performed on a prototype in a hydrodynamic test tank at IFREMER in order to evaluate the approach, additional tests are necessary.

The development of marine energy devices is in its infancy. Composites can play a leading role in this development but it is essential that procedures be developed to enable them to be certified under realistic conditions. Material failures during demonstrator projects at sea could seriously limit the development of this industry.

References

[1] *IFREMER, Synthèse de l'étude prospective sur les énergies renouvelables marines à l'horizon 2030, (March 2008)*

[2] *IEA/ICOE annual report, (2007)*

[3] *EC, Ocean Energy Conversion in Europe, (2006)*

[4] *Frau J., Tidal energy : promising projects : La Rance, a successful industrial scale experiment. Energy Conversion, IEEE Transactions.* ***8****(3): p. 552-558, (1993).*

[5] *Davies P. and Lemoine L. Nautical applications of composite materials. in 'Proceedings of 3rd IFREMER Conference', Paris, (1992).*

[6] *Greene E. Marine composites Second Edition. [Available from: http://www.marinecomposites.com/]*

[7] *Davies P. and Choqueuse D., Ageing of composites in marine vessels, in 'Ageing of composites', R. Martin, Editor, Woodhead Publishers, (2008).*

[8] *Smith C.S., Design of marine structures in composite materials, Elsevier Science Publishers: London, (1990).*

[9] *Lemière Y. The evolution of composite materials in submarine structures. in 'Proceedings of International conference on nautical construction with composite materials', Paris (France): IFREMER, (1992).*

[10] *Gibson A., The cost effective use of fibre reinforced composite offshore, HSE report 39, (2003)*

[11] *Baldwin D.D., Newhouse N., and Lo K. Composite production riser design. in 'Proceedings of Twenty-ninth annual offshore technology conference', Houston, USA, (1997).*

[12] *Chauchot P., et al. Composite pressure vessels: towards a composite subsea separator. in 'Proceedings of Fourth International Conference on Composite Material and Structures for offshore operations (CMOO-4)', Houston Texas, USA, (October 4-6, 2005).*

[13] *Gisman, modular buoys. [Available from: http://www.gisman-ocea.com/]*

[14] *in 'Proceedings of IALA Workshop on Developments in Floating Aids and Associated Moorings', Brest, France, (1-4 April 2008).*

[15] *Springer G.S., ed. Environmental Effects on Composite Materials. (Vol1 (1980), Vol2 (1984)).*

[16] *Davies P., et al. Aging and long term behavior of composite tubes. in 'Proceedings of Recent Developments in durability analysis of composite systems, Duracosys', (1999).*

[17] *Richard F. and Perreux D., The safety-factor calibration of laminates for long-term applications: behavior model and reliability method. Composites Science and Technology.* ***61****(14): p. 2087-2094, (2001).*

[18] *Harris B., ed. Fatigue in Composites. Woodhead Publishers, (2003).*

[19] *Echtermeyer A.T., et al. Method to predict fatigue lifetimes of GRP wind turbine blades and comparison with experiments. in 'Proceedings of the 1996 European Union wind energy conference and exhibition', Göteborg, Sweden: Stephens and Associates, (20–24 May,1996).*

[20] *Nijssen R.P.L., VanWingerde A.M., and VanDelft D.R.V., Wind turbine rotor blade materials : Estimating service lives. S.A.M.P.E. journal ISSN 0091-1062* ***vol. 43****(no2): p. pp. 7-15, (2007).*

[21] *Guedes R.M., Creep and fatigue lifetime prediction of polymer matrix composites based on simple cumulative damage laws. Composites Part A: Applied Science and Manufacturing.* ***39****(11): p. 1716-1725, (2008).*

[22] *Sutherland H.J. and Mandell J.F. Application of the U.S. high cycle fatigue data base to wind turbine blade lifetime predictions. in 'Proceedings of Energy Week 1996, ASME', (1996).*

[23] *Ronold K.O. and Christensen C.J., Optimization of a design code for wind-turbine rotor blades in fatigue. Engineering Structures.* ***23****(8): p. 993-1004, (2001).*

[24] *Marsh G., Tidal turbines harness the power of the sea. Reinforced Plastics.* ***48****(6): p. 44-47, (2004).*

[25] *Fraenkel P.L., Tidal Current Energy Technologies. p. 145-151, (2006).*

[26] *SeaGen Project. [Available from: http://www.seageneration.co.uk/]*

[27] *McKee L., Trouble hits tide power turbine as the blades fly off, in Belfast Telegraph, (23 July 2008).*

[28] *Sabella Project. [Available from: http://www.sabella.fr/]*

[29] *OpenHydo project. [Available from: http://www.openhydro.com/]*

[30] *Shichiri A., et al. Study of the Characteristic and Possibility for Applying Composite Materials to the Blades of Tidal Power Generation. in 'Proceedings of The 27th International Conference on Offshore Mechanics and Arctic Engineering', Estoril, Portugal, (5-20 June, 2008).*

[31] *Annual book of ASTM standards. p. C177-D1600 08.01 plastics (I), (1991).*

[32] *Sims G. Harmonised standards arrive at last. in 'Proceedings of European Conference on Composites Testing and Standardisation', Lisbon, (Sept 1998).*

[33] *Perrot Y., Influence des propriétés de la matrice sur le comportement mécanique de matériaux composites verre/polyester utilisés en construction navale de plaisance - Cas des résines polyester limitant les émissions de styrène., PhD Thesis, Université de Bretagne Sud (2006).*

[34] *Ellyin F. and Kujawski D., Tensile and fatigue behaviour of glassfibre/epoxy laminates. Construction and Building Materials.* ***9****(6): p. 425-430, (1995).*

[35] *Philippidis T.P. and Vassilopoulos A.P., Complex stress state effect on fatigue life of GRP laminates.: part I, experimental. International Journal of Fatigue.* ***24****(8): p. 813-823, (2002).*

[36] *Kujawski D., Width effects on the tensile strength and fatigue behavior of angle-ply laminates. International Journal of Fatigue.* ***20****(8): p. 575-580, (1998).*

[37] *Pauchard V., Etude des mécanismes de rupture des fibres dans les composites verre/epoxy sous sollicitation de fatigue longitudinale en milieu humide : Application d'un modèle de corrosion sous contrainte, PhD Thesis, Matériaux, Ecole Centrale de Lyon (2001).*

[38] *Pauchard V., Etude des mécanismes de rupture des fibres dans les composites verre/epoxy sous sollicitation de fatigue longitudinale en milieu humide : Application d'un modèle de corrosion sous contrainte, PhD Thesis, Ecole Centrale de Lyon (2001).*

[39] *Schultheisz C.R. and Waas A.M., Compressive failure of composites, Part I : Testing and micromechanical theories. Prog. Aerospace Sci.* ***32****: p. 1-42, (1996).*

[40] *Tan S.C. and Knight M., An extrapolation method for the evaluation of compression strength of laminated composites, in 'Compression response of composite structures, ASTM STP 1185', S.E. Grooves and A.L. Highsmith, Editors), American Society for Testing and Materials: Philadelphia. p. 323-337, (1994).*

[41] *Caprino G. and Giorleo G., Fatigue lifetime of glass fabric/epoxy composites. Composites Part A: Applied Science and Manufacturing.* ***30****(3): p. 299-304, (1999).*

[42] *Caprino G. and D'Amore A., Flexural fatigue behaviour of random continuous-fibre-reinforced thermoplastic composites. Composites Science and Technology.* ***58****(6): p. 957-965, (1998).*

*[43] Kim J., Lee W.I., and Tsai S.W., Modeling of mechanical property degradation by short-term aging at high temperatures. Composites Part B: Engineering. **33**(7): p. 531-543, (2002).*

*[44] Gilchrist M.D., et al., Mechanical performance of carbon-fibre- and glass-fibre-reinforced epoxy I-beams: I. Mechanical behaviour. Composites Science and Technology. **56**(1): p. 37-53, (1996).*

*[45] Ben Zineb T., Sedrakian A., and Billoet J.L., An original pure bending device with large displacements and rotations for static and fatigue tests of composite structures. Composites Part B: Engineering. **34**(5): p. 447-458, (2003).*

*[46] Ferry L., et al., Fatigue behaviour of composite bars subjected to bending and torsion. Composites Science and Technology. **59**(4): p. 575-582, (1999).*

[47] Davies P., Blackman B., and Brunner A., Mode II delamination, in 'Frature Mechanics Testing Methods for Polymers, Adhesives and Composites', Moore, Williams, and Pavan, Editors), ESIS Publication, (2001).

[48] O'Brien T., Murri G., and Salpekar S., Interlaminar Shear Fracture Toughness and Fatigue Thresholds for Composite Materials, in 'Composite Materials: Fatigue and Fracture, Second Volume - Proceedings of the Second ASTM Symposium', P.A. Lagace, Editor: Cincinnati, OH, (27, 28 Apr. 1987).

*[49] Yerramalli C.S. and Waas A.M., A failure criterion for fiber reinforced polymer composites under combined compression-torsion loading. International Journal of Solids and Structures. **40**(5): p. 1139-1164, (2003).*

*[50] Post N.L., et al., Residual strength prediction of composite materials: Random spectrum loading. Engineering Fracture Mechanics. **75**(9): p. 2707-2724, (2008).*

*[51] Nyman T., Composite fatigue design methodology: a simplified approach. Composite Structures. **35**(2): p. 183-194, (1996).*

*[52] El Kadi H. and Al-Assaf Y., Energy-based fatigue life prediction of fiberglass/epoxy composites using modular neural networks. Composite Structures. **57**(1-4): p. 85-89, (2002).*

[53] Initiation à la mécanique des plastiques renforcés par les fibres, Centre d'actualisation scientifique et technique, Recueil de conférences, (1974)

*[54] Ferreira J.A.M., et al., Analysis of fatigue and damage in glass-fibre-reinforced polypropylene composite materials. Composites Science and Technology. **59**(10): p. 1461-1467, (1999).*

*[55] Dyer K.P. and Isaac D.H., Fatigue behaviour of continuous glass fibre reinforced composites. Composites Part B: Engineering. **29**(6): p. 725-733, (1998).*

*[56] Shan Y. and Liao K., Environmental fatigue behavior and life prediction of unidirectional glass-carbon/epoxy hybrid composites. International Journal of Fatigue. **24**(8): p. 847-859, (2002).*

[57] Optimat Optimat project. [Available from: http://www.wmc.eu/optimatblades.php]

*[58] Salvia M., et al., Flexural fatigue behaviour of UDGFRP experimental approach. International Journal of Fatigue. **19**(3): p. 253-262, (1997).*

*[59] Salvia M. and Vincent L., Modelling of flexural fatigue behaviour in UD glass-fibre-reinforced polymer. Composites Science and Technology. **56**(7): p. 797-802, (1996).*

*[60] O'Brien T.K., et al., Transverse tension fatigue life characterization through flexure testing of composite materials. International Journal of Fatigue. **24**(2-4): p. 127-145, (2002).*

[61] Fiore L. and Vincent L., Contribution à la caractérisation en fatigue de matériaux composites unidirectionnels, Laboratoire de Mécanique des Solides, Ecole Centrale de Lyon,

*[62] Roudet F., Desplanques Y., and Degallaix S., Fatigue of glass/epoxy composite in three-point-bending with predominant shearing. International Journal of Fatigue. **24**(2-4): p. 327-337, (2002).*

*[63] Bellenger V., Tcharkhtchi A., and Castaing P., Thermal and mechanical fatigue of a PA66/glass fibers composite material. International Journal of Fatigue. **28**(10): p. 1348-1352, (2006).*

*[64] Van Paepegem W. and Degrieck J., Experimental set-up for and numerical modelling of bending fatigue experiments on plain woven glass/epoxy composites. Composite Structures. **51**(1): p. 1-8, (2001).*

*[65] Van Paepegem W. and Degrieck J., Modelling damage and permanent strain in fibre-reinforced composites under in-plane fatigue loading. Composites Science and Technology. **63**(5): p. 677-694, (2003).*

*[66] El-Assal A.M. and Khashaba U.A., Fatigue analysis of unidirectional GFRP composites under combined bending and torsional loads. Composite Structures. **79**(4): p. 599-605, (2007).*

*[67] Degallaix G., Hassaïni D., and Vittecoq E., Cyclic shearing behaviour of a unidirectional glass/epoxy composite. International Journal of Fatigue. **24**(2-4): p. 319-326, (2002).*

*[68] Read P.J.C.L. and Shenoi R.A., A review of fatigue damage modelling in the context of marine FRP laminates. Marine Structures. **8**(3): p. 257-278, (1995).*

*[69] Owen M. and Dukes R., Failure of glass-reinforced plastics under single and repeated loading. The Journal of Strain Analysis for Engineering Design. **2**(4): p. 272-279, (1967).*

[70] Schultz K., Reese E., and Chou T.W. Fatigue behaviour and damage development in woven fabric composites. in 'Proceedings of ICCM VI and ECCM 2', London, (1987).

*[71] Halpin J.C., Johnson T.A., and Waddoups M.E., Kinetic fracture models and structural reliability. International Journal of Fracture. **8**(4): p. 465-468, (1972).*

[72] Wolff R.V. and Lemon G.H., Reliability Prediction for Adhesive Bonds, General Dynamics Fort Worth Tex Convair Aerospace Division, (Oct 1972)

[73] Sendeckyj G.P., Life-prediction for resin-matrix composite materials, in 'Fatigue of composite materials', K.L. Reinfsnider, Editor, Elsevier Science. p. 431-483, (1990).

*[74] Epaarachchi J.A. and Clausen P.D., An empirical model for fatigue behavior prediction of glass fibre-reinforced plastic composites for various stress ratios and test frequencies. Composites Part A: Applied Science and Manufacturing. **34**(4): p. 313-326, (2003).*

*[75] Van Paepegem W. and Degrieck J., A new coupled approach of residual stiffness and strength for fatigue of fibre-reinforced composites. International Journal of Fatigue. **24**(7): p. 747-762, (2002).*

*[76] Van Paepegem W., Degrieck J., and De Baets P., Finite element approach for modelling fatigue damage in fibre-reinforced composite materials. Composites Part B: Engineering. **32**(7): p. 575-588, (2001).*

*[77] Sedrakian A., Zineb T.B., and Billoet J.L., Contribution of industrial composite parts to fatigue behaviour simulation. International Journal of Fatigue. **24**(2-4): p. 307-318).*

*[78] Abd Allah M.H., et al., Effect of fibre volume fraction on the fatigue behaviour of GRP pultruded rod composites. Composites Science and Technology. **56**(1): p. 23-29, (1996).*

*[79] Salvia M., et al., Flexural fatigue behaviour of UDGFRP : experimental approach. International Journal of Fatigue. **19**(3): p. 9, (1997).*

*[80] Vauthier E., et al., Interactions between hygrothermal ageing and fatigue damage in unidirectional glass/epoxy composites. Composites Science and Technology. **58**(5): p. 687-692, (1998).*

*[81] Pauchard V., et al., Application of a stress-corrosion-cracking model to an analysis of the durability of glass/epoxy composites in wet environments. Composites Science and Technology. **62**(4): p. 493-498, (2002).*

*[82] Pauchard V., et al., In situ analysis of delayed fibre failure within water-aged GFRP under static fatigue conditions. International Journal of Fatigue. **24**(2-4): p. 447-454, (2002).*

*[83] Chateauminois A. and Pauchard V., Vieillissement hygrothermique et tenue en fatigue de composites unidirectionnels. Prise en compte du couplage par un modèle de corrosion sous contrainte. Revue des Composites et des Matériaux Avancés. **12**(1): p. 51-69, (2002).*

*[84] Attia O., Kinloch A.J., and Matthews F.L., Modelling the fatigue life of polymer-matrix fibre-composite components. Composites Science and Technology. **61**(15): p. 2273-2283, (2001).*

*[85] Gilchrist M.D., Kinloch A.J., and Matthews F.L., Mechanical performance of carbon-fibre- and glass-fibre-reinforced epoxy I-beams: III. fatigue performance. Composites Science and Technology. **59**(2): p. 179-200, (1999).*

*[86] Dai J. and Thomas Hahn H., Flexural behavior of sandwich beams fabricated by vacuum-assisted resin transfer molding. Composite Structures. **61**(3): p. 247-253, (2003).*

*[87] Kanny K. and Mahfuz H., Flexural fatigue characteristics of sandwich structures at different loading frequencies. Composite Structures. **67**(4): p. 403-410, (2005).*

*[88] Philippidis T.P. and Vassilopoulos A.P., Complex stress state effect on fatigue life of GRP laminates. Part II, Theoretical formulation. International Journal of Fatigue. **24**(8): p. 825-830, (2002).*

*[89] Lafarie-Frenot M.-C., Damage mechanisms induced by cyclic ply-stresses in carbon-epoxy laminates: Environmental effects. International Journal of Fatigue. **28**(10): p. 1202-1216, (2006).*

*[90] Gamby D., et al., The prediction of the long-term mechanical behaviour of aeronautical laminates. Composites Science and Technology. **61**(3): p. 439-443, (2001).*

*[91] Kensche C.W., Fatigue of composites for wind turbines. International Journal of Fatigue. **28**(10): p. 1363-1374, (2006).*

*[92] Kong C., Bang J., and Sugiyama Y., Structural investigation of composite wind turbine blade considering various load cases and fatigue life. Energy. **30**(11-12): p. 2101-2114, (2005).*

[93] Talreja R., Fatigue of Composite Materials: Damage Mechanisms and Fatigue-Life Diagrams. p. 461-475, (1981).

*[94] Spera D., Dynamics loads in horizontal-axis wind turbines Part II ; empirical equations. Windpower' 93. **282**(9), (1993).*

[95] Lemaitre J. and Chaboche J.L., Mécanique des matériaux solides, ed. Dunod. (1985).

*[96] Van Paepegem W. and Degrieck J., Effects of Load Sequence and Block Loading on the Fatigue Response of Fiber-Reinforced Composites. J Mechanics of Advanced Materials and Structures. **9**(1): p. 19 - 35, (2002).*

*[97] Zhifei S., Yanhua C., and Limin Z., Micromechanical damage modeling of fiber/matrix interface under cyclic loading. Composites Science and Technology. **65**(7-8): p. 1203-1210, (2005).*

*[98] Shi Z.F. and Zhou L.M., Interfacial damage in fibre-reinforced composites subjected to tension fatigue loading. Fatigue & Fracture of Engineering Materials & Structures. **25**(5): p. 445-457, (2002).*

*[99] Miyano Y., Nakada M., and Sekine N., Accelerated testing for long-term durability of GFRP laminates for marine use. Composites Part B: Engineering. **35**(6-8): p. 497-502).*

[100] Comyn J., Introduction to polymer permeability and the mathematics of diffusion, in 'Polymer permeability', J. Comyn, Editor, Elsevier applied science, (1985).

[101] Muniandy K., Southern E., and Thomas A.G., Diffusion of liquids and solids in rubber, in 'Natural Rubber Science and Technology', A.D. Roberts, Editor, Oxford Science Publications, (1988).

[102] Riley J.P. and Skirrow G., Chemical oceanography. Vol. 1. London, (1965).

[103] Culkin F., The major constituents of sea water, in 'Chemical oceanography', J.P. Riley and G. Skirrow, Editors): London. p. 121-161, (1965).

*[104] Lyman L. and Fleming H., Composition of sea water. J. Marine Res. **3**: p. 134-146, (1940).*

[105] Standard specification for substitute ocean water, ASTM-D 1141, (1990).

[106] Verdu J., Vieillissement des plastiques, AFNOR-Technique, Editor, Eyrolles, (1984).

[107] Ward I.M., Mechanical properties of solid polymers, ed. Wiley. (1983).

*[108] Carter H.G. and Kibler K.G., Langmuir-type model for anomalous moisture diffusion in composite resins. Journal of Composite Materials. **12**(2): p. 118-131, (1978).*

*[109] Fick A., Über Diffusion. Ann Phys. **94**(59), (1855).*

[110] Crank J., The Mathematics of Diffusion. Oxford University Press, (1979).

[111] Fourier J., Théorie analytique de la chaleur, ed. F. Didot. Paris, (1822).

[112] Browning C., Husman G., and Whitney J., Moisture Effects in Epoxy Matrix Composites, in 'Composite materials : testing and design (fourth conference)', ASTM, Editor, (1977).

*[113] Perreux D. and Suri C., A study of the coupling between the phenomena of water absorption and damage in glass/epoxy composite pipes. Composites Science and Technology. **57**(9-10): p. 1403-1413, (1997).*

[114] Mercier J., Prise en compte du vieillissement et de l'endommagement dans le dimensionnement de structures en matériaux composites, PhD Thesis, Science et Génie des Matériaux, Ecole Nationale Supérieure des Mines de Paris (2006).

[115] Frankle and R S., Stress corrosion cracking in fibreglass composite structures : A case study. Vol. 6. Shrewsbury, UK: Rapra Technology, (1998).

[116] Renaud C.M. and Greenwood M.E., Effect of Glass Fibres and Environments on Long-Term Durability of GFRP Composites. (2002).

[117] Weitsman Y.J., Penumadu D., and Siriuk A. On the immersed and dry fatigue of carbon fiber/vinyl ester composite material. in 'Proceedings of 17th International Conference on Composite Materials', Edinburgh, UK, (2009).

[118] Lin, et al., Effects of fibre content on mechanical properties and fracture behaviour of short carbon fibre reinforced geopolymer matrix composites. Vol. 32. Heidelberg, Germany: Springer. 5, (2009).

*[119] Chen J.H., et al., Effect of fibre content on the interlaminar fracture toughness of unidirectional glass-fibre/polyamide composite. Composites Part A: Applied Science and Manufacturing. **30**(6): p. 747-755, (1999).*

*[120] Lee N.-J. and Jang J., The effect of fibre content on the mechanical properties of glass fibre mat/polypropylene composites. Composites Part A: Applied Science and Manufacturing. **30**(6): p. 815-822, (1999).*

*[121] Sjögren A., et al., Effects of fibre coating (size) on properties of glass fibre/vinyl ester composites. Composites Part A: Applied Science and Manufacturing. **30**(8): p. 1009-1015, (1999).*

*[122] Bayraktar E., Antolovich S.D., and Bathias C., New developments in non-destructive controls of the composite materials and applications in manufacturing engineering. Journal of Materials Processing Technology. **206**(1-3): p. 30-44, (2008).*

[123] Fisher-Cripps A.C., Nanoindentation, ed. Springer. (2004 (2nd Edition)).

*[124] Oliver W.C. and Pharr G.M., An improved technique for determining hardness and elastic modulus using load and displacement sensing indentation experiments. J. Mater. Res. **7**(6), (1992).*

[125] Ducloux A., Mise en place d'une procédure de réalisation de plaques en verre/epoxy par le procédé d'infusion à chaud - Mise en place de procédures de caractérisation en tension cyclique de composites verre/epoxy, IFREMER, Mémoire de stage, (2009)

[126] Messager T., Optimisation d'enceintes sous-marines composites, PhD Thesis, Mécanique, Université des Sciences et Technologies de Lille I (2000).

[127] Messager T., Chauchot P., and Bigourdan B. Optimal design of stiffened composite underwater hulls. in 'Proceedings of III European Conference on Computational Mechanics. Solids, Structures and Coupled Problems in Engineering', Lisbon (Portugal), (2006).

*[128] Olivier P., Cottu J.P., and Ferret B., Effects of cure cycle pressure and voids on some mechanical properties of carbon/epoxy laminates. Composites. **26**(7): p. 509-515, (1995).*

[129] Olivier P., Marguerès P., and Mascaro B. Assessment of the effects of voids on some physical, mechanical and damage mechanics properties of carbon/polymeric composites. in 'Proceedings of 12th European Conference on Composite Materials', Biarritz, France, (2006).

*[130] Rubin A.M. and Jerina K.L., Evaluation of porosity in composite aircraft structures. Mechanics of Composite Materials. **30**(6): p. 587-600, (1994).*

[131] Maurin R., Etude des facteurs limitant l'usage des matériaux composites Carbone/Epoxy pour la réalisation de bateau de course, PhD Thesis, Laboratoire LIMATB, Université de Bretagne Sud (2009).

*[132] Perrin F.X., Nguyen M.H., and Vernet J.L., Water transport in epoxy-aliphatic amine networks - Influence of curing cycles. European Polymer Journal. **45**(5): p. 1524-1534, (2009).*

[133] Gay D., Matériaux composites, in 'Traité des Nouvelles Technologies, Série Mécanique', Hermès, Editor, (1987).

[134] Nijssen R.P.L., et al. Fatigue and residual strength degradation in wind turbine rotor blade composites. in 'Proceedings of European Wind Energy Conference & Exhibition', London, UK, (22-25 November 2004).

[135] Post N.L., Modeling the Residual Strength Distribution of Structural GFRP Composite Materials Subjected to Constant and Variable Amplitude Tension-Tension Fatigue Loading, PhD Thesis, Science in Engineering Mechanics, Faculty of the Virginia Polytechnic Institute and State University (2005).

[136] Shokrieh M.M. and Lessard L.B., Fatigue under multiaxial stress systems, in 'Fatigue in composites: Science and technology of the fatigue response of fibre-reinforced plastics', B. Harris, Editor: University of Bath, UK. p. 63-114, (2003).

[137] Bakis E., Simonds R.A., and Stinchcomb W.W., A test method to measure the response of composite materials under reversed cyclic loads, in Test methods for design allowables for fibrous composites, ASTM, Editor. p. 93-110, (1989).

[138] Simonds R.A. and Stinchcomb W.W., Response of notched AS4/PEEK laminates to tension/compression loading, in Advances in thermoplastic matrix composite materials ASTM, Editor, G.M.Newaz. p. 133-145, (1989).

[139] Stinchcomb W.W. and Bakis C.E., Fatigue behaviour of composite laminates, in 'Fatigue of composite materials', K.L. Reifsnider, Editor, Elsevier Sciences. p. 105-180, (1990).

[140] Evaluation of measurement data — Guide to the expression of uncertainty in measurement, Joint Committee for Guides in Metrology-100:2008, (September 2008)

*[141] Sutherland L.S. and Soares C.G., Contact indentation of marine composites. Composite Structures. **70**(3): p. 287-294, (2005).*

*[142] Chen P., et al., Failure mechanisms of laminated composites subjected to static indentation. Composite Structures. **75**(1-4): p. 489-495, (2006).*

[143] Yang S.H. and Sun C.T., Indentation law for composite laminates ASTM STP 787. p. 425-449, (1982).

[144] Yousseff G., Jacquemin F., and Fréour S. Moisture penetration into composites under external stresses : A scale transition analysis. in 'Proceedings of 17th International Conference on Composite Materials', Edimburgh, (27-31 July 2009).

*[145] Colin X., Audouin L., and Verdu J., Towards a non empirical kinetic model for the lifetime prediction of polyethylene pipes transporting drinking water. Macromolecular Symposia. **286**: p. 81-88, (2009).*

*[146] Lafarie-Frenot M.-C., et al., Thermo-oxidation behaviour of composite materials at high temperatures: A review of research activities carried out within the COMEDI program. Polymer Degradation & Stability. **95**(6): p. 965-974, (2010).*

*[147] Richaud E., et al., Radiochemical ageing of poly(ether ether ketone). European Polymer Journal. **46**: p. 731-743, (2010).*

[148] Olivier L., Prévision du vieillissement thermo-oxydant de composites à matrice organique dédiés à l'aéronautique : prise en compte des couplages multiphysiques, PhD Thesis, Sciences pour l'Ingénieur et Aéronautique, Université de Poitiers (2008).

*[149] Smith L.V. and Weitsman Y., The immersed fatigue response of polymer composites. International Journal of Fracture. **82**: p. 31-42, (1996).*

*[150] Thomason J.L. and Adzima L.J., Sizing up the interphase: an insider's guide to the science of sizing. Composites Part A: Applied Science and Manufacturing. **32**(3-4): p. 313-321).*

*[151] Watson J.C., Influence of fiber glass sizing on the performance of composites for wind turbine blades. SAMPE Journal. **46**(6): p. 8-15, (November/December 2010).*

[152] Fraenkel P.L. Development and testing of Marine Current Turbine's SeaGen 1.2 MW tidal stream turbine. in 'Proceedings of 3rd International Conference on Ocean Energy', Bilbao, (October 2010).

*[153] Post N.L., Case S.W., and Lesko J.J., Modeling the variable ampliude fatigue of composite materials : A review and evaluation of the state of the art for spectrum loading. International Journal of Fatigue. **30**: p. 2064-2086, (2008).*

[154] OptiDAT database. [Available from: www.kc-wmc.nl]

[155] CNRS Ferme d'hydroliennes pour la production d'énergie au fil de l'eau. [Available from: http://www.cnrs.fr/insis/recherche/faits-marquants/2008/ferme.htm]

*[156] Zanette, et al., A design methodology for cross flow water turbines. Renewable Energy. **35**(5): p. 997-1009, (2010).*

[157] Nicholls-Lee R.F., Turnock S.R., and Boyd S.W. Performance prediction of a free stream tidal turbine with composite bend-twist coupled blades. in 'Proceedings of 2nd

International Conference on Ocean Energy', Brest, France, (15th-17th October 2008).

[158] Bard J. Dynamic performance analysis of tidal energy converters using acoustic sensors. in 'Proceedings of 3rd International Conference on Ocean Energy', Bilbao, (October 2010).

[159] Davies P., et al., Summary of flume tank tests performed to study the deformation of a model tidal turbine blade, IFREMER Report, ERT/MS - 09-201, (August 2009)

[160] Davies P., et al., Summary of flume tank tests performed to study the deformation of a model tidal turbine blade, Second Series, IFREMER Report, RDT/MS-10-202, (August 2010)

[161] Maganga F., Caractérisation numérique et expérimentale des effets d'interaction fluide/structure engendrés par la présence d'hydroliennes, PhD Thesis, Université du Havre (2010).

Annexes

Annex 1

Analytical development of the Langmuir-type formulation

We assume that at a given time and place there are n mobile H_2O molecules per unit volume which diffuse with a coefficient diffusion $D\gamma$ and become bound at a rate per unit volume γn. At the same time and place there are N bound molecules per unit volume which become mobile at a rate per unit volume βN. The number-densities of mobile and bound molecules at equilibrium, n_∞ and N_∞ respectively, depend upon the relative humidity H and satisfy the relation

$$\gamma \cdot n_\infty(H) = \beta \cdot N_\infty(H) \qquad \textit{(Eqn. 51)}$$

The long-term solubility of water, expressed as percent by weight of the dry resin is

$$m_\infty(H) = \left(\frac{100 \cdot M_w}{N_A \cdot \rho_r}\right)\left(n_\infty(H) + N_\infty(H)\right) \qquad \textit{(Eqn. 52)}$$

where M_w is the molecular weight of water, N_A is Avogadro's number and ρ_r is the density of the dry resin.

We assume that the diffusion of mobile molecules conforms to simple diffusion theory augmented by sources and sinks. Thus, for the one dimensional case, the number densities of position z and time t satisfy the coupled pair of equations

$$\begin{cases} D_\gamma \dfrac{\partial^2 n}{\partial z^2} = \dfrac{\partial n}{\partial t} + \dfrac{\partial N}{\partial t} \\ \dfrac{\partial N}{\partial t} = \gamma \cdot n - \beta \cdot N \end{cases} \qquad \textit{(Eqn. 53)}$$

In the usual experimental case of an initially dry plate of thickness 2δ exposed to a constant moisture environment on both sides at $t=0$, the appropriate boundary and initial conditions are

$$n(z,0) = 0 \quad \text{and} \quad N(z,0) = 0 \quad \text{for} \quad |z| < \delta$$

and $\qquad \textit{(Eqn. 54)}$

$$n(\delta,t) = n_\infty \quad \text{and} \quad n(-\delta,t) = n_\infty \quad \text{for} \quad \text{all } t$$

Thanks to these boundary conditions and according to Laplace transforms we can obtain an exact solution of the above problem and determine the spatial distribution of bound molecules.

$$N(z,t) = \frac{\gamma}{\beta} n_\infty \left\{ 1 - \frac{4}{\pi} \sum_{p=1}^{\infty(odd)} \frac{(-1)^{(p-1)/2}}{p\left(r_{\bar{p}}^{+} - r_{\bar{p}}^{-}\right)} \left[r_{\bar{p}}^{+} \exp\left(-r_{\bar{p}}^{-} t\right) - r_{\bar{p}}^{-} \exp\left(-r_{\bar{p}}^{+} t\right) \right] \cos\frac{\pi p z}{2\delta} \right\} \qquad \textit{(Eqn. 55)}$$

where

$$r_{\bar{p}}^{\pm}=\frac{1}{2}\left[\left(kp^2+\gamma+\beta\right)\pm\sqrt{\left(kp^2+\gamma+\beta\right)^2-4k\beta p^2}\right] \qquad \textit{(Eqn. 56)}$$

$$k=\frac{\pi^2 D_\gamma}{(2\delta)^2} \qquad \textit{(Eqn. 57)}$$

Then from the second equation of *(Eqn. 53)*, the spatial distribution of mobile molecules is found to be

$$\begin{aligned} n(z,t)= \; & n_\infty\left\{1-\frac{4}{\pi}\sum_{p=1}^{\infty(odd)}\frac{(-1)^{(p-1)/2}}{p\left(r_{\bar{p}}^{+}-r_{\bar{p}}^{-}\right)}\left[r_{\bar{p}}^{+}\exp\left(-r_{\bar{p}}^{-}t\right)-r_{\bar{p}}^{-}\exp\left(-r_{\bar{p}}^{+}t\right)\right]\cos\frac{\pi pz}{2\delta}\right\} \\ & +n_\infty\left\{\frac{4}{\pi\beta}\sum_{p=1}^{\infty(odd)}\frac{(-1)^{(p-1)/2}}{p\left(r_{\bar{p}}^{+}-r_{\bar{p}}^{-}\right)}\left(r_{\bar{p}}^{+}\cdot r_{\bar{p}}^{-}\right)\left(\exp\left(-r_{\bar{p}}^{-}t\right)-\exp\left(-r_{\bar{p}}^{+}t\right)\right)\cos\frac{\pi pz}{2\delta}\right\} \end{aligned} \qquad \textit{(Eqn. 58)}$$

Integration of the above results over the plate thickness gives the following expression for m_t, the percentage by weight of moisture uptake after a time t.

$$m_t=m_\infty\left\{1-\frac{8}{\pi^2}\sum_{p=1}^{\infty(odd)}\frac{r_{\bar{p}}^{+}\exp\left(-r_{\bar{p}}^{-}t\right)-r_{\bar{p}}^{-}\exp\left(-r_{\bar{p}}^{+}t\right)}{p^2\left(r_{\bar{p}}^{+}-r_{\bar{p}}^{-}\right)}+\frac{8}{\pi^2}\left(\frac{k\beta}{\gamma+\beta}\right)\sum_{p=1}^{\infty(odd)}\frac{\exp\left(-r_{\bar{p}}^{-}t\right)-\exp\left(-r_{\bar{p}}^{+}t\right)}{r_{\bar{p}}^{+}-r_{\bar{p}}^{-}}\right\} \qquad \textit{(Eqn. 59)}$$

where the long term solubility m_∞ is related to the equilibrium particle densities by *(Eqn. 52)*.

A convenient approximation to *(Eqn. 59)* applies when 2β and 2γ are both small compared to k. It can be valid at all times t provided the error is referred to the exact result for m_t rather than the difference between m_∞ and m_t. This approximation for the total moisture uptake in an initially dry plate is

$$\frac{m_t}{m_\infty}=\frac{\beta}{\gamma+\beta}\exp(-\gamma t)\left[1-\frac{8}{\pi^2}\sum_{p=1}^{\infty}\frac{\exp\left(-kp^2t\right)}{p^2}\right]+\frac{\beta}{\gamma+\beta}\left[\exp(-\beta t)-\exp(-\gamma t)\right]+\left[1-\exp(-\beta t)\right] \qquad \textit{(Eqn. 60)}$$

For the initial part of the water uptake, *(Eqn. 59)* becomes

$$\frac{m_t}{m_\infty}=\frac{4}{\pi^{3/2}}\cdot\frac{\beta}{\gamma+\beta}\sqrt{kt} \qquad \text{for} \quad kt\le 0.7 \qquad \textit{(Eqn. 61)}$$

For the final part of the water uptake, *(Eqn. 59)* becomes

$$\frac{m_t}{m_\infty}=1-\frac{\gamma}{\gamma+\beta}\exp(-\beta t) \qquad \text{for} \quad kt<<1 \qquad \textit{(Eqn. 62)}$$

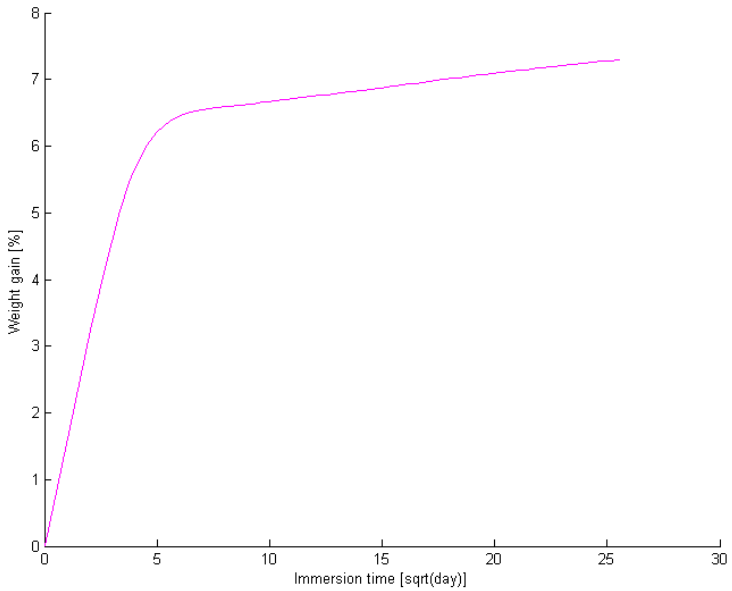

Fig. 1. *Water uptake according to the Langmuir-type model*

Annex 2

Infusion process

FICHE PROCESS INFUSION — DATE : 06/04/21 Heure : 14h00 .

Opérateurs : A.D / A.B — N° Expérience : 12

Température atelier :	35°C (Etuve)
Échantillonnage:	Verre E Quasi UD
Tirage du vide:	0,6 Bars

Dimension plaque:	400*500 mm
Epaisseur du stratifié:	5 mm (6 plis)

Tâches à effectuer :	Durée :	Opérateurs :	Remarques :
Nettoyage du moule	5 min	A.D	
Cirage du marbre (x3)	15 min	"	
Lustrage du marbre (x3)	15 min	"	
Découpe des fibres	Variable	"	Masse : 1,460 Kg
Découpe de bande UD (x3)	5 min	"	
Découpe du tissu de délaminage (x2)	5 min	"	Dimension : 650*800 mm
Découpe du treillis	3 min	"	Dimension : 450*450 mm
Découpe du film micro-perforé	3 min	"	Dimension : 400*500 mm
Découpe de la bâche à vide	5 min	"	Dimension : 1300*1000 mm
Pose du Gutta	5 min	"	
Pose du tissu de délaminage	2 min	"	
Pose des fibres	Variable	"	
Pose du second tissu de délaminage	2 min	"	
Pose du film micro-perforé	2 min	"	600 x 500 mm.
Pose du treillis	2 min	"	
Découpe et pose du tuyau spiralé	5 min	"	Ø Tuyau spiralé: 10/12 mm
Pose des raccords en T	2 min	"	
Découpe et pose des tuyaux de vide et d'alimentation de résine	5 min	"	Ø Tuyau d'alimentation: 10/12 mm
Pose de feutre sur les extrémités des tuyaux	2 min	"	
Pose de la bâche	25 min	"	
Mise sous vide et vérification de l'étanchéité	15 min	"	Tirage de vide: 0,6 Bars Durée : 10 min
Mise en place du montage en étuve	30 min	"	Température de l'étuve: 35 °C
Préparation de la résine	5 min	A.D / A.B	Masse: 2 Kg
Préparation du durcisseur	5 min	"	% : 30% en masse M: 600 g
Dégazage de la résine	20 min	"	Vide: 1 Bars Durée : 15 minutes
Chauffage de la résine	20 min	"	Température: 35°C Durée :30 min
Infusion de la plaque (En étuve à 35°C/pendant 24H)	Variable	"	Heure de début: 16H45 Heure de Fin: 16H55
Démoulage de la plaque	10 min		Le / / à H
Nettoyage complet du site	5 min		
Peser la plaque	2 min		Masse : Kg

Annex 3

Imaging techniques results

The overall quality of a composite material can be assessed and controlled by different imaging techniques. Scanning Electron Microscopy (SEM) has been used to observe the fibres, optical microscopy has been used to observe the distribution of the reinforcement in laminates and X-ray micro-tomography has been used to create a 3D image of tested specimens.

A specific treatment of the fibres or of the specimens is needed for the SEM and the optical microscopy, whereas the X-ray micro-tomography creates a 3D-view without the need for sectioning or polishing.

1- Scanning Electron Microscopy (SEM)

Fig. 2 represents the views obtained at two different scales (x *400* and x *6 000*) for the E-glass fibre, *Fig. 3* represents the views obtained for the Advantex® fibres and *Fig. 4* represents the views obtained for the HiPer-tex™ fibres.

(a)

(b)

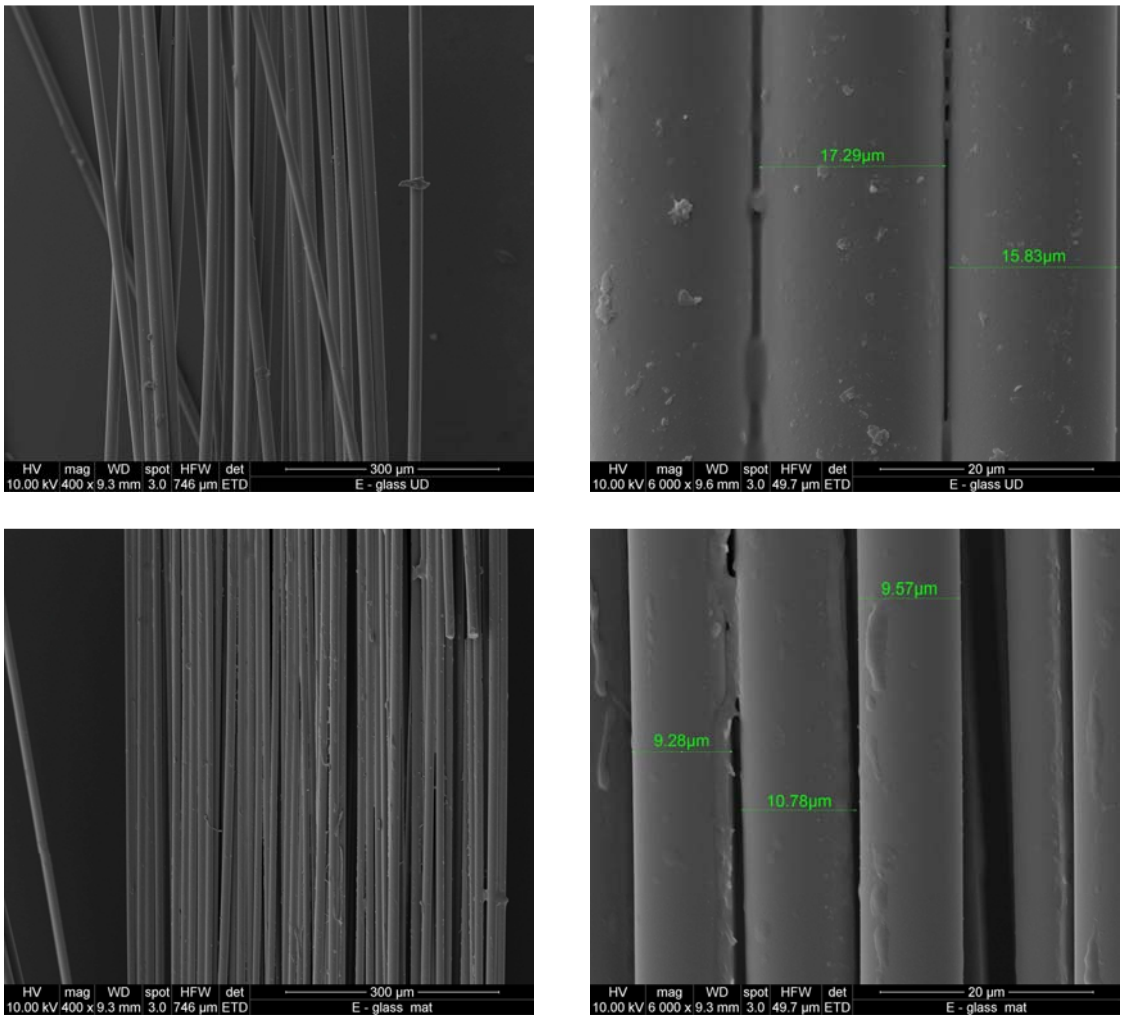

Fig. 2. *Views of E-glass fibres obtained with the SEM : a) warp fibres, b) mat fibres*

(a)

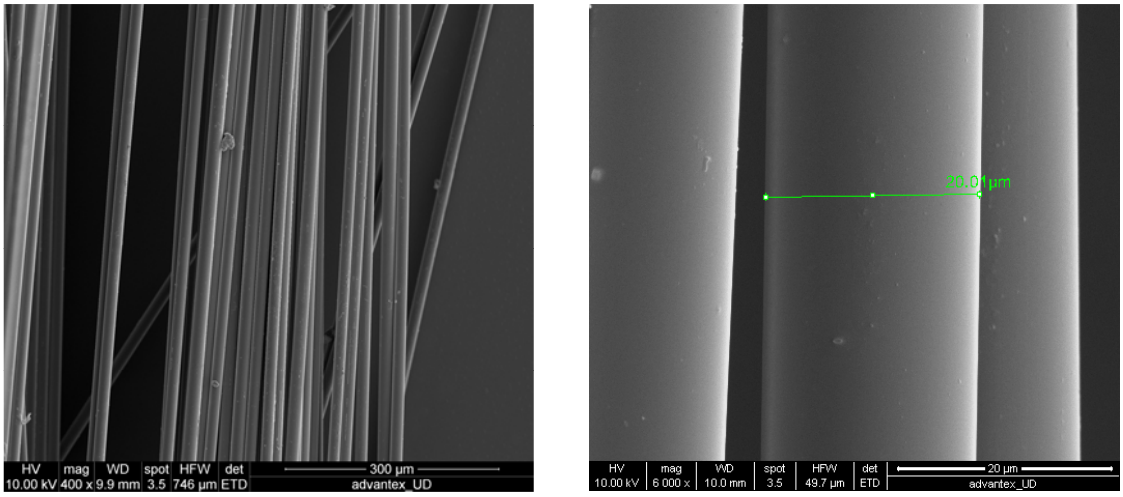

(b)

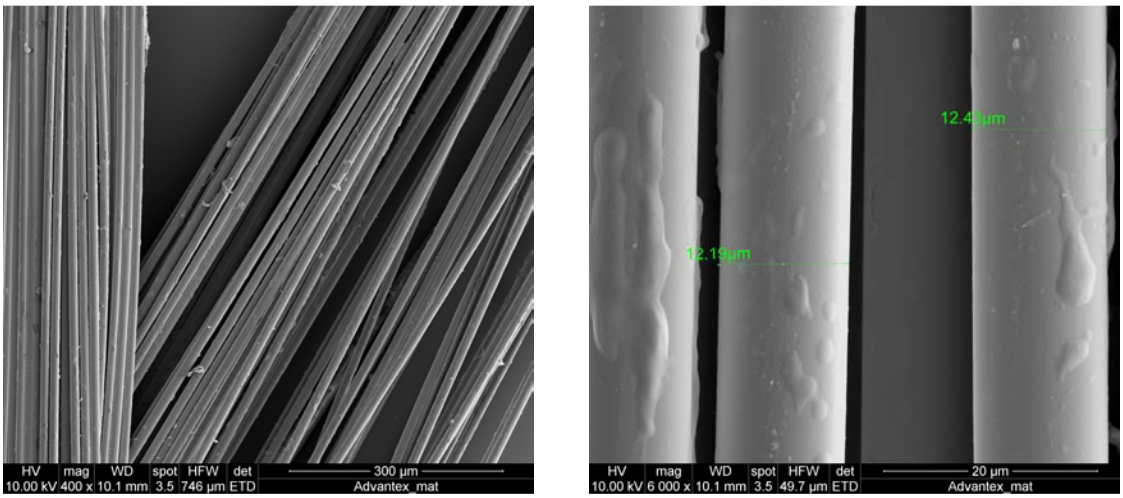

Fig. 3. *Views of E-Advantex® fibres obtained with the SEM : a) warp fibres, b) mat fibres*

(a)

(b)

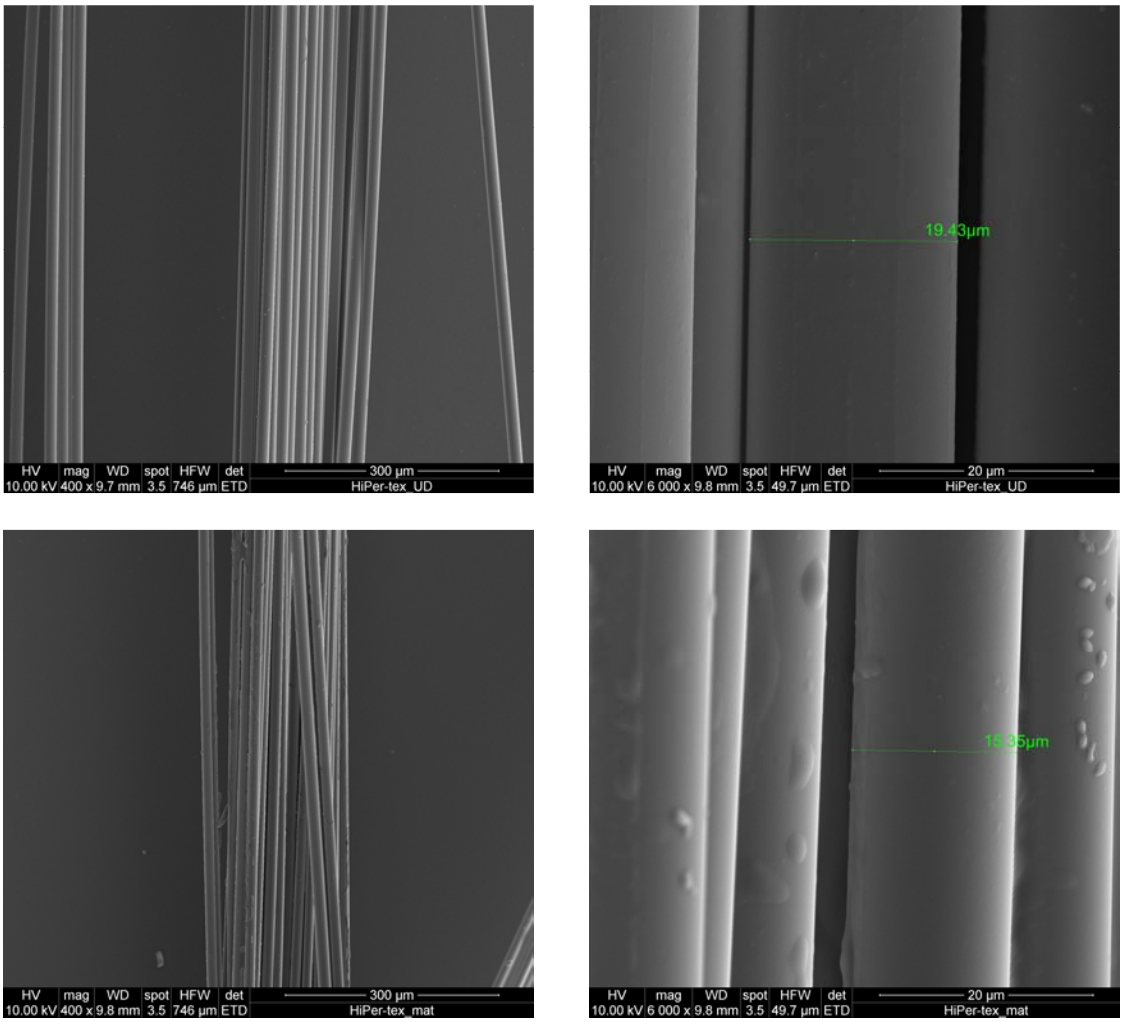

Fig. 4. *Views of HiPer-tex™ fibre obtained with the SEM : a) warp fibres, b) mat fibres*

2- Optical microscopy

Fig. 5 shows examples of cross-section views for the infused E-glass specimen, *Fig. 6* represents the views obtained for the infused Advantex® specimen and *Fig. 7* represents the views obtained for the infused HiPer-tex™ specimen.

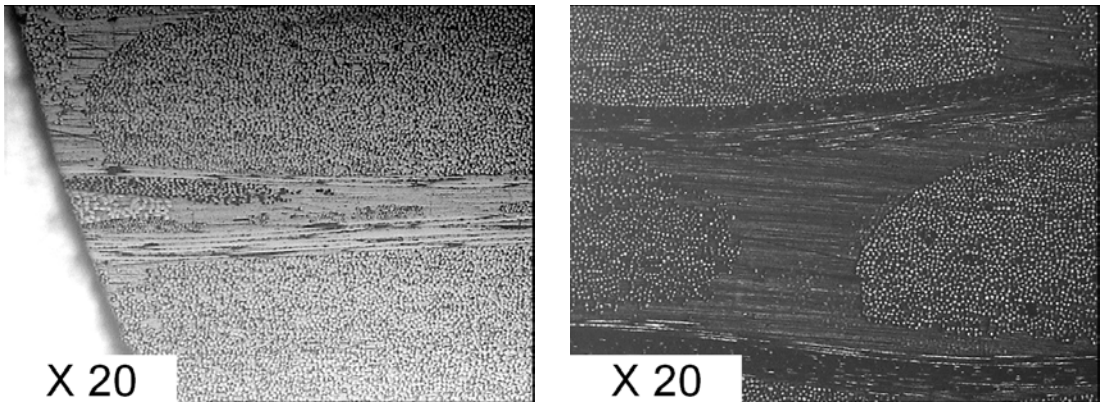

Fig. 5. *Cross-section views of an infused E-glass specimen*

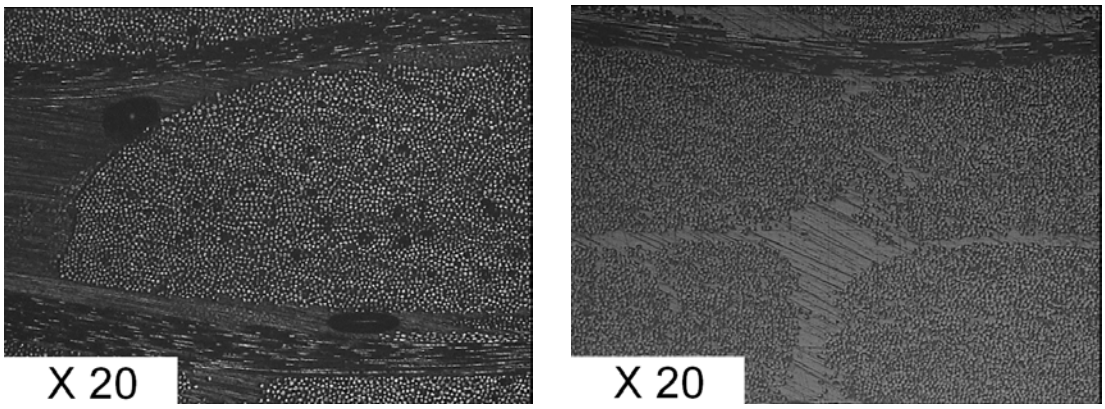

Fig. 6. *Cross-section views of an infused Advantex© specimen*

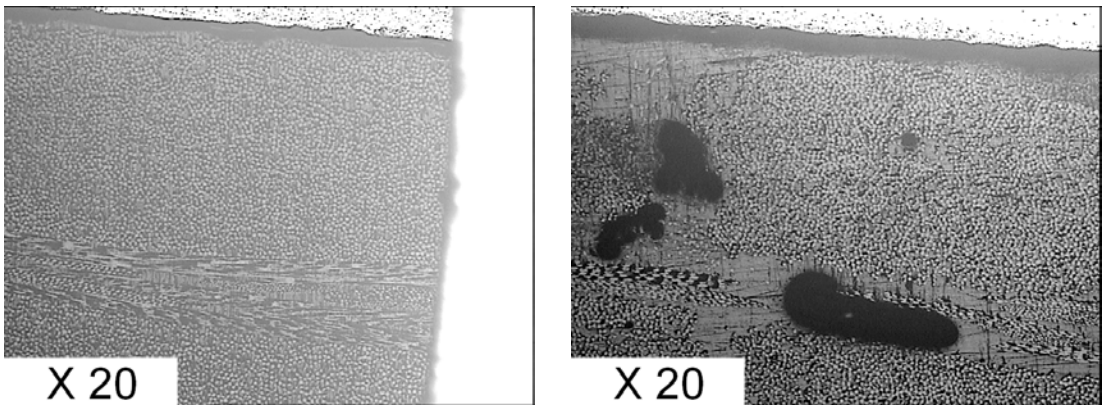

Fig. 7. *Cross-section views of an infused HiPer-tex™ specimen*

3- X-ray micro-tomography

Fig. 8 shows examples of 3D views for the infused E-glass specimen, *Fig. 9* represents the views obtained for the infused Advantex® specimen and *Fig. 10* represents examples of the views obtained for the infused HiPer-tex™ specimen. These specimens were examined after fatigue tests.

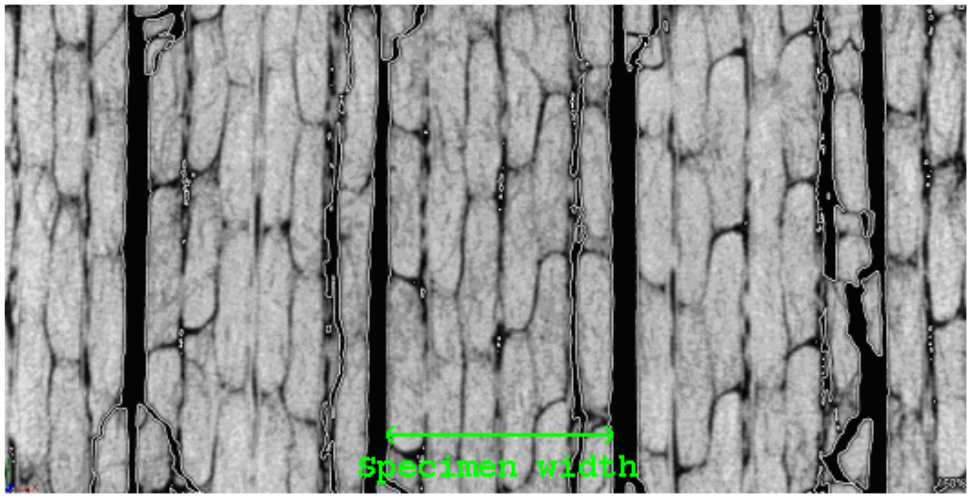

Fig. 8. *Tomography images of infused E-glass dog-bone specimens*

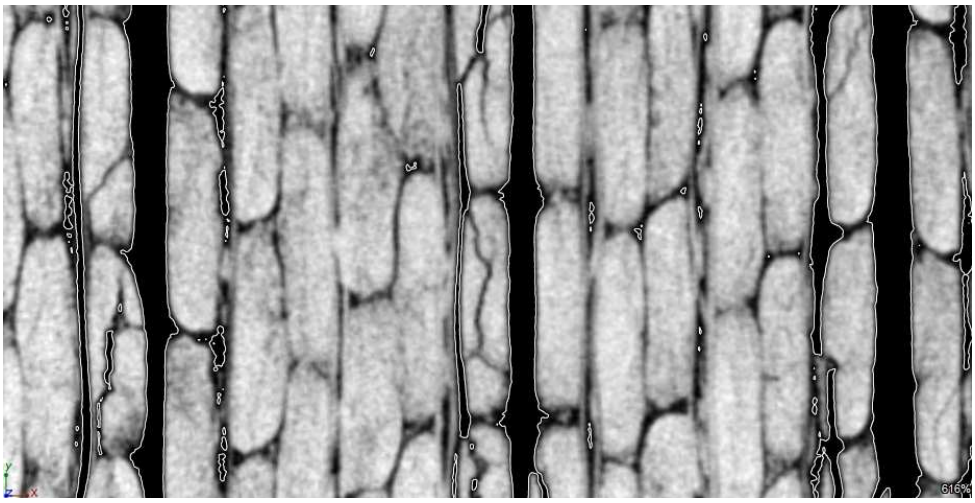

Fig. 9. *Tomography images of infused Advantex® dog-bone specimens*

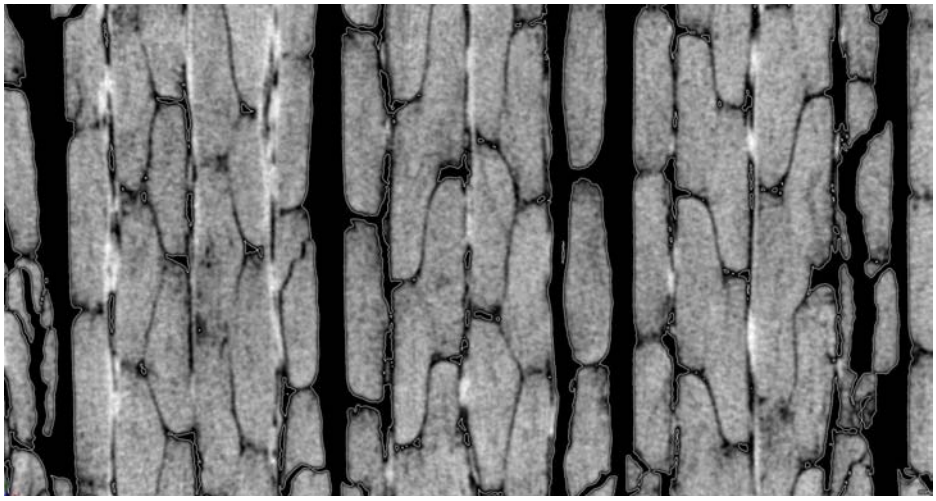

Fig. 10. *Tomography images of infused HiPer-tex™ dog-bone specimens*

Annex 4

Mean dimensions and initial weights of specimens

In order to perform the natural sea water ageing and the mechanical tests, different specimen geometries have been used. Square samples have been chosen for the sea water ageing and dog-bone specimens for the mechanical tests.

1- Natural sea water ageing specimens

For the natural sea water ageing, twenty square specimens (*Fig. 11*) have been cut in the different plates of pure resin or infused composite materials. Each coupon obtained has been numbered, measured and weighed. Five measurements of each side and five measurements of the thickness have been performed in order to have a mean dimension and a standard deviation.

All the results are summarized in the following tables. Pure resin specimens in *Table 43*, infused E-glass specimens in *Table 44*, infused Advantex® specimens in *Table 45* and infused HiPer-tex™ specimens in *Table 46*. *a* represents the length of the coupon, *e* the thickness and *m* the weight.

Fig. 11. *View of the sea water ageing specimens (pure resin at 20°C and 40°C)*

Table 43. *Mean dimensions and initial weight of the twenty specimens of pure resin*

	CR1	**CR2**	**CR3**	**CR4**	**CR5**	**CR6**	**CR7**	**CR8**	**CR9**	**CR10**
a $[mm]$ (SD)	50.49 (0.49)	52.76 (1.98)	50.11 (0.76)	50.26 (0.34)	50.19 (0.68)	50.85 (0.20)	50.46 (0.35)	50.61 (0.24)	50.23 (0.61)	51.16 (0.11)
e $[mm]$ (SD)	4.99 (0.05)	5.03 (0.02)	4.95 (0.02)	4.99 (0.01)	4.93 (0.03)	4.90 (0.02)	4.96 (0.04)	5.04 (0.03)	4.95 (0.02)	5.03 (0.03)
m $[g]$	14.6372	16.0703	14.3388	14.4895	14.2654	14.5204	14.6019	14.8787	14.4259	15.2044

	CR11	**CR12**	**CR13**	**CR14**	**CR15**	**CR16**	**CR17**	**CR18**	**CR19**	**CR20**
a $[mm]$ (SD)	50.71 (0.17)	50.85 (0.16)	51.31 (0.16)	50.73 (0.18)	50.40 (0.39)	50.66 (0.03)	50.44 (0.41)	50.57 (0.47)	50.58 (0.48)	50.42 (0.48)
e $[mm]$ (SD)	4.99 (0.02)	5.00 (0.05)	4.90 (0.02)	4.98 (0.01)	4.98 (0.06)	4.99 (0.04)	5.12 (0.02)	5.11 (0.03)	5.09 (0.02)	4.92 (0.02)
m $[g]$	14.8137	14.8542	14.7820	14.7820	14.5199	14.7696	15.0650	15.1183	15.0969	14.4021

Table 44. *Mean dimensions and initial weight of the twenty infused E-glass specimens*

	HE4 C1	**HE4 C2**	**HE4 C3**	**HE4 C4**	**HE4 C5**	**HE4 C6**	**HE4 C7**	**HE4 C8**	**HE4 C9**	**HE4 C10**
a $[mm]$ (SD)	49.94 (0.12)	49.93 (0.15)	49.90 (0.17)	50.15 (0.35)	49.76 (0.26)	49.99 (0.20)	50.01 (0.27)	49.67 (0.34)	49.93 (0.14)	49.84 (0.18)
e $[mm]$ (SD)	5.40 (0.04)	5.48 (0.05)	5.51 (0.10)	5.40 (0.06)	5.47 (0.05)	5.42 (0.06)	5.53 (0.09)	5.56 (0.10)	5.45 (0.06)	5.39 (0.05)
m $[g]$	25.6246	25.5138	25.5563	25.8237	25.6467	25.5176	25.7535	25.7341	25.4932	25.2778

	HE4 C11	**HE4 C12**	**HE4 C13**	**HE4 C14**	**HE4 C15**	**HE4 C16**	**HE4 C17**	**HE4 C18**	**HE4 C19**	**HE4 C20**
a $[mm]$ (SD)	49.79 (0.09)	49.62 (0.30)	49.98 ((0.44)	49.81 (0.18)	50.00 (0.10)	49.76 (0.15)	50.06 (0.29)	49.69 (0.42)	49.71 (0.34)	50.20 (0.48)
e $[mm]$ (SD)	5.43 (0.05)	5.48 (0.18)	5.61 (0.06)	5.59 (0.08)	5.39 (0.03)	5.50 (0.08)	5.54 (0.14)	5.56 (0.06)	5.59 (0.05)	5.36 (0.12)
m $[g]$	25.4623	25.1775	26.1606	25.8503	25.5187	25.6628	26.0152	25.6723	25.6590	25.6420

Table 45. *Mean dimensions and initial weight of the twenty infused Advantex® specimens*

	HA5 C1	**HA5 C2**	**HA5 C3**	**HA5 C4**	**HA5 C5**	**HA5 C6**	**HA5 C7**	**HA5 C8**	**HA5 C9**	**HA5 C10**
a $[mm]$ (SD)	48.95 (1.15)	49.87 (0.11)	49.68 (0.29)	50.24 (0.08)	49.67 (0.32)	50.18 (0.17)	49.71 (0.24)	49.96 (0.22)	46.77 (0.08)	49.71 (0.40)
e $[mm]$ (SD)	5.68 (0.09)	5.50 (0.04)	5.65 (0.06)	5.44 (0.19)	5.67 (0.08)	5.56 (0.06)	5.53 (0.02)	5.62 (0.10)	5.40 (0.08)	5.46 (0.24)
m $[g]$	25.5534	25.9261	26.3116	25.7358	26.3142	26.5776	26.0737	25.8983	24.8820	25.0514

	HA5 C11	**HA5 C12**	**HA5 C13**	**HA5 C14**	**HA5 C15**	**HA5 C16**	**HA5 C17**	**HA5 C18**	**HA5 C19**	**HA5 C20**
a $[mm]$ (SD)	49.86 (0.17)	49.77 (0.16)	49.69 (0.30)	49.79 (0.17)	49.85 (0.26)	49.13 (0.85)	49.93 (0.14)	49.95 (0.38)	49.62 (0.06)	49.41 (0.58)
e $[mm]$ (SD)	5.60 (0.15)	5.36 (0.15)	5.59 (0.12)	5.64 (0.16)	5.63 (0.14)	5.42 (0.12)	5.61 (0.29)	5.53 (0.06)	5.59 (0.10)	5.50 (0.04)
m $[g]$	26.3905	25.1019	26.1414	25.9419	26.2346	25.1048	25.5241	26.3385	25.3324	25.5983

Table 46. *Mean dimensions and initial weight of the twenty infused HiPer-tex™ specimens*

	3BHd C1	**3BHd C2**	**3BHd C3**	**3BHd C4**	**3BHd C5**	**3BHd C6**	**3BHd C7**	**3BHd C8**	**3BHd C9**	**3BHd C10**
a $[mm]$ (SD)	51.07 (0.43)	50.71 (0.67)	50.72 (0.76)	50.76 (0.75)	51.09 (0.45)	51.36 (0.36)	50.43 (0.66)	50.69 (0.84)	50.36 (0.81)	50.83 (0.73)
e $[mm]$ (SD)	5.39 (0.08)	5.34 (0.13)	5.33 (0.05)	5.37 (0.07)	5.45 (0.04)	5.32 (0.12)	5.27 (0.10)	5.45 (0.04)	5.43 (0.04)	5.46 (0.02)
m $[g]$	29.9090	29.1579	29.2292	29.7360	29.9085	29.8549	29.3822	29.4794	29.4091	29.4372

	3BHd C11	**3BHd C12**	**3BHd C13**	**3BHd C14**	**3BHd C15**	**3BHd C16**	**3BHd C17**	**3BHd C18**	**3BHd C19**	**3BHd C20**
a $[mm]$ (SD)	50.85 (0.77)	50.95 (0.78)	51.32 (0.46)	51.00 (0.68)	50.84 (0.64)	50.92 (0.66)	50.90 (0.49)	51.09 (0.50)	50.71 (0.54)	50.88 (0.62)
e $[mm]$ (SD)	5.49 (0.03)	5.44 (0.02)	55.52 (0.07)	5.43 (0.07)	5.45 (0.07)	5.44 (0.05)	5.44 (0.08)	5.45 (0.08)	5.32 (0.09)	5.27 (0.11)
m $[g]$	29.1672	29.3800	29.8899	29.9841	29.5811	29.6201	29.6383	29.5930	29.4003	29.4056

2- Mechanical test specimens

In order to perform the mechanical tests, dog-bone specimens have been cut in the different plates of pure resin or infused composite materials using a high pressure water jet (*Fig. 12*). Each specimen obtained has been numbered, measured and weighed. Five measurements of each dimension have been performed in order to have a mean dimension and a standard deviation for each specimen.

The measurements obtained for each plate, by averaging the dimensions of the specimens, are summarized in the following tables, infused E-glass specimens in *Table 47*, infused Advantex® specimens in *Table 48*, infused HiPer-tex™ specimens in *Table 49* and pure resin specimens in *Table 50*. L_T represents the overall length, b the overall width, b_0 the width in the middle of the specimen (*Fig. 13*), h the thickness, m the weight, V the volume and ρ the density.

Fig. 12. *Infused E-glass plate (IE1) after high pressure water jet cutting*

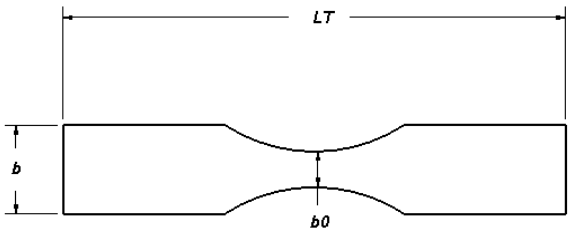

Fig. 13. *Mechanical tests specimens*

Table 47. *Mean dimensions and initial weight of the infused E-glass specimens*

Plate HE3		
	Mean Value	Stand. Dev.
L_T $[mm]$	140.07	0.10
b $[mm]$	25.09	0.07
b_0 $[mm]$	10.10	0.06
h $[mm]$	5.52	0.07
m $[g]$	31.19	0.35
V $[mm^3]$	16592.20	220.15
ρ $[kg/m^3]$	1879.84	15.97

Plate HE4		
	Mean Value	Stand. Dev.
L_T $[mm]$	140.03	0.04
b $[mm]$	25.03	0.03
b_0 $[mm]$	10.04	0.03
h $[mm]$	5.52	0.17
m $[g]$	31.15	0.21
V $[mm^3]$	16533.29	517.49
ρ $[kg/m^3]$	1886.12	67.24

Plate IE1		
	Mean Value	Stand. Dev.
L_T $[mm]$	139.83	0.04
b $[mm]$	24.79	0.75
b_0 $[mm]$	10.00	0.06
h $[mm]$	5.10	0.05
m $[g]$	29.58	0.22
V $[mm^3]$	15117.64	422.35
ρ $[kg/m^3]$	1958.26	67.25

Plate IE2		
	Mean Value	Stand. Dev.
L_T $[mm]$	139.83	0.05
b $[mm]$	24.91	0.03
b_0 $[mm]$	9.93	0.03
h $[mm]$	5.15	0.05
m $[g]$	29.37	0.18
V $[mm^3]$	15312.62	149.00
ρ $[kg/m^3]$	1917.92	11.46

Table 48. *Mean dimensions and initial weight of the infused Advantex® specimens*

Plate HA6		
	Mean Value	Stand. Dev.
L_T $[mm]$	140.02	0.07
b $[mm]$	25.04	0.05
b_0 $[mm]$	10.07	0.05
h $[mm]$	5.46	0.11
m $[g]$	31.30	0.55
V $[mm^3]$	16372.20	341.31
ρ $[kg/m^3]$	1912.01	27.01

Table 49. *Mean dimensions and initial weight of the infused HiPer-tex™ specimens*

Plate HH1		
	Mean Value	Stand. Dev.
L_T $[mm]$	139.91	0.04
b $[mm]$	24.97	0.03
b_0 $[mm]$	10.01	0.03
h $[mm]$	5.47	0.08
m $[g]$	31.24	0.38
V $[mm^3]$	16336.24	238.61
ρ $[kg/m^3]$	1912.67	23.36

Plate IH1		
	Mean Value	Stand. Dev.
L_T $[mm]$	139.83	0.03
b $[mm]$	24.91	0.05
b_0 $[mm]$	10.02	0.06
h $[mm]$	5.14	0.05
m $[g]$	30.02	0.30
V $[mm^3]$	15320.93	157.81
ρ $[kg/m^3]$	1959.51	14.75

Table 50. *Mean dimensions and initial weight of the pure resin specimens*

Plate IR		
	Mean Value	Stand. Dev.
L_T $[mm]$	149.95	0.05
b $[mm]$	19.03	0.06
b_0 $[mm]$	9.02	0.08
h $[mm]$	5.50	0.51
m $[g]$	11.98	1.14
V $[mm^3]$	10046.34	958.90
ρ $[kg/m^3]$	1150.86	6.27

Annex 5

Detailed analytical results of the natural sea water ageing

Thanks to a *Matlab*© routine, based on the least squares method and Fick's law of diffusion, and the experimental data at *4°C*, *20°C*, *40°C* and *60°C*, we are able to determine the diffusion coefficient *D* of each material at each temperature.

The experimental results obtained at *80°C* have not been used because this temperature is very close to or higher than the glass transition temperature of the dry materials (*72°C* for the pure resin, *77°C* for the infused E-glass, *76°C* for the infused Advantec® and *82°C* for the infused HiPer-tex™).

1- Pure resin material

When the weight gain is plotted versus the square root of time (*Fig. 14*), it appears that the diffusion in the pure resin material follows Fick's law. So, the *Matlab*© routine has been applied to the four sets of data obtained at each test temperature.

The graphical representations of the experimental data and the mean value of optimization at each temperature are summarized in *Fig. 15* (*4°C*), *Fig. 16* (*20°C*), *Fig. 17* (*40°C*) and *Fig. 18* (*60°C*). The main geometrical data of the specimens and the diffusion coefficients obtained at each temperature are summarized in *Table 51* (*4°C*), *Table 52* (*20°C*), *Table 53* (*40°C*) and *Table 54* (*60°C*).

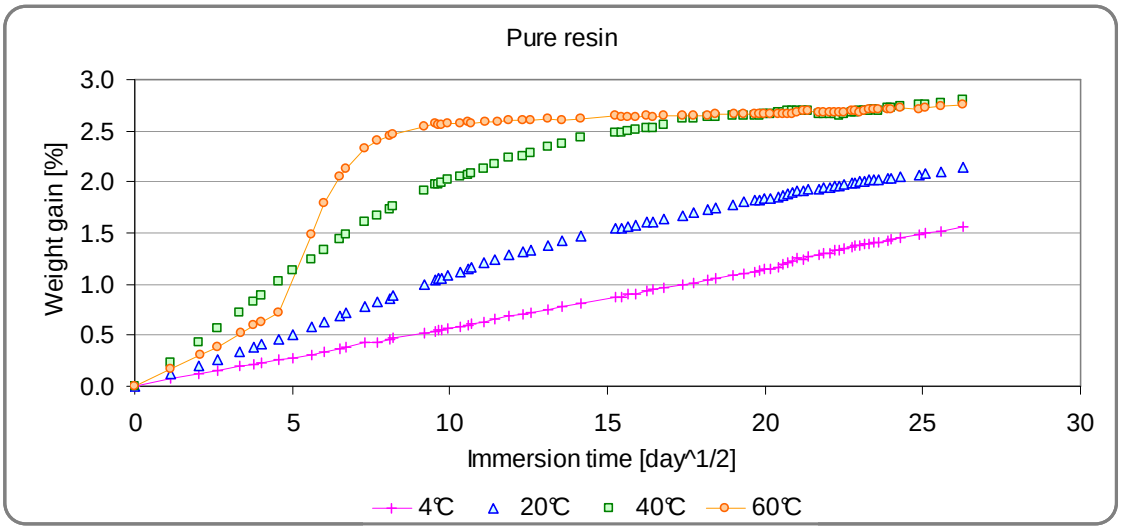

Fig. 14. *Comparative curves of the kinetics of diffusion of the pure resin specimens at five temperatures in natural circulating sea water*

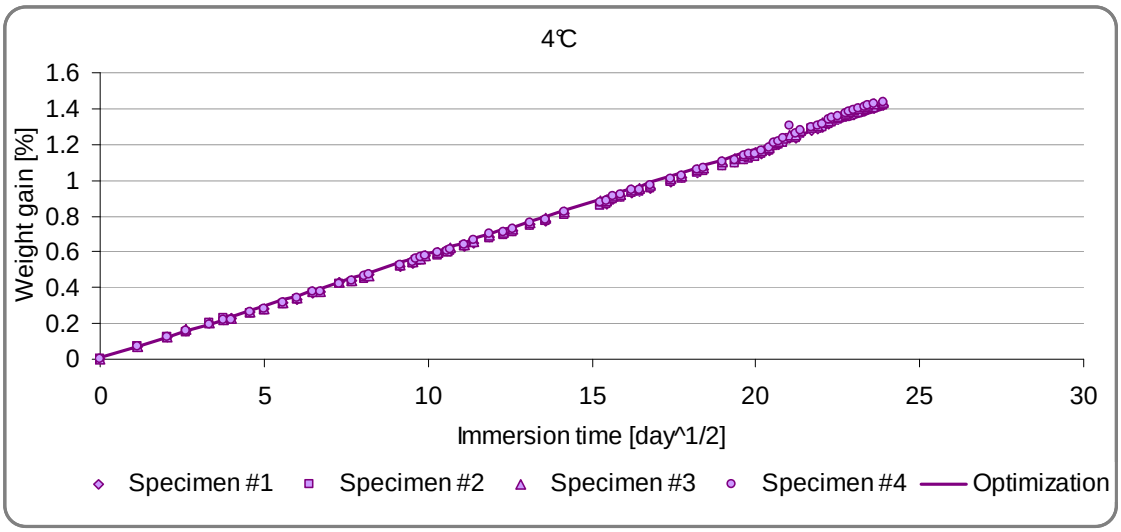

Fig. 15. *Comparative curves between experimental data and optimization in natural circulating sea water at 4°C for pure resin specimens*

Table 51. *Report of data obtained for pure resin specimens in natural circulating sea water at 4°C*

Pure resin 4°C	Thickness [*mm*]	Length [*mm*]	m0 [*g*]	D [*mm²/day*]	[*m²/s*]
CR1	4.99	50.49	14.6372	0.0022	2.55E-14
CR2	5.03	52.76	16.0703	0.0022	2.55E-14
CR3	4.95	50.11	14.3388	0.0022	2.55E-14
CR4	4.99	50.26	14.4895	0.0023	2.66E-14
Mean	**4.99**	**50.91**	**14.8840**	**0.0022**	**2.58E-14**
Stand. Dev.	**0.03**	**1.25**	**0.8002**	**0.0001**	**5.79E-16**

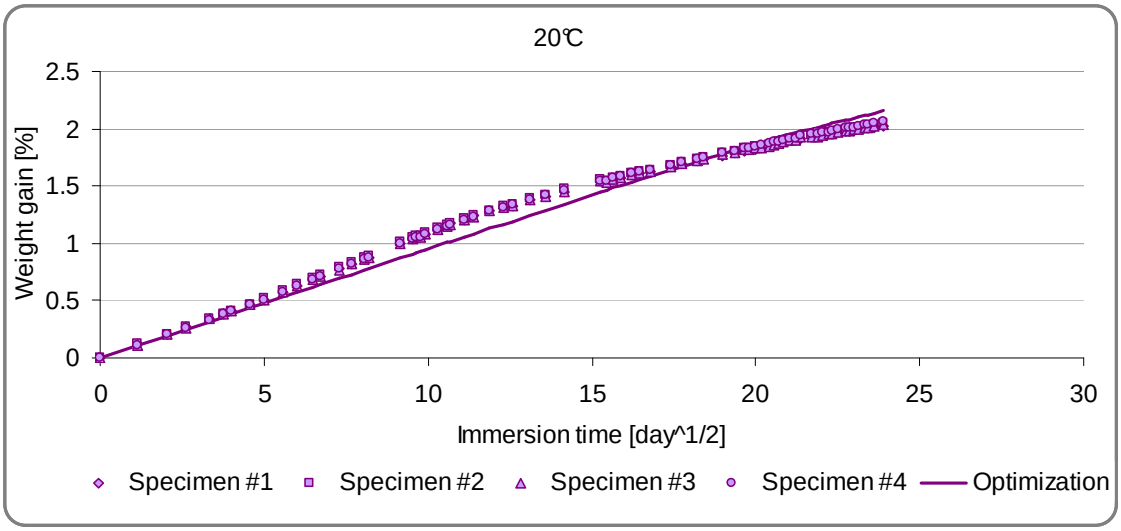

Fig. 16. *Comparative curves between experimental data and optimization in natural circulating sea water at 20°C for pure resin specimens*

Table 52. *Report of data obtained for pure resin specimens in natural circulating sea water at 20°C*

Pure resin 20°C	Thickness [*mm*]	Length [*mm*]	m0 [*g*]	D [*mm²/day*]	[*m²/s*]
CR5	4.93	50.19	14.2654	0.0056	6.48E-14
CR6	4.90	50.85	14.5204	0.0057	6.60E-14
CR7	4.96	50.46	14.6019	0.0057	6.60E-14
CR8	5.04	50.61	14.8787	0.0060	6.94E-14
Mean	**4.96**	**50.53**	**14.5666**	**0.0058**	**6.66E-14**
Stand. Dev.	**0.06**	**0.28**	**0.2527**	**0.0002**	**2.00E-15**

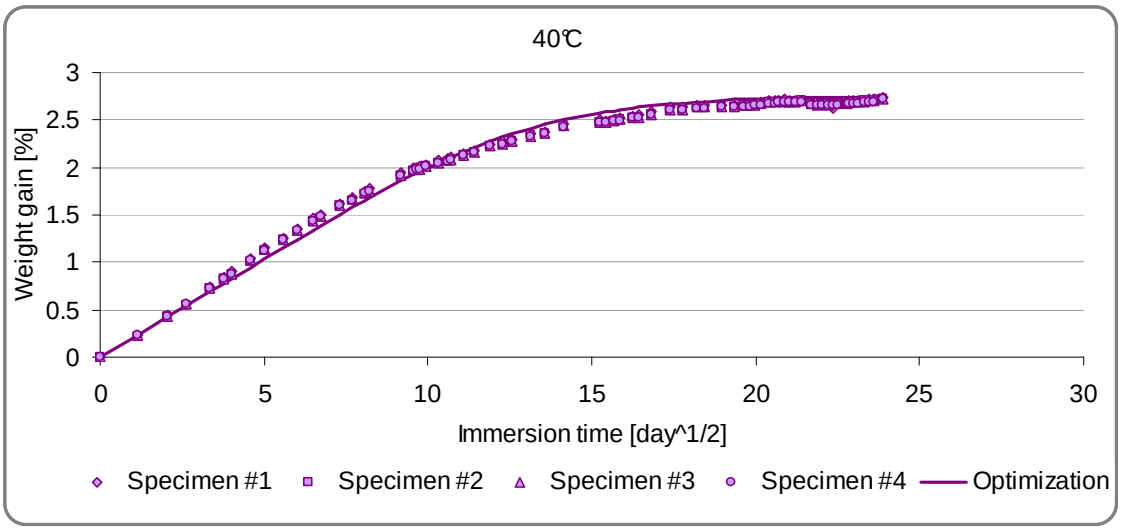

Fig. 17. *Comparative curves between experimental data and optimization in natural circulating sea water at 40°C for pure resin specimens*

Table 53. *Report of data obtained for pure resin specimens in natural circulating sea water at 40°C*

Pure resin 40°C	Thickness [*mm*]	Length [*mm*]	m0 [*g*]	D [*mm²/day*]	[*m²/s*]
CR9	4.95	50.23	14.4259	0.0279	3.23E-13
CR10	5.03	51.16	15.2044	0.0276	3.19E-13
CR11	4.99	50.71	14.8137	0.0273	3.16E-13
CR12	5.00	50.85	14.8542	0.0272	3.15E-13
Mean	**4.99**	**50.74**	**14.8246**	**0.0275**	**3.18E-13**
Stand. Dev.	**0.03**	**0.39**	**0.3184**	**0.0003**	**3.66E-15**

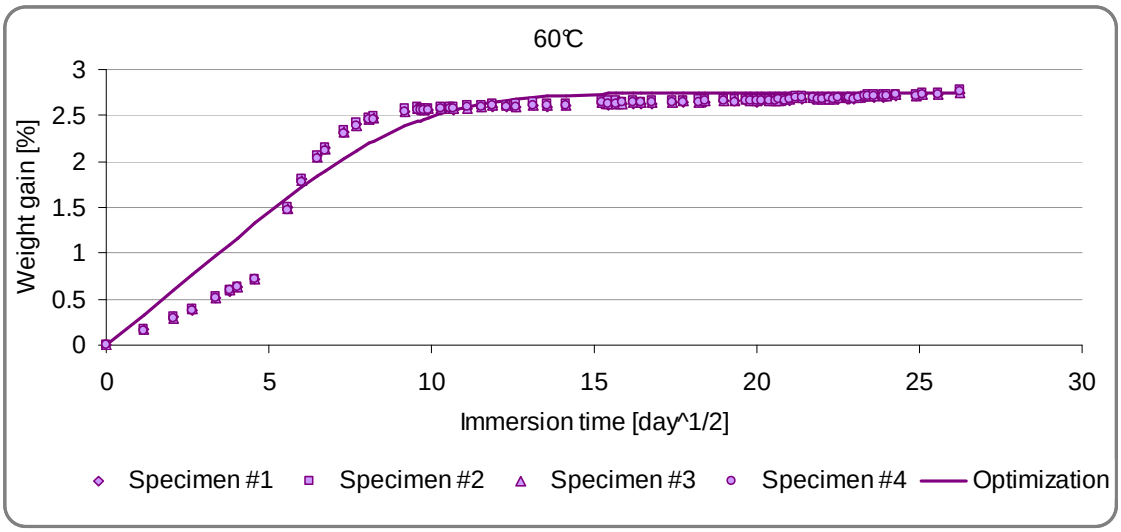

Fig. 18. *Comparative curves between experimental data and optimization in natural circulating sea water at 60°C for pure resin specimens*

Table 54. *Report of data obtained for pure resin specimens in natural circulating sea water at 60°C*

Pure resin 60°C	Thickness [*mm*]	Length [*mm*]	m0 [*g*]	D [*mm²/day*]	[*m²/s*]
CR13	4.90	51.31	14.7820	0.0517	5.98E-13
CR14	4.98	50.73	14.7894	0.0545	6.31E-13
CR15	4.98	50.40	14.5199	0.0534	6.18E-13
CR16	4.99	50.66	14.7696	0.0531	6.15E-13
Mean	**4.96**	**50.78**	**14.7152**	**0.0532**	**6.15E-13**
Stand. Dev.	**0.04**	**0.38**	**0.1305**	**0.0012**	**1.33E-14**

2- Infused E-glass composite material

When the weight gain is plotted versus the square root of time (*Fig. 19*), it appears that the diffusion in infused E-glass composite material follows Fick's law to a first approximation, at least initially. So, the *Matlab*© routine has been applied to the four sets of data obtained at each test temperature.

The graphical representations of the experimental data and the mean value of optimization at each temperature is summarized in *Fig. 20* (*4°C*), *Fig. 21* (*20°C*), *Fig. 22* (*40°C*) and *Fig. 23* (*60°C*). The main geometrical data of the specimens and the diffusion coefficients obtained at each temperature are summarized in *Table 55* (*4°C*), *Table 56* (*20°C*), *Table 57* (*40°C*) and *Table 58* (*60°C*).

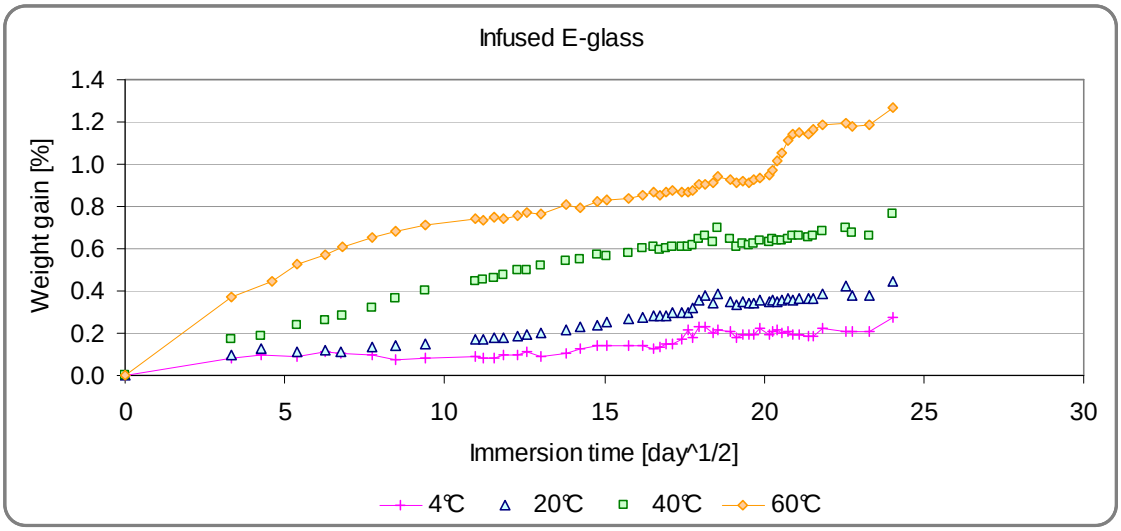

Fig. 19. *Comparative curves of the kinetics of diffusion of the infused E-glass specimens at five temperatures in natural circulating sea water*

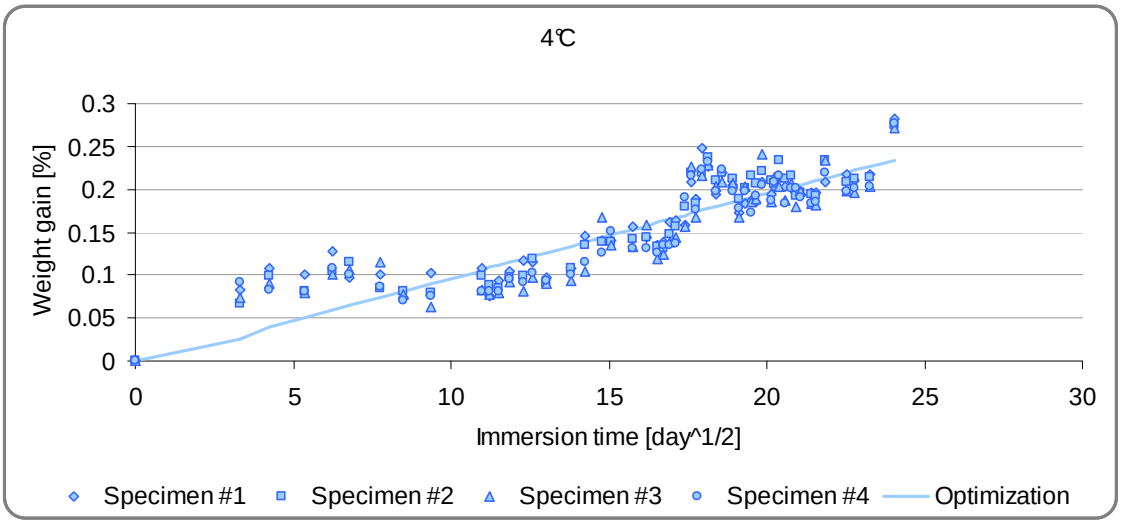

Fig. 20. *Comparative curves between experimental data and optimization in natural circulating sea water at 4°C for infused E-glass specimens*

Table 55. *Report of data obtained for infused E-glass specimens in natural circulating sea water at 4°C*

E-glass 4°C	Thickness [*mm*]	Length [*mm*]	m0 [*g*]	D [*mm²/day*]	[*m²/s*]
HE4 C1	5.40	49.94	25.6246	0.0010	1.16E-14
HE4 C2	5.48	49.93	25.5138	0.0011	1.27E-14
HE4 C3	5.51	49.90	25.5563	0.0010	1.12E-14
HE4 C4	5.40	50.15	25.8237	0.0009	1.08E-14
Mean	**5.45**	**49.98**	**25.6296**	**0.0010**	**1.16E-14**
Stand. Dev.	**0.06**	**0.11**	**0.1372**	**0.0001**	**8.47E-16**

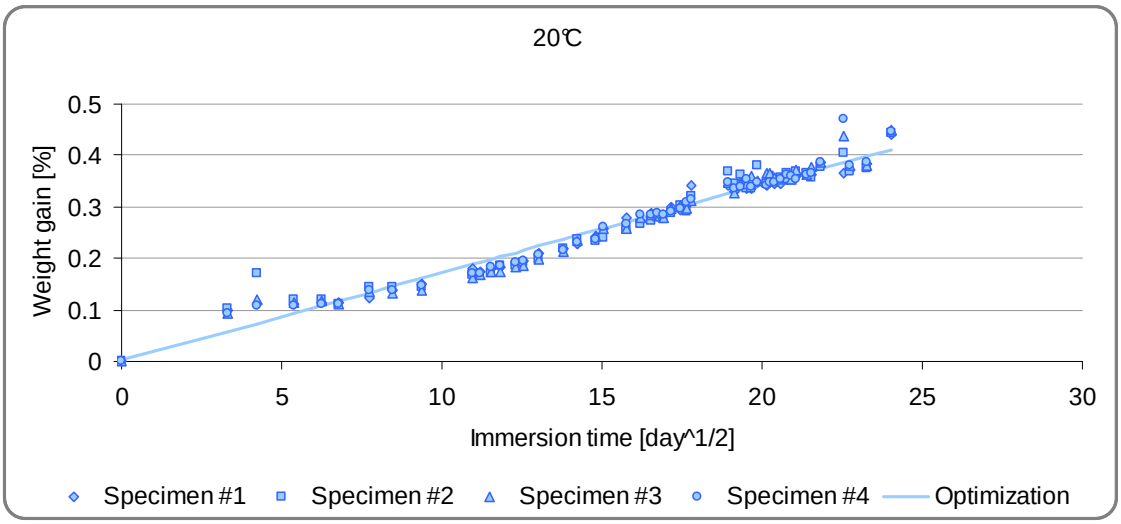

Fig. 21. *Comparative curves between experimental data and optimization in natural circulating sea water at 20°C for infused E-glass specimens*

Table 56. *Report of data obtained for infused E-glass specimens in natural circulating sea water at 20°C*

E-glass 20°C	Thickness [*mm*]	Length [*mm*]	m0 [*g*]	D [*mm²/day*]	[*m²/s*]
HE4 C5	5.47	49.76	25.6467	0.0030	3.47E-14
HE4 C6	5.42	49.99	25.5176	0.0030	3.47E-14
HE4 C7	5.53	50.01	25.7535	0.0032	3.70E-14
HE4 C8	5.56	49.67	25.7341	0.0032	3.70E-14
Mean	**5.50**	**49.86**	**25.6630**	**0.0031**	**3.59E-14**
Stand. Dev.	**0.06**	**0.17**	**0.1075**	**0.0001**	**1.34E-15**

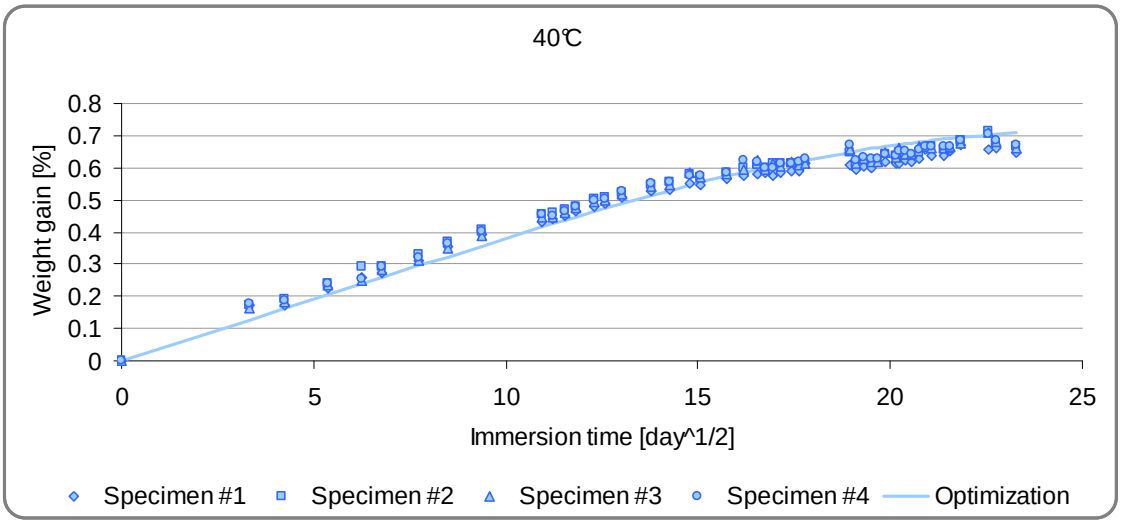

Fig. 22. *Comparative curves between experimental data and optimization in natural circulating sea water at 40°C for infused E-glass specimens*

Table 57. *Report of data obtained for infused E-glass specimens in natural circulating sea water at 40°C*

E-glass 40°C	Thickness [*mm*]	Length [*mm*]	m0 [*g*]	D [*mm²/day*]	[*m²/s*]
HE4 C9	5.45	49.93	25.4932	0.0137	1.59E-13
HE4 C10	5.39	49.84	25.2778	0.0152	1.76E-13
HE4 C11	5.43	49.79	25.4623	0.0151	1.75E-13
HE4 C12	5.48	49.62	25.1775	0.0159	1.84E-13
Mean	**5.44**	**49.80**	**25.3527**	**0.0150**	**1.73E-13**
SD	**0.04**	**0.13**	**0.1506**	**0.0009**	**1.07E-14**

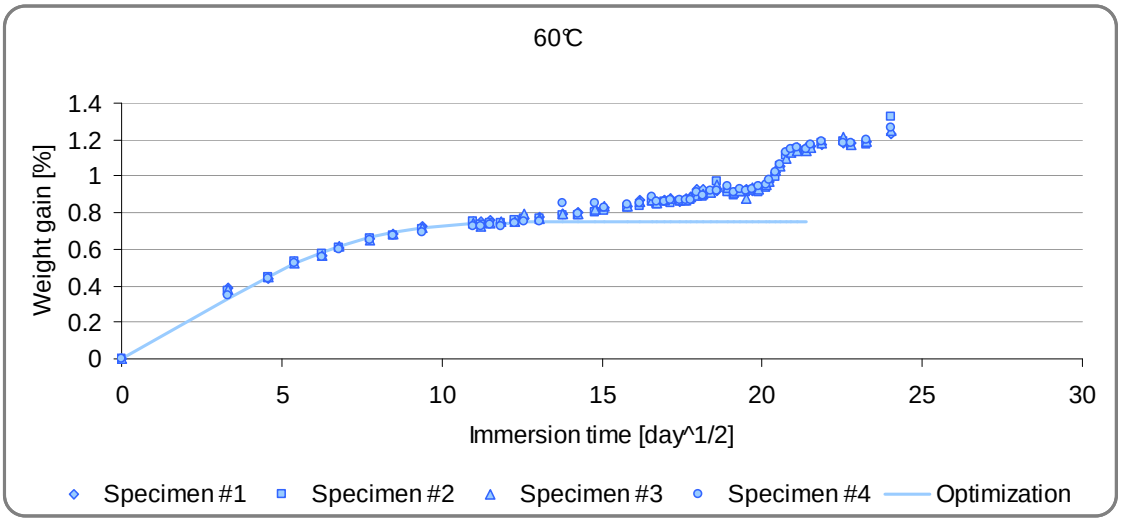

Fig. 23. *Comparative curves between experimental data and optimization in natural circulating sea water at 60°C for infused E-glass specimens*

Table 58. *Report of data obtained for infused E-glass specimens in natural circulating sea water at 60°C*

E-glass 60°C	Thickness [*mm*]	Length [*mm*]	m0 [*g*]	D [*mm²/day*]	[*m²/s*]
HE4 C13	5.61	49.98	26.1606	0.1093	1.27E-12
HE4 C14	5.59	49.81	25.8503	0.107	1.24E-12
HE4 C15	5.39	50.00	25.5187	0.0996	1.15E-12
HE4 C16	5.50	49.76	25.6628	0.0965	1.12E-12
Mean	**5.52**	**49.89**	**25.7981**	**0.1031**	**1.19E-12**
SD	**0.10**	**0.12**	**0.2772**	**0.0060**	**6.99E-14**

3- Infused Advantex® composite material

As previously, when the weight gain is plotted versus the square root of time (*Fig. 24*), it appears that the diffusion in infused Advantex® composite material follows Fick's law. So, the *Matlab*© routine has again been applied to the four sets of data obtained at each test temperature.

The graphical representations of the experimental data and the mean value of optimization at each temperature are summarized in *Fig. 25* (*4°C*), *Fig. 26* (*20°C*), *Fig. 27* (*40°C*) and *Fig. 28* (*60°C*). The main geometrical data of the specimens and the diffusion coefficients obtained at each temperature are summarized in *Table 59* (*4°C*), *Table 60* (*20°C*), *Table 61* (*40°C*) and *Table 62* (*60°C*).

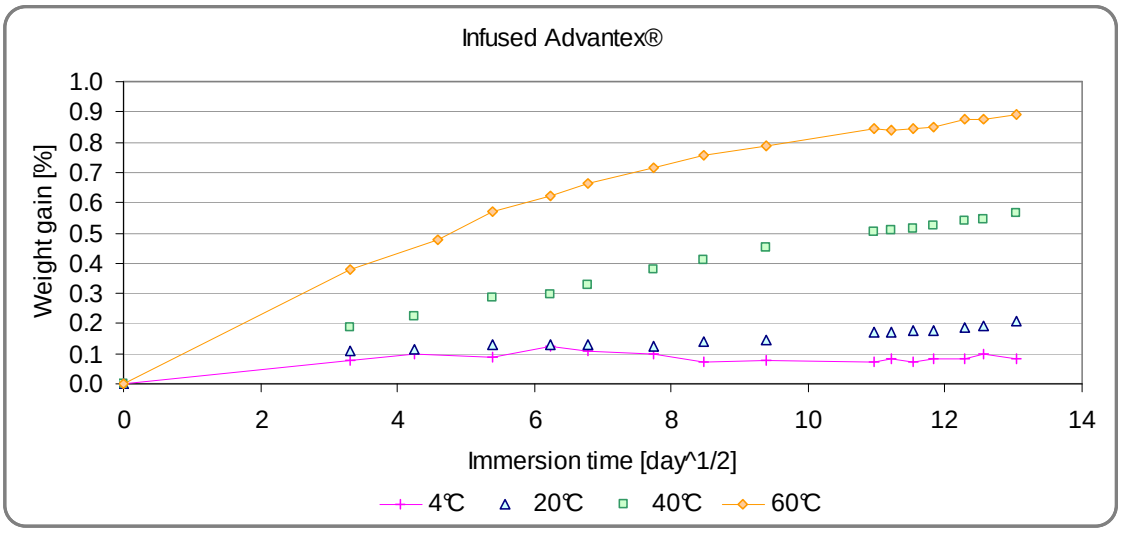

Fig. 24. *Comparative curves of the kinetics of diffusion of the infused Advantex® specimens at five temperatures in natural circulating sea water*

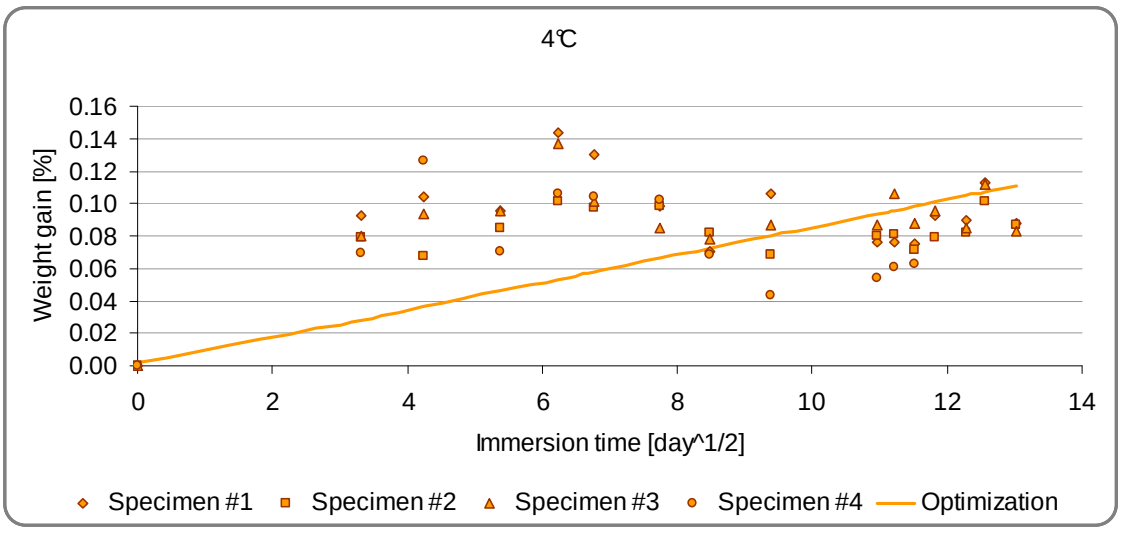

Fig. 25. *Comparative curves between experimental data and optimization in natural circulating sea water at 4°C for infused Advantex® specimens*

Table 59. *Report of data obtained for infused Advanex® specimens in natural circulating sea water at 4°C*

Advantex® ***4°C***	Thickness [*mm*]	Length [*mm*]	m0 [*g*]	D	
				[*mm²/day*]	[*m²/s*]
HA5 C1	5.68	48.95	25.5534	0.0010	1.16E-14
HA5 C2	5.50	49.87	25.9261	0.0008	8.96E-15
HA5 C3	5.65	49.68	26.3116	0.0010	1.16E-14
HA5 C4	5.44	50.24	25.7358	0.0006	6.50E-15
Mean	**5.57**	**49.69**	**25.8817**	**0.0008**	**9.65E-15**
Stand. Dev.	**0.12**	**0.54**	**0.3245**	**0.0002**	**2.44E-15**

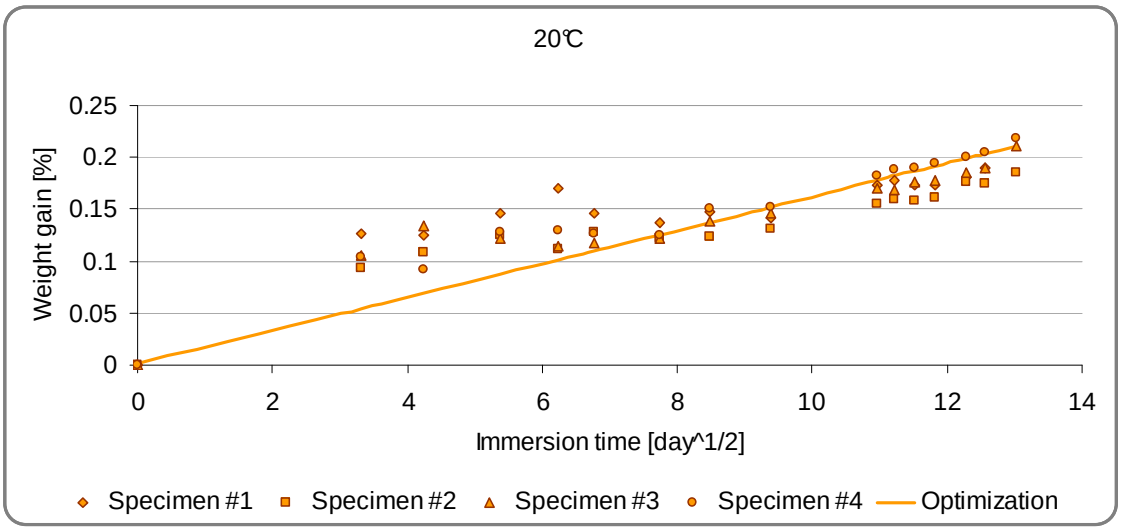

Fig. 26. *Comparative curves between experimental data and optimization in natural circulating sea water at 20°C for infused Advantex® specimens*

Table 60. *Report of data obtained for infused Advanex® specimens in natural circulating sea water at 20°C*

Advantex® ***20°C***	Thickness [*mm*]	Length [*mm*]	m0 [*g*]	D	
				[*mm²/day*]	[*m²/s*]
HA5 C5	5.67	49.67	26.3142	0.0033	3.82E-14
HA5 C6	5.56	50.18	26.5776	0.0025	2.89E-14
HA5 C7	5.53	49.71	26.0737	0.0029	3.36E-14
HA5 C8	5.62	49.96	25.8983	0.0034	3.94E-14
Mean	**5.60**	**49.88**	**26.2160**	**0.0030**	**3.50E-14**
Stand. Dev.	**0.06**	**0.24**	**0.2953**	**0.0004**	**4.76E-15**

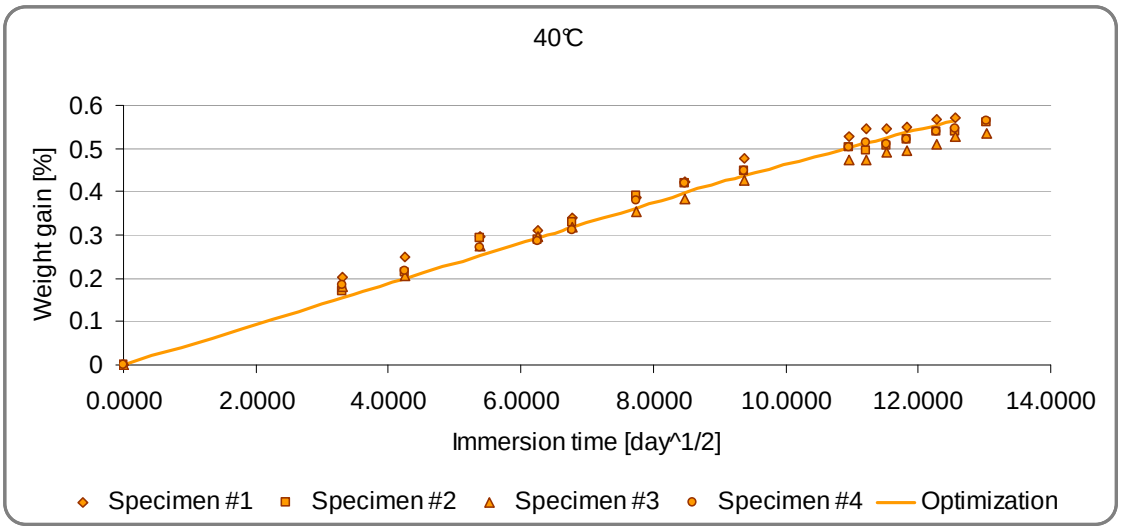

Fig. 27. *Comparative curves between experimental data and optimization in natural circulating sea water at 40°C for infused Advantex® specimens*

Table 61. *Report of data obtained for infused Advanex® specimens in natural circulating sea water at 40°C*

Advantex® 40°C	Thickness [*mm*]	Length [*mm*]	m0 [*g*]	D [*mm²/day*]	[*m²/s*]
HA5 C9	5.40	49.77	24.8820	0.0269	3.11E-13
HA5 C10	5.46	49.71	25.0514	0.0240	2.78E-13
HA5 C11	5.60	49.86	26.3905	0.0226	2.62E-13
HA5 C12	5.36	49.77	25.1019	0.0232	2.69E-13
Mean	**5.46**	**49.78**	**25.3565**	**0.0242**	**2.80E-13**
Stand. Dev.	**0.11**	**0.06**	**0.6958**	**0.0019**	**2.20E-14**

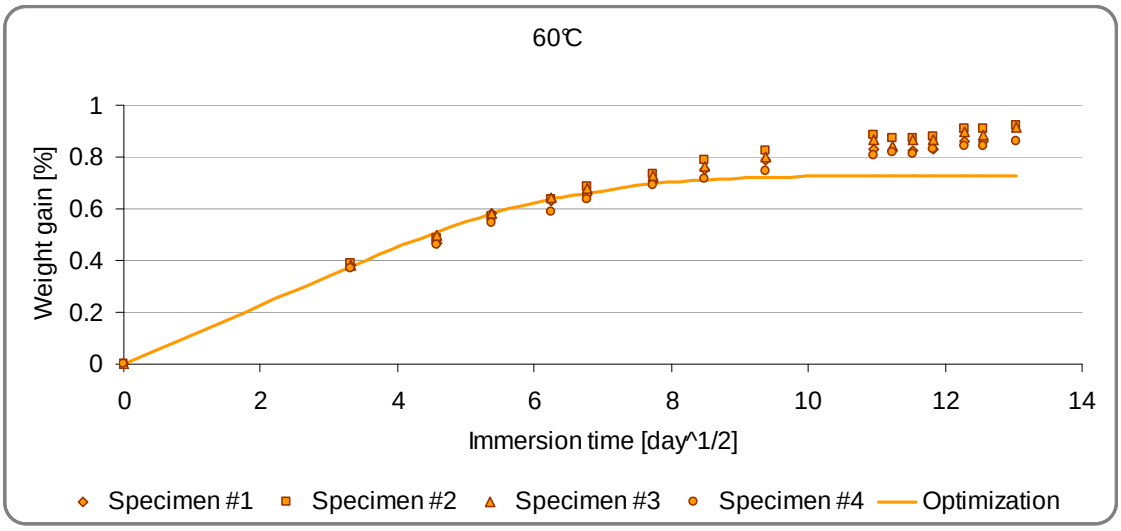

Fig. 28. *Comparative curves between experimental data and optimization in natural circulating sea water at 60°C for infused Advantex® specimens*

Table 62. *Report of data obtained for infused Advanex® specimens in natural circulating sea water at 60°C*

Advantex® 60°C	Thickness [*mm*]	Length [*mm*]	m0 [*g*]	D	
				[*mm²/day*]	[*m²/s*]
HA5 C13	5.59	49.69	26.1414	0.1493	1.73E-12
HA5 C14	5.64	49.79	25.9419	0.0163	1.89E-13
HA5 C15	5.63	49.85	26.2346	0.1634	1.89E-12
HA5 C16	5.42	49.13	25.1048	0.1248	1.44E-12
Mean	**5.57**	**49.62**	**25.8557**	**0.1135**	**1.31E-12**
Stand. Dev.	**0.10**	**0.33**	**0.5153**	**0.0667**	**7.72E-13**

4- Infused HiPer-tex™ composite material

As for pure resin material, the infused E-glass and Advantex® composites, the weight gain is plotted versus the square root of time (*Fig. 29*). We can observe that the diffusion in infused HiPer-tex™ composite material again follows Fick's law. So, the *Matlab©* routine has been applied to the four sets of data obtained at each test temperature.

The graphical representations of the experimental data and the mean value of optimization at each temperature are summarized in *Fig. 30* (*4°C*), *Fig. 31* (*20°C*), *Fig. 32* (*40°C*) and *Fig. 33* (*60°C*). The main geometrical data of the specimens and the diffusion coefficients obtained at each temperature are summarized in *Table 63* (*4°C*), *Table 64* (*20°C*), *Table 65* (*40°C*) and *Table 66* (*60°C*).

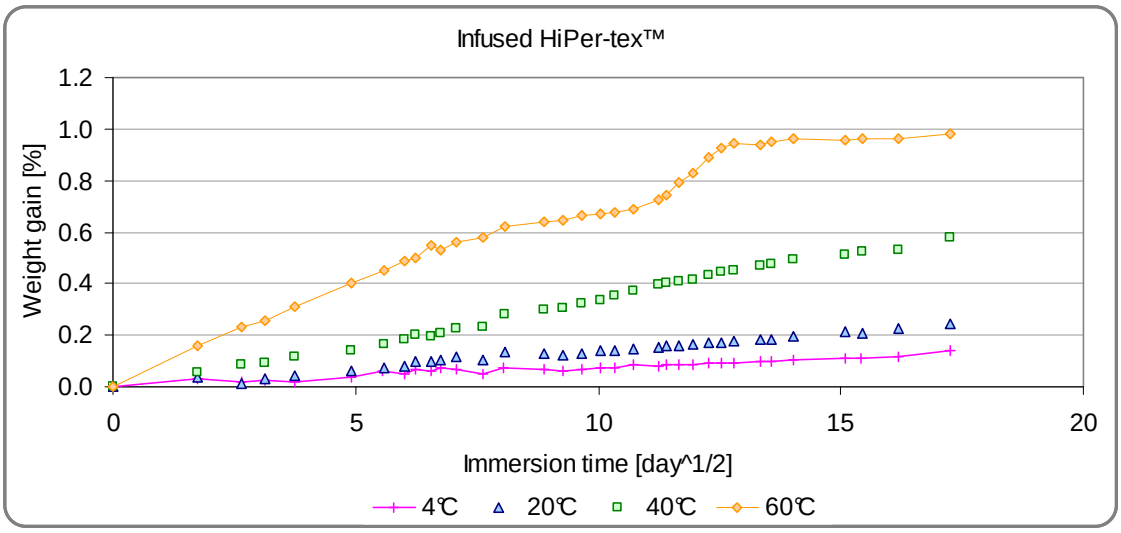

Fig. 29. *Comparative curves of the kinetics of diffusion of the infused HiPer-tex™ specimens at five temperatures in natural circulating sea water*

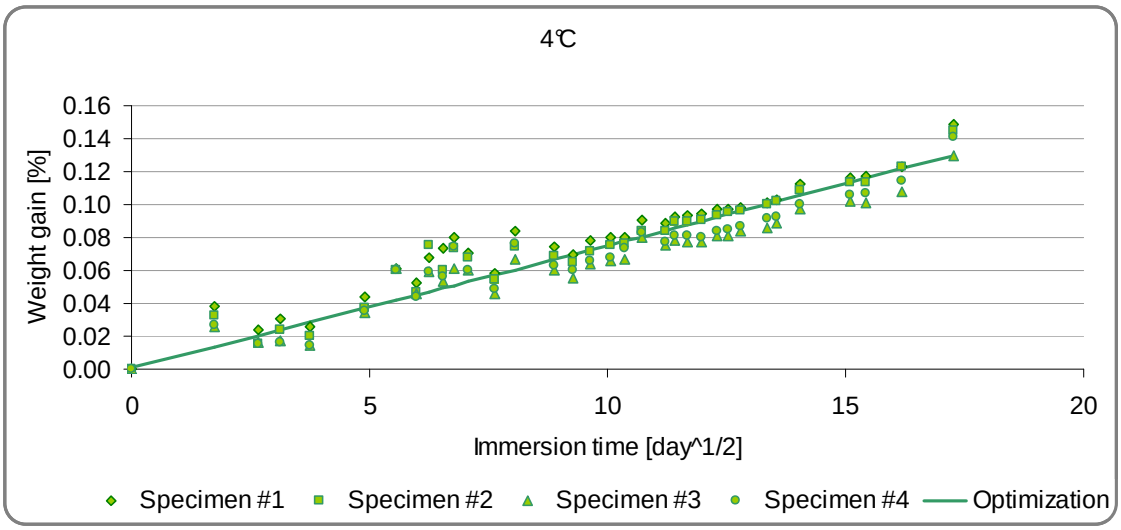

Fig. 30. *Comparative curves between experimental data and optimization in natural circulating sea water at 4°C for infused HiPer-tex™ specimens*

Table 63. *Report of data obtained for infused HiPer-tex™ specimens in natural circulating sea water at 4°C*

HiPer-tex™ 4°C	Thickness [*mm*]	Length [*mm*]	m0 [*g*]	D [*mm²/day*]	[*m²/s*]
3BHd C1	4.99	51.07	26.9477	0.0007	7.64E-15
3BHd C2	5.34	50.71	26.4633	0.0007	8.03E-15
3BHd C3	5.33	50.72	26.4730	0.0005	6.20E-15
3BHd C4	5.37	50.76	26.6965	0.0006	6.97E-15
Mean	**5.26**	**50.81**	**26.6451**	**0.0006**	**7.21E-15**
Stand. Dev.	**0.18**	**0.17**	**0.2287**	**0.0001**	**8.01E-16**

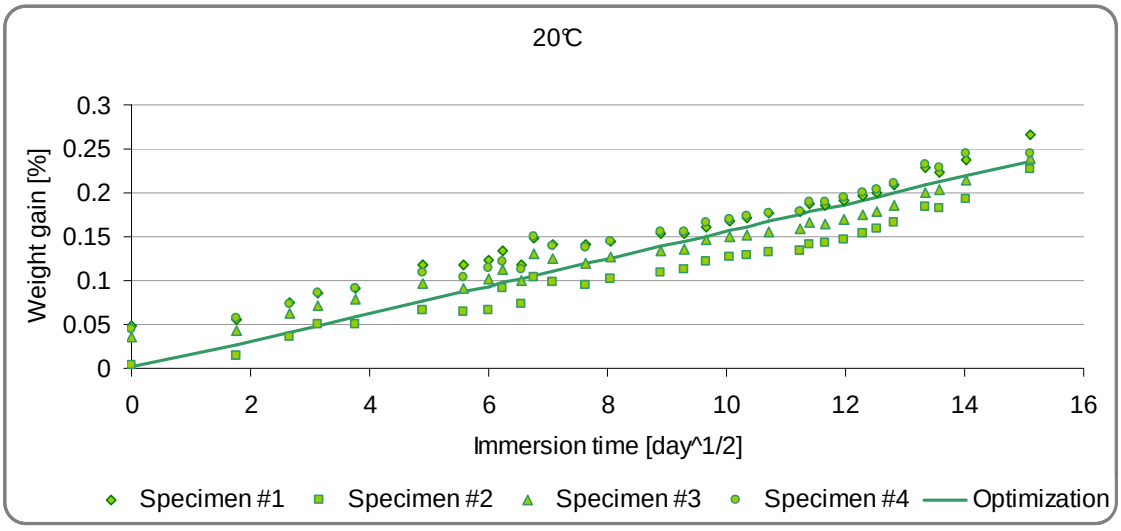

Fig. 31. *Comparative curves between experimental data and optimization in natural circulating sea water at 20°C for infused HiPer-tex™ specimens*

Table 64. *Report of data obtained for infused HiPer-tex™ specimens in natural circulating sea water at 20°C*

HiPer-tex™ 20°C	Thickness [*mm*]	Length [*mm*]	m0 [*g*]	D	
				[*mm²/day*]	[*m²/s*]
3BHd C5	5.45	51.09	27.3741	0.0035	4.05E-14
3BHd C6	5.32	51.36	27.1011	0.0019	2.20E-14
3BHd C7	5.27	50.43	26.3806	0.0026	3.01E-14
3BHd C8	5.45	50.69	26.9155	0.0035	4.05E-14
Mean	**5.37**	**50.89**	**26.9428**	**0.0029**	**3.33E-14**
Stand. Dev.	**0.09**	**0.42**	**0.4195**	**0.0008**	**8.98E-15**

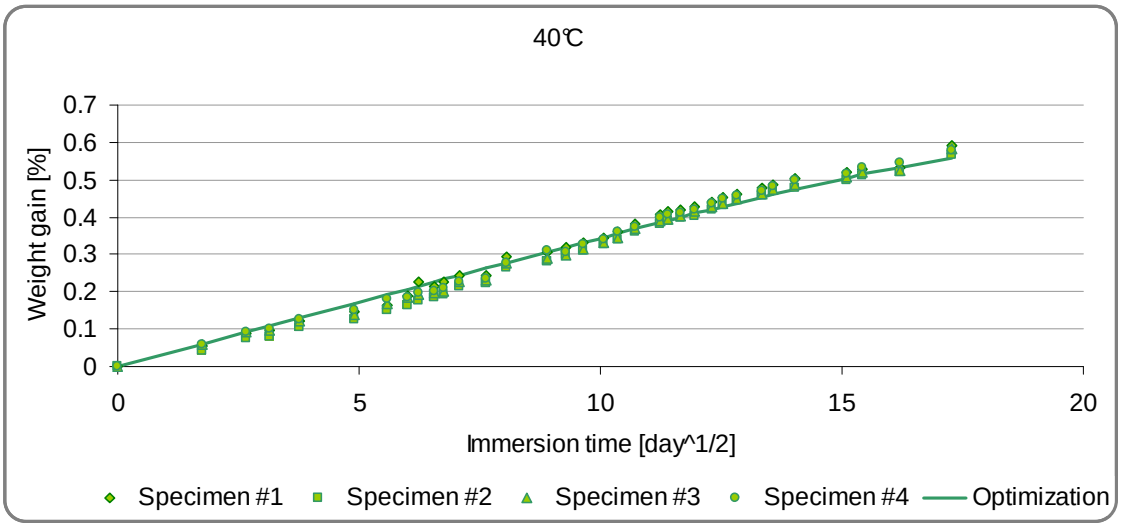

Fig. 32. *Comparative curves between experimental data and optimization in natural circulating sea water at 40°C for infused HiPer-tex™ specimens*

Table 65. *Report of data obtained for infused HiPer-tex™ specimens in natural circulating sea water at 40°C*

HiPer-tex™ 40°C	Thickness [*mm*]	Length [*mm*]	m0 [*g*]	D	
				[*mm²/day*]	[*m²/s*]
3BHd C9	5.43	50.36	26.5281	0.0148	1.71E-13
3BHd C10	5.46	50.83	27.1116	0.0132	1.53E-13
3BHd C11	5.49	50.85	27.2698	0.0140	1.62E-13
3BHd C12	5.44	50.95	27.2389	0.0144	1.67E-13
Mean	**5.46**	**50.75**	**27.0371**	**0.0141**	**1.63E-13**
Stand. Dev.	**0.03**	**0.26**	**0.3462**	**0.0007**	**7.91E-15**

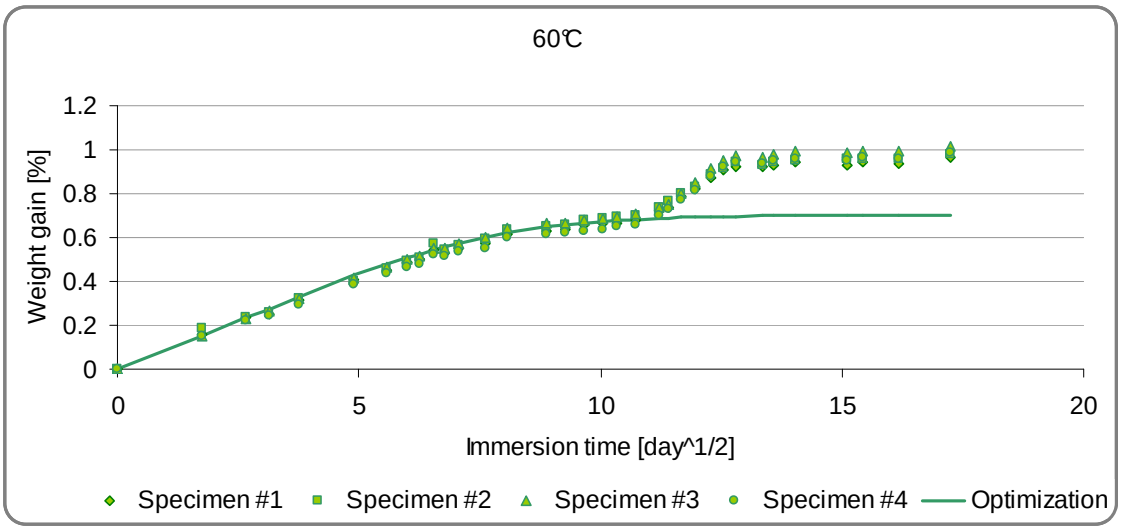

Fig. 33. *Comparative curves between experimental data and optimization in natural circulating sea water at 60°C for infused HiPer-tex™ specimens*

Table 66. *Report of data obtained for infused HiPer-tex™ specimens in natural circulating sea water at 60°C*

HiPer-tex™ 60°C	Thickness [*mm*]	Length [*mm*]	m0 [*g*]	D	
				[*mm²/day*]	[*m²/s*]
3BHd C13	5.54	51.32	27.8851	0.0920	1.06E-12
3BHd C14	5.43	51.00	27.1876	0.0946	1.09E-12
3BHd C15	5.45	50.84	26.9246	0.0970	1.12E-12
3BHd C16	5.44	50.92	26.9952	0.0818	9.47E-13
Mean	**5.47**	**51.02**	**27.2481**	**0.0914**	**1.06E-12**
Stand. Dev.	**0.05**	**0.21**	**0.4390**	**0.0067**	**7.74E-14**

5- Comparison of the four materials

An important part of the study is to compare the effect of the fibre on the behaviour of the composite material in natural sea water. So, with all the results presented previously and summarized in *Table 67*, we can compare the kinetics of diffusion for pure resin and infused composites in natural sea water at *4°C* (*Fig. 34*), *20°C* (*Fig. 35*), *40°C* (*Fig. 36*), and *60°C* (*Fig. 37*).

Table 67. *Summary of the natural sea water ageing data obtained for pure resin, infused E-glass, Advantex® and HiPer-tex™ composites*

		Pure resin	Infused E-glass	Infused Advantex®	Infused HiPer-tex™
Weight gain at saturation		2.75%	0.75%	0.73%	0.70%
Mean diffusion coefficient D (Stand. Dev.) $[m^2/s]$	SW at 4°C	2.58-14 (5.79E-16)	1.16E-14 (8.47E-16)	9.65E-15 (2.44E-15)	7.21E-15 (8.01E-16)
	SW at 20°C	6.66E-14 (2.00e-15)	3.59E-14 (1.34E-15)	3.50E-14 (4.76E-15)	3.33E-14 (8.98E-15)
	SW at 40°C	3.18E13 (3.66E15)	1.73E-13 (1.07E-14)	2.80E-13 (2.20E-14)	1.63E-13 (7.91E-15)
	SW at 60°C	6.15E-13 (.33E-14)	1.19E-12 (6.99E-14)	1.31E-12 (7.72E-13)	1.06E-12 (7.74E-14)

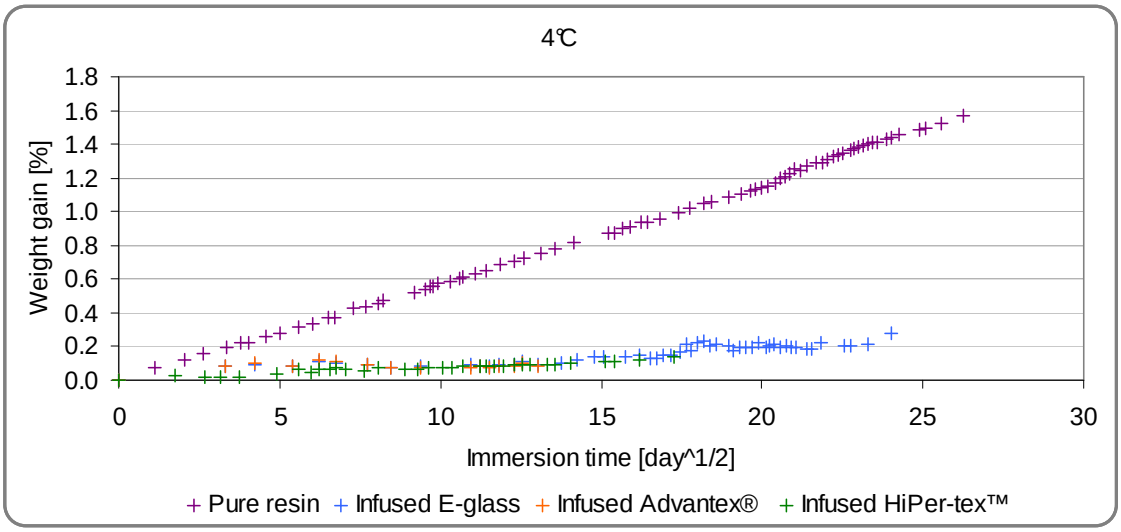

Fig. 34. *Comparative curves of the kinetics of diffusion of the four materials in natural circulating sea water at 4°C*

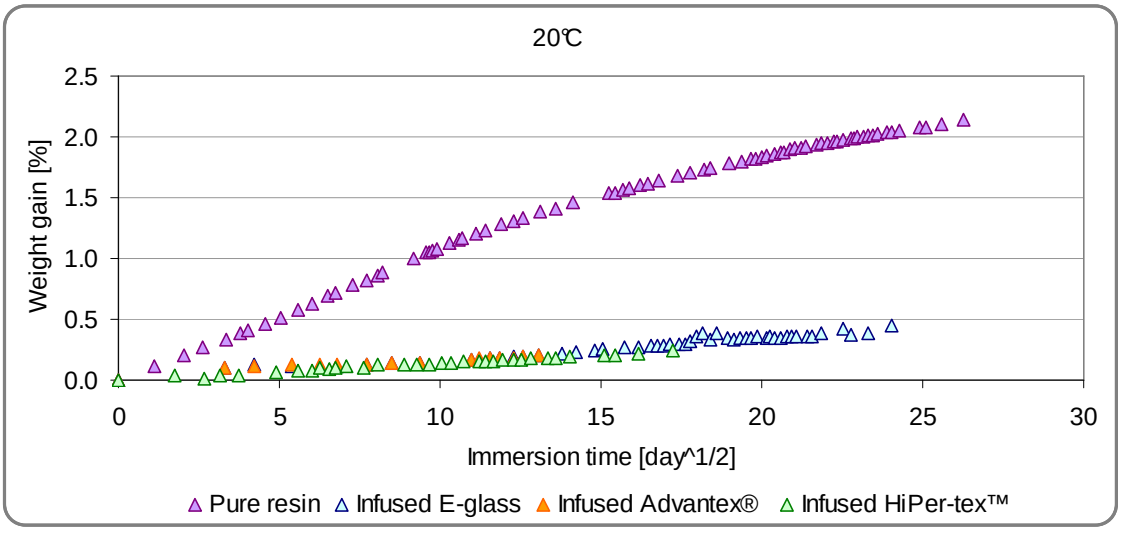

Fig. 35. *Comparative curves of the kinetics of diffusion of the four materials in natural circulating sea water at 20°C*

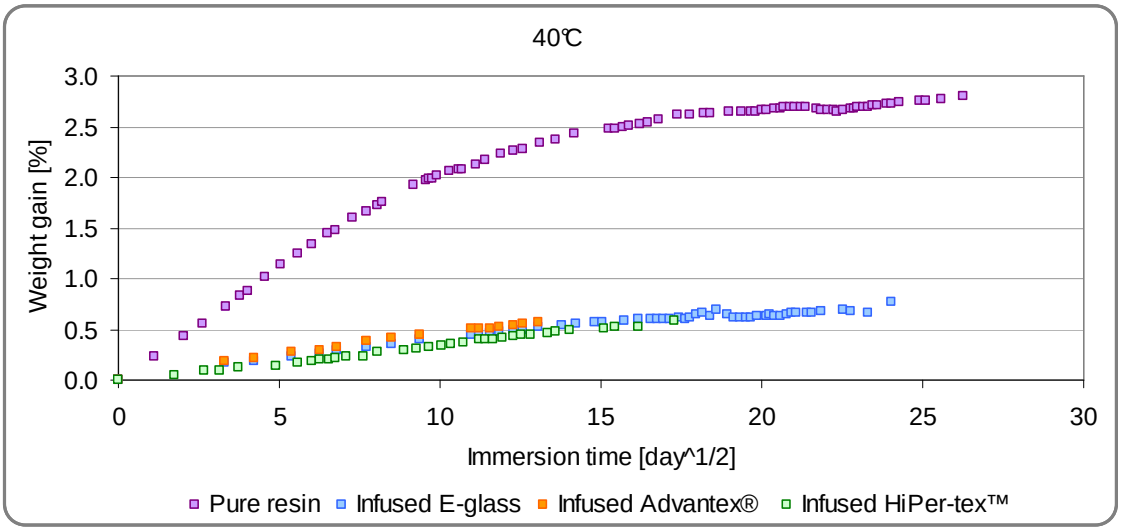

Fig. 36. *Comparative curves of the kinetics of diffusion of the four materials in natural circulating sea water at 40°C*

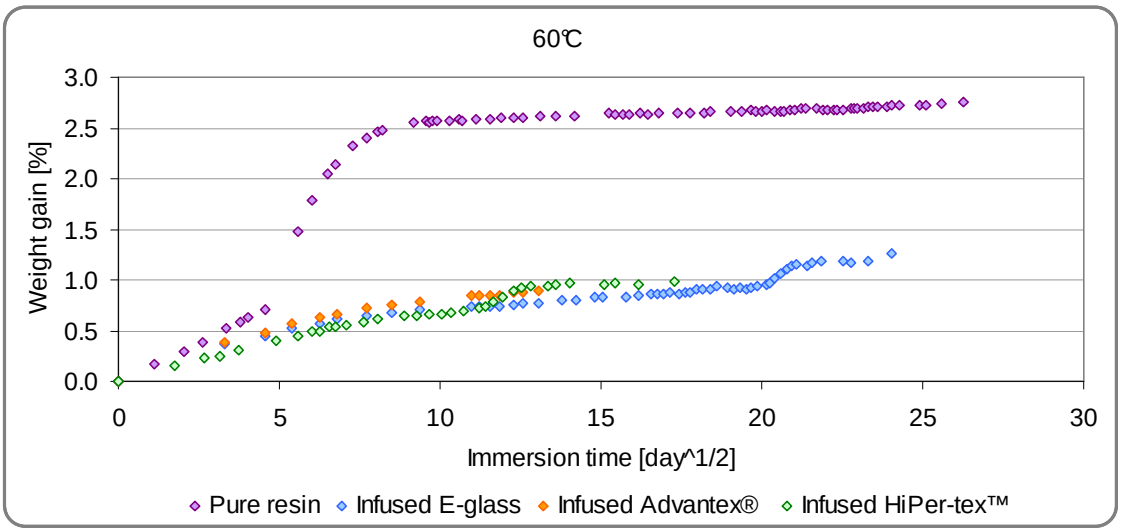

Fig. 37. *Comparative curves of the kinetics of diffusion of the four materials in natural circulating sea water at 60°C*

Annex 6

Summary of the experimental data obtained during fatigue tests

The flexural fatigue tests have been carried out in air and in natural circulating sea water on *31* infused E-glass specimens (*12* in air and *19* in natural sea water), *19* infused Advantex® specimens in natural sea water and *29* infused HiPer-tex™ specimens (*10* in air and *19* in natural sea water), at *9* different loading levels ($45\% \leq R\sigma \leq 85\%$).

For each specimen, the section is given as well as the number of cycles until failure, the maximum stress applied and the corresponding stress level.

1- Tests performed on infused E-glass composites

	Specimen	Section $[mm]$ b x h	Lifetime	Maximum stress $[MPa]$	Stress level Rσ
Fatigue tests in air	HE4_14	10.06 x 5.64	606 023	562.5	0.49
	HE3_28	10.06 x 5.62	700 735	566.5	0.50
	IE2_16	9.95 x 5.17	919 976	568.5	0.50
	HE4_09	10.05 x 5.57	1 516 886	577.3	0.51
	HE3_27	10.05 x 5.57	180 340	692.8	0.61
	HE3_26	10.06 x 5.47	214 369	717.6	0.63
	HE4_08	10.07 x 5.54	51 711	829.9	0.73
	HE4_07	10.04 x 5.53	38 470	835.4	0.73
	HE4_03	10.00 x 5.50	40 282	847.9	0.75
	IE1_27	10.01 x 5.14	1 552	1109.4	0.98
	IE1_28	10.11 x 5.09	930	1120.1	0.98
	IE1_25	9.98 x 5.04	591	1157.4	1.02
Fatigue tests in natural circulating sea water	HE4_15	10.07 x 5.57	1 229 018	469.6	0.41
	HE3_29	10.05 x 5.56	405 781	579.4	0.51
	HE4_05	10.01 x 5.53	154 495	588.0	0.52
	HE4_06	10.07 x 5.46	342 408	599.6	0.53
	HE4_13	10.04 x 5.61	62 358	638.0	0.56
	HE4_10	10.01 x 5.55	91 871	653.8	0.57
	HE3_19	10.09 x 5.64	15 504	673.0	0.59
	HE3_18	10.14 x 5.61	31 315	676.8	0.59
	IE1_48	9.99 x 4.97	108 294	682.0	0.60
	IE1_35	9.97 x 5.18	46 872	682.9	0.60
	HE3_30	10.08 x 5.54	46 575	698.2	0.61
	HE4_11	10.07 x 5.71	15 369	726.4	0.64
	HE3_17	10.15 x 5.40	19 397	729.8	0.64
	HE4_12	10.05 x 5.63	34 745	748.7	0.66
	IE1_33	10.04 x 5.15	10 162	811.2	0.71
	HE4_01	10.10 x 5.54	5 630	827.5	0.73
	HE4_02	10.02 x 5.55	8 519	831.1	0.73
	IE1_32	9.96 x 5.07	7 751	843.7	0.74
	HE4_04	10.01 x 5.49	10 560	850.2	0.75

2- Tests performed on infused Advantex® composites

	Specimen	Section $[mm]$ b x h	Lifetime	Maximum stress $[MPa]$	Stress level Rσ
Fatigue tests in natural circulating sea water	HA1_21	10.04 5.37	1 661 321	432.1	0.50
	HA1_20	10.03 5.35	3 304 545	432.6	0.50
	HA1_16	10.05 5.42	956 096	432.9	0.50
	HA1_19	10.04 5.43	818 206	477.3	0.55
	HA1_22	10.05 5.37	145 355	518.6	0.60
	HA1_11	10.05 5.40	192 517	519.0	0.60
	HA6_20	10.10 5.32	82 448	519.5	0.60
	HA6_21	10.04 5.43	266 872	519.9	0.60
	HA1_12	10.01 5.39	196 122	519.9	0.60
	HA1_32	10.06 5.36	51 829	520.0	0.60
	HA1_23	10.08 5.40	188 501	520.5	0.60
	HA1_15	10.09 5.40	22 268	605.7	0.70
	HA1_13	10.01 5.47	111 748	607.0	0.70
	HA1_14	10.07 5.41	29 811	607.7	0.70
	HA1_18	10.07 5.48	18 017	648.8	0.75
	HA1_17	10.06 5.35	32 846	650.1	0.75
	HA1_02	10.01 5.38	5 719	745.5	0.86
	HA1_05	10.04 5.37	3 124	746.1	0.86
	HA1_03	10.01 5.37	3 852	748.3	0.86

3- Tests performed on infused HiPer-tex™ composites

	Specimen	Section $[mm]$ b x h		Lifetime	Maximum stress $[MPa]$	Stress level Rσ
Fatigue tests in air	HH1_11	9.98	5.40	686 538	742.2	0.56
	HH1_25	10.02	5.63	192 284	750.9	0.57
	HH1_23	10.04	5.56	84 704	768.4	0.58
	HH1_24	10.03	5.52	60 315	780.4	0.59
	IH1_21	9.97	5.16	35 613	813.7	0.62
	HH1_21	10.03	5.54	64 839	833.2	0.63
	HH1_22	10.00	5.49	43 398	851.0	0.65
	IH1_33	10.01	5.19	295	1 088.2	0.83
	IH1_34	9.96	5.19	941	1 093.6	0.83
	IH1_35	9.97	5.18	3 101	1 096.7	0.83
Fatigue tests in natural circulating sea water	HH1_12	9.96	5.45	1 043 248	608.4	0.46
	HH1_10	9.97	5.44	850 812	610.1	0.46
	HH1_09	9.99	5.39	986 988	620.2	0.47
	HH1_19	10.02	5.47	168 952	672.4	0.51
	HH1_18	10.09	5.42	278 083	680.1	0.52
	HH1_03	10.00	5.50	53 168	714.0	0.54
	HH1_04	9.98	5.44	65 529	731.4	0.56
	HH1_01	10.03	5.40	102 530	738.5	0.56
	HH1_02	10.01	5.40	108 634	740.0	0.56
	HH1_17	10.06	5.53	40 519	775.2	0.59
	HH1_16	10.05	5.48	34 127	790.2	0.60
	IH1_40	10.08	5.12	44 263	817.4	0.62
	HH1_06	9.99	5.54	12 314	836.6	0.64
	HH1_05	9.99	5.42	21 858	874.0	0.67
	HH1_07	10.02	5.36	13 859	891.0	0.68
	HH1_08	9.98	5.33	11 576	904.7	0.69
	HH1_13	9.98	5.44	6 974	993.4	0.76
	HH1_14	10.00	5.43	5 572	995.1	0.76
	IH1_36	9.98	5.24	5 025	1 070.7	0.81

Annex 7

Summary of the analytical results used to describe the evolution of the apparent stiffness during fatigue

In order to describe the evolution of the damage and integrate this in a numerical model, an analytical study has been performed based on the experimental results and empirical formulations. The experimental results are issued from fatigue tests performed on infused E-glass, Advantex® and HiPer-tex™ composite specimens. These tests were carried out in four-point bending in air (except for infused Advantex® specimens) and in natural circulating sea water with different stress level, a High Stress Level (HSL) with $R\sigma$ varying between *0.75* and *0.83* and a Low Stress Level (LSL) with $R\sigma$ varying between *0.51* and *0.6*.

As the evolution of the damage does not follow a known law, the analytical study is based on the general shape of the experimental curves. That is the reason why we have developed several formulations with several coefficients to determine by using a *Matlab*© routine or a genetic algorithm.

If we consider

$$y=\frac{F}{Displacement} \qquad x=\frac{N}{N_f}$$

We can write the evolution of the ratio of the applied load divided by the displacement as a function of the ratio number of cycles/fatigue life, using the four following equations. *(Eqn. 63)* is the simplest form of equation used to describe the evolution of the experimental curve (noted Function #1), *(Eqn. 64)* is an inverse cosine function (noted Function #2), *(Eqn. 65)* is a power function (noted Function #3) and *(Eqn. 66)* is an hyperbolic function (noted Function #4).

$$y=D-\frac{A\cdot x\cdot\left(1+x^B\right)-A\cdot(1-x)^C}{1+A} \qquad \textbf{(Eqn. 63)}$$

$$y=C\cdot\left(\arccos\left(2x^A-1\right)\right)^B \qquad \textbf{(Eqn. 64)}$$

$$y=C\cdot\left(1-x^A\right)^B \qquad \textbf{(Eqn. 65)}$$

$$y=C\cdot\frac{1-x^A}{1+x^B} \qquad \textbf{(Eqn. 66)}$$

1- Optimisation with the first function

The first function defined is the simplest one and is written as :

$$y = D - \frac{A \cdot x \cdot \left(1 + x^B\right) - A \cdot (1 - x)^C}{1 + A} \qquad \text{With} \quad y = \frac{F}{Displacement} \quad \text{and} \quad x = \frac{N}{N_f}$$

In order to determine these four coefficients, *A*, *B*, *C* and *k*, we have developed an optimisation routine in *Matlab*© which uses the least squares method and a genetic algorithm to investigate the accuracy of the results.

As genetic algorithm is a method based on mutation, selection and crossover, several families of results can be found as presented on *Fig. 38*. The results are summarized in *Table 68*.

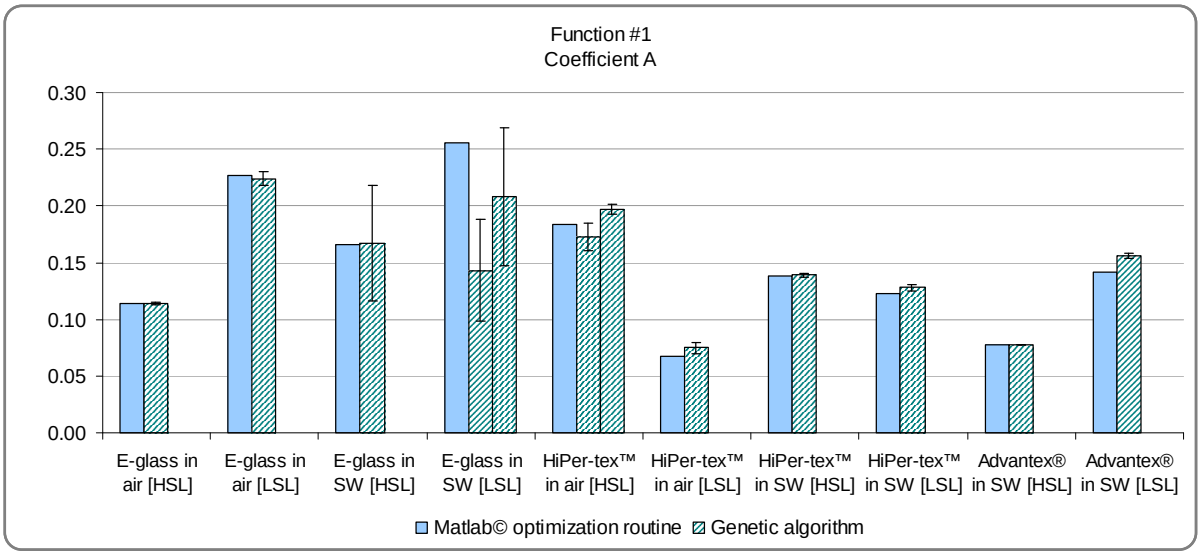

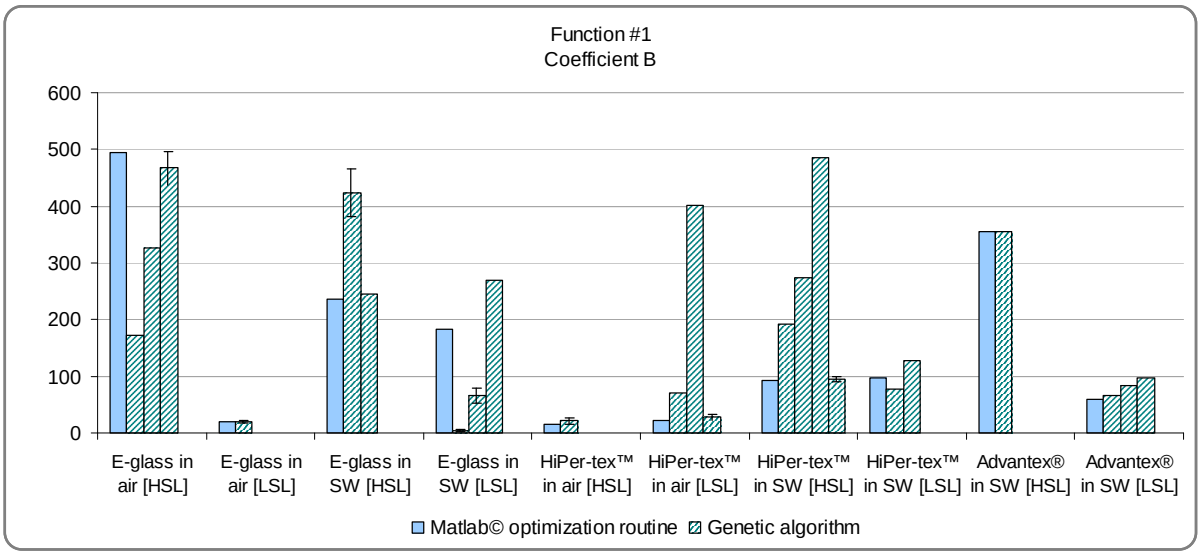

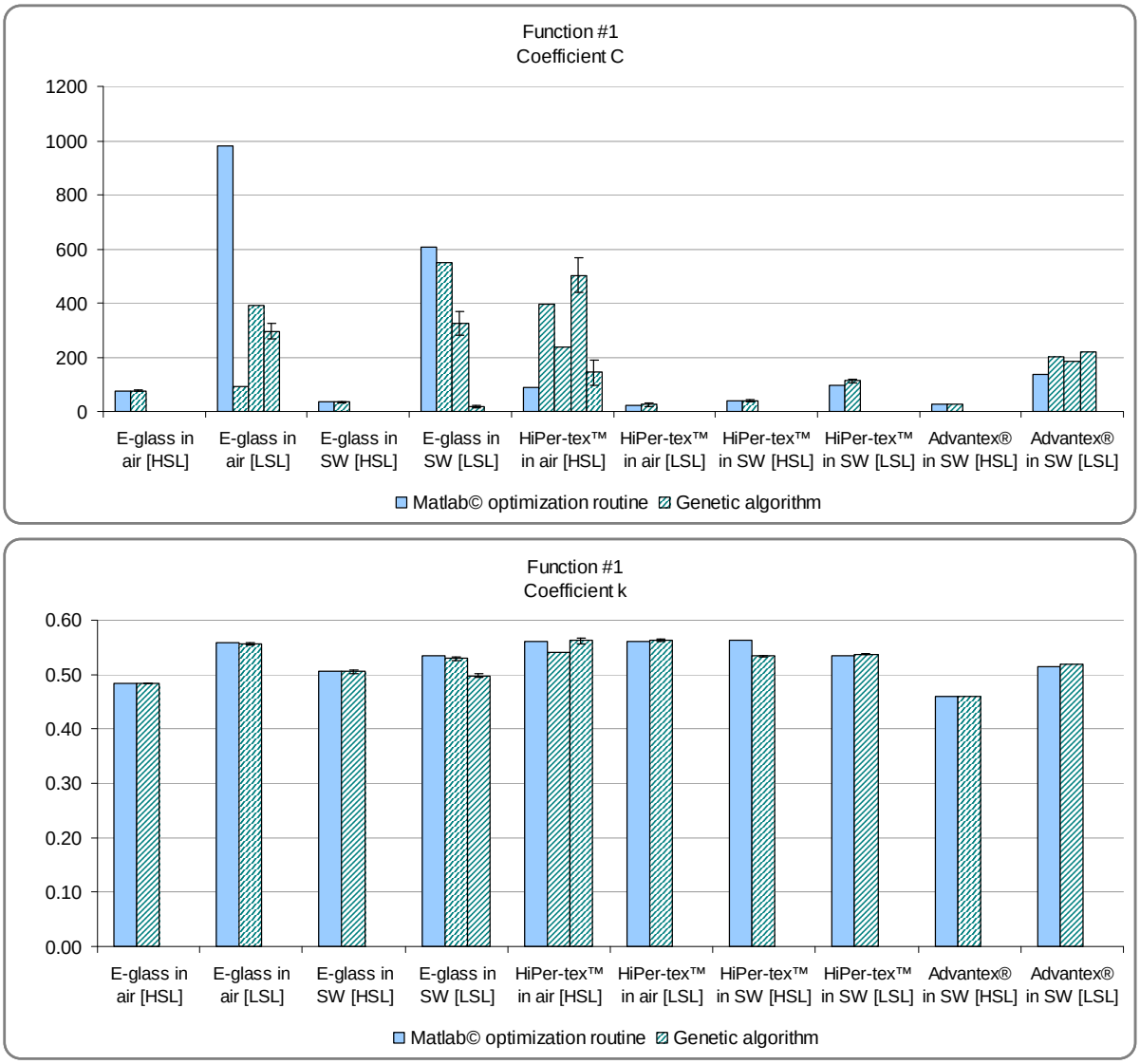

Fig. 38. *Graphical representation of the results obtained by Matlab© routine and genetic algorithm with the first function*

Table 68. *Summary of the results obtained by Matlab© routine and genetic algorithm with the first function*

Function #1	Matlab© routine	Genetic algorithm		
E-glass in air $[HSL]$				
Coefficient A (SD)	0.1142	0.114 (0.001)		
Coefficient B (SD)	493.3897	171.469	326.632	466.621 (30.714)
Coefficient C (SD)	73.8426	74.831 (2.217)		
Coefficient k (SD)	0.4836	0.484 (0.001)		
E-glass in air $[LSL]$				
Coefficient A (SD)	0.2273	0.224 (0.006)		
Coefficient B (SD)	19.6213	19.887 (1.193)		
Coefficient C (SD)	978.121	90.992	391.840	296.067 (28.859)
Coefficient k (SD)	0.5576	0.556 (0.002)		

E-glass in SW [*HSL*]					
Coefficient A (SD)	0.166	0.167 (0.051)			
Coefficient B (SD)	236.4894	423.584 (42.596)		244.41 (13.486)	
Coefficient C (SD)	35.2759	34.572 (2.337)			
Coefficient k (SD)	0.5051	0.505 (0.003)			
E-glass in SW [*LSL*]					
Coefficient A (SD)	0.2557	0.143 (0.045)		0.208 (0.061)	
Coefficient B (SD)	184.1718	4.712 (1.916)	66.775 (13.678)		269.789
Coefficient C (SD)	604.7168	549.087	323.408 (43.681)		18.198 (5.457)
Coefficient k (SD)	0.5346	0.529 (0.003)		0.498 (0.003)	
HiPer-tex™ in air [*HSL*]					
Coefficient A (SD)	0.1838	0.173 (0.012)		0.197	
Coefficient B (SD)	14.7902	21.259 (5.812)			
Coefficient C (SD)	89.7363	395.172	236.892	502.964 (65.228)	144.204 (45.854)
Coefficient k (SD)	0.561	0.541		0.562 (0.005)	
HiPer-tex™ in air [*LSL*]					
Coefficient A (SD)	0.0676	0.075 (0.005)			
Coefficient B (SD)	21.8695	71.302	401.47		27.62 (4.715)
Coefficient C (SD)	20.8909	26.241 (6.542)			
Coefficient k (SD)	0.5602	0.563 (0.002)			
HiPer-tex™ in SW [*HSL*]					
Coefficient A (SD)	0.1382	0.139 (0.002)			
Coefficient B (SD)	92.293	191.149	272.851	486.246	94.661 (4.130)
Coefficient C (SD)	38.2513	39.767 (2.795)			
Coefficient k (SD)	0.5636	0.534 (0.001)			
HiPer-tex™ in SW [*LSL*]					
Coefficient A (SD)	0.1228	0.128 (0.003)			
Coefficient B (SD)	96.9205	77.932		128.831 (18.541)	
Coefficient C (SD)	97.4224	112.536 (7.849)			
Coefficient k (SD)	0.5351	0.537 (0.001)			
Advantex® in SW [*HSL*]					
Coefficient A (SD)	0.077638	0.078 (0.000)			
Coefficient B (SD)	354.69	354.690 (0.000)			
Coefficient C (SD)	24.702	24.702 (0.000)			
Coefficient k (SD)	0.45968	0.460 (0.000)			
Advantex® in SW [*LSL*]					
Coefficient A (SD)	0.1421	0.156 (0.002)			
Coefficient B (SD)	58.9356	66.097 (10.642)	84.309 (2.816)		97.218 (4.528)
Coefficient C (SD)	137.4357	200.760 (3.405)	183.673 (6.286)		219.081 (2.628)
Coefficient k (SD)	0.5156	0.520 (0.001)			

2- Optimisation with the second function

The second function is an inverse cosine function written as :

$$y = C \cdot \left(\arccos\left(2x^{A} - 1\right)\right)^{B} \qquad \text{With} \quad y = \frac{F}{Displacement} \quad \text{and} \quad x = \frac{N}{N_f}$$

As for the first function, a routine *Matlab©* using the least squares method and a genetic algorithm has been developed to determine the three coefficients, *A*, *B* and *C*, which describe the curve. The results are summarized in *Fig. 39*and *Table 69*.

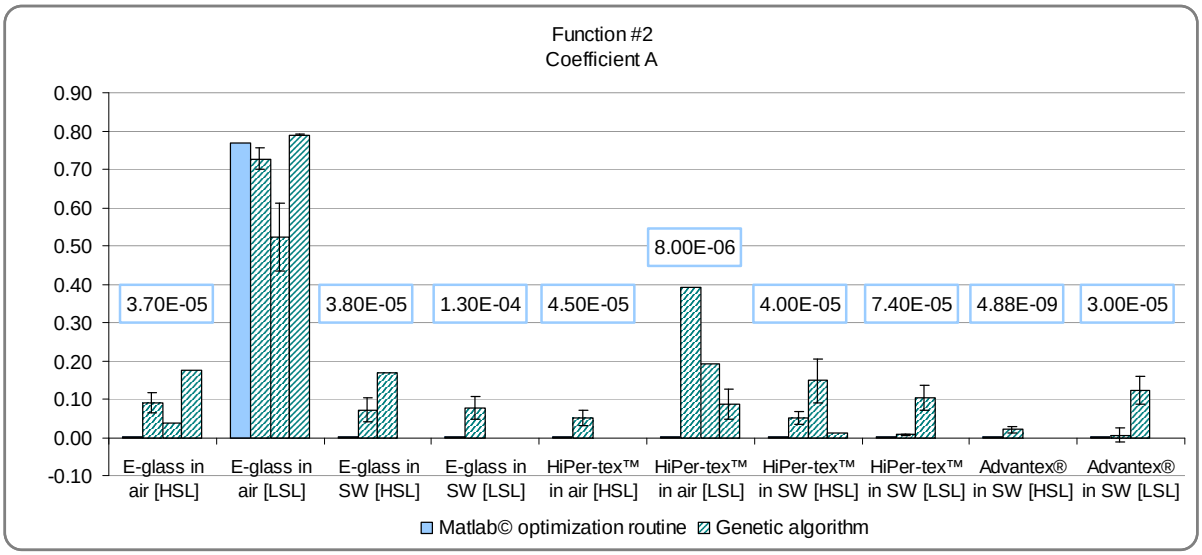

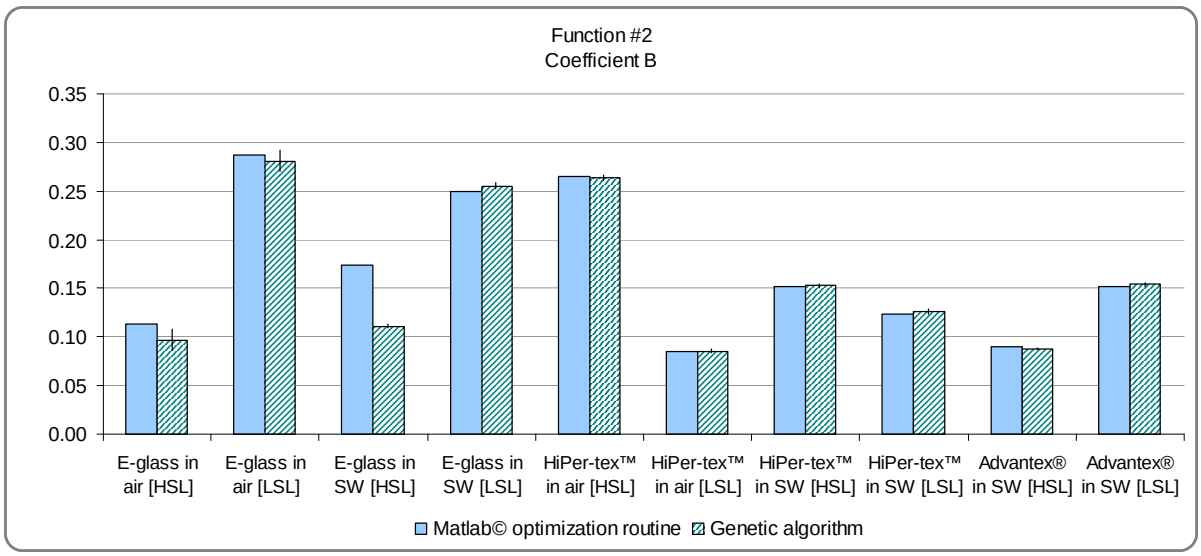

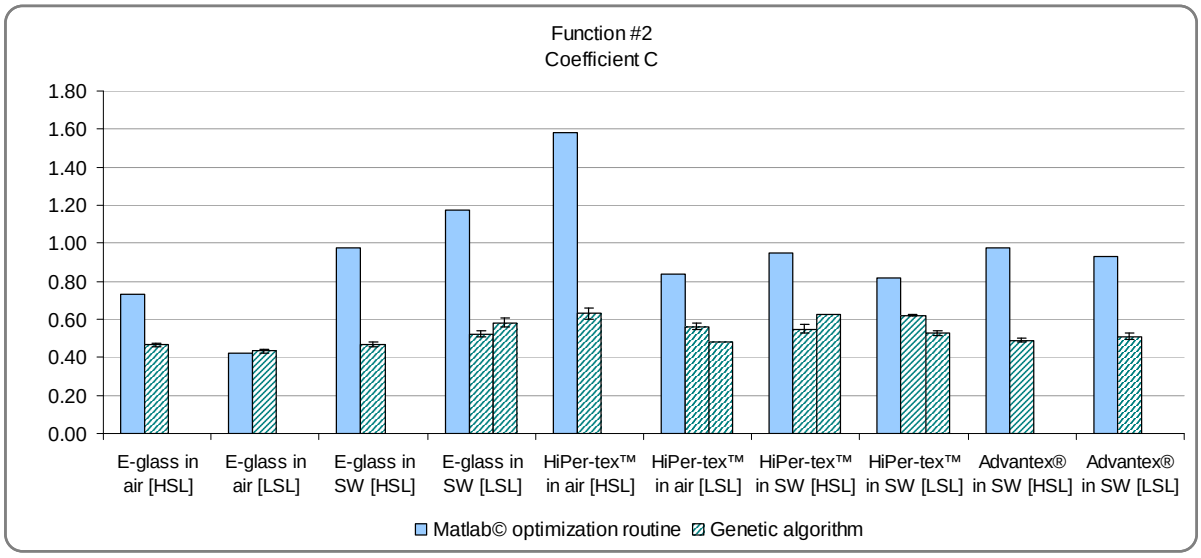

Fig. 39. *Graphical representation of the results obtained by Matlab© routine and genetic algorithm with the second function*

Table 69. *Summary of the results obtained by Matlab© routine and genetic algorithm with the second function*

Function #2	Matlab© routine	Genetic algorithm		
E-glass in air $[HSL]$				
Coefficient A (SD)	3.70E-05	0.090 (0.0026)	0.037	0.177
Coefficient B (SD)	0.1126	0.097 (0.011)		
Coefficient C (SD)	0.7325	0.467 (0.009)		
E-glass in air $[LSL]$				
Coefficient A (SD)	0.7682	0.727 (0.028)	0.523 (0.088)	0.79 (0.003)
Coefficient B (SD)	0.2867	0.281 (0.011)		
Coefficient C (SD)	0.4246	0.433 (0.012)		
E-glass in SW $[HSL]$				
Coefficient A (SD)	3.80E-05	0.072 (0.031)	0.17	
Coefficient B (SD)	0.1734	0.111 (0.002)		
Coefficient C (SD)	0.9751	0.467 (0.013)		
E-glass in SW $[LSL]$				
Coefficient A (SD)	1.30E-04	0.077 (0.031)		
Coefficient B (SD)	0.2496	0.255 (0.003)		
Coefficient C (SD)	1.176	0.523 (0.016)	0.582 (0.022)	
HiPer-tex™ in air $[HSL]$				
Coefficient A (SD)	4.50E-05	0.05 (0.020)		
Coefficient B (SD)	0.2647	0.264 (0.003)		
Coefficient C (SD)	1.5802	0.63 (0.032)		
HiPer-tex™ in air $[LSL]$				
Coefficient A (SD)	8e.6	0.392	0.193	0.087 (0.038)
Coefficient B (SD)	0.0844	0.085 (0.002)		
Coefficient C (SD)	0.8362	0.561 (0.016)	0.481	

HiPer-tex™ in SW $[HSL]$				
Coefficient A (SD)	4.00E-05	0.051 (0.015)	0.148 (0.057)	0.01
Coefficient B (SD)	0.1519	0.153 (0.002)		
Coefficient C (SD)	0.9499	0.550 (0.023)	0.629	
HiPer-tex™ in SW $[LSL]$				
Coefficient A (SD)	7.40E-05	0.007 (0.001)	0.103 (0.034)	
Coefficient B (SD)	0.1261	0.126 (0.003)		
Coefficient C (SD)	0.8185	0.622 (0.003)	0.527 (0.013)	
Advantex® in SW $[HSL]$				
Coefficient A (SD)	4.884E-09	0.020 (0.008)		
Coefficient B (SD)	0.09021	0.088 (0.001)		
Coefficient C (SD)	0.97301	0.490 (0.009)		
Advantex® in SW $[LSL]$				
Coefficient A (SD)	2.996E-05	0.058 (0.018)	0.123 (0.036)	
Coefficient B (SD)	0.15174	0.154 (0.002)		
Coefficient C (SD)	0.93253	0.510 (0.015)		

3- Optimisation with the third function

The third function is a power function written as :

$$y=C\cdot\left(1-x^{A}\right)^{B} \qquad \text{With} \quad y=\frac{F}{Displacement} \quad \text{and} \quad x=\frac{N}{N_f}$$

As previously, the three coefficients, *A*, *B* and *C*, have been determined by using a *Matlab*© optimisation routine and a genetic algorithm. The results are summarized in *Fig. 40* and *Table 70*.

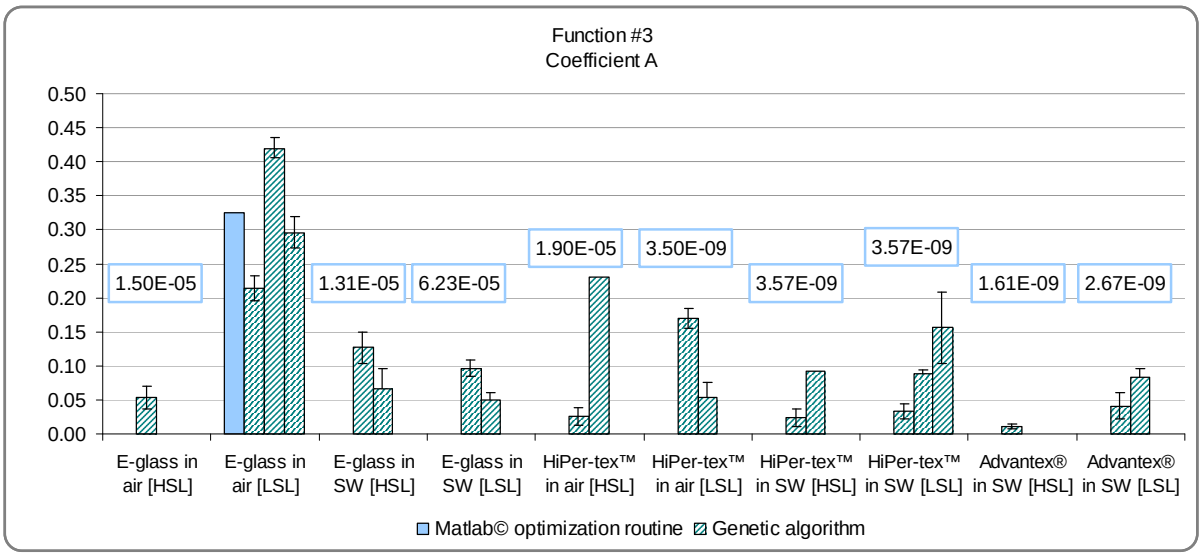

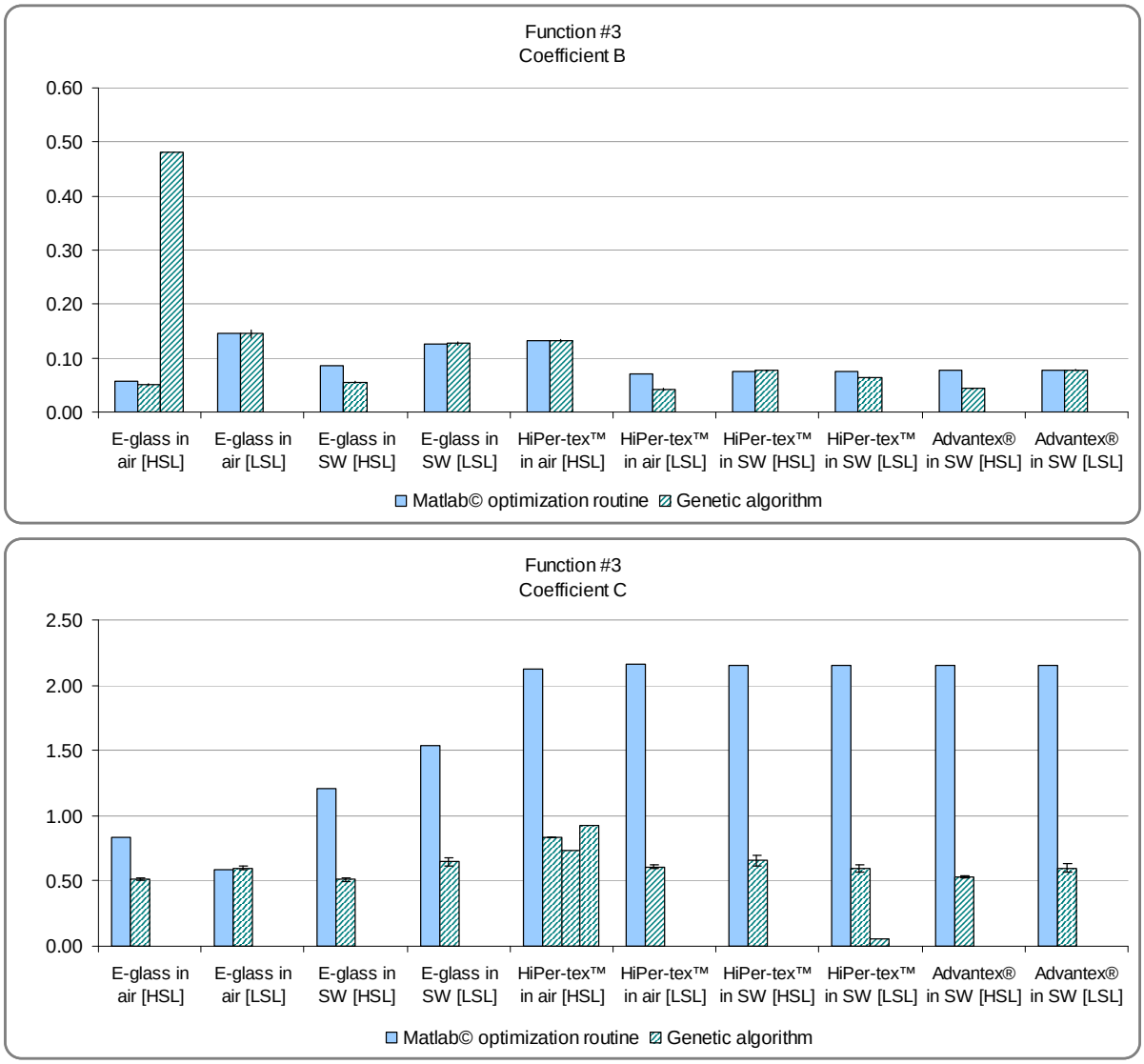

Fig. 40. *Graphical representation of the results obtained by Matlab© routine and genetic algorithm with the third function*

Table 70. *Summary of the results obtained by Matlab© routine and genetic algorithm with the third function*

Function #3	Matlab© optimization routine	Genetic algorithm		
E-glass in air $[HSL]$				
Coefficient A (SD)	1.50E-05	0.053 (0.017)		
Coefficient B (SD)	0.0563	0.050 (0.002)	0.480	
Coefficient C (SD)	0.835	0.515 (0.01)		
E-glass in air $[LSL]$				
Coefficient A (SD)	0.3248	0.214 (0.018)	0.418 (0.018)	0.296 (0.023)
Coefficient B (SD)	0.1458	0.145 (0.008)		
Coefficient C (SD)	0.5907	0.596 (0.014)		

E-glass in SW $[HSL]$						
Coefficient A (SD)	1.31E-05	0.127 (0.023)			0.067 (0.029)	
Coefficient B (SD)	0.0867	0.056 (0.001)				
Coefficient C (SD)	1.2059	0.510 (0.013)				
E-glass in SW $[LSL]$						
Coefficient A (SD)	6.23E-05	0.096 (0.012)			0.049 (0.011)	
Coefficient B (SD)	0.1248	0.127 (0.003)				
Coefficient C (SD)	1.5351	0.646 (0.03)				
HiPer-tex™ in air $[HSL]$						
Coefficient A (SD)	1.90E-05	0.025 (0.013)			0.23	
Coefficient B (SD)	0.1324	0.132 (0.002)				
Coefficient C (SD)	2.1282	0.835 (0.002)		0.732		0.929
HiPer-tex™ in air $[LSL]$						
Coefficient A (SD)	3.50E-09	0.17 (0.015)			0.053	
Coefficient B (SD)	0.070531	0.042 (0.002)				
Coefficient C (SD)	2.1582	0.608 (0.017)				
HiPer-tex™ in SW $[HSL]$						
Coefficient A (SD)	5.19E+09	0.024 (0.0013)			0.093	
Coefficient B (SD)	0.0711	0.077 (0.001)				
Coefficient C (SD)	2.1498	0.659 (0.041)				
HiPer-tex™ in SW $[LSL]$						
Coefficient A (SD)	3.57E-09	0.034 (0.011)		0.088 (0.007)		0.156 (0.052)
Coefficient B (SD)	0.0757	0.063 (0.001)				
Coefficient C (SD)	21530	0.594 (0.027)			0.059	
Advantex® in SW $[HSL]$						
Coefficient A (SD)	1.61E-09	0.011 (0.003)				
Coefficient B (SD)	7.81E-02	0.044 (0.001)				
Coefficient C (SD)	2.149	0.533 (0.007)				
Advantex® in SW $[LSL]$						
Coefficient A (SD)	2.67E-09	0.041 (0.019)			0.083 (0.013)	
Coefficient B (SD)	0.076986	0.078 (0.001)				
Coefficient C (SD)	2.15	0.599 (0.029)				

4- Optimisation with the fourth function

The fourth function is an hyperbolic function written as :

$$y = C \cdot \frac{1 - x^A}{1 + x^B} \qquad \text{With} \quad y = \frac{F}{Displacement} \quad \text{and} \quad x = \frac{N}{N_f}$$

In the case of the fourth function, only genetic algorithms have been used to determine the coefficients, *A*, *B* and *C*. The results are summarized in *Fig. 41*and *Table 71*.

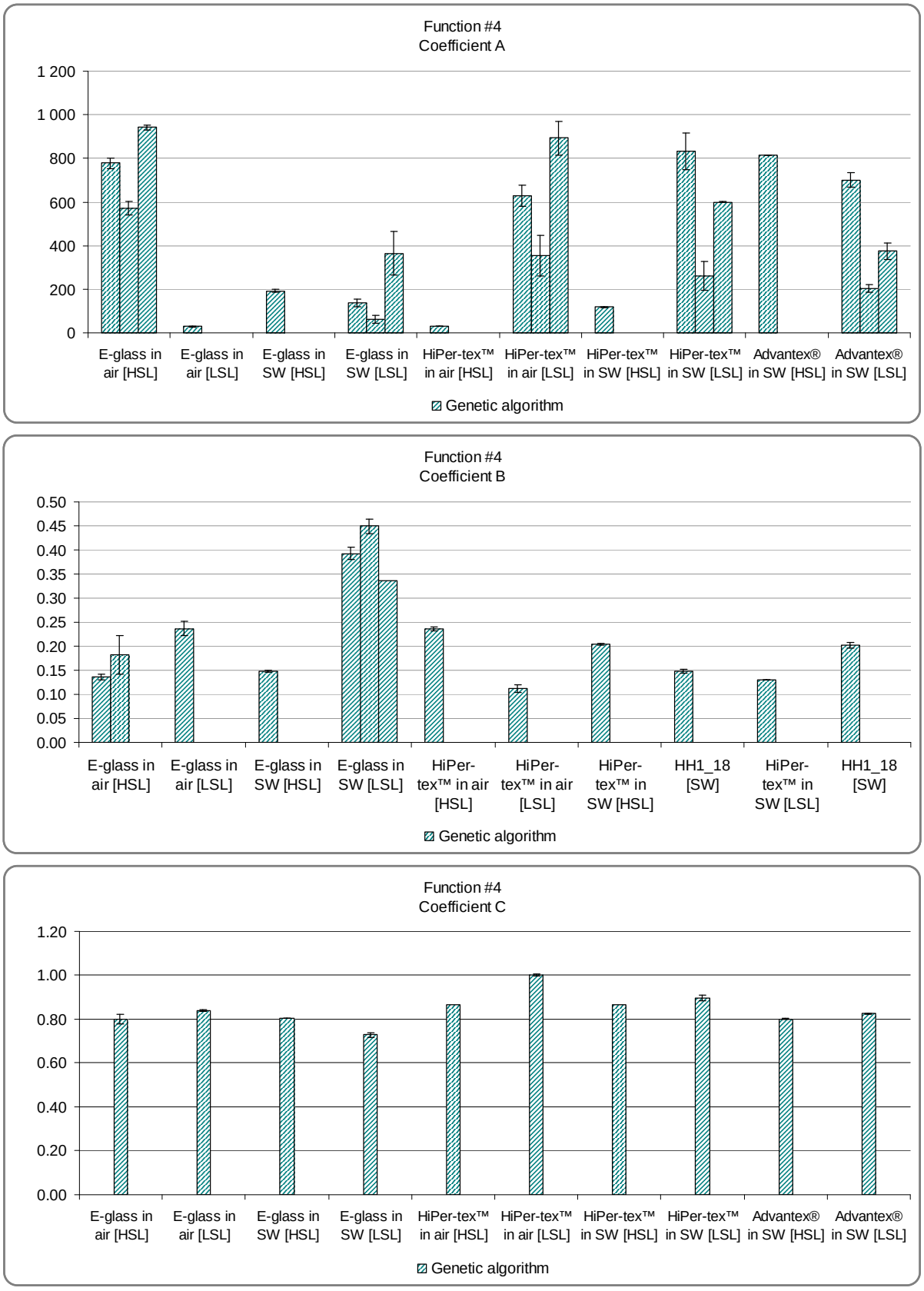

Fig. 41. *Graphical representation of the results obtained by Matlab© routine and genetic algorithm with the fourth function*

Table 71. *Summary of the results obtained by genetic algorithm with the fourth function*

Function #4	Genetic algorithm		
E-glass in air $[HSL]$			
Coefficient A (SD)	778.00 (24.30)	572.333 (30.892)	941.500 (12.021)
Coefficient B (SD)	0.136 (0.006)	0.182 (0.040)	
Coefficient C (SD)	0.800 (0.020)		
E-glass in air $[LSL]$			
Coefficient A (SD)	29.5 (2.654)		
Coefficient B (SD)	0.237 (0.015)		
Coefficient C (SD)	0.839 (0.005)		
E-glass in SW $[HSL]$			
Coefficient A (SD)	191.3 (6.378)		
Coefficient B (SD)	0.149 (0.002)		
Coefficient C (SD)	0.804 (0.001)		
E-glass in SW $[LSL]$			
Coefficient A (SD)	136.00 (17.349)	63.000 (16.971)	365.000 (99.602)
Coefficient B (SD)	0.393 (0.013)	0.450 (0.015)	0.337
Coefficient C (SD)	0.728 (0+011)		
HiPer-tex™ in air $[HSL]$			
Coefficient A (SD)	30.53 (0.411)		
Coefficient B (SD)	0.237 (0.004)		
Coefficient C (SD)	0.867 (0.004)		
HiPer-tex™ in air $[LSL]$			
Coefficient A (SD)	630.00 (49.497)	354.333 (92.089)	892.400 (78.986)
Coefficient B (SD)	0.112 (0.009)		
Coefficient C (SD)	1.003 (0.014)		
HiPer-tex™ in SW $[HSL]$			
Coefficient A (SD)	117.800 (1.814)		
Coefficient B (SD)	0.205 (0.002)		
Coefficient C (SD)	0.865 (0.001)		
HiPer-tex™ in SW $[LSL]$			
Coefficient A (SD)	833.500 (85.004)	261.500 (67.025)	599.000 (1.414)
Coefficient B (SD)	0.148 (0.004)		
Coefficient C (SD)	0.896 (0.003)		
Advantex® in SW $[HSL]$			
Coefficient A (SD)	815.942 (0.000)		
Coefficient B (SD)	0.131 (0.000)		
Coefficient C (SD)	0.802 (0.000)		
Advantex® in SW $[LSL]$			
Coefficient A (SD)	700.736 (32.125)	205.461 (18.060)	374.689 (38.043)
Coefficient B (SD)	0.202 (0.006)		
Coefficient C (SD)	0.825 (0.002)		

Annex 8

Preliminary study of the water absorption modelling
Influence of the variations of the parameters used

In order to define and quantify the influence of each parameter entered in the water absorption numerical modelling, a preliminary parametric study was performed. This study is divided into two parts. The first part is focussed on the influence of the geometric parameters. The second part is focussed on the influence of the parameters used to describe the kinetics of diffusion.

1- Influence of the geometric parameters

First we examine the influence of the geometric parameters such as the length, the width or the thickness of the specimen. For the global shape, the numerical models of water absorption have been create with a square shape, as weight gain coupons were square.

In order to define the influence of each geometric parameters on the computed results, it is necessary to specify an initial set of geometric data, summarized in *Table 72*. Then, each geometric parameter (the length and the thickness) has been increased and reduced by *20 %*. So, we obtain four new numerical models in addition to the initial one, as presented in *Table 73*. All these models have been characterized with the same physics settings (diffusion coefficient and initial conditions) and the same mesh (distributed mapped Lagrange quadratic elements).

The computed results observed for each geometry are the evolution of the normalized weight gain as a function of the time and the distribution of the normalized concentration in the coupon at a given time (*56* days). These comparative curves for the five geometries are presented on *Fig. 42*.

We can see that the different geometries all influence the maximum weight gain, but only the variations of the length of the specimen show an influence on the rate of the diffusion (*Fig. 42a*). By contrary, only the variations of the thickness of the specimen show an influence on the concentration in the coupon at a given time (*Fig. 42b*).

Table 72. *Set of initial geometric data*

Length [*mm*]	50
Thickness [*mm*]	5

Table 73. *Summary of the five set of geometric data*

	Length [*mm*]	Width [*mm*]	Notation
Initial geometry	50	5	Init
Geometry #1	**60**	5	L (+)
Geometry #2	**40**	5	L (-)
Geometry #3	50	**6**	th (+)
Geometry #4	50	**4**	th (-)

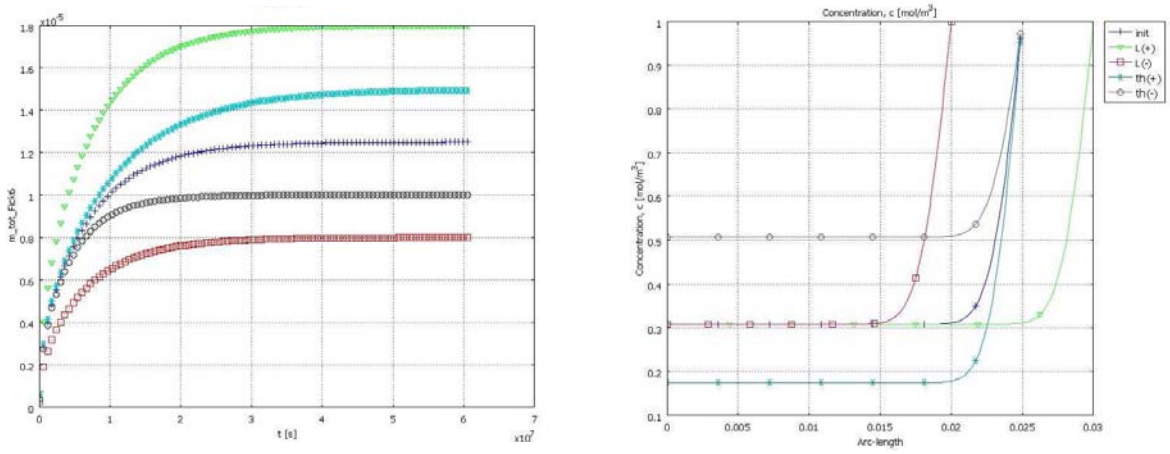

(a) *(b)*

Fig. 42. *Comparatives curves obtained with the five geometries :*
a) Evolution of the normalized weight gain, b) Distribution of the concentration

2- Influence of the material parameters

The second aspect studied is the influence of material parameters such as the diffusion coefficient *D* for a Fickian model and the diffusion coefficients D, β and γ for a Langmuir-type model.

An initial set of data has been defined and summarized in *Table 74*. With the same method as the one used for studying the influence of the geometric parameters, *3* Fickian models and *7* Langmuir-type models have been created. Their characteristics are summarized in *Table 75*.

Once again, the computed results observed for each geometry are the evolution of the normalized weight gain as a function of the time and the distribution of the normalized concentration in the coupon at a given time (*56* days). These comparative curves for the *3* geometries of the Fickian models are presented on *Fig. 43*. The results obtained for the Langmuir-type models are presented on *Fig. 44* (variations of *D*) and on *Fig. 45* (variations of β and γ*).*

We can see that the different sets of parameters all influence the rate of the diffusion without any change of the maximum weight gain.

Table 74. *Set of initial material parameters*

Fickian model	
D $[m^2/s]$	3.18E-13
Langmuir-type model	
D $[m^2/s]$	3.39E-13
β $[s^{-1}]$	1.16E-5
γ $[s^{-1}]$	7.28E-7

Table 75. *Summary of the 10 set of material data*

Fickian models	D $[m^2/s]$	Notation
Initial parameters	3.18E-13	Init
Model #1	3.81E-13	D (+)
Model #2	2.54E-13	D (-)

Langmuir-type models	D $[m^2/s]$	β $[s^{-1}]$	γ $[s^{-1}]$	Notation
Initial parameters	3.39E-13	1.16E-5	7.28E-7	Init
Model #1	**4.07E-13**	1.16E-5	7.28E-7	D (+)
Model #2	**2.71E-13**	1.16E-5	7.28E-7	D (-)
Model #3	3.39E-13	**1.40E-5**	7.28E-7	beta (+)
Model #4	3.39E-13	**0.90E-5**	7.28E-7	beta (-)
Model #5	3.39E-13	1.16E-5	**8.74E-7**	gamma (+)
Model #6	3.39E-13	1.16E-5	**5.82E-7**	gamma (-)

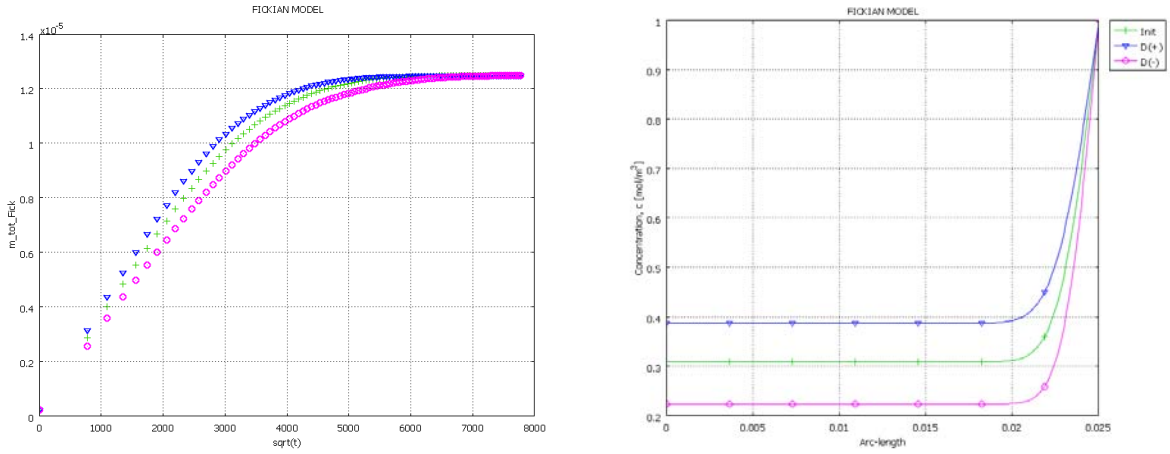

(a) *(b)*

Fig. 43. *Comparatives curves obtained with the three sets of parameters of the Fickian model : a) Evolution of the normalized weight gain, b) Distribution of the concentration*

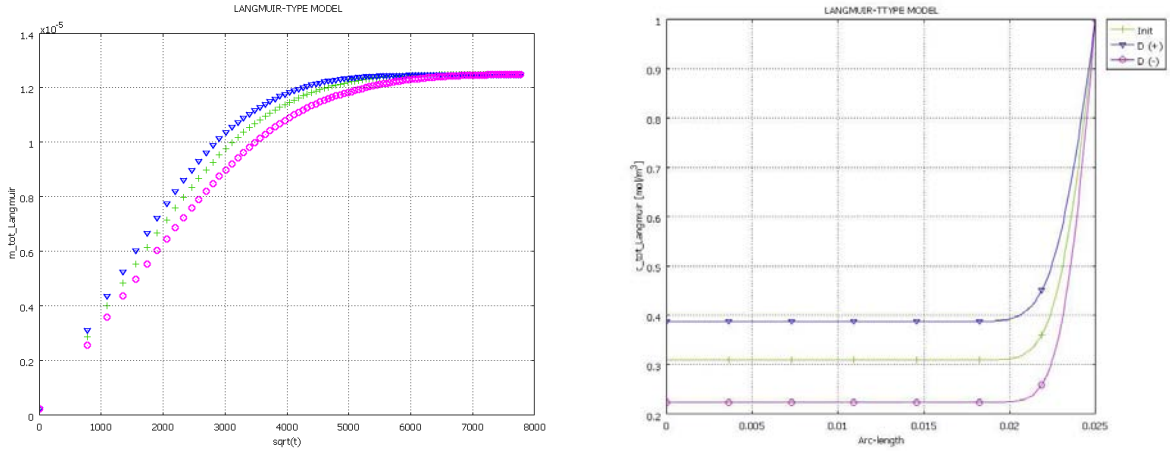

(a) *(b)*

Fig. 44. *Comparatives curves obtained with the three first sets of parameters of the Langmuir-type model : a) Evolution of the normalized weight gain, b) Distribution of the concentration*

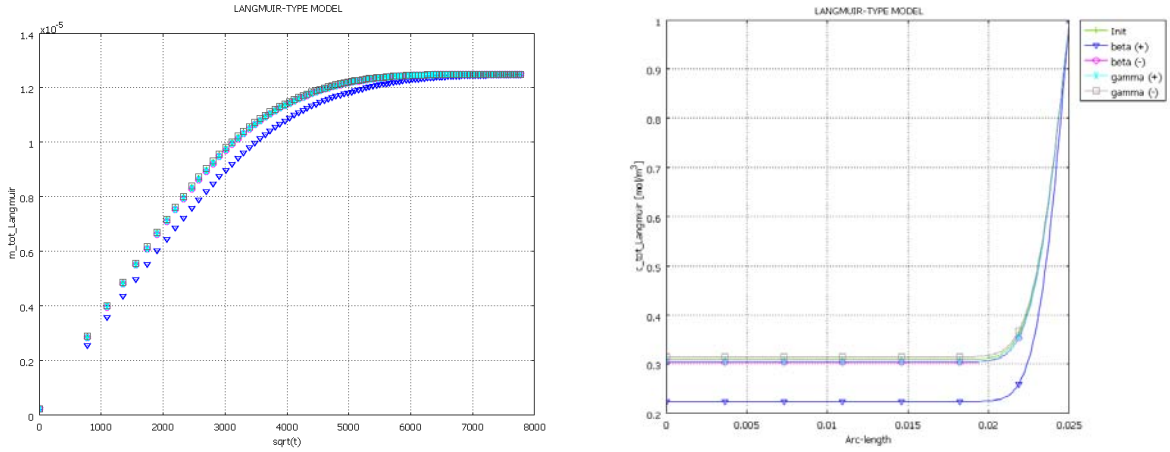

(a) *(b)*

Fig. 45. *Comparatives curves obtained with the four latest sets of parameters of the Langmuir-type model : a) Evolution of the normalized weight gain, b) Distribution of the concentration*

Annex 9

Summary of the modelling data used for the water absorption models

In order to define the physics settings of the water diffusion models, several constants and expressions have been defined.

The constants are summarized in *Table 76* for the pure resin material, in *Table 77* for the infused E-glass composite and in *Table 78* for the infused HiPer-tex™ composite. *Table 79* summarizes the global expressions used in these four numerical models.

Table 76. *Summary of the constants defined in the water diffusion modelling in the pure resin material*

Pure resin constants		
M_inf	2.75/100	Mass at saturation in [%]
D_pure_resin_4	0.0022 [mm^2/day]	Diffusion coefficient in SW at 4°C
M0_4	14.8840 [g]	Initial mass of the specimen at 4°C
length_4	50.91 [mm]	Length of the specimen at 4°C
thickness_4	4.99 [mm]	Thickness of the specimen at 4°C
D_pure_resin_20	0.0058 [mm^2/day]	Diffusion coefficient in SW at 20°C
M0_20	14.5666 [g]	Initial mass of the specimen at 20°C
length_20	50.53 [mm]	Length of the specimen at 20°C
thickness_20	4.96 [mm]	Thickness of the specimen at 20°C
D_pure_resin_40	0.0275 [mm^2/day]	Diffusion coefficient in SW at 40°C
M0_40	14.8246 [g]	Initial mass of the specimen at 40°C
length_40	50.74 [mm]	Length of the specimen at 40°C
thickness_40	4.99 [mm]	Thickness of the specimen at 40°C
D_pure_resin_60	0.0532 [mm^2/day]	Diffusion coefficient in SW at 60°C
M0_60	14.7152 [g]	Initial mass of the specimen at 60°C
length_60	50.78 [mm]	Length of the specimen at 60°C
thickness_60	4.96 [mm]	Thickness of the specimen at 60°C

***Table 77. Sum**mary of the constants defined in the water diffusion modelling in the infused E-glass composite*

Infused E-glass constants		
M_inf	0.75/100	Mass at saturation in [%]
D_Eglass_4	0.0010 [$mm^2/days$]	Diffusion coefficient in SW at 4°C
M0_4	25.6296 [g]	Initial mass of the specimen at 4°C
length_4	49.98 [mm]	Length of the specimen at 4°C
thickness_4	5.45 [mm]	Thickness of the specimen at 4°C
D_Eglass_20	0.0031 [$mm^2/days$]	Diffusion coefficient in SW at 20°C
M0_20	25.6630 [g]	Initial mass of the specimen at 20°C
length_20	49.86 [mm]	Length of the specimen at 20°C
thickness_20	5.50 [mm]	Thickness of the specimen at 20°C
D_Eglass_40	0.0150 [$mm^2/days$]	Diffusion coefficient in SW at 40°C
M0_40	25.3527 [g]	Initial mass of the specimen at 40°C
length_40	49.80 [mm]	Length of the specimen at 40°C
thickness_40	5.44 [mm]	Thickness of the specimen at 40°C
D_Eglass_60	0.1031 [$mm^2/days$]	Diffusion coefficient in SW at 60°C
M0_60	25.7981 [g]	Initial mass of the specimen at 60°C
length_60	49.89 [mm]	Length of the specimen at 60°C
thickness_60	5.52 [mm]	Thickness of the specimen at 60°C

***Table 78.** Summary of the constants defined in the water diffusion modelling in the infused HiPer-tex™ composite*

Infused HiPer-tex™ constants		
M_inf	0.70/100	Mass at saturation in [%]
D_HiPertex_4	0.0006 [$mm^2/days$]	Diffusion coefficient in SW at 4°C
M0_4	26.6451 [g]	Initial mass of the specimen at 4°C
length_4	50.81 [mm]	Length of the specimen at 4°C
thickness_4	5.26 [mm]	Thickness of the specimen at 4°C
D_HiPertex_20	0.0029 [$mm^2/days$]	Diffusion coefficient in SW at 20°C
M0_20	26.9428 [g]	Initial mass of the specimen at 20°C
length_20	50.89 [mm]	Length of the specimen at 20°C
thickness_20	5.37 [mm]	Thickness of the specimen at 20°C
D_HiPertex_40	0.0141 [$mm^2/days$]	Diffusion coefficient in SW at 40°C
M0_40	27.0371 [g]	Initial mass of the specimen at 40°C
length_40	50.75 [mm]	Length of the specimen at 40°C
thickness_40	5.46 [mm]	Thickness of the specimen at 40°C
D_HiPertex_60	0.0914 [$mm^2/days$]	Diffusion coefficient in SW at 60°C

M0_60	27.2481 $[g]$	Initial mass of the specimen at 60°C
length_60	51.02 $[mm]$	Length of the specimen at 60°C
thickness_60	5.47 $[mm]$	Thickness of the specimen at 60°C

Table 79. *Summary of the global expressions defined in the water diffusion modelling*

Global expressions		
m_tot_4	8*m_4	Water uptake at 4°C
V_4	(length_4)²*thickness_4	Volume of the specimen at 4°C
m_abs_4	M_inf*M0_4	Maximal water uptake at 4°C
c0_4	m_abs_4/V_4	Initial applied concentration at 4°C
m_tot_20	8*m_20	Water uptake at 20°C
V_20	(length_20)²*thickness_20	Volume of the specimen at 20°C
m_abs_20	M_inf*M0_20	Maximal water uptake at 20°C
c0_20	m_abs_20/V_20	Initial applied concentration at 20°C
m_tot_40	8*m_40	Water uptake at 40°C
V_40	(length_40^2*thickness_40	Volume of the specimen at 40°C
m_abs_40	M_inf*M0_40	Maximal water uptake at 40°C
c0_40	m_abs_40/V_40	Initial applied concentration at 40°C
m_tot_60	8*m_60	Water uptake at 60°C
V_60	(length_60)²*thickness_60	Volume of the specimen at 60°C
m_abs_60	M_inf*M0_60	Maximal water uptake at 60°C
c0_60	m_abs_60/V_60	Initial applied concentration at 60°C

Annex 10

Preliminary study of mechanical behaviour modelling
Influence of the variations of the parameters used

In order to define and quantify the influence of each parameter entered in the mechanical behaviour numerical modelling, a preliminary study has been performed. This study is divided in two parts. The first part is focussed on the influence of the geometric parameters such as the global shape, the dimensions, or the environment. The second part is focussed on the influence of the material properties such as the Young's moduli, the Poisson's ratio or the shear moduli.

1- Influence of the geometric parameters

The influence of the geometric parameters will be presented first. This study is divided in three parts, the influence of the global shape of the specimen on the mechanical behaviour, the influence of the variations of the dimensions and the modifications of the environment.

1.1- Study of the global shape of the specimen

In order to understand the influence of the global shape of the specimen in the mechanical behaviour modelling, two types of specimen have been defined in four-point bending and in tension. So, the responses of a rectangular and a dog-bone specimen have been studied.

The two geometries are defined according to an initial set of data (*Table 80*), with the same physics settings (mechanical properties and initial conditions) and the same mesh (tetrahedric Lagrange quadratic elements).

The computed results observed for each geometry are the longitudinal stresses. These results are estimated in the middle of the lower face and in the thickness of the specimens loaded in four-point bending and in the middle and along the specimens loaded in tension. In addition, the numerical results obtained for each type of specimen have been compared to the analytical results issued from a strength of materials approach (*Table 81*). The results are presented on *Fig. 46* for the rectangular specimen and on *Fig. 47* for the dog-bone specimen.

We can see that the computed and the analytical stresses are very similar for the two specimens in the two loading cases. The main differences are in the evolutions of the stresses along the two specimens loaded in tension because of the hypotheses of the analytical formulation. But, as the observed area is in the middle of the specimens, these variations are not critical for our study.

Table 80. *Set of initial geometric data for the rectangular and the dog-bone specimen*

Rectangular specimen	
Length $[mm]$	140
Width $[mm]$	25
Thickness $[mm]$	5
Dog-bone specimen	
Length $[mm]$	140
Width $[mm]$	25
Width (in the middle of the specimen) $[mm]$	10
Thickness $[mm]$	5

Table 81. *Summary of the analytical law used to define the mechanical behaviour*

	Rectangular specimen	Dog-bone specimen
Longitudinal stress in bending	$\sigma_{xx}=\frac{3FL}{4bh^2}$	$\sigma_{xx}=\frac{3FL}{4bh^2}$
Longitudinal stress in tension	$\sigma_{xx}=\frac{F}{S}$	$\sigma_{xx}=\frac{F}{S}$
Reference surface	$S=h\times b$	$S=h\times 2\left[\left(Rc+\frac{b_0}{2}\right)-\sqrt{Rc^2-x^2}\right]$ for $-25\le x\le 25$ $S=h\times b$ for $x<-25,\ x>25$

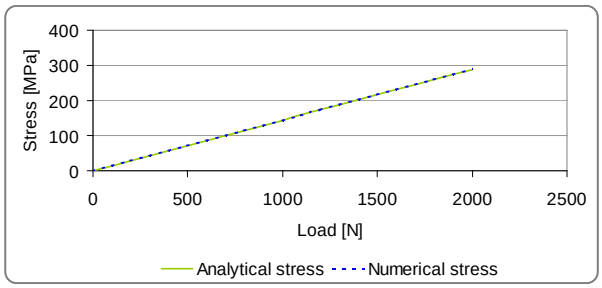

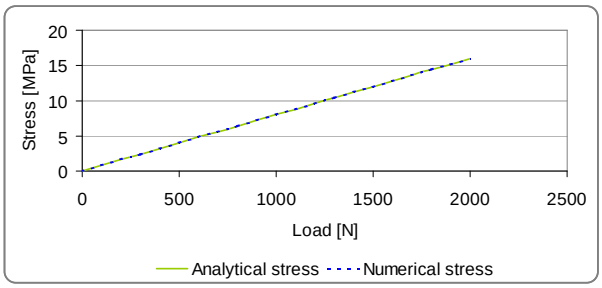

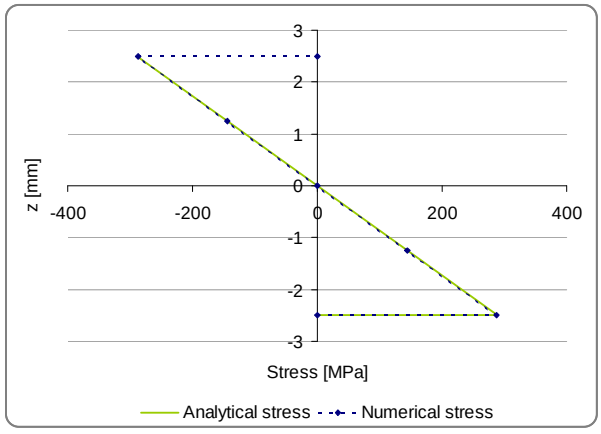

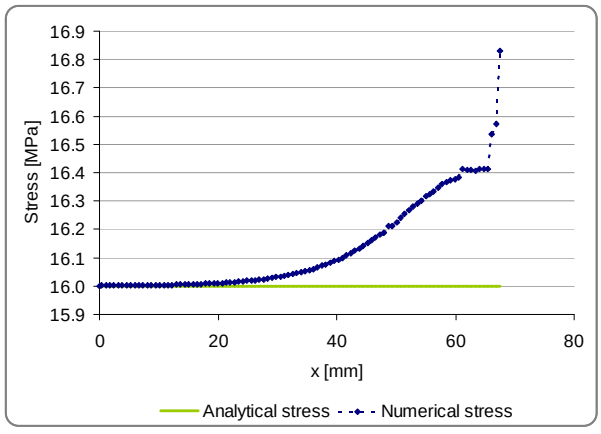

Rectangular specimen in bending *Rectangular specimen in tension*

Fig. 46. *Computed results obtained for the rectangular specimen in bending and in tension*

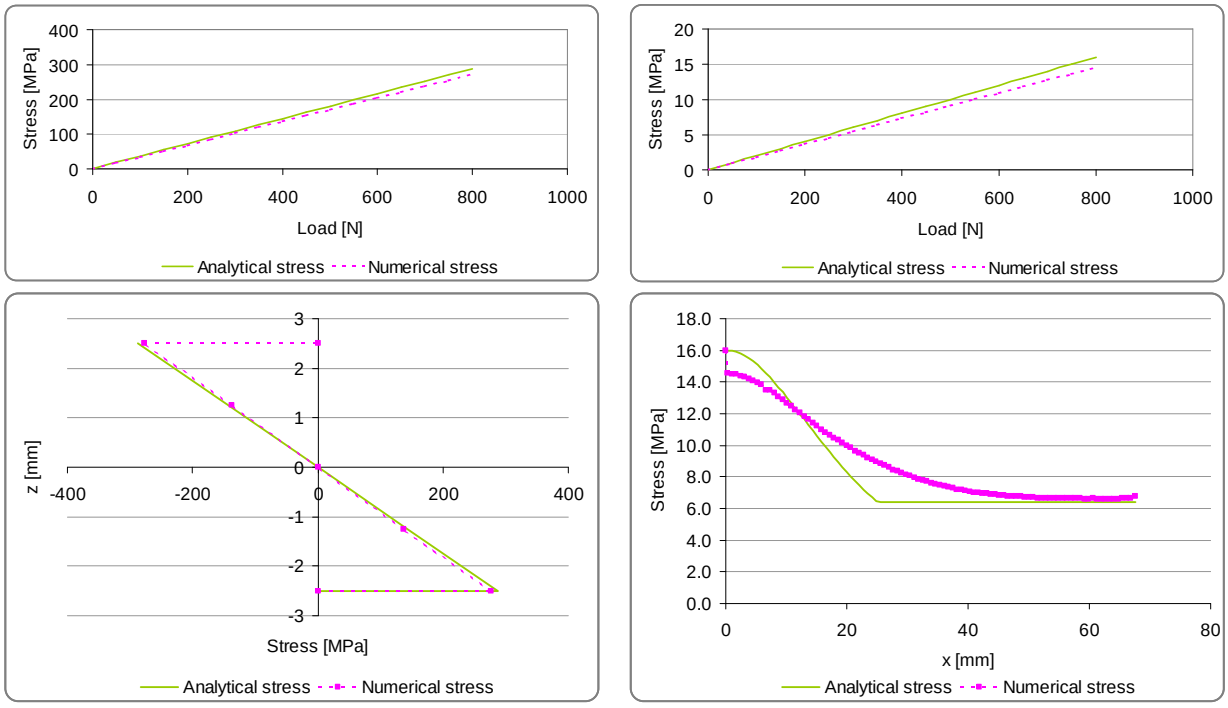

Dog-bone specimen in bending *Dog-bone specimen in tension*

Fig. 47. *Computed results obtained for the dog-bone specimen in bending and in tension*

1.2- Study of the variation of the dimensions of the specimens

The influence of the variations of the dimensions of the specimen on the mechanical response was then examined. In order to define the impact of each geometric parameter (length, width, thickness) on the computed results, an initial model has been defined. This model is defined as a dog-bone specimen with the initial dimensions (*Table 80*) which is loaded in four-point bending. Then, each geometric parameter has been increased by *20 %*. So, we obtain four new numerical models in addition to the initial one, as summarized in *Table 82*. All these models have been defined with the same physics settings (mechanical properties and initial conditions) and the same mesh (tetrahedric Lagrange quadratic elements).

The computed results observed for each geometry and compared are the evolution, as a function of the applied load, of the vertical displacement under the upper loading points (*Fig. 48a*) and the longitudinal stress on the lower face of the specimen (*Fig. 48b*).

When we compare the results obtained for the five geometries, we observe that the most influent parameter is the thickness of the specimen. This result is expected, based on the analytical formulation of the displacement and the stress in which the thickness has a more important weight than the other parameters.

Table 82. *Summary of the five sets of geometric data*

	Length [*mm*]	Width 1 [*mm*]	Width 2 [*mm*]	Thickness [*mm*]	Notation
Initial geometry	140	25	10	5	Init
Geometry #1	140	**30**	10	5	w1 (+)
Geometry #2	140	25	**12**	5	w2 (+)
Geometry #3	140	25	10	**6**	th (+)
Geometry #4	**168**	25	10	5	L (+)

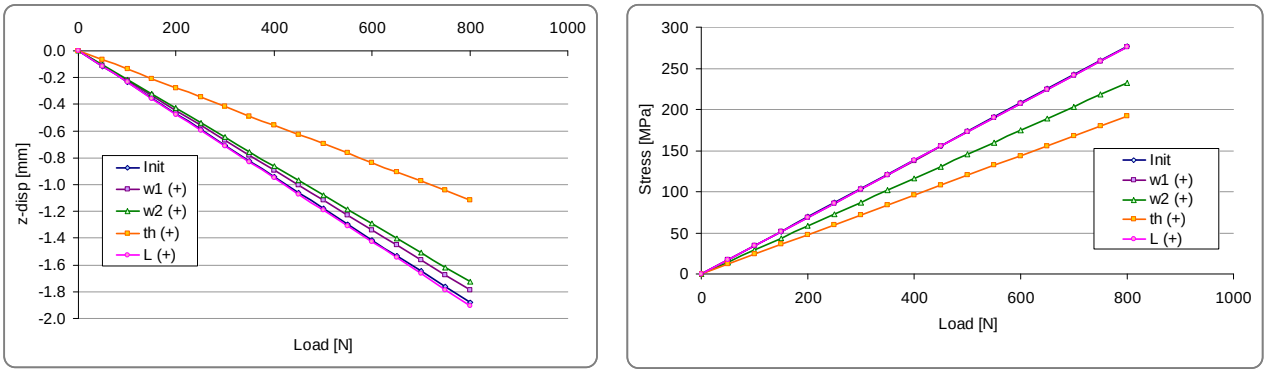

(a) *(b)*

Fig. 48. *Comparatives curves obtained with the five geometries : a) Evolution of the vertical displacement, b) Evolution of the longitudinal stress*

1.3- Study of the variation of the environment of the specimen

The final investigation of the geometric parameters examines the influence of the variations of the environment of the specimen, *i.e.* the distance between the loading points and their positions. All these models have been defined with the same physics settings (mechanical properties and initial conditions) and the same mesh (tetrahedric Lagrange quadratic elements).

Initial distances between loading points and the associated positions have been defined. Then, each parameter has been increased, the upper and the lower spans, and the loading points have been moved with the same distance between them. So, four new models have been defined in addition to the initial one (*Table 83*).

The computed results observed for each geometry and compared are the evolution, as a function of the applied load, of the vertical displacement under the upper loading points (*Fig. 49a*) and the longitudinal stress on the lower face of the specimen (*Fig. 49b*).

When we compare the computed results obtained for the five geometries, we can see that the most influent parameters are the distances between the loading points (upper and lower span), which is coherent with the analytical formulation which take into account the effective length of the specimen which is linked to the distance between the loading points. In addition, we can observe that a small horizontal displacement of the loading does not have an impact on the results computed at a given point. But, because of the specific shape of the dog-bone specimen, the conditions of symmetry are important as presented on *Fig. 50*.

Table 83. *Summary of the five sets of geometric data*

	Upper span [*mm*]	Lower span [*mm*]	Symmetry	Notation
Initial geometry	60	120	YES	Init
Geometry #1	**72**	120	YES	US (+)
Geometry #2	60	**138**	YES	LS (+)
Geometry #3	60	120	**NO** ***Displacement of 5 mm***	disp (5)
Geometry #4	60	120	**NO** ***Displacement of 10 mm***	disp (10)

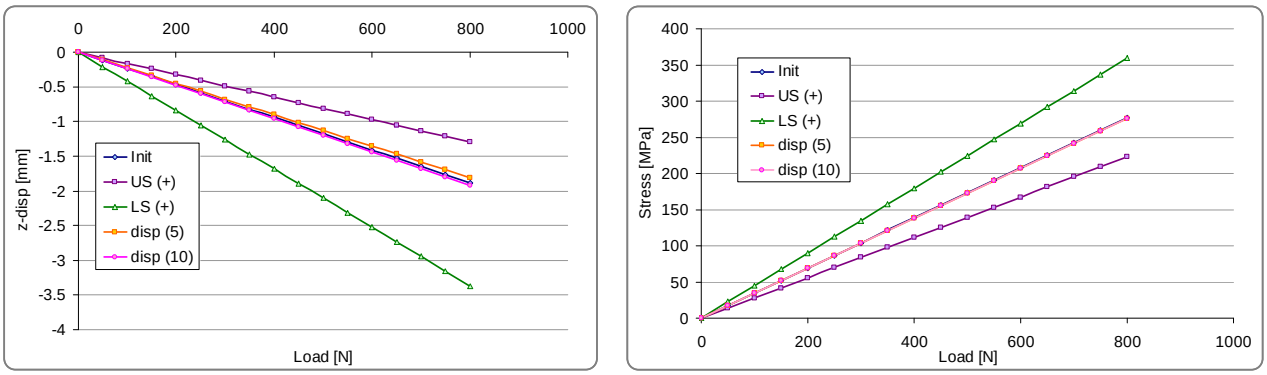

(a) *(b)*

Fig. 49. *Comparatives curves obtained with the five geometries : a) Evolution of the vertical displacement, b) Evolution of the longitudinal stress*

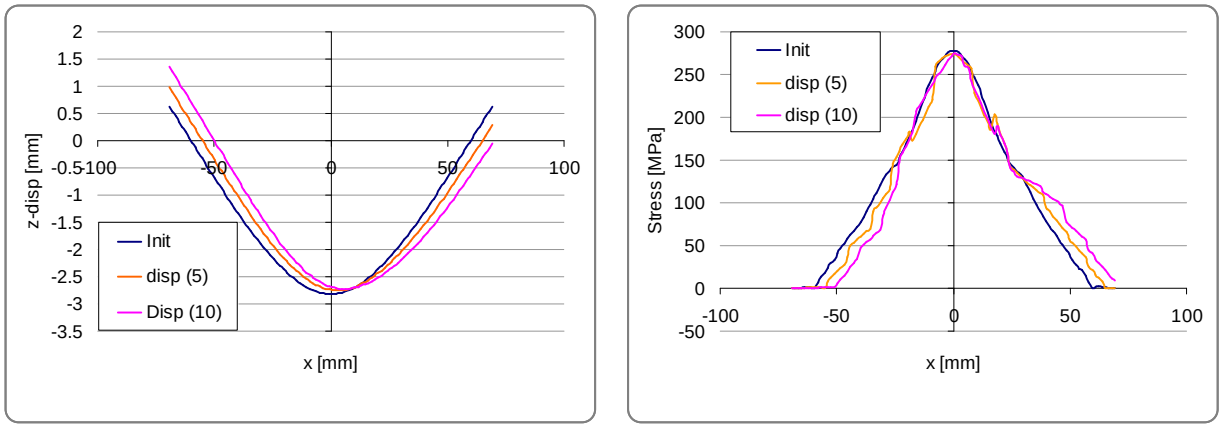

(a) *(b)*

Fig. 50. *Comparatives curves obtained with three geometries : a) Evolution of the vertical displacement, b) Evolution of the longitudinal stress*

2- Influence of the material parameters

The second investigation examines the influence of the material parameters, such as the Young's moduli, the Poisson's ratio or the shear moduli, on the mechanical response of a dog-bone specimen loaded in four-point bending. In order to have a complete understanding of the impacts of the material parameters, two hypotheses have been formulated. The first one

is to consider the composite material as an homogeneous orthotropic material according to the unidirectional orientation of the fibres. The second one is to define the composite material as a "bi-material" to simulate separately the lower part of the specimen loaded in tension and the upper part loaded in compression.

2.1- Study of an homogeneous orthotropic material

An homogeneous orthotropic material is defined with *9* independent constants of elasticity, *3* Young's moduli, *3* Poisson's ratio and *3* shear moduli. In order to define the influence of each parameter, an initial set of data has been defined, then nine new models have been defined by increasing by *20 %* each parameter (*Table 84*). These data are based on test results (CRP tests plus some additional transverse tests such as those in *Fig. 51*), together with literature values for the shear moduli.

The computed results have been defined according to the experimental data available. So, the vertical displacement of the loading points and the longitudinal strain in the middle of the specimen are observed (*Fig. 52*).

By comparing the ten models, we can see as expected that the most influent parameter is the longitudinal Young's modulus *Ex* as expected whatever the results considered.

Table 84. *Summary of the ten sets of material data*

	Ex [*GPa*]	Ey [*GPa*]	Ez [*GPa*]	Gxy [*GPa*]	Gyz [*GPa*]	Gxz [*GPa*]	νxy	νyz	νxz	Notation
Initial parameters	46.6	15.3	15.0	6.7	5.1	6.1	0.318	0.394	0.298	Init
Model #1	**55.92**	15.3	15.0	6.7	5.1	6.1	0.318	0.394	0.298	E_x (+)
Model #2	46.6	**18.36**	15.0	6.7	5.1	6.1	0.318	0.394	0.298	E_y (+)
Model #3	46.6	15.3	**18.00**	6.7	5.1	6.1	0.318	0.394	0.298	E_z (+)
Model #4	46.6	15.3	15.0	**8.02**	5.1	6.1	0.318	0.394	0.298	G_xy (+)
Model #5	46.6	15.3	15.0	6.7	**6.12**	6.1	0.318	0.394	0.298	G_yz (+)
Model #6	46.6	15.3	15.0	6.7	5.1	**7.32**	0.318	0.394	0.298	G_xz (+)
Model #7	46.6	15.3	15.0	6.7	5.1	6.1	**0.382**	0.394	0.298	nu_xy (+)
Model #8	46.6	15.3	15.0	6.7	5.1	6.1	0.318	**0.473**	0.298	nu_yz (+)
Model #9	46.6	15.3	15.0	6.7	5.1	6.1	0.318	0.394	**0.358**	nu_xz (+)

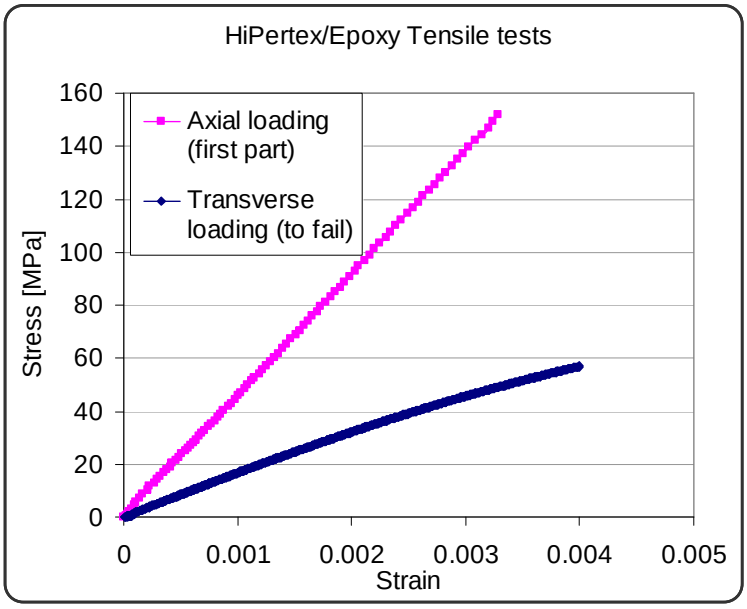

Fig. 51. *Example of results from tests to define longitudinal and transverse moduli*

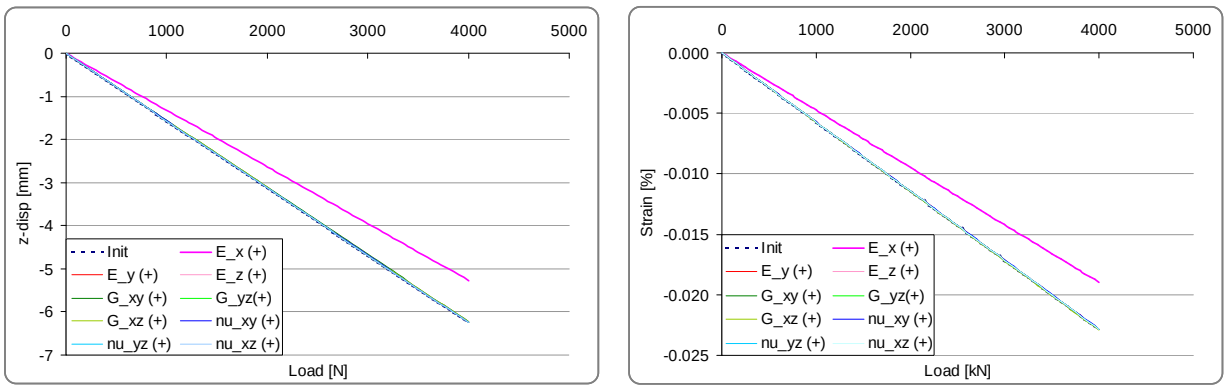

(a) *(b)*

Fig. 52. *Comparatives curves obtained with the ten set of parameters : a) Evolution of the vertical displacement, b) Evolution of the longitudinal strain*

2.2- Study of a “bi-material”

As seen previously, the longitudinal Young’s modulus is the most influent parameter in the mechanical response of a specimen loaded in four-point bending. However, the composite material studied does not have exactly the same material characteristics in tension and in compression. So, if we consider that the bending is a coupling between tension on the lower face of the specimen and compression in the upper face of the specimen, we can simulate the two loadings separately with two homogeneous orthotropic materials defined with two set of material parameters. The boundary between the two materials is considered to be the neutral fibre. Two cases have been studied, in the first one the position of the neutral fibre is fixed and the material parameters are varying, in the second one the material parameters are fixed and the position of the neutral fibre is varying.

a) First case : position of the neutral fibre fixed and variation of the material parameters

If we consider that the loading is fully symmetric and that the material is fully homogeneous, we can define the position of the neutral fibre in the middle of the specimen as presented on *Fig. 53*.

As seen previously, the most influent material parameter in the mechanical response of the specimen loaded in four-point bending is the longitudinal Young's modulus. So, the study has focussed on the variations of the longitudinal Young's moduli describing the tension and the compression while the other parameters (Poisson's ratio and shear moduli) are considered constant. The different sets of material parameters have been defined according to the ratio R between the tensile and the compressive Young's moduli. The initial set of parameters in tension (T) and in compression (C), summarized in *Table 85*, has been defined according to experimental data. The other sets of mechanical data have been defined with $0.5 \leq R \leq 1.5$.

The computed results are the vertical displacement of the loading points and the longitudinal strain in the middle of the specimens. The variations of these results are presented on *Fig. 54* as a function of the R parameter.

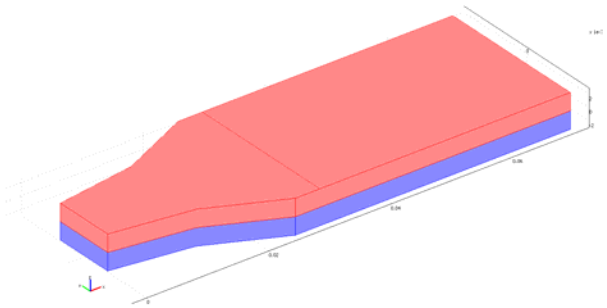

Fig. 53. *Graphical representation of a "bi-material" specimen*

Table 85. *Summary of the initial set of material data*

Initial parameters	Ex [*GPa*]	Ey [*GPa*]	Ez [*GPa*]	Gxy [*GPa*]	Gyz [*GPa*]	Gxz [*GPa*]	νxy	νyz	νxz	Notation
Lower part (T)	46.9	15.3	15.0	6.7	5.1	6.1	0.318	0.394	0.298	Init (*R=1.038*)
Upper part (C)	45.2									

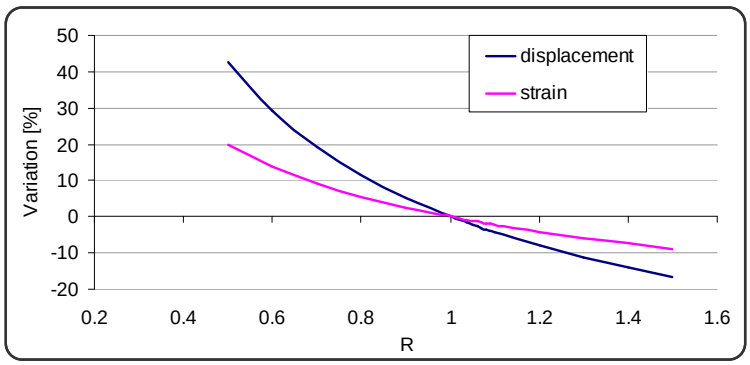

Fig. 54. *Variations of the vertical displacement and the longitudinal strain as a function of the R parameter*

b) Second case : material parameters fixed and displacement of the neutral fibre

If we consider that the loading is not fully symmetric and the material is not fully homogeneous, the neutral fibre may not be in the middle of the specimen. So, in order to quantify the influence of the position of the neutral fibre during four-point bending, three new models have been defined. The first one is defined with the neutral fibre in the middle, the second with the neutral fibre above the middle and the third with the neutral fibre below the middle. All these three models have been characterized with the same material parameters (*Table 86*).

The computed results observed are the vertical displacement of the loading point and the longitudinal strain in the middle of the specimen. By comparing their variations (*Table 87*), we can see that the displacement of the neutral fibre has a more important effect on the longitudinal strain than on the vertical displacement.

Table 86. *Summary of the initial set of material data*

Initial parameters	Ex [*GPa*]	Ey [*GPa*]	Ez [*GPa*]	Gxy [*GPa*]	Gyz [*GPa*]	Gxz [*GPa*]	νxy	νyz	νxz	Notation
Lower part (T)	54.2	15.3	15.0	6.7	5.1	6.1	0.318	0.394	0.298	Init (*R=1.038*)
Upper part (C)	45.2									

Table 87. *Summary of the variations of the vertical displacement and the longitudinal strain as a function of the position of the neutral fibre*

	Neutral fibre above the middle of the specimen (*z = 0.92 mm*)	Neutral fibre above the middle of the specimen (*z = - 0.92 mm*)
Variation of the vertical displacement	- 0.4 %	0.6 %
Variation of the longitudinal strain	6.6 %	8.2 %

Annex 11

Preliminary study of mechanical behaviour modelling
Influence of the loading points in four-point bending modelling
Influence of the number of layers in the modelling of the evolution of damage

In order to quantify the influence of the loading points in a the four-point bending tests modelling, a preliminary study was performed. Two different models were created and compared. In the first one the loading points were modelled. In the second model, the loading point were not modelled but their effects on the specimen were simulated.

In addition, a second preliminary study focussed on the influence of the number of layers in the modelling of the evolution of damage. During this study, four models with different numbers of layers were created and compared.

1- Influence of the loading points

During the four-point bending tests, the load is applied on the specimen through cylindrical loading points. This loading points do not provide a perfectly linear load but a load which is distributed on a surface, the contact surface. To simulate this, the loading points can be modelled and linked with the faces of the specimen using a contact relationship. But such contact problems are highly non-linear, and require significant computer resources to solve them. In addition, contact parameters are difficult to determine. So, in order to simplify the numerical model and thus reduce the computational time, the loading points might be removed from the model and replaced by their projections on the specimen. Two models, with the same material properties have been created and compared to validate this hypothesis.

The first numerical model has been created with a quarter of dog-bone specimen and two half loading points (upper and lower span) as presented on *Fig. 55*. Frictionless contacts have been determined with two sets of boundaries, a slave and a master domain (the slave boundaries cannot penetrate the master boundaries). The loading points were determined as the master sub-domains and the specimen as the slave sub-domain. In addition their meshes have to be coherent with this condition. The slave must be meshed at least two times finer than the master. The load is applied to the upper loading points and passed to the specimen while the lower loading point is fixed.

The second numerical model is defined without the loading points (*Fig. 56*). A surface representing the contact surface has been created on the upper face of the specimen to simulate the upper span. A linear edge has been created on the lower face to simulate the lower span. The applied load has been defined as a follower distributed load on the upper face of the specimen.

The main computed results observed are the evolution of the vertical displacement along the specimen and the distribution of the longitudinal stress along the specimen. These results have been computed for different values of load. They are presented on *Fig. 57* and *Fig. 58*.

When we compare the curves, we can note that there are no significant differences between the two numerical models, neither in terms of vertical displacement, nor in terms of longitudinal stress. So, in our case, provided we do not need to study damage mechanisms

under the load points in detail, modelling the contact between the loading points and the specimen is not necessary. The loading points can be simulated by a distributed follower load on the upper face of the specimen.

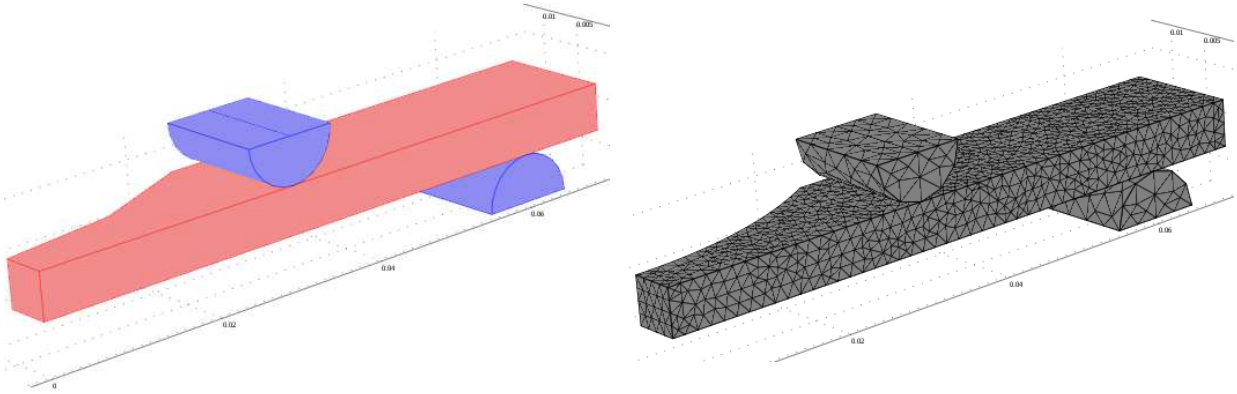

Fig. 55. *Geometrical view and mesh of the quarter specimen modelled with the loading points*

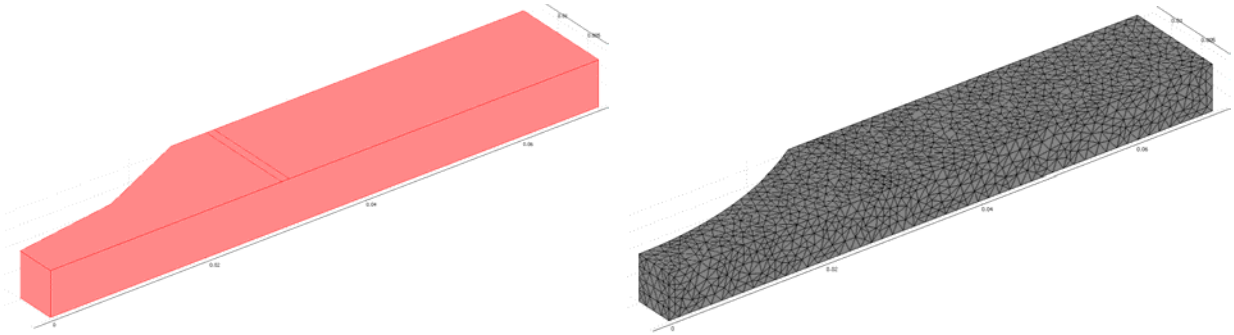

Fig. 56. *Geometrical view and mesh of the quarter specimen modelled without the loading points*

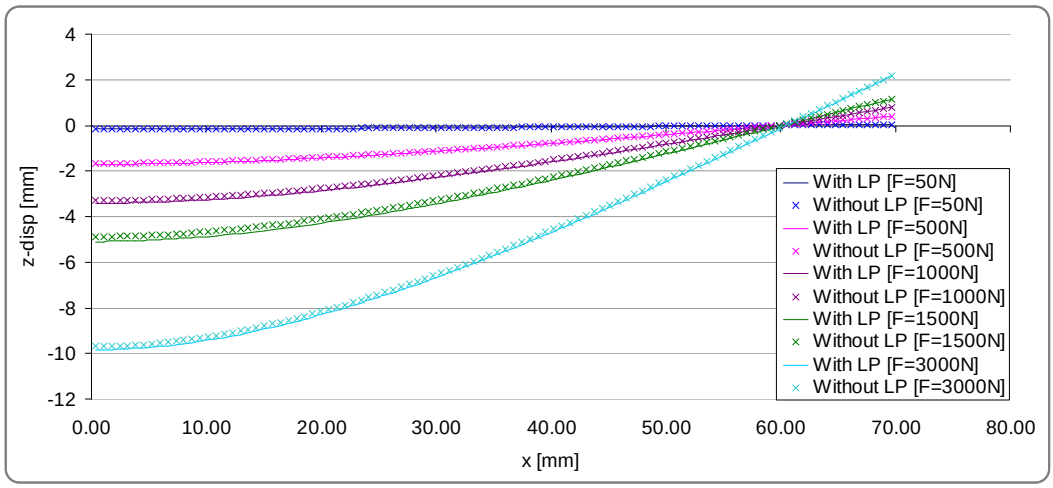

Fig. 57. *Evolution of the vertical displacement of the specimens for different loads (LP is Load Point model)*

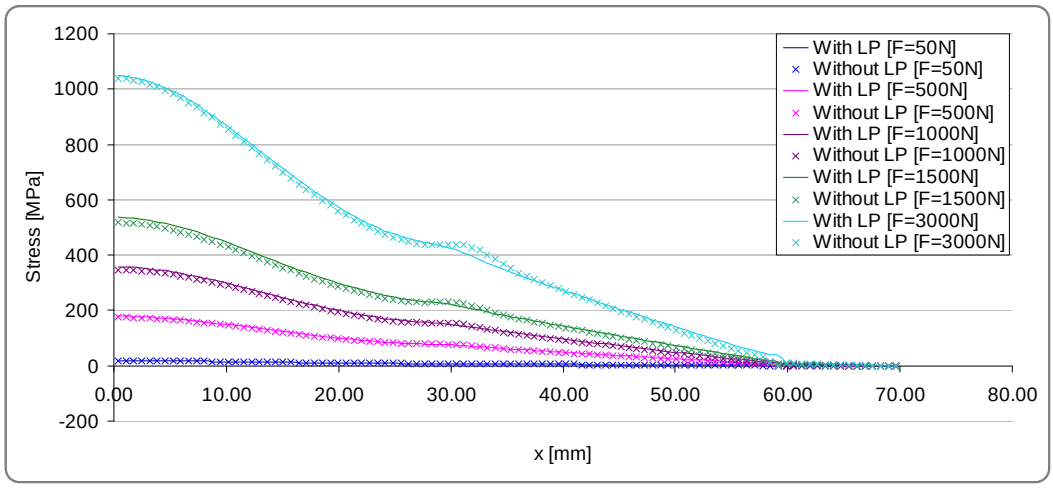

Fig. 58. *Evolution of the longitudinal stress of the specimens for different loads*

2- Influence of the number of layers

To simulate the evolution of damage during fatigue experiments, the specimen is divided into layers. Each layer is considered as an homogeneous independent material with its own material properties which vary during the modelling. Increasing the number of layers may be more accurate but increases modelling time significantly. In order to check the influence of the number of layers on the mechanical behaviour, four numerical models were defined and compared. The first one is formed of only one layer, the second is formed of six layers, the third is formed of ten layers and the last one is formed of fifteen layers as presented on *Fig. 59*.

For this comparison of numerical models, all the layers were defined with the same mechanical characteristics. The same boundary settings and the same loading conditions were applied. The main results observed are the evolution of the vertical displacement (*Fig. 60*) of the neutral axis considered to be in the middle of the specimen, and the longitudinal stress (*Fig. 61*) in the thickness of the specimen.

When we compare the computed results obtained for the different numerical models, we can note that there is no difference between them in terms of displacement whatever the number of layers considered. If we compare the computed results obtained in terms of distribution of longitudinal stress in the thickness of the specimens, we observe that there are again no significant differences between the four models. When we focus on the upper face of the specimens where the longitudinal compressive stress is maximal (*Fig. 62*), we can note some differences in the distribution. As these differences are less than *5 %*, we can consider that they might only be due to the differences in mesh size between the different models.

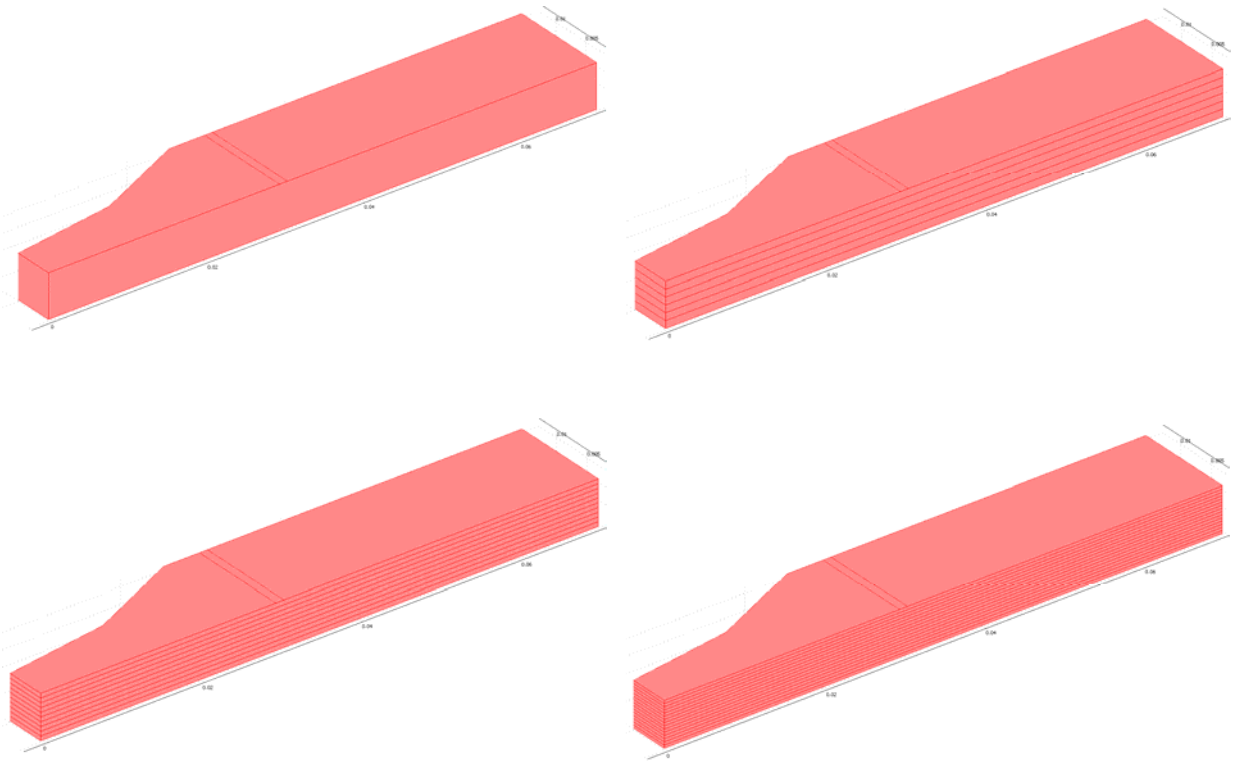

Fig. 59. *Views of the four different numerical models used to study the influence of the number of layers*

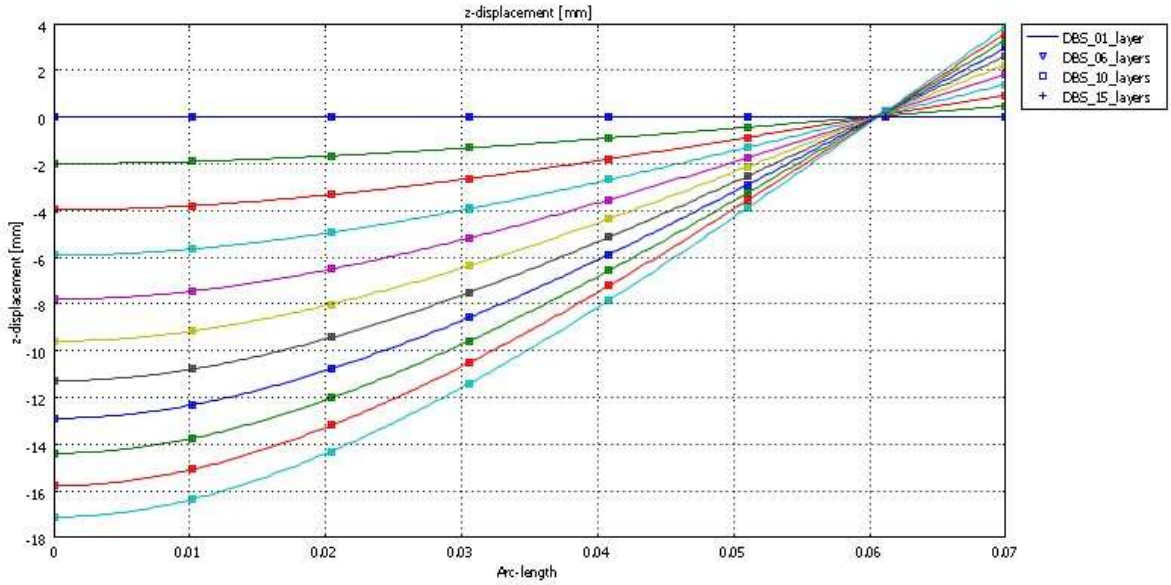

Fig. 60. *Evolution of the vertical displacements of the different specimens for different load values*

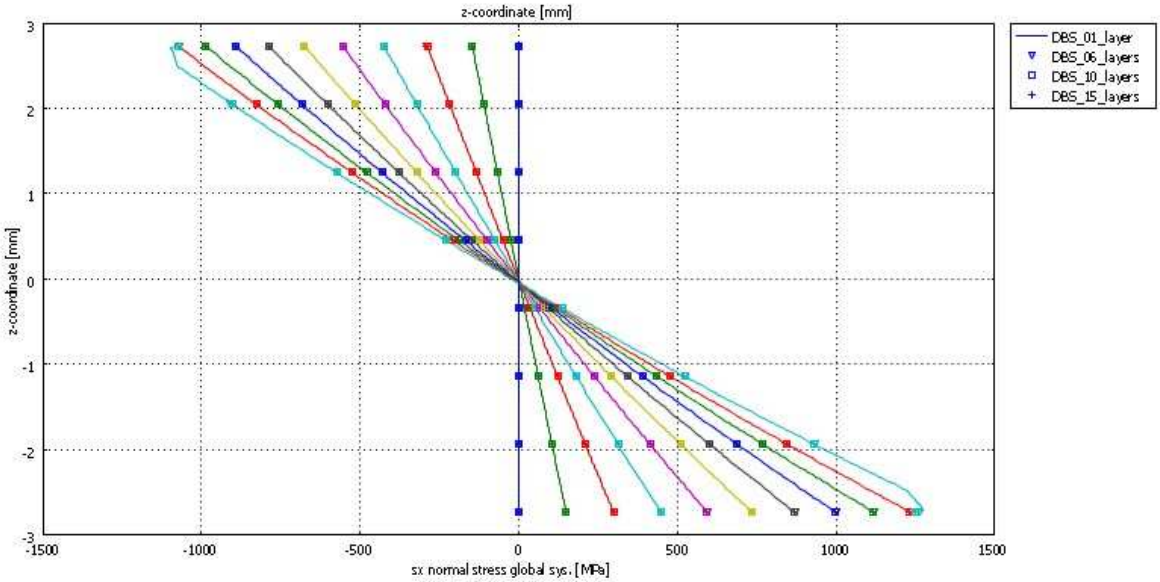

Fig. 61. *Evolution of the distribution of stress in the thickness of the different specimens*

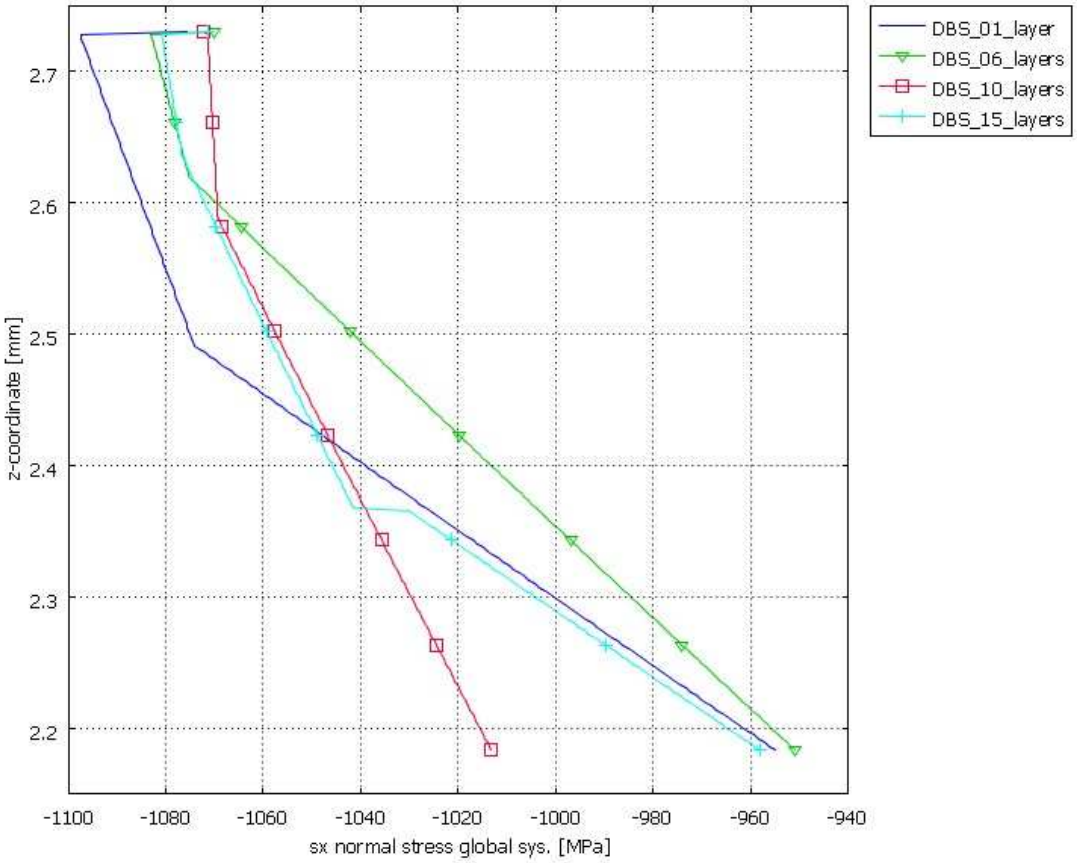

Fig. 62. *Zoom view of the evolution of the distribution of stress in the thickness of the different specimens*